UNIVERSIDADE ESTADUAL PAULISTA "JÚLIO DE MESQUITA FILHO"
FACULDADE DE ENGENHARIA
CAMPUS DE ILHA SOLTEIRA

Rafael de Oliveira Teloli

New Contributions in the Analysis and Identification of Mechanical Systems with Hysteresis

Ilha Solteira

2021

Rafael de Oliveira Teloli

New Contributions in the Analysis and Identification of Mechanical Systems with Hysteresis

A thesis submitted to the Faculdade de Engenharia de Ilha Solteira - UNESP in partial fulfillment of the requirements for obtaining the Doctorate in Mechanical Engineering.
Knowledge area: Solid Mechanics

Advisor: Prof. Dr. Samuel da Silva

Ilha Solteira

2021

FICHA CATALOGRÁFICA
Desenvolvido pelo Serviço Técnico de Biblioteca e Documentação

T277n

Teloli, Rafael de Oliveira.
New contributions in the analysis and identification of mechanical systems with hysteresis / Rafael de Oliveira Teloli. -- Ilha Solteira: [s.n.], 2021
257 f. : il.

Tese (doutorado) - Universidade Estadual Paulista. Faculdade de Engenharia de Ilha Solteira. Área de conhecimento: Mecânica dos Sólidos, 2021

Orientador: Samuel da Silva
Inclui bibliografia

1. Hysteresis. 2. Non-smooth oscillators. 3. Bouc-Wen model. 4. Duffing-Van der Pol model. 5. Orion beam. 6. Bolted structures.

Raiane da Silva Santos
Supervisora Técnica de Seção
Seção Técnica de Referência, Atendimento ao usuário e Documentação
Diretoria Técnica de Biblioteca e Documentação
CRB/8 - 9999

unesp

UNIVERSIDADE ESTADUAL PAULISTA

Câmpus de Ilha Solteira

CERTIFICADO DE APROVAÇÃO

TÍTULO DA TESE: New Contributions in the Analysis and Identification of Mechanical Systems with Hysteresis

AUTOR: RAFAEL DE OLIVEIRA TELOLI
ORIENTADOR: SAMUEL DA SILVA

Aprovado como parte das exigências para obtenção do Título de Doutor em ENGENHARIA MECÂNICA, área: Mecânica dos Sólidos pela Comissão Examinadora:

SAMUEL DA SILVA:26693971822 Assinado de forma digital por SAMUEL DA SILVA:26693971822 Dados: 2021.07.30 12:48:44 -03'00'

Prof. Dr. SAMUEL DA SILVA (Participaçao Virtual)
Departamento de Engenharia Mecânica / Faculdade de Engenharia de Ilha Solteira - UNESP

Prof. Dr. JOAO ANTONIO PEREIRA (Participaçao Virtual)
Departamento de Engenharia Mecânica / Faculdade de Engenharia de Ilha Solteira - UNESP

Prof. Dr. PAULO SÉRGIO VAROTO (Participaçao Virtual)
Departamento de Engenharia Mecânica / Escola de Engenharia de São Carlos - USP

Prof. Dr. DANIEL ALVES CASTELLO (Participaçao Virtual)
Departamento de Engenharia Mecânica / Universidade Federal do Rio de Janeiro - UFRJ

Prof. Dr. MATTHEW ROBERT WILLIAM BRAKE (Participaçao Virtual)
Department of Mechanical Engineering / William Marsh Rice University

Ilha Solteira, 30 de julho de 2021

To my wife, Daniele, and to my family
and friends, who always have been
there for the adventure.

Acknowledgments

The work presented in this document is the consequence of a project that I have dedicated my efforts to make a modest contribution to the solid mechanics area. But, of course, none of this would be possible without the people to whom I am grateful.

Halfway through my undergraduate experience, Professor Samuel da Silva extended me an invitation that completely transformed my journey towards research: ‘‘Would you like to learn how to do research and write a good scientific report?’’ And here I am, just over seven years under his guidance, I am pleased to write that his promise has been sufficiently fulfilled. We have established a friendly relationship, and I am grateful for our working in progress meetings, not forgetting the counterpart, the drink in progress, for motivating me with his motivation to do research, and especially for giving me enough freedom to explore my own ideas, but always around ‘‘to bring me back on track’’ and accomplish our primary goals.

I am also grateful to Professor Gaël Chevallier, who, even without knowing me properly at that time, welcomed me with open arms during my research internship at FEMTO-ST. Our discussions, sometimes in French, sometimes in English, sometimes in Portuguese, or even a mixture of all three, have inspired me not only on a professional level but also personally. Thank you for sharing your scientific and human qualities with me.

I extend my gratitude to Professors João Antônio Pereira, Americo Cunha Jr., Thiago Ritto, Pauline Butaud and Michael D. Todd, who directly contributed to this Thesis with much advice. I would also like to thank the members of the Thesis Jury for reviewing this work, Prof. Matthew Brake, Prof. Paulo Varoto, and Prof. Daniel Castello.

To the Mechanical Engineering Department of UNESP/FEIS, and all the technical staff, especially my colleague Carlos Santana, has always been there adjusting several experimental test-rigs and ‘‘putting out fires’’ when something went wrong.

To the financial support provided by São Paulo Research Foundation (FAPESP) for my direct doctorate (Grant No. 2016/21973-5), my research internship at the Institut FEMTO-ST (Grant No. 2019/06540-3) and for the regular project from Prof. Samuel

da Silva (Grant No. 2019/19684-3). I also acknowledge the Universal project from the National Council for Scientific and Technological Development (CNPq) (Grant No. 306526/2019-0).

If today I believe that happiness is a journey and not a destination, it is because of the fantastic people I met during my doctoral studies; I could not have wished for a better place. There were endless coffees, scientific discussions in between breaks, lunches, countless help I received during laboratory experiments, insights and inspirations that helped me conduct my research, and master and doctoral students who contributed to constructing a pleasant atmosphere to be in. I thank João Trentin, Maurício Iwanaga, Fred Albuquerque, and Lucas Chaim whose friendship I have had the pleasure of sharing since my undergraduate studies. Furthermore, I thank my friends Luís Villani, João Brogin, Gabriel Moimás, and Marcus Omori, who, besides being housemates for a long time, contributed decisively to the researcher that I am today; thank you all. Finally, I appreciate good friends I have found over the past few years, Luccas Miguel, Andreyson, Zanovello, Jessé, Léo Manetti, Iago Lessa, Vinícius, Oscar Scussel, Lucas Zanetti. You have been my family during this period, and I thank each of you from the bottom of my heart!

My colleagues in FEMTO-ST and the D-SMART Group provided all the help I needed during my research internship at Besançon. Furthermore, I am deeply grateful to my friends Svenja, Kevin, Margaux and Manu Bachy, with whom I had the pleasure to share the famous ‘‘miam’’ time, for the good mood when we were together either during the coffees or during the ≪soirées≫, and for all the scientific discussion we had, you collaborated to the progress of this Thesis. You have made my stay in France better, and I wish them all the best.

I dedicate this work to my parents, Antônia (*in memoriam*) and Nelson, for all their unprecedented support, love, and encouragement during this endeavor.

Most importantly, I extend my eternal gratitude to my soul mate, Daniele Olgado, who has always been by my side, sharing dreams and adventures. Your unconditional support and love are my driving force, you motivated me more than I deserved, and I could not have done any of this without you. Thank you very much!

I hope that you enjoy the reading!

FAPESP

CNPq

femto-st
SCIENCES &
TECHNOLOGIES

unesp

S.H.M. LAB
UNESP/ILHA SOLTEIRA
StructuralHealthMonitoring

PPGEM
PROGRAMA DE PÓS-GRADUAÇÃO
EM ENGENHARIA MECÂNICA

''Je suis de ceux qui pensent que la science est d'une grande beauté. Un scientifique dans son laboratoire est non seulement un technicien: il est aussi un enfant placé devant des phénomènes naturels qui l'impressionnent comme des contes de fées.''

Marie Curie ($\star$1867, †1934).

''God made the bulk; surfaces were invented by the devil.''

Wolfgang Ernst Pauli ($\star$1900, †1958).

Abstract

Structures exhibiting hysteresis behavior may present complex dynamic effects that restrict the application of conventional identification techniques. Among several systems in which these effects are present, structures assembled by bolted joints stand out. Thus, focusing on this subject, the dissertation presents new contributions in analyzing and identifying mechanical systems with hysteresis. Firstly, it is proposed a smoothing process to be applied on systems with hysteresis. For an equivalent system composed by a smooth nonlinear operator, the harmonic probing algorithm is then used to derive the higher-order frequency response functions (FRFs) computed by the Volterra series. To illustrate the applicability of the proposed approach, a Bouc-Wen model is simulated through a numerical integration scheme. Based on the smoothing process of the Bouc-Wen oscillator's restoring force, some practical regards on applying the harmonic balance method (HBM) for predicting the hysteresis behavior of such a model are also addressed. Then, through the analytical formulation of the higher-order FRFs for systems with hysteresis, an identification procedure formulated into a white-box Bayesian modeling framework is proposed to calibrate a stochastic Bouc-Wen model for predicting the dynamics of a BoltEd strRucTure (BERT) benchmark. The dissertation then introduces the proposition of a new lap-joint configuration, the so-called Orion beam. The new setup comprises two thin beams connected by three bolted joints with contact patches on each connecting bolt, in which there are bolts dedicated to ''static'' functions to guarantee structural integrity and those that perform ''damping'' functions to increase energy dissipation due to frictional contact. Additionally, a Duffing-Van der Pol oscillator is proposed to evaluate, through its calibrated parameters, the impact of several tightening torque conditions and multiple excitation amplitudes on the structural stiffness and damping. Finally, the dissertation introduces the use of the GP-NARX model to approximate dynamic systems with hysteresis. Initially, the proposed model's predictive applicability is evaluated on a numerical application involving the Bouc-Wen oscillator with hysteretic damping. Then, the GP-NARX model is proposed to describe the dynamics of the BERT benchmark.

Keywords: Hysteresis; Non-smooth oscillators; Bouc-Wen model; Duffing-Van der Pol model; Orion beam; BERT benchmark; GP-NARX; Bayesian inference; Volterra series; Harmonic balance method; Bolted structures; Uncertainties.

Resumo

As estruturas que exibem comportamento de histerese podem apresentar efeitos dinâmicos complexos que restringem a aplicação de técnicas convencionais de identificação. Entre os vários sistemas nos quais estes efeitos estão presentes, destacam-se as estruturas montadas por juntas parafusadas. Neste contexto, esta tese de doutorado apresenta novas contribuições na análise e identificação de sistemas mecânicos com histerese, tendo como foco estas estruturas. Primeiramente, é proposto um procedimento de suavização para ser aplicado em sistemas com histerese. Para um sistema equivalente composto por um operador não linear suave, o algoritmo de sondagem harmônica é então utilizado para obter as funções de resposta de frequência (FRF) de alta ordem computadas pela série de Volterra. Para ilustrar a aplicabilidade da abordagem proposta, um modelo Bouc-Wen é simulado através de um esquema de integração numérica. Com base no processo de suavização da força de restauração do oscilador Bouc-Wen, alguns aspectos sobre a aplicação do método de balanço harmônico para prever o comportamento de histerese de tal modelo também são abordados. Então, através da formulação analítica das FRFs de alta ordem, um procedimento de identificação formulado em uma estrutura de modelagem Bayesiana do tipo caixa branca é proposto para calibrar um modelo estocástico de Bouc-Wen para prever a dinâmica de uma estrutura montada por juntas parafusadas, nomeada como *benchmark BoltEd strRucTure* (BERT). A tese então propõe uma nova configuração de junção, a chamada viga de Orion, em que há parafusos dedicados a funções ‘‘estáticas’’, para garantir a integridade estrutural, e parafusos que realizam funções ‘‘amortecedoras’’, para aumentar a dissipação de energia devido ao contato friccional. Além disso, um oscilador de Duffing-Van der Pol é proposto para avaliar, através de seus parâmetros calibrados, o impacto de várias condições de torque de aperto e múltiplas amplitudes de excitação sobre a rigidez estrutural e amortecimento considerando o modo de vibração que promove uma deformação mais pronunciada ao redor da junção. Finalmente, a tese introduz o uso do modelo *GP-NARX* para aproximar a dinâmica de sistemas com histerese. Inicialmente, a aplicabilidade preditiva do modelo proposto é avaliada em um exemplo numérico envolvendo novamente o oscilador Bouc-Wen com amortecimento histérico. Em seguida, este trabalho propõe um modelo *GP-NARX* para descrever a dinâmica da BERT.

Palavras-chave: Histerese; Osciladores não-suaves; Modelo de Bouc-Wen; Modelo de Duffing-Van der Pol; Viga de Orion; *GP-NARX*; Inferência Bayesiana; Série de Volterra; Método do balanço harmônico; Estruturas parafusadas; Incertezas.

List of Figures

1 Examples of industrial scale structure specimens assembled with joint connections. 34
2 Damping efficiency according to operational conditions in terms of temperature and frequency. 36
3 Number of publications per decade in the engineering community involving the keyword ‘‘dry friction’’ according to the SCOPUS database. 36
4 Illustrative example of a bolted joint with emphasis on slipping motion. . . 39
5 Graphical abstract on the state-of-art review 46
6 Schemes of several bolted joints. (a) Single bolted joint (AHMADIAN; JALALI, 2007a; AHMADIAN; JALALI, 2007b); (b) Full symmetric double bolted joint (SONG, 2004); (c) Double bolted joints (JALALI *et al.*, 2019; FESTJENS; CHEVALLIER; DION, 2013);(d) Brake-Reuß beam (BRB), three bolted connections (BRAKE *et al.*, 2014). 48
7 Clamped-clamped beam with transverses interfaces (PEYRET *et al.*, 2010; DION; CHEVALLIER; PEYRET, 2013). 49
8 Other assembly designs. 51
9 Schematic representation of different types of setup. (a) bolted joint in free-free conditions (SONG, 2004; BRAKE *et al.*, 2014; JALALI *et al.*, 2019); (b) bolted joint in clamped-clamped or clamped-free conditions (FESTJENS; CHEVALLIER; DION, 2013; PEYRET *et al.*, 2010; DION; CHEVALLIER; PEYRET, 2013; PEYRET; DION; CHEVALLIER, 2016); (c) bolted joint with inertial loadings (GAUL; LENZ, 1997);(d) Impact hammer;(e) Vibration shaker; (f) Voice coil; (g) Piezoelectric device. 55
10 Comparison between different excitation types. 59
11 Schematic illustration of stress distribution described by the Mindlin model (MINDLIN, 1949) between a sphere and a plane regarding (a) the contact area and (b) the contact between a sphere and a plane under the influence of the tangential force. In both figures, $2c$ and $2c$ are the stick zone diameter and the surface diameter, respectively; $\mu\sigma_0$ and τ represent are the stress due to the normal and tangential loads, respectively. 61

12 Schematic illustration of fretting contact of nominally flat rough surfaces investigated by Eriten, Polycarpou and Bergman (2010), in which z exemplifies the asperity height. 61
13 Schematic illustration of the (a) linear elastic element and the (b) Adjusted Iwan element. In both figures, V and M are the shear forces and bending moments, respectively; each element contains 2-DoF, Θ and u, which are the rotation angle and the vertical deflection, respectively; k is the stiffness; l and h are the length and height of the beam element. 64
14 Schematic illustration of: (a) thin layer element, in which G, τ and φ are the shear modulus, stress and angle; A is the contact area; d and u are the layer thickness and relative displacement, respectively. (b) ZTE, in which $\xi \times \eta$ is the tangential plane natural coordinate and n is the normal direction. 65
15 Schematic illustration of (a) whole joint element; (b) node-to-node element, in which k_T and k_n are the tangential and normal stiffness, N_0 is the normal force and μ is the friction coefficient. 66
16 Example of hysteresis loop in time continuous domain for a bounded loading-unloading input. – – – is the loading output and – the unloading output. 75
17 Illustrative example of the hysteresis loop. —— represents unloading regime of motion whereas —— represents the loading one. 78
18 Convergence analysis of the nonlinear operator representing the hysteretic restoring force of the Bouc-Wen benchmark. ■ represents $N_s = 1$, ■ represents $N_s = 2$, ■ represents $N_s = 3$ and ■ is for $N_s = 4$. 94
19 Comparison between the restoring forces obtained from the Bouc-Wen oscillator and through the nonlinear operator. – – – for the Bouc-Wen's response and – • – is for the nonlinear operator. The NMSE obtained is 2.15% and the dissipated energy of both hysteretic loops is ≈ 42.35 N.mm. 95
20 Frequency Response Functions. -- represents the kernel $\mathcal{H}_1(\omega)$, whereas --•-- is for the kernel $\mathcal{H}_1(3\omega)$. 96
21 Second-order Volterra kernels. 98
22 Leading diagonals of the second-order Volterra kernels. -- represents the kernels with $\lambda_2 > 0$, whereas --•-- is for the kernels that have $\lambda_2 < 0$. 99
23 Third-order Volterra kernels. 100
24 Leading diagonals of the third-order Volterra kernels. 102

25 Output of the identified Volterra model in a close-up view over 6 – 18 seconds. – represents the response of the Bouc-Wen oscillator by numerical integration and • is the response of the proposed Volterra model. The value of NMSE computed between the outputs is 2.7%. 103
26 Comparison between the outputs spectrum. – represents the output spectrum simulated from the Bouc-Wen and • is the spectrum predicted by the proposed Volterra model. 104
27 Representation of the Volterra model contributions. –, $y_1(t)$; – • –, $y_2(t)$ and – ▲ –, $y_3(t)$ 104
28 Comparison between the hysteresis loop responses with excitation amplitude of $A = 40$ N. – represents the restoring force of the Bouc-Wen model and • is the restoring force estimated through the Volterra model output. . 105
29 Bouc-Wen hysteresis loop for different forcing amplitudes. – represents the restoring force calculated through numerical integration and • is the restoring force by the Volterra model output. 105
30 Comparison between the response amplitudes for a sweep sine input. – represents the numerical response from the Bouc-Wen and • is the spectrum predicted by the proposed Volterra model. 106
31 Comparative error between different numbers of terms used in the Taylor series for approaching the hysteresis loop of the Bouc-Wen model. ■ represents $n = 2$ terms, ■ represents $n = 3$ terms, ■ represents $n = 4$ terms and ■ represents $n = 5$ terms. 112
32 Comparison between the hysteretic restoring forces of the Bouc-Wen model obtained from numerical integration of equations (4)-(4) and through the four different paths approached by the Taylor series. ▬ is the $\mathcal{Z}(y, \dot{y})$ term response by numerical integration, whereas --■-- represents $\mathcal{Z}_1$, --•-- represents $\mathcal{Z}_2$, --■-- represents $\mathcal{Z}_3$ and --•-- is $\mathcal{Z}_4$. 112
33 Comparison between the frequency response curves of the Bouc-Wen model obtained with numerical integration and through harmonic balance method considering an input level of 10N. ··· is the numerical integrated response, whereas –– is the fundamental harmonic and ▬ is the fundamental added to the third harmonic. 114

34 Normalized mean square error between the numerical integrated solution and the analytical responses. −− is the error between the fundamental harmonic and the numerical integrated curve, whereas ▬ is the error derived from the fundamental harmonic added to the third harmonic. The straight line ····· corresponds to the threshold error value of 5%. 114

35 Direct comparison between the hysteresis loop obtained by numerical integration and through the harmonic balance method considering different forcing conditions applied on the Bouc-Wen oscillator. ····· is the numerical integrated response, whereas ▬ corresponds to the analytical response. . . 115

36 Output identified by the harmonic balance method considering as input $u(t) = 40\sin\left(\frac{\omega_n}{3}t\right)$, in zoom between 11.15 and 11.5 seconds. ····· is the integrated numerical response, whereas ▬ corresponds to the analytical response. 116

37 Output identified by the harmonic balance method considering as input $u(t) = 40\sin\left(\omega_n t\right)$, in zoom between 11.15 and 11.5 seconds. ····· is the integrated numerical response, whereas ▬ corresponds to the analytical response. 116

38 Flowchart of the estimation procedure. *Step (1)* provides experimental measurements for each next step. *Step (2)* computes values for ω_n and ζ and provides prior knowledge about them; in *Step (3)*, after computing the experimental third-order kernel, the PDFs of $\{\zeta, \alpha, \delta\}^T$ are updated, including the PDF $\pi(\zeta)$ because of the uncertainty regarding experimental visualizations on the parameter, whereas ω_n is held at the mean value; estimated MAP of $\{\zeta, \alpha, \delta, \omega_n\}^T$ are used to construct the computational model in *Step (4)* and update $\pi(\gamma)$, then to evaluate and to validate the constructed model. 131

39 Experimental setup and the schematic representation illustrating the cantilever beam which carries a bolted joint connection. 132

40 Frequency response plots for different excitation amplitudes: ▬ for low amplitude level (0.05 V), △ for medium amplitude level (0.10 V), and ∘ for high amplitude level (0.20 V). 133

41 Variation of the Frequency Response Function calculated for different excitation amplitudes with 99% of confidence bands. ■ represents the confidence bands, whereas ▬ is the mean values. 134

42 Harmonic Amplitude filtered from the system output. △ for $Y(3\omega)$ and $*$ represents the $Y(\omega)$ amplitude. 135
43 Convergence test applied in the third-order Volterra kernel. 137
44 PDF of the random variables $\boldsymbol{\theta} = \{\zeta, \alpha, \delta\}^T$. In (a), — - — represents the PDF estimated after modal analysis, whereas in (a), (b) and (c), - - - is the Uniform PDF and —— is the posterior one. 138
45 Comparison between the leading diagonal of the third-order Volterra kernel estimated versus the experimental data. ▇ represents the 99% model response confidence bands, —— is the model response mean and • represents three experimental realizations. 139
46 PDF of the random variable γ. - - - represents the prior PDF, whereas —— is the posterior one. 140
47 Comparison between the frequency response functions estimated from the numerical Bouc-Wen versus the experimental data around the first vibrating mode. ▇ represents the 99% model response confidence bands, —— is the model response mean and • represents three experimental realizations. 140
48 Comparison between the frequency response functions estimated from the numerical Bouc-Wen model versus the experimental data around the first vibrating mode. ▇ represents the 99% model response confidence bands, —— is the model response mean and • represents three experimental realizations. 141
49 Verification and validation of the Bouc-Wen model for high excitation amplitude (0.20 V) considering a sweeping sine test. ▇ represents the 99% model response confidence bands, —— is the model response mean and • represents three experimental realizations. 141
50 Comparison between the identified hysteresis loop through the Bouc-Wen versus experimental data for several excitation amplitudes. ▇ represents the 99% model response confidence bands, —— is the model response mean and • represents three experimental realizations. 142
51 (a) Lap-joint 3D model CAD, which highlights the three contact patches, present only in one beam. (b) Patches beam picture. The central patch without friction marks because of the fully tightening, the external patch with friction marks because of the light tightening. (c) Lap-joint drawings CAD (lengths are in mm) - 2 beams, two clamp holes Ø4 mm, one excitation hole Ø5 mm, three contact patches. 147

52 Experimental setup picture. 148
53 Block diagram of the feedback controller of the excitation force. The current excitation force is compared to the desired one (setpoint), and the error is calculated. Then, the controller evaluates at which position of the control law it is must actuate. The voltage control signal is converted and applied to the shaker, which excites the Orion beam. The load cell measures the force applied and feeds back their values so it can be compared to the setpoint once again, and the process is restarted. 153
54 Representative example of the real-time controller actuating on the excitation amplitude. 154
55 FRF velocity from the experimental result. 156
56 Nonlinear behavior of the Orion lap-joint around 280 and 300 Hz for different torques (80 cNm and 20 cNm) distinguished by different colors, and for multiple excitation level (10 mN to 200 mN) distinguished by different line types and gradient color. 158
57 Nonlinear behavior of the Orion lap-joint around 280 and 300 Hz for different torques (80 cNm and 20 cNm) distinguished by different colors, and for multiple excitation level (10 mN to 200 mN) distinguished by different line types and gradient color. 159
58 Repeatability of the measurements for seven experimental runs in frequency response curves considering a tightening torques of 80 cNm and excitation amplitudes of 10 mN (solid line ——) and 250 mN (dash line – –); ——— represents the mean value for 7 lap-joint disassemblies, see Table 5. 161
59 Repeatability of the measurements in frequency response curves considering a tightening torque of 20 cNm and low excitation amplitude 10 mN. Figure 59(a) represents the measurements with the complete disassembly of the lap-joint (solid-lines), whereas Fig. 59(b) depicts the measurements without the disassembly, but with tightening/loosening of the bolts (——), see Table 6. 162
60 Torque impact at 10 mN excitation level. 164
61 Excitation level impact at 10 cNm torque. 166

62 Nonlinear behavior of the Orion lap-joint around 1665 and 1775 Hz for different torques (80 cNm, 30 cNm, 20 cNm, and 10 cNm) distinguished by different colors, and for multiple excitation level (10 mN to 250 mN) distinguished by different line types and gradient color. The greyscale curves show the behavior of a glued assembly. 167
63 Analysis of the Orion beam around 1665 and 1775 Hz. Torque and level impact on (a) the natural frequency, (b) the maximum amplitude and (c) the half-power bandwidth. 169
64 Evolution of calibrated parameters as function of several tightening torque conditions. 172
65 Comparison between the frequency response curves predicted by the Duffing-Van der Pol model (dashed lines — —) *versus* experimental measurements (solid lines ——) for different torques (Glued, 80 cNm, 30 cNm, 20 cNm and 10 cNm) considering an excitation amplitude of 200 mN. 173
66 Lags optimization surface $n_y \times n_u \times fit$. The optimal value of the lags (•) corresponds to 20 lags in the output and 17 lags in the input for a fit of 92.4 %. 186
67 Verification of the GP-NARX model for low excitation amplitude (10 N) considering a swept sine test. ▩ represents the 99% model-predicted output confidence bands, —— is the model response mean and • represents the Bouc-Wen data obtained by numerical integration. 187
68 Verification of the GP-NARX model for medium excitation amplitude (50 N) considering a swept sine test. ▩ represents the 99% model-predicted output confidence bands, —— is the model response mean and • represents the Bouc-Wen data obtained by numerical integration. 188
69 Verification of the GP-NARX model for high excitation amplitude (80 N) considering a swept sine test. ▩ represents the 99% model-predicted output confidence bands, —— is the model response mean and • represents the Bouc-Wen data obtained by numerical integration. 189
70 Validation of the GP-NARX model for low excitation amplitude (10 N) considering a sinusoidal input with excitation frequency at the linear resonance ω_n = 35.59 Hz. ▩ represents the 99% model-predicted output confidence bands, —— is the model response mean and • represents the Bouc-Wen data obtained by numerical integration. 191

71 Validation of the GP-NARX model for medium excitation amplitude (50 N) considering a sinusoidal input with excitation frequency at the linear resonance ω_n = 35.59 Hz. ▇ represents the 99% model-predicted output confidence bands, — is the model response mean and • represents the Bouc-Wen data obtained by numerical integration. 192
72 Validation of the GP-NARX model for high excitation amplitude (80 N) considering a sinusoidal input with excitation frequency at the linear resonance ω_n = 35.59 Hz. ▇ represents the 99% model-predicted output confidence bands, — is the model response mean and • represents the Bouc-Wen data obtained by numerical integration. 193
73 Validation of the GP-NARX model for low excitation amplitude (10 N) considering a random phase multisine excitation. ▇ represents the 99% model-predicted output confidence bands, — is the model response mean and • represents the Bouc-Wen data obtained by numerical integration. . 194
74 Validation of the GP-NARX model for medium excitation amplitude (50 N) considering a random phase multisine excitation. ▇ represents the 99% model-predicted output confidence bands, — is the model response mean and • represents the Bouc-Wen data obtained by numerical integration. . 195
75 Validation of the GP-NARX model for high excitation amplitude (80 N) considering a random phase multisine excitation. ▇ represents the 99% model-predicted output confidence bands, — is the model response mean and • represents the Bouc-Wen data obtained by numerical integration. . 196
76 BERT setup and the schematic representation illustrating the clamped-free beam conveying a bolted joint connection. 198
77 Frequency response curves for different excitation amplitudes: — is low (0.05 V), △ medium (0.10 V), and ∘ high (0.20 V) amplitude levels. 199
78 Variation of the Frequency Response Function calculated for different excitation amplitudes with 99% of confidence bands. ▇ represents the confidence bands, whereas — is the mean values. 199
79 Lags optimization surface $n_y \times n_u \times fit$. The optimal value of the lags (•) corresponds to 16 lags in the output and 10 lags in the input for a fit of 96.1 %. 201

80 Verification of the GP-NARX model for low excitation amplitude (0.05 V) considering a swept sine test. ▇ represents the 99% model-predicted output confidence bands, — is the model response mean and • represents ten experimental realizations. 202
81 Verification of the GP-NARX model for medium excitation amplitude (0.10 V) considering a swept sine test. ▇ represents the 99% model-predicted output confidence bands, — is the model response mean and • represents ten experimental realizations. 203
82 Verification of the GP-NARX model for high excitation amplitude (0.20 V) considering a swept sine test. ▇ represents the 99% model-predicted output confidence bands, — is the model response mean and • represents ten experimental realizations. 204
83 Validation of the GP-NARX model for medium excitation amplitude (0.15 V) considering a swept sine test. ▇ represents the 99% model-predicted output confidence bands, — is the model response mean and • represents ten experimental realizations. 205
84 Validation of the GP-NARX model for a high excitation amplitude (0.15 V) considering a sinusoidal amplitude with excitation frequency at 18 Hz. ▇ represents the 99% model-predicted output confidence bands, — is the model response mean and • represents ten experimental realizations. 206
85 Validation of the GP-NARX model for an excitation amplitude of 0.30 V considering a white noise input. ▇ represents the 99% model-predicted output confidence bands, — is the model response mean and • represents the experimental data. 207
A.1 Schematic illustration of two bodies subjected to sliding motion, with emphasis on the variables of interest considered throughout the Chapter. . 247
A.2 Schematic illustration of the friction force produced by (a) the Coulomb friction model and by (b) the Stribeck friction model. 249
A.3 Schematic illustration of the friction force produced by the Dahl model. . . 251
A.4 (a) represents a schematic illustration of Masing model, whereas (b) is the force × displacement plane, — is the backbone curve and ◯ are the reversal points. 254
A.5 Different arrangements of the Iwan model: (a) is the parallel-series arrangement, whereas (b) is the series-parallel. 255

A.6 Schematic illustration of a hysteresis loop generated by the Iwan model following the Masing hypothesis, where — is the backbone curve. 256

List of Tables

1 List of pictograms and their meanings (TELOLI *et al.*, 2022). 50
2 Bouc-Wen benchmark parameters. 93
3 MAP estimator, mean value μ and CV for each random variable. 137
4 Associated force and the equivalent joint pressure for each tightening torque applied and its coefficient of variation. 149
5 Repeatability of the measurements for seven experimental runs with disassembly of the lap-joint and considering a tightening torque of 80 Nm at two excitation amplitudes of 10 mN (low-level) and 250 mN (high-level). Mean values (μ), standard deviations (σ) and coefficients of variation (CV) of the parameters f_n, $A_{\max}$ and Δ_{BW}, see Fig. 58. 161
6 Repeatability of the measurements considering a tightening torque of 20 cNm and an excitation level of 10 mN. Mean values (μ), standard deviations (σ) and coefficients of variation (CV) of the parameters f_n, $A_{\max}$ and Δ_{BW}; for four measurements with the disassembly of the lap-joint and 4 measurements without the disassembly, but considering tightening/loosening of the bolts in different orders, see Fig. 59. 163
7 Torque impact at 10 mN excitation level. 165
8 Variations of Δf_n and $\Delta A_{\max}$ in absolute values. 168
9 Model parameters considering the glued condition for all excitation amplitudes. 171
10 Normalized mean square error between analytical responses and experimental data for several tightening torque conditions and multiple excitation level. 174
11 Bouc-Wen benchmark parameters (NOËL; SCHOUKENS, 2016b). 184

List of Acronyms

AFT	-	Alternating frequency-time
BERT	-	BoltEd stRucTure benchmark
BIBO	-	Bounded-input bounded-output
BRB	-	Brake-Reuß beam
CV	-	Coefficient of variation
DEP	-	Damping-energy plot
DIC	-	Digital Image Correlation
DoF	-	Degree-of-freedom
EMA	-	Experimental modal analysis
EMD	-	Empirical mode decomposition
EPMC	-	Extended periodic motion concept
FE	-	Finite element
FEP	-	Frequency-energy plot
FORSE	-	FOrced Response SuitE
FRF	-	Frequency response function
GP	-	Gaussian process
HBM	-	Harmonic balance method
KL	-	Kullback-Leibler
LNM	-	Linear normal mode
MCMC	-	Markov Chain-Monte Carlo
MISO	-	Multiple-input single-output
MRSE	-	Mean relative square error
NARX	-	Nonlinear AutoRegressive with eXogenous inputs
NNM	-	Nonlinear normal mode
NMSE	-	Normalized mean square error
NSI	-	Nonlinear system identification
PDF	-	Probability density function
PLL	-	Phase-locked loop

PNLSS	-	Polynomial nonlinear state-space
PSD	-	Power spectral density
QSMA	-	Quasi-static modal analysis
RIH	-	Rate-independent hysteresis
RMS	-	Root mean square
ROM	-	Reduced-order model
SDoF	-	Single-degree-of-freedom
SHM	-	Structural health monitoring
SISO	-	Single-input single-output
SQP	-	Sequential quadratic programming
ZTE	-	Zero-thickness element

List of Symbols

Latin Symbols

$\mathcal{L}(\bullet)$ Likelihood operator

$\ddot{y}$ Acceleration output signal

$\ddot{y}_1$ Second derivative with respect to time of the first-order contribution of the Volterra series

$\ddot{y}_2$ Second derivative with respect to time of the second-order contribution of the Volterra series

$\ddot{y}_3$ Second derivative with respect to time of the third-order contribution of the Volterra series

Δ_{BW} -3dB frequency bandwidth

$\dot{u}$ First derivative with respect to time of the input signal

$\dot{y}$ Velocity output signal

$\dot{y}_1$ First derivative with respect to time of the first-order contribution of the Volterra series

$\dot{y}_2$ First derivative with respect to time of the second-order contribution of the Volterra series

$\dot{y}_3$ First derivative with respect to time of the third-order contribution of the Volterra series

$\hat{\mathcal{H}}_3^{\mathrm{exp}}(\omega)$ Experimental third-order Volterra kernel

$\hat{F}$ RMS force amplitude

$\hat{y}^{\mathrm{exp}}$ Experimental displacement output

$\mathbb{X}$ Normalized random variable

$\mathbf{I}$ Identity matrix

$\mathbf{K}(\cdot,\cdot)$ Covariance matrix

$\mathbf{M}$ Mass matrix

$\mathbf{x}_i$ Input observations

$\mathbf{y}_i$ Process observations

$\dot{\mathcal{Z}}$ First derivative with respect to time of the hysteretic restoring force

$\mathcal{A}$ Cosinusoidal coefficients of the nonlinear restoring force

$\mathcal{A}_0$ Zero-order coefficient of the nonlinear restoring force

$\mathcal{B}$ Sinusoidal coefficients of the nonlinear restoring force

$\mathcal{H}_1(\bullet)$ Multi-dimensional Fourier transform of the first-order Volterra kernel

$\mathcal{H}_2(\bullet)$ Multi-dimensional Fourier transform of the second-order Volterra kernel

$\mathcal{H}_3(\bullet)$ Multi-dimensional Fourier transform of the third-order Volterra kernel

$\mathcal{H}_\eta^{(u_p,u_k,\ldots,u_n)}(\bullet)$ Multi-dimensional Fourier transform of the Volterra kernel of η–order with multiple inputs

$\mathcal{H}_\eta^{p,q,r,s,v,\varpi}(\bullet)$ Generalized multi-dimensional Fourier transform of the Volterra kernel of η–order with multiple inputs

$\mathcal{K}$ Uniform prior distribution domain

$\mathcal{Q}$ Fundamental harmonic amplitude

$\mathcal{X}$ Regression matrix

$\mathcal{Y}$ Output vector

$\mathcal{Z}$ Hysteretic restoring force

$\mathcal{Z}_1$ Hysteretic restoring force in first interval

$\mathcal{Z}_2$ Hysteretic restoring force in second interval

$\mathcal{Z}_3$ Hysteretic restoring force in third interval

$\mathcal{Z}_4$ Hysteretic restoring force in fourth interval

$\mathscr{D}$ System observations

$\mathscr{F}[\bullet]$ Nonlinear operator

$\mathscr{F}^{\downarrow}[\bullet]$ Continuous unloading bounding function

$\mathscr{F}^{\uparrow}[\bullet]$ Continuous loading bounding function

$\mathscr{F}_n l$ Nonlinear restoring force

$\mathscr{N}(\cdot,\cdot)$ Normal distribution

$\mathscr{U}(\cdot,\cdot)$ Uniform distribution

$\overline{\mathcal{Q}}$ Complex conjugate

$\tilde{k}$ Normalized stiffness coefficient

$\tilde{u}$ Mass-normalized input signal

A Amplitude of the input signal

a_0 Zero-order output terms

A_k $k-$th Amplitude of the additional input signal

A_N Voltage amplitude

a_n Cosinusoidal output terms

$A_{\max}$ Frequency peak amplitude

b_n Sinusoidal output terms

c Damping coeficient

$E(\bullet)$ Minimizing error function

$f(\cdot)$ Nonlinear mapping function

$f(x)$ Continuous function in x

$f_0 + f_1 + \cdots + f_n$ and $d_0 + d_1 + \cdots + d_n$ Bounding function coefficients

f_n Frequency in [Hz]

$h_1^{(u_p}(\bullet)$ First-order Volterra kernel

$h_2^{(u_p,u_k)}(\bullet)$ Cross or direct second-order Volterra kernel

$h_3^{(u_p,u_k,u_l)}(\bullet)$ Cross or direct third-order Volterra kernel

$h_\eta^{(u_p,u_k,\ldots,u_n)}(\bullet)$ Cross or direct Volterra kernel of $\eta-$order

j Imaginary unit $j = \sqrt{-1}$

k Linear stiffness

$k(\cdot,\cdot)$ Covariance function

k_3 Cubic stiffness

m Mass coeficient

M_k Maximum number of harmonic terms

n Number of terms in a series approximation

N_s Number of terms in the Fourier series

n_s Monte Carlo simulations

n_x Regressors in the output

n_y Regressors in the input

$N_{\max}$ Maximum iterations in the feedback controler

$P(x)$ Polynomial form in x

T Period

t Continuous time variable

u Input signal

u_0 Additional input signal

u_1 First probing input signal

u_2 Second probing input signal

u_3 Third probing input signal

Y Absolute maximum value of displacement

y Displacement output signal

y_0 Treshold displacement

y_1 First-order contribution of the Volterra series

y_2 Second-order contribution of the Volterra series

$y_2^{\downarrow}$ Unloading second-order contribution of the Volterra series

$y_2^{\uparrow}$ Loading second-order contribution of the Volterra series

y_3 Third-order contribution of the Volterra series

y_η $\eta-$order contribution of the Volterra series

$y_{\max}$ Maximum displacement

$y_{\min}$ Minimum displacement

Greek Symbols

α Bouc-Wen parameter

α_n Nonlinear stiffness coefficient

β Bouc-Wen parameter

β_n Nonlinear damping coefficient

δ Bouc-Wen parameter

ϵ Approximation error

η Order of the Volterra series expansion

γ Bouc-Wen parameter

κ Time-constant parameter

λ Coefficient of variation

λ_0 Amplitude component of the nonlinear operator

λ_1 Linear stiffness

λ_2 Quadratic stiffness

λ_3	Cubic stiffness
$\mathbf{\Phi}$	Eigenvector matrix
θ	Random variables
μ	Mean value
$\mu(\cdot)$	Model mean output
μ_*	Posterior predictive mean
ν	Bouc-Wen parameter
ω	Frequency in [rad/s]
ω_1	Frequency representing the first-order Volterra kernel
ω_2	Frequency representing the second-order Volterra kernel
ω_3	Frequency representing the third-order Volterra kernel
ω_η	Frequency representing the $\eta-$order Volterra kernel
ω_n	Linear ressonance frequency in [rad/s]
ϕ	Output phase
$\Phi[\bullet]$	Square wave function
$\pi(\bullet)$	Probability density function
σ	Standard deviation
σ_*^2	Posterior predictive variance
σ_ϵ^2	Covariance
σ_p	Random walk step
τ_1	Time delay for the first-order Volterra kernel
τ_2	Time delay for the second-order Volterra kernel
τ_3	Time delay for the third-order Volterra kernel
τ_η	Time delay for the $\eta-$order Volterra kernel

Θ Hyperparameters vector

$\varepsilon_i^{(y)}$ Stochastic variable

ϖ Integer Value

ϱ Nonlinear operator parameter

ζ Damping ratio

Number Sets

$\mathbb{R}^+$ Positive Real Numbers

$\mathbb{R}^1$ Real Numbers of first-order

$\mathbb{R}^2$ Real Numbers of second-order

$\mathbb{R}^3$ Real Numbers of third-order

$\mathbb{R}^\eta$ Real Numbers of $\eta-$order

$\mathbb{Z}^+$ Positive Integer Numbers

Contents

1 INTRODUCTION 33
1.1 INDUSTRIAL CONTEXT 33
1.2 MOTIVATION 37
1.3 SCOPE OF THE THESIS 41
1.4 OBJECTIVES 42
1.5 MAIN CONTRIBUTIONS OF THE THESIS 43
1.6 OUTLINE 43

2 A BRIEF STATE-OF-THE-ART REVIEW 46
2.1 ARCHITECTURE OF JOINTS 47
2.1.1 Designing overview 47
2.1.2 Presence of uncertainties in joint design 51
2.1.3 Design of bolted joints to structural damping 53
2.2 DESIGN OF EXPERIMENTAL SETUPS 54
2.2.1 Boundary Conditions 54
2.2.2 Vibration sensing 55
2.2.3 Excitation devices 56
2.2.4 Excitation design 57
2.3 MODELING JOINT CONTACTS 59
2.4 MODELING GLOBAL NONLINEAR BEHAVIOR 67
2.5 STATE-OF-THE-ART OVERVIEW 72

3 ON THE APPLICATION OF FREQUENCY DOMAIN TECHNIQUES FOR HYSTERESIS MODELS 73
3.1 ON SMOOTH NONLINEAR OPERATOR 74
3.1.1 Nonlinear operator 74
3.1.2 Application example on the Bouc-Wen oscillator 76
3.2 VOLTERRA SERIES AND THE HARMONIC PROBING METHOD 81
3.2.1 Higher-order frequency response functions applied on the nonlinear smooth operator 85

3.2.2 Total response in time domain 90
3.3 NUMERICAL APPLICATION OF THE HIGHER-ORDER FRFs 92
3.3.1 Numerical example of the nonlinear operator 93
3.3.2 Bouc-Wen benchmark 96
3.4 HARMONIC BALANCE METHOD 107
3.4.1 General Harmonic Balance Method 108
3.4.2 Particularities of the harmonic balance method for hysteretic system 110
3.4.3 Numerical application for the Bouc-Wen model 111
3.5 COMPARISONS BETWEEN FREQUENCY DOMAIN TECHNIQUES . . . 117
3.6 CONCLUDING REMARKS 118

4 HIGHER-ORDER FREQUENCY RESPONSE FUNCTIONS FOR STRUCTURES ASSEMBLED BY BOLTED JOINTS: AN EXPERIMENTAL APPLICATION 120
4.1 ON THE PARAMETER ESTIMATION PROCEDURE 122
4.2 BAYESIAN INFERENCE STRATEGY 128
4.3 EXPERIMENTAL APPLICATION 131
4.3.1 Experimental setup 131
4.3.2 Identification of the stochastic Bouc-Wen model 134
4.4 CONCLUDING REMARKS 142

5 EXPERIMENTAL TESTING OF DYNAMICALLY EXCITED JOINTED STRUCTURES 145
5.1 THE ORION BEAM 146
5.1.1 Experimental setup 148
5.1.2 Vibration sensing 150
5.2 EXCITATION DESIGN 150
5.3 UNDERLYING LINEAR STRUCTURE 155
5.4 ON THE ORION BEAM'S RESPONSE 157
5.4.1 On the third vibrating mode's response 157
5.4.2 Measurements repeatability 159
5.4.3 On the influence of the tightening torque 163
5.4.4 On the influence of the excitation amplitudes 165
5.5 EVALUATION OF DUFFING VAN-DER POL OSCILLATOR FOR DESCRIBING THE ORION BEAM'S RESPONSE 169
5.6 CONCLUDING REMARKS 174

6 NON-PARAMETRIC APPROACH FOR PREDICTING HYSTERETICAL BEHAVIOR OF JOINTS 177
6.1 GP-NARX model . . . 179
6.2 IDENTIFICATION FRAMEWORK . . . 182
6.3 NUMERICAL ASSESSMENT OF THE GP-NARX MODEL: THE BOUC-WEN BENCHMARK . . . 183
6.3.1 Model training . . . 185
6.3.2 GP-NARX model verification and validation . . . 186
6.4 EXPERIMENTAL ASSESSMENT OF THE GP-NARX MODEL: THE BERT BENCHMARK . . . 197
6.4.1 Description of the experimental setup . . . 197
6.4.2 Model training . . . 200
6.4.3 GP-NARX model verification and validation . . . 201
6.5 CONCLUDING REMARKS . . . 208

7 FINAL REMARKS 210
7.1 SUMMARY . . . 210
7.2 PERSPECTIVES OF FUTURE WORK . . . 213
7.2.1 Vibration reduction of assembled structures by the control of the tightening torque . . . 213
7.2.2 Structural health monitoring of bolted joint structures . . . 214
7.2.3 Hysteresis model for predicting internal rolling displacement of tires . . . 214
7.3 CONTRIBUTIONS TO THE LITERATURE . . . 215

REFERENCES 218

Appendix A – CONSTITUTIVE MODELS FOR REPRESENTING HYSTERESIS 247
A.1 STATIC MODELS . . . 248
A.1.1 Coulomb friction model . . . 248
A.1.2 Stribeck friction model . . . 248
A.2 DYNAMIC MODELS . . . 250
A.2.1 Dahl model . . . 250
A.2.2 LuGre model . . . 251
A.2.3 Bouc-Wen model . . . 252
A.2.4 Masing model . . . 253
A.2.5 Iwan model . . . 254

1 INTRODUCTION

This Chapter first introduces the industrial interest behind assembled structures. The focus then turns to the motivation of the Thesis, pointing out the main challenges in dealing with this class of system. Next, the scope of the Thesis paves the way for all the aspects that will be covered throughout this work. Objectives and main contributions of the Thesis are also addressed, and the Chapter ends with the work's outline.

1.1 INDUSTRIAL CONTEXT

During the multiple stages involved in designing a project, we are faced with whether to decide on using monolithic structures, i.e., those formed by a single uninterrupted component or an entire system built by assembling several pieces. When compared, it turns out that jointed structures can offer potential financial savings to the final project, which are justified due to the lightweight nature of the last system, the possibility of building complex structures with modular geometry, which often requires less complexity in the manufacturing process, or even facilitate the replacement of damaged components by healthy counterparts. Moreover, in some systems, structural joints are responsible for more than 90% of their damping (BEARDS, 1996).

Considering the automotive industry, where the trade-offs between cost-effectiveness and satisfying diverse customer choices are of utmost importance, the use of modular design platforms for car product families with simultaneous size, shape, and topology represents a lower cost in the final product (TORSTENFELT; KLARBRING, 2007). Other examples range from joints within aero turbines (SIEWERT *et al.*, 2010; BEAUDOIN; BEHDINAN, 2019) to bolted-flange joints that constitute pipelines in oil and gas plants (REZA *et al.*, 2014). It is a fact that the use of joined structures in an industrial context is gaining more attention. Currently, much of the structural dynamics applied to industrial cases are effectively based on the assumption of linearity or assumes that structures are sufficiently close to linear behavior (EWINS, 2016). However, joint connections are a local

source of nonlinearity, which sometimes makes impractical the modeling by commercial software.

Figure 1 illustrates examples of industrial-scale structure specimens that are commonly used as case studies in the literature to validate and improve the dynamic models of systems under test. The F-16 aircraft, depicted in Fig. 1(a), was proposed as a benchmark by Noël and Schoukens (2016a) to evaluate the influence that the coupling of two dummy payloads (they simulate wingtip-mounted missile) at the wingtips has on the aircraft dynamics. The connection interface was the predominant source of nonlinear distortions in the aircraft vibration response during the ground vibration tests, featuring damping and stiffness nonlinearities related to friction and clearance, respectively.

Figure 1 – Examples of industrial scale structure specimens assembled with joint connections.

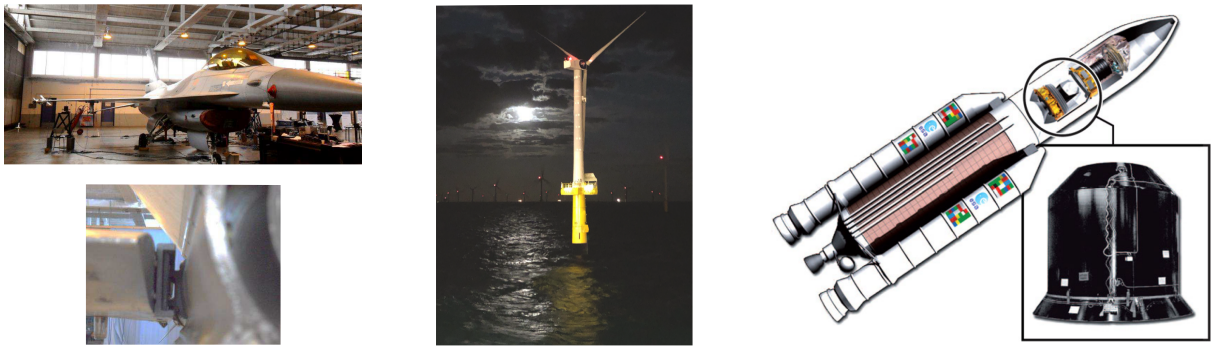

(a) F-16 Benchmark (b) Wind Turbine (c) ARIANE 5 launcher and the SYLDA 5 component

Source: Adapted from (a) Noël and Schoukens (2016a), (b) Cabboi *et al.* (2021) and (c) Caignot *et al.* (2010).

Wind turbines are also in the list of industrial applications that contain connected parts. Cabboi *et al.* (2021) investigated the vibration-assisted decommissioning process of the turbine shown in Fig. 1(b). The lower tower of the wind turbine is connected to the monopile base using a slip-joint, i.e.; this assembly relies on frictional interfaces connected by pressure fit without the need to use bolted flanges. The slip-joint is an alternative to grouted connections, where it is argued this design solution offers better structural integrity to the connection, as well as decreased installation and subsequent maintenance cost (LOTSBERG, 2013; SAH *et al.*, 2018). Another example of application involving wind turbines, within a reduced specimen scale because it refers to an academic benchmark, is the AmpAir 600 [1] (MAYES, 2012). This benchmark is assembled from several components. One of the main objectives of the proposed work on this turbine lies in modeling the dynamic characteristics linked to the presence of nonlinearities due to

[1]Further details available on: http://substructure.engr.wisc.edu/

the blade assembly. Results coming from the collaborative effort between researchers are helping the development in the area of joint dynamics (ROETTGEN; ALLEN, 2018).

Figure 1(c) shows the ARIANE 5 launcher with emphasis on the SYLDA 5[1,2] component, a layered aerospace structure composed of a combination of conical and cylindrical shells made of composite material (CHRONOPOULOS *et al.*, 2014). The presence of joints in this system, essentially glued joints between composite materials and bolted joints to connect the component to the rest of the structure, has been the subject of study in the ''Prediction of Damping in Launchers'' research program supported by the French Space Agency (CAIGNOT *et al.*, 2005; CAIGNOT *et al.*, 2010), with the aim of modeling and identifying damping to improve the space launcher design.

Notwithstanding, vibration reduction is an old-fashioned topic. Depending on the phenomena intended to highlight, the designing choices are not the same mainly because of difficulties to obtain good performances when environmental conditions vary during the life-cycle of a product. Many researchers worked and are still working on polymers, active devices, tuned mass dampers, or meta-materials to mitigate vibrations. In this context, Fig. 2 qualitatively illustrates the damping efficiency depending on the type of system (active or passive damping sources) and operating conditions based on temperature and frequency range. Polymeric materials are of great interest, being widely used due to their viscoelastic properties with high damping capacities. Nevertheless, they are susceptible to vibration frequency, and wide temperature ranges (SABA *et al.*, 2016). Piezoelectric materials are a technological solution with the ability to transfer mechanical (or electrical) energy into electrical (or mechanical) energy. Due to this principle, piezos have been used to dissipate or absorb energy through a suitable electrical circuit or re-transformed into mechanical energy to control vibrations (NEUBAUER *et al.*, 2006; COLLET; OUISSE; ICHCHOU, 2012). The choice of different piezoelectric materials and the assembly architecture with other systems components of interest can be seen as a limitation in their use as a damping source. Although active control sources offer significant damping efficiency, their use can represent an increase in the operational cost since they require solutions that are exogenous to the structure and external power supply systems (PREUMONT, 2018).

Dry friction stands out as a damping source with an interesting trade-off between several operating conditions, i. e. damps structures ranging from low temperatures

[1] SYstéme de Lancement Double d'Ariane 5.

[2] https://www.esa.int/Enabling_Support/Space_Transportation/Launch_vehicles/Ariane_5_ECA2

Figure 2 – Damping efficiency according to operational conditions in terms of temperature and frequency.

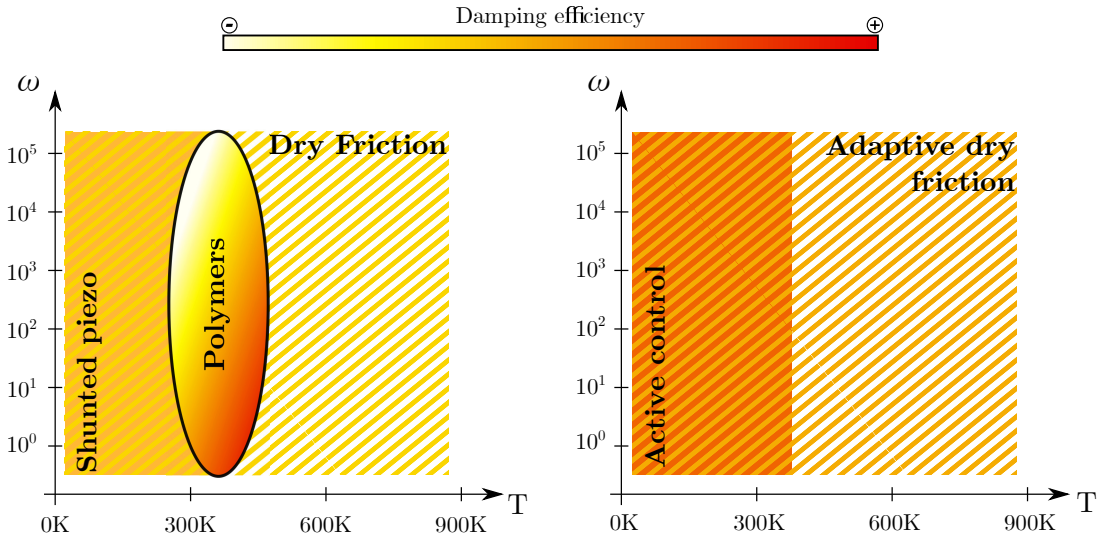

(a) Passive Damping (b) Active Damping

Source: Prepared by the author.

Figure 3 – Number of publications per decade in the engineering community involving the keyword "dry friction" according to the SCOPUS database.

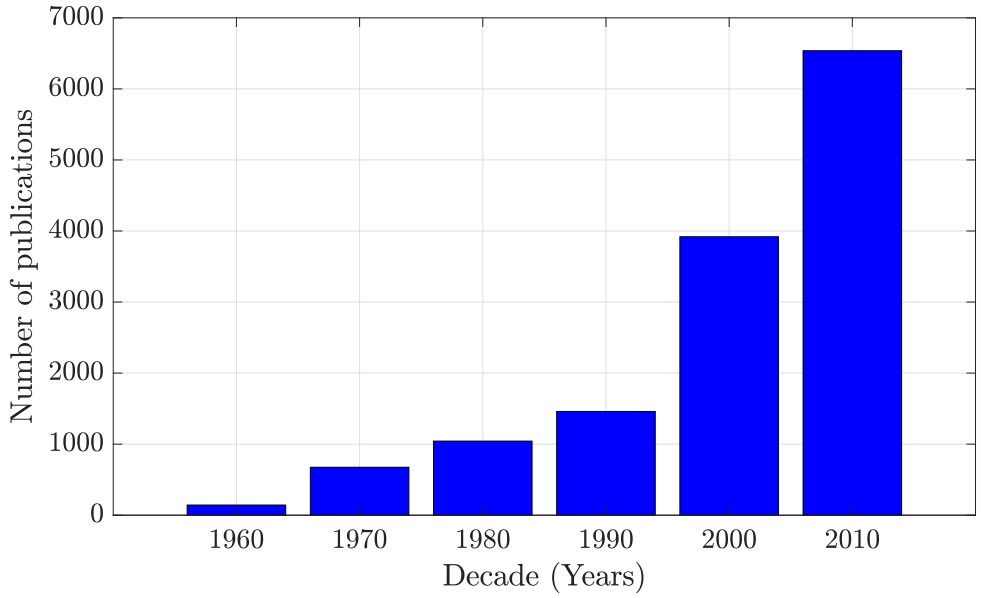

Source: Prepared by the author.

(aeronautics and space) to high (engines, power generation, and brakes), and an average damping efficiency. Dry friction dampers are constantly used to dissipate energy in turbine blades and consequently mitigate excessive vibration amplitudes (GRIFFIN, 1990; KOH *et al.*, 2004; PESARESI *et al.*, 2018; KRACK; SALLES; THOUVEREZ, 2017; LI *et al.*, 2019; DENIMAL *et al.*, 2021). To show how active the engineering community

is on this subject, a survey of available research in the engineering field is depicted in Fig. 3 based on the SCOPUS[1] search engine. The figure highlights that the number of publications with the keyword ‘‘dry friction’’ is still growing, which may be directly related to recent advances in research on the topic of ‘‘nonlinear damping’’, as investigated by Al-Hababi *et al.* (2020). Feeny *et al.* (1998) provided a historical review of structures and mechanical systems with friction.

On the one hand, the vibration properties of most assembled mechanical systems depend on friction damping at the joints; on the other hand, damping links are present everywhere and can prevent unwanted vibrations (CHEN; DENG, 2005). Thus, it stands out that there is industrial interest in using joints not only to maintain rigid systems but also as a design tool to promote energy dissipation, with companies helping to develop components adapted to this end (KRACK; BERGMAN; VAKAKIS, 2016; BRAKE; EWINS; WYNN, 2018).

1.2 MOTIVATION

Over the past decades, the scientific community that investigates the dynamics of jointed structures has devoted a significant level of interest in designing tools for new lap-joints configurations, further insights on experimental measurements, proposing reliable predictive models, and developing contributions toward the identification field (BRAKE, 2018b).

The presence of local joints turns the transmission of motion between frictional interfaces into the dominant damping mechanism (GAUL; NITSCHE, 2001). Figure 4(a) depicts an illustrative example of a bolted joint, with emphasis on the relative slipping motion of the contact surfaces in the area close to the bolt. At first, both bodies are pressed by a normal force resulting from the tightening torque applied to the bolt. The frictional force, which acts in the tangential direction, increases monotonically as a function of the vibration amplitude level to which the joint region is subjected. Under these circumstances, an amount of relative tangential slipping (on the order of μm) starts at the interface, known as micro slip (see Fig. 4(b)). As the vibration amplitude increases, the micro slip progressively becomes the partial slip until the tangential force reaches a maximum value. From this threshold on, the entire interface exhibits relative motion, the so-called macro slip (see Fig. 4(b)) (PEYRET *et al.*, 2017; MATHIS *et al.*, 2020). Figure

[1] https://www.scopus.com/standard/marketing.uri

4(c) exemplifies a typical ‘‘backbone curve’’, which corresponds to the monotonic initial load slope of the tangential force as a function of the relative tangential displacement that occurs at the contact area, considering only a quarter of the whole vibratory cycle. It is worth noting that macro slips are not expected in well-designed jointed structures, as this would lead to plastic deformation of the interface. Thus, the frictional forces, especially until the partial slip field, induce energy dissipation. Further details on this subject will be addressed in section 2.1.

These effects that take place on a local scale result in a global nonlinear behavior of the structure. Variations in contact stiffness are seen, as the amount of slip between connected surfaces results in a less stiff system (softening effects), as well as increased damping, when compared to the intrinsic structural damping of the materials (SEGALMAN, 2006; SEGALMAN *et al.*, 2009). Thus, to provide a greater understanding of jointed assemblies with the assessment of different vibration environments, many experimental benchmarks have been studied from testing and the modeling point of view. The suggestion of a new benchmark must fulfill some basic requirements to popularize its use in the literature, namely, to consist of a simple experimental bench that would permit its reproduction by other research groups, good presence of nonlinearities that address the influence of the joint on the global behavior of the structure, excitation design that is consistent with practical engineering applications, open access experimental data set, among others (BRAKE, 2018d). Chapter 2 discusses some available benchmarks as well as the joint architecture in some cases.

After selecting a benchmark that fits the research interests that will be conducted, the focus shifts to predicting the behavior of such systems, which is the subject of an ongoing research effort; finite element (FE)-based models are commonly used on an industrial scale (even millions of degrees of freedom around the contact interface) to predict energy dissipation and stress distribution of assembled structures. However, handling contact problems involves nonlinearities governed by micro and mesoscale parameters, e.g., geometry, roughness, and contact pressure (ROJAS *et al.*, 2020). Due to this reason, the computational cost required to simulate these models during a nonlinear regime of motion, especially in the context of obtaining responses in the time domain, is sometimes prohibitive when a dynamic response that spans several oscillation cycles is desired.

Under certain circumstances, frequency-domain formulations are advantageous in dealing with assembled structures. Their use from three perspectives is noted: nonlinear modal analysis procedures, in which the main interest lies in tracking the evolution

Figure 4 – Illustrative example of a bolted joint with emphasis on slipping motion.

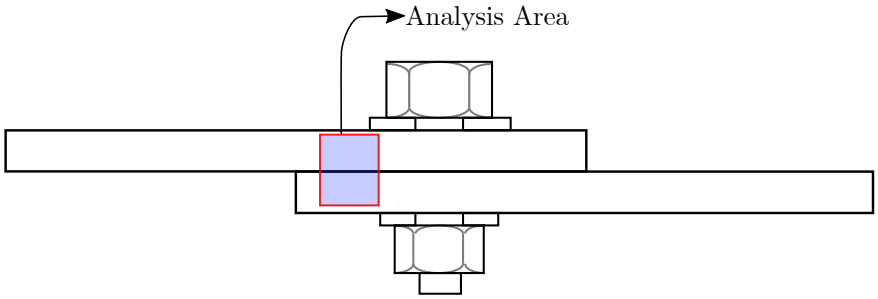

(a) Schematic of a bolted joint.

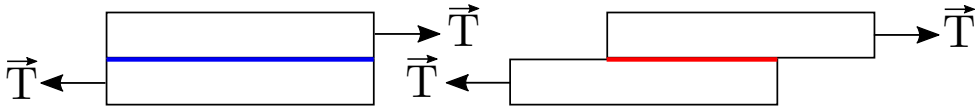

(b) Schematic of the slipping motion.

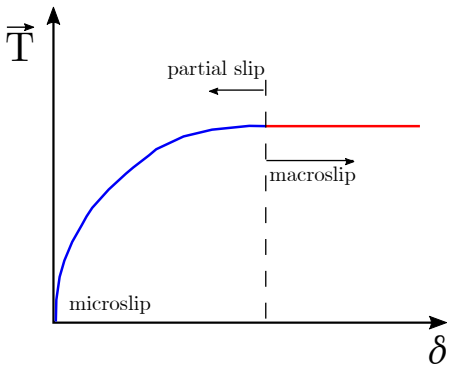

(c) Tangential force as function of relative displacement:

Source: Prepared by the author.

of resonance frequencies and damping ratios depending on the vibrational energy, the so-called ‘‘modal backbone’’ curves (PEYRET; DION; CHEVALLIER, 2016; SCHEEL *et al.*, 2018; KARAAĞAÇLI; ÖZGÜVEN, 2021); frequency-domain solvers to reduce the computational cost in predicting the nonlinear behavior of assembled structures, including continuation and shooting methods (JAUMOUILLÉ; SINOU; PETITJEAN, 2010; SÜSS; WILLNER, 2015; CLAEYS *et al.*, 2016a; LACAYO *et al.*, 2019). In this context, special attention is given to the harmonic balance method, which stands out as a regular periodic solution for nonlinear mechanical problems (KRACK; GROSS, 2019); lastly, parameter estimation procedures formulated into a white-box modeling framework (AHMADIAN; JALALI, 2007b; JALALI; AHMADIAN; MOTTERSHEAD, 2007), i. e., under conditions in which the nonlinear dynamics of a mechanical system is represented

by a phenomenological model with an approximated closed-form solution.

The multidimensional Fourier transform of the Volterra kernels is a possible approach to apply. The so-called higher-order frequency response functions (FRFs) generalize the concept of the FRFs for nonlinear systems, exploiting the convolution structure on these kernels (BEDROSIAN; RICE, 1971; SCHETZEN, 1980). The computation of the higher-order FRFs is performed having the mathematical model of the system or structure of interest by using the harmonic probing method, which consists of exciting the nonlinear system with a proper combination of harmonic inputs (RUGH, 1991). This methodology is an attractive white-box modelling approach used in structural dynamics for nonlinear modal analysis (CAFFERTY; TOMLINSON, 1997; TAWFIQ; VINH, 2003), system identification problems (CHATTERJEE; VYAS, 2003; CHATTERJEE; VYAS, 2004; CHATTERJEE, 2010a; LIN; NG, 2018), aeroelastic approaches (MILANESE; MARZOCCA, 2009), output-only applications (SCUSSEL; SILVA, 2017), structural damage assessment (CHATTERJEE, 2010b) and others (CHENG *et al.*, 2017). However, most hysteresis models involved in describing bolted joints are non-smooth, with nonlinear functional forms that do not admit a series expansion. Thus, there is a lack of contributions in the literature involving the Volterra series for approximating systems with hysteresis, which is a subject of investigation addressed by this work.

Some applications involving bolted joints, such as detection of bolt loosening for structural health monitoring (SHM) purposes (LI; JING, 2017; LI; JING, 2020), require predictive models that demand a relatively less-expensive computational cost for decision making while relying on input and output data. Towards this objective, data-based models that do not depend directly on physical parameters to be identified, so-called black-box models, facilitate the qualitative and global analysis, and pave the way for using probabilistic methods. These models have only been slightly explored within this context due to limitations in capturing the hysteresis effect (LEVA; PIRODDI, 2002; WORDEN *et al.*, 2007; MARTINS; AGUIRRE, 2016). In summary, the structure of black-box models should be carefully selected to reproduce the memory effect of hysteresis (input-output dependency) while avoiding these models from being restricted to produce only output signals with the same character used during their identification process (BILLINGS, 2013). Thus, circumventing these limitations and popularizing the use of black-box models in capturing hysteresis is part of the following perspectives on the analysis of bolted joints.

1.3 SCOPE OF THE THESIS

Having briefly addressed the main industrial interests surrounding the presence of joints, as well as the motivation behind their analysis, the Thesis covers the basics needed before tackling real-life structures, which is to demonstrate the use of algorithms based on physics-guided techniques applied on numerical and experimental academic benchmarks that present hysteresis and resonant softening effects. The scope of the subjects handled in the Thesis is presented below.

The first part of the dissertation aims to derive analytical expressions of the Volterra kernels from predicting the output and the hysteresis loop from a non-smooth system, which was previously not possible due to technical limitations, such as the presence of module functions in most examples involving hysteresis and the fading memory property that exists in the Volterra series. The strategy adopted to overcome these limitations lies in using a smooth nonlinear operator based on bounding functions capable of individually reproducing the loading and unloading regime of the restoring force in systems that carry the rate-independent hysteresis (RIH) property. To illustrate the applicability of the proposed approach, the challenging benchmark with hysteretic damping introduced by Noël and Schoukens (2016b) and described by a Bouc-Wen model is simulated through a numerical integration scheme. Then, based on the smoothing process of the Bouc-Wen oscillator's restoring force, this work investigates some practical regards applying the harmonic balance method (HBM) for predicting the hysteretic behavior of such a model.

Through an analytical formulation of the higher-order FRFs, an identification procedure formulated into a white-box Bayesian modeling framework is proposed to calibrate a stochastic Bouc-Wen model for predicting the dynamics of a structure named BoltEd stRucTure (BERT) benchmark. A state-of-the-art review of the Bouc-Wen oscillator shows that although the model can accommodate a wide range of hysteresis loops in the restoring force *versus* displacement plane, its for capturing the dynamic behavior in jointed structures still modest. The benchmark's experimental setup consists of two aluminum beams assembled by double bolted joints in clamped-free boundary conditions, presents softening effects in the resonant frequency vicinity, and data variation related to the presence of uncertainties in the measurement process. It is important to stress that the hysteretic model is not used to describe the frictional forces directly in the contact interfaces, which is beyond the scope of the Thesis, but rather the whole restoring forces related to the mode of interest. Using higher-order FRFs to calibrate the Bouc-Wen parameters provides a clear physical meaning about the global structure behavior and is

conducted with traditional experimental tests.

The second part of the dissertation focuses on proposing a new lap-joint configuration, the so-called Orion beam, under the perspective of good practices for designing and experimental testing of dynamically excited jointed structures. The setup is composed of two thin beams connected by three bolted joints with contact patches on each connecting bolt. The Orion beam suggests an assembly configuration in which there are bolts dedicated to ‘‘static’’ functions to guarantee structural integrity and those that perform ‘‘damping’’ functions to increase the energy dissipation due to frictional contact. In particular, it is analyzed the influence of the Orion beam's design in the repeatability of experimental measurements and the impact of the tightening torque and excitation amplitudes on the system's response. Additionally, a single-degree-of-freedom (SDF) Duffing-Van der Pol oscillator is proposed to evaluate, through its calibrated parameters, the impact of several tightening toque conditions and multiple excitation amplitudes on the structural stiffness and damping considering the vibration mode that promotes pronounced deformation around the lap-joint.

Finally, the third part discusses using the non-parametric GP-NARX model to obtain the response of nonlinear systems with a hysteresis. First, the use of the GP-NARX model to approximate the dynamics of systems with a hysteresis is presented. The predictive applicability of the proposed model is discussed in a numerical assessment involving a Bouc-Wen oscillator. Next, using the non-parametric model for describing the nonlinear dynamics of the BERT benchmark considering experimental variability is at the center of discussion.

1.4 OBJECTIVES

The main objective of this doctorate is to propose new contributions in the analysis and identification of mechanical systems with hysteresis, focusing mainly on gaining better comprehension of structures assembled with bolted joints. In summary:

- to propose a new way to describe hysteretic systems with dynamic nonlinearity by using the analytical approximations;
- to apply frequency-domain methods for predicting, through closed-form equations, the response of bolted jointed structures;
- to investigate the use of physics-based and non-parametric models to describe

the dynamics bolted jointed structures, with insight on aleatoric and epistemic uncertainties related to the measurement process and lap-joint design.

1.5 MAIN CONTRIBUTIONS OF THE THESIS

The main contributions of this Thesis to the literature are:

- a proposal of a new way to identify parametrically, by using a harmonic probing algorithm and a smooth nonlinear operator, the higher-order FRFs of a Bouc-Wen oscillator (TELOLI; SILVA, 2019);
- a proposal of a new identification strategy to describe the dynamics of a structure assembled by bolted joints considering uncertainties in vibration data. The identification approach is expressed into a Bayesian framework to consider the data fluctuations related to uncertainties in the measurement process. A stochastic version of the Bouc-Wen model is considered to reproduce the nonlinear behavior of the assembled structure, and the calibration of the model parameters uses the analytical expressions of the higher-order FRFs (TELOLI *et al.*, 2021);
- a proposal of a new lap-joint design, so-called the Orion beam. The beam is built with contact patches dedicated to ‘‘static’’ functions to guarantee structural integrity and perform ‘‘damping’’ functions to increase energy dissipation. A Duffing-Van der Pol oscillator is proposed to evaluate the impact of several tightening torque conditions on the structural stiffness and damping. The calibration of the model parameters is performed through the harmonic balance method (TELOLI *et al.*, 2021. No prelo.; TELOLI *et al.*, 2022);
- a proposal of using the GP-NARX model for predicting the behavior of hysteretic systems with natural probabilistic confidence intervals based on the model uncertainties (TELOLI *et al.*, 2021).

1.6 OUTLINE

This dissertation is structured into the following chapters:

- **Chapter 1 - INTRODUCTION**: covers the motivation, objectives, main contributions, and scope of the Thesis.

- **Chapter 2 - A BRIEF STATE-OF-THE-ART REVIEW:** presents the contributions of the literature that have damping at the center of the discussion from four axes of investigation, which are modeling, experiments, local and global scale of analysis.

- **Chapter 3 - SOME REGARDS ON THE APPLICATION OF FREQUENCY DOMAIN TECHNIQUES FOR HYSTERESIS MODELS:** shows the assumptions used to develop the smooth bounding functions that compose the nonlinear operator. Then, it introduces the Volterra theory and the harmonic probing method employed to derive analytical expressions for the higher-order FRFs. A numerical application involving the Bouc-Wen benchmark is addressed. Still, based on the smoothing procedure previously developed, the dissertation presents the use of the harmonic balance method and particularities involving its application in the same Bouc-Wen benchmark. Concluding remarks are made, and a comparison is drawn between the applicability of the Volterra series with respect to the harmonic balance formulation.

- **Chapter 4 - HIGHER-ORDER FREQUENCY RESPONSE FUNCTIONS FOR STRUCTURES ASSEMBLED BY BOLTED JOINTS: AN EXPERIMENTAL APPLICATION:** starts presenting a complete description of the parameter estimation procedure proposed based on the higher-order FRFs. Then the Chapter goes on the Bayesian inference strategy, describing the Markov Chain Monte Carlo (MCMC) Metropolis-Hastings algorithm to update the probability density functions of each random variable that compose the stochastic Bouc-Wen model. Next, an experimental application of the identification procedure for predicting a structure assembled with bolted joints, the BERT benchmark, exemplifying the applicability of the stochastic Bouc-Wen oscillator in representing the linear and nonlinear behavior of the experimental test-bench structure. Since this model is not commonly used to describe bolted joints, this dissertation shows that the Bouc-Wen model operates well, assuming the available experimental data. Finally, final remarks are addressed.

- **Chapter 5 - EXPERIMENTAL TESTING OF DYNAMICALLY EXCITED JOINTED STRUCTURES:** starts introducing the Orion beam's design, the experimental setup, and considerations regarding experimental measurements. The experimental results of the Orion beam around the vibrating mode most affected by the presence of nonlinearities are addressed by discussing the repeatability of

measurements, influences of the tightening torque, and impact of several excitations. It also reports the Orion beam's concluding remarks and expected contributions for the joint structures' community.

- **Chapter 6 - NON-PARAMETRIC APPROACH FOR PREDICTING HYSTERETICAL BEHAVIOR OF JOINTS:** firstly introduces an overview of the main aspects present in the identification of a GP-NARX model. To evaluate the model's applicability to describe hysteretic systems, the Chapter goes on the assessment of the GP-NARX model for approximating the outputs and hysteresis loops of the Bouc-Wen benchmark. Then, after establishing a methodology of model identification for the numerical benchmark with hysteresis, it presents a practical application of the proposed model to reproduce the nonlinear dynamic behavior present in the first vibrating mode of the BERT benchmark. Finally, it reports the partial remarks.
- **Chapter 7 - FINAL REMARKS:** comprises a discussion on the contributions to the literature, main conclusions, and path forward for future work.

2 A BRIEF STATE-OF-THE-ART REVIEW

This Chapter extends some discussions started in the motivation of the Thesis with a brief literature review on the state-of-the-art in bolted joints. To facilitate the Chapter's flow, four axes of analysis on the subject are considered: modeling, experiments, local and global scales of analysis. A graphical abstract is presented in Fig. 5.

Figure 5 – Graphical abstract on the state-of-art review

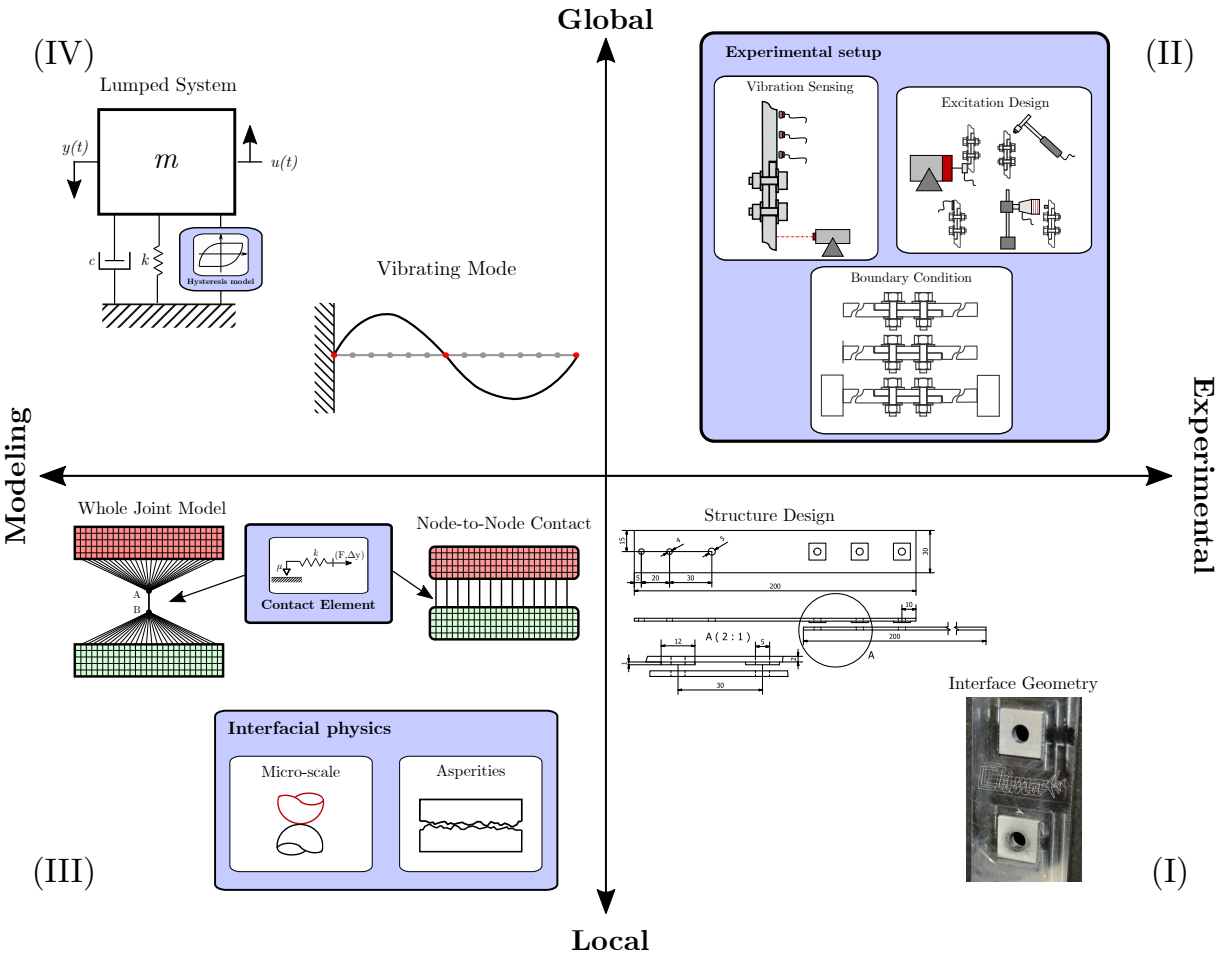

Source: Prepared by the author.

Four quadrants are in focus:

(I) **Architecture of joints:** it is related to the architecture of bolted joints, with appropriate selection of the materials that will compose the analysis system, properties of the contact interface, such as roughness, size, use or not of lubrication, tightening torques applied, as well as the making and idealization of a project executable by manufacturing processes.

(II) **Design of experimental setups:** it consists in the careful selection of the entire experimental apparatus, such that the test bench contributes as little as possible to the vibration behavior of the primary system, having as object of study the design of the excitation applied, boundary conditions, vibration sensing, among other elements.

(III) **Modeling joint contacts:** it mainly consists of models focused on describing the contact interface from models that emulate physical laws. Although it is a subject of great interest in the literature, this topic is beyond the scope of the results presented in this work but will be addressed nonetheless due to its importance to the Thesis' object of study.

(IV) **Modeling global nonlinear behavior:** it comprises modeling of bolted structures on a global analysis scale of the vibratory behavior of the system. It is generally based on the nonlinear normal modes of vibration or on the proposal of lumped models that encode the hysteretic behavior acting on a whole mode of interest through phenomenological models.

Throughout these topics, the Chapter brings forward elements of nonlinear system identification based on experimental data and commonly used numerical tools for predicting nonlinear responses. Finally, the Chapter closes with partial remarks.

2.1 ARCHITECTURE OF JOINTS

2.1.1 Designing overview

Many benchmarks have been studied from the testing and the modeling point of view, considering different possible architectures. Figures 6 and 7 summarize the main configurations using pictograms, which are defined in the Tab. 1, to highlight their properties. Ahmadian and Jalali (2007a) and Ahmadian and Jalali (2007b) proposed a simple assembly illustrated in Fig. 6(a), which is composed of two beams and a single

bolted connection. This setup is supposed to be the simplest one, but due to a single bolt and the lack of structural symmetry, dynamic clearance may occur between interfaces. These effects lead to quite complex dynamics that are not representative of well-designed assemblies. Recently, Jalali *et al.* (2019) investigated the variability of the dynamic characteristics in a very similar test structure but composed by a double bolted connection. The new assembly configuration minimizes the sensitivity of the normal load applied to the bolts to dynamic vibration but still features important measure-to-measure variability and does not ensure structural symmetry. Such configurations ((a) and (c)) are quite sensitive to shape uncertainties and roughness, especially at the low-pressure contact areas, represented by orange lines in Fig. 6.

The drawbacks involving the setup design in Fig. 6(a) have been (partially) circumvented by Festjens, Chevallier and Dion (2013), who proposed the configuration illustrated in Fig. 6(c). The authors proposed a two bolts assembly with better structural symmetry that allows minimizing parasitic clearance. Recently, Jalali *et al.* (2019) investigated the variability of the dynamic characteristics in a very similar test structure. The new assembly configuration minimizes the sensitivity of the normal load applied to the bolts to dynamic vibration but still features important measure-to-measure variability and does not ensure structural symmetry. Thus, such configurations ((a) and (c)) are quite sensitive to shape uncertainties and roughness, especially at the low-pressure contact areas, represented by orange lines in Fig. 6.

Figure 6 – Schemes of several bolted joints. (a) Single bolted joint (AHMADIAN; JALALI, 2007a; AHMADIAN; JALALI, 2007b); (b) Full symmetric double bolted joint (SONG, 2004); (c) Double bolted joints (JALALI *et al.*, 2019; FESTJENS; CHEVALLIER; DION, 2013);(d) Brake-Reuß beam (BRB), three bolted connections (BRAKE *et al.*, 2014).

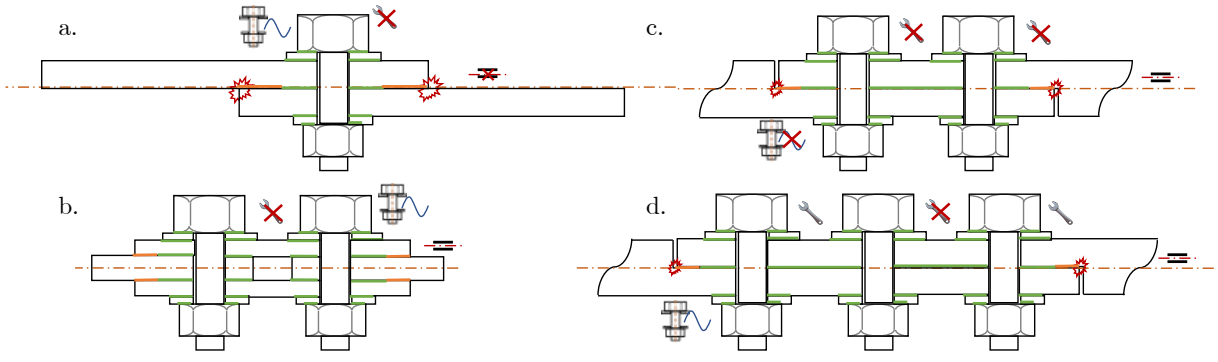

Source: Teloli *et al.* (2022)

Song (2004) proposed a full symmetric setup that minimizes dynamic clearance and uncertainties due to surface imperfections, as presented in Fig. 6(b). Moreover, this

specimen avoids coupling between the normal and tangential stress. Brake *et al.* (2014) have introduced the Brake-Reuß beam (BRB), a 2-thick-beams assembly with three bolts at its center, as seen in Fig. 6(d). Several research groups have tested this well-known setup worldwide and have been derived in various versions considering different contact shapes. The BRB's main improvement compared to previous setups lies in the possibility of decreasing the tightening torque in the three bolts to increase the damping without loss of stiffness. Due to the beam thickness, the setup is significantly sensitive to contact imperfections once the contact stiffness strongly depends on the volume stiffness.

Peyret *et al.* (2010) and Dion, Chevallier and Peyret (2013) proposed the clamped-clamped beam, which is depicted in Fig. 7, for experimental characterization of the damping induced by friction and partial slip on a planar transverse interface. The setup enables us to perfectly fit the friction effects with Masing's assumptions as there is no coupling between the normal load and the tangential load in such a configuration. The setup is fully symmetric and allows tunability of the normal load.

Figure 7 – Clamped-clamped beam with transverses interfaces (PEYRET *et al.*, 2010; DION; CHEVALLIER; PEYRET, 2013).

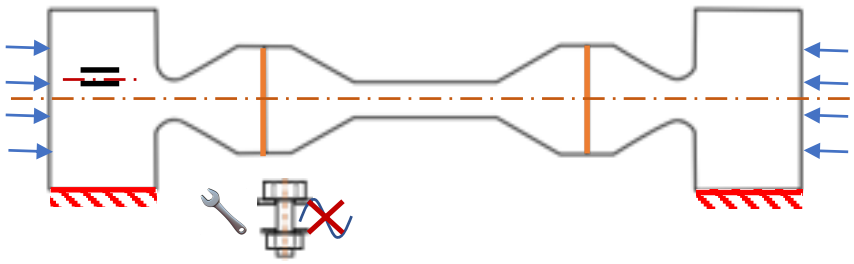

Source: Teloli *et al.* (2022)

Other assemblies with a similar design to the previous setups have been propose, as illustrated in Fig. 8. For example, the assembly proposed by Heller, Foltete and Piranda (2009) consists of two beams, one thin and one thick, joined by three bolts. The authors' interesting analysis lies in testing several tightening torques for four different configurations at the contact interface: beams directly connected and another three conditions with a washer inserted between the beams and the bolt axis of different diameters for each test condition. The results indicate that the damping is related to the size of the contact area and the tightening torque applied, i.e., conditions with low tightening torque and large contact area (directly connected and larger diameter washer) have higher damping values. In contrast, for high torques, the behavior of the structure in terms of damping and stiffness is nearly the same for all sizes of the contact area.

Table 1 – List of pictograms and their meanings (TELOLI *et al.*, 2022).

Pictogram	Signification
	The normal load can be set without changing the nominal frequency
	The joint is almost symmetric
	The contact pressure is slightly sensitive to shape imperfections
	The contact pressure is highly sensitive to shape imperfections
	The normal load is sensitive to vibrations
	Dynamic clearance may occur
	Negation to previous propositions

Source: Teloli *et al.* (2022).

The Sumali beam (DEANER *et al.*, 2015) consists of 2-thin-beams connected by four bolts, as shown in Fig. 8(b). Due to its shape, thin thickness, and applied torque levels, the structure does not exhibit nonlinear behavior suitable for measurements and modeling, which shows that often the benchmark design might come with challenges. Conversely, the Gaul resonator (GAUL; LENZ, 1997; SÜSS; WILLNER, 2015; SÜSS; JANEBA; WILLNER, 2018; SCHEEL *et al.*, 2018), depicted in Fig. 8(c), stands out as an academic structure capable of isolating the influence of a single joint on the structural damping from other disturbances related to boundary conditions as well as minimizing asymmetry and clearance effects presented by the structure in Fig. 6(a). Figure 8(d) presents the S-4 Beam proposed by Singh *et al.* (2019), in which the assembly consists of two C-shaped beams bolted together at their extremities. The test setup presents remarkable nonlinearity in its damping, but the joints can experience breathing effects (dynamic clearance) depending on the mode shape due to its design.

Still, other benchmarks in literature contribute to the characterization of nonlinear behavior in assembled structures and provide experimental data assessing numerical models. Initially proposed by Claeys *et al.* (2016a), the Harmony structure is a metallic assembly composed of a central body, a base plate, which is clamped to a shaker, and four blades that connect the central body to an external envelope by using contact joints. Due to its size, the Harmony benchmark is representative of industrial-scale specimens

Figure 8 – Other assembly designs.

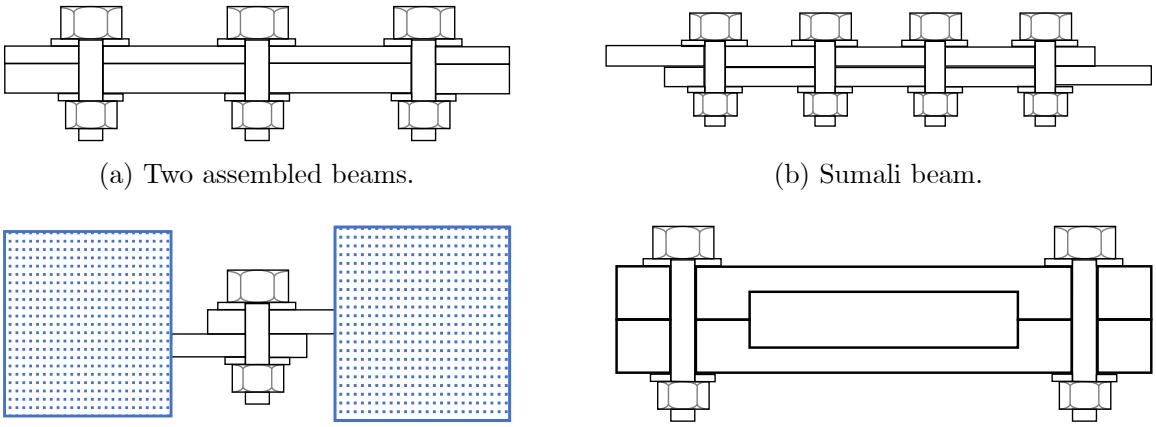

(a) Two assembled beams.

(b) Sumali beam.

(c) Gaul Resonator.

(d) S4-Beam.

Source: Adapted from (a) Heller, Foltete and Piranda (2009), (b) Deaner *et al.* (2015), (c) Gaul and Lenz (1997) and (d) Singh *et al.* (2019).

(CLAEYS *et al.*, 2016b). During vibration tests, the slip motion around the contact interface was the source of the nonlinear behavior, presenting pronounced softening effects and asymptotic resonance (flattening of the resonance peak for high excitation levels, which indicates the presence of macro slip motion (SCHEEL; SCHULZ; KRACK, 2020)). Recently, Scheel, Weigele and Krack (2020) proposed a new design for lap-joint structures, which is composed of a cantilever beam that permits to vary the joint's position to study different setup configurations and severeness of nonlinearity. The specimen presents a strong influence of dry friction effects, with a significant increase of modal damping and decreasing in resonant frequencies.

2.1.2 Presence of uncertainties in joint design

From the designing point of view, many issues remain open. First of all, to assess experimentally the performances for which the structure has been designed, it is mandatory to reduce uncertainties influence, which may arise of aletoric or epistemic nature. Simply put by Beer, Ferson and Kreinovich (2013), irreducible uncertainty is classified as aleatoric and is associated with variabilities in the response data due to inaccuracies in the measurement procedure or properties of the system that are sensitive to fluctuations in environmental conditions. This class of uncertainty can be handled with the frequentist interpretation of the probability theory. On the other hand, reducible uncertainty is classified as epistemic and refers to limited data or lack of knowledge, which may cause problems in analysis or interpretation of measured data (EWINS, 2016).

Although it may not seem straightforward, uncertainties of an epistemic nature are more difficult to resolve, either because it is impossible to measure data that clarify the source of this uncertainty or even because it is not completely obvious which experiment parameters are responsible for its appearance.

Joints are a source of epistemic uncertainties, which mainly appear from shape imperfections (non-flatness of surfaces), dynamic clearance, and pressure distribution over the contact area, as seen in Fig. 6, and are directly related to mesoscale and microscale parameters in the joint design. For example, to ensure repeatability between tests, benchmark structures usually have an assembly protocol for tests involving successive measurements after complete assembly and disassembly of the joint. Although after each assembly the structural condition is the same, i.e., the overall picture of the test-bench is maintained, pressure variations in the contact area caused by the tightening torque, or even by the order in which the bolts are tightened, can lead to significant changes in the vibration behavior of the system, such that the measurement uncertainty may be more pronounced than variations in frequency and damping caused by nonlinear behavior on its (BRAKE; SCHWINGSHACKL; REUSS, 2019; JALALI *et al.*, 2019). One can also mention the occurrence of wear between the surfaces due to micro slip, which is influenced by the surface roughness and, when accumulated, also results in global changes to the joint dynamics (ZHANG *et al.*, 2018; LI *et al.*, 2020a).

With variability and repeatability of jointed structures as essential subjects, Brake, Schwingshackl and Reuß (2019) conducted a campaign of tests to verify the role that the experimental setup, interface of roughness, settling versus wear, interface geometry, and the structure surrounding the joint play on the dynamic response of the BRB benchmark. In summary: conditions with reduced contact area have high-pressure regions at the interface, reducing micro slip and ensuring higher test-to-test repeatability. However, care should be taken, as the absence of micro slip also leads to a lack of nonlinearity, which is not interesting for modeling purposes; areas where the contact pressure is sensitive to shape imperfections, especially at edges far from the bolt hole (see Fig. 6), may exhibit wear as vibration tests are run; surfaces with higher roughnesses also show lower repeatability between tests. In general, the natural contact areas are formed by micro-contacts randomly distributed over the surface, and thus, they are hardly arranged in the same configuration after complete disassembly (STACHOWIAK; BATCHELOR, 2013).

In this dissertation, both types of uncertainties are addressed. Chapters 4 and 6 present experimental tests conducted on the BERT benchmark. In this structure,

variations in data are related to uncertainties in the measurement process performed on different days but without complete disassembly of the joint. Chapter 5 discusses the repeatability of the Orion beam response after complete assembly and disassembly of the lap-joint to assess how much we can trust the experimental data.

2.1.3 Design of bolted joints to structural damping

Vibration reduction in bolted joints is at the center of the discussion. In outline, the primary use of joints is to provide resistance to static and dynamic loads, such that the structure can undergo through different vibration regimes without dismantling or without self-loosening of bolts, as this may imply a catastrophic failure that will cost resources or even human lives in a worst-case scenario. Thus, the following question arises: ‘‘how to achieve considerable damping and stiffness simultaneously?’’

For damping, low contact pressures are required. The main variables to guarantee this objective may be summarized as interface positions, bolts diameter, and the tightening torque (NANDA, 2006). To illustrate an application involving induced damping due to interface adjustments, the focus is turned to the clamped-clamped beam shown in Fig. 7. First, the beam is built up with three components assembled by two planar joints. Then, in this assembly configuration, the damping is induced by micro slip according to the applied normal load, such that for lower load values, higher damping values are obtained.

Regarding bolted joints, to generate damping from frictional effects, the connections' requirements must generally be modified. For instance, if on the one hand conditions in which a low tightening torque is applied may lead to higher frictional energy dissipation (BRAKE, 2018b), on the other hand, the structural integrity may be compromised.

In this context, this dissertation introduces in Chapter 5 a new lap-joint configuration, so-called ‘‘Orion beam’’[1], aiming both to provide experimental data for modeling and design purposes. In this new assembly design, 2-thin-beams are assembly by three bolts that are playing different structural functions. Contact patches have been added at each bolt connection to retain the contact between both beams in a small area, minimizing uncertainties on the structure's response and enhancing the repeatability between measurements. The central bolt is dedicated to ‘‘static’’ functions to ensure structural integrity and resist dynamic loads without substantial stiffness changes. The

[1]The name ‘‘Orion beam’’ derives from the Orion constellation, in which four stars are forming a roughly rectangular shape are linked in the center by three stars that form Orion's belt, similar to the three bolts proposed by the lap-joint configuration.

external bolts, in turn, perform ‘‘damping’’ functions to increase energy dissipation due to frictional contact, in which the torque preload can be set without changing the nominal frequency. Thus, the Orion beam presents the benefit of amplitude attenuation without significant losses in the contact stiffness, which paves the way for proposing new control techniques in jointed structures by combining vibration amplitude attenuation and bolt preload. Preliminary investigations on vibration reduction by control of tightening load were addressed by Bouaziz *et al.* (2016), but there is still a lack of contributions in the literature that needs to be addressed, and this might advance with the Orion beam.

2.2 DESIGN OF EXPERIMENTAL SETUPS

2.2.1 Boundary Conditions

It should be stressed that one of the main objectives behind bolted joint applications lies in determining the evolution of the resonance frequency and damping according to the amplitude of the solicitations, the so-called ‘‘modal backbone’’ (see Peyret, Dion and Chevallier (2016)). To achieve this goal, one must try to excite only one vibration mode at a time and cover a wide range of amplitudes. First of all, the boundary conditions applied to the structure make it possible to stress the joint with more or less amplitude. Three sets of boundary conditions are found in the literature; see Fig. 9 (a)-(c). The simplest testing conditions are the free-free conditions fully inspired by linear modal analysis, see (SONG, 2004; BRAKE *et al.*, 2014; JALALI *et al.*, 2019). This boundary condition avoids parasitic effects, such as added damping or lack of rigidity that comes from boundary conditions. Unfortunately, the free-free condition does not allow the testing structure to reach large vibration magnitudes. The second classical way is to work in clamped-clamped or clamped-free conditions (FESTJENS; CHEVALLIER; DION, 2013; PEYRET *et al.*, 2010; DION; CHEVALLIER; PEYRET, 2013; PEYRET; DION; CHEVALLIER, 2016), as illustrated in Fig. 9(b). Unlike the free-free case, these boundary conditions can reach large vibration magnitudes, which is fundamental to characterize the nonlinearity. Nonetheless, the clamp design must be carried out carefully. As connections are a source of energy dissipation, fixed boundaries may influence and/or generate confusion when analyzing the structural damping of bolted joints. Ritto, Sampaio and Aguiar (2016) discuss the presence of uncertainty in the stiffness of boundary conditions, which can reduce over time due to wear and clearance, as well as the need to include this effect in the dynamic model of a mechanical system considering a stochastic framework. Catalfamo

et al. (2016), in turn, proposed a clamped-free condition to the BRB benchmark. However, after dynamic tests measuring the vibration response in the vicinity of the clamped end, the authors found the presence of pronounced acceleration, indicating that the connection behaved as a pinned joint instead of a fixed boundary. Thus, one can conclude that ensuring a clamped condition can mitigate the appearance of epistemic uncertainties in the response data of a structure.

One last alternative is to connect inertia to the ends of the specimen to increase the loading of the joint even in free-free conditions, as illustrated in Fig. 9(c). Gaul and Lenz (1997) have suggested this alternative, which was explored again by Scheel *et al.* (2018). This boundary is a simple way of loading the joints, but, in contrast, it is technologically more difficult to design since the added weights can generate parasitic preloads.

Figure 9 – Schematic representation of different types of setup. (a) bolted joint in free-free conditions (SONG, 2004; BRAKE *et al.*, 2014; JALALI *et al.*, 2019); (b) bolted joint in clamped-clamped or clamped-free conditions (FESTJENS; CHEVALLIER; DION, 2013; PEYRET *et al.*, 2010; DION; CHEVALLIER; PEYRET, 2013; PEYRET; DION; CHEVALLIER, 2016); (c) bolted joint with inertial loadings (GAUL; LENZ, 1997);(d) Impact hammer;(e) Vibration shaker; (f) Voice coil; (g) Piezoelectric device.

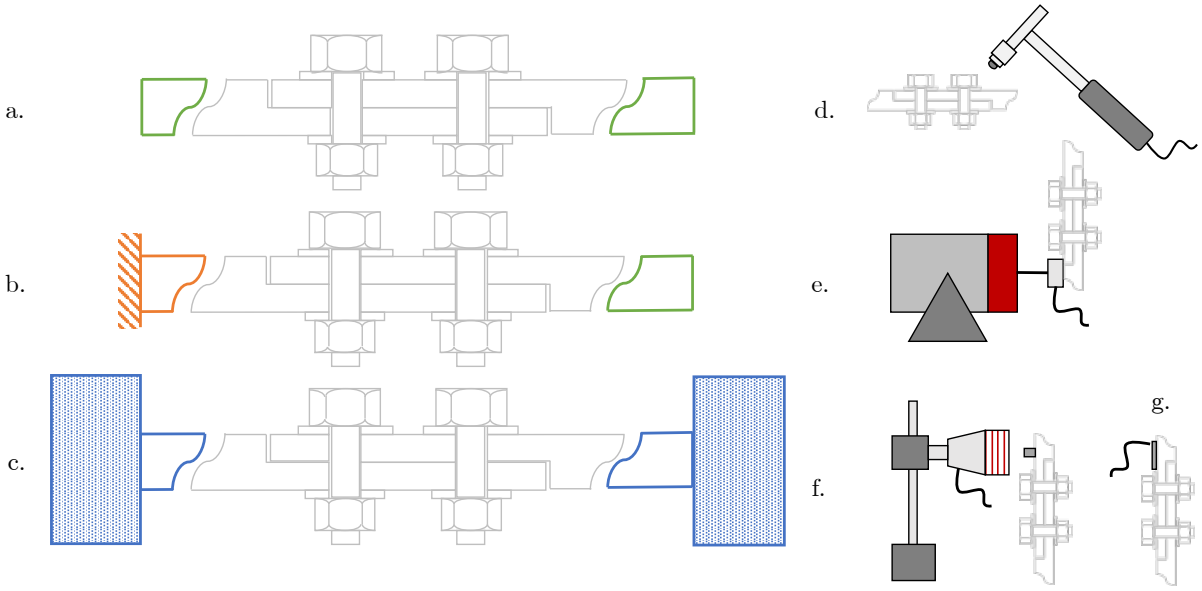

Source: Teloli *et al.* (2022).

2.2.2 Vibration sensing

There are several available ways to measure vibration signals of bolted joints. The most traditional ones found in the industry are accelerometers, which have become popular due to their relatively low cost compared to non-contact sensors and practical operation

in acquisition systems. Still, some limitations need to be underlined: as these sensors are attached (usually adhered with glue or wax) to the structure, changing their position between experimental tests may be a limitation; attention must also be paid to the orientation of the cables since triboelectric effects due to cable vibration can generate exogenous noise to the measured signal; and finally, the presence of accelerometers generates mass loading effects, especially for vibrating modes present at high-frequency values, which are sensitive to inertial effects. Depending on the position of accelerometers, the measurement data may show inconsistencies since, for different accelerometer positioning configurations, different characteristics in frequencies are likely to be obtained. At the end of the day, it does not matter whether it is a lightweight or heavyweight structure for these effects to occur, but rather how representative the mass of the measuring equipment used is on the structure (MCCONNELL; VAROTO, 1995; EWINS, 2009; AVITABILE, 2017).

One of the less invasive ways to acquire response signals during experimental tests is through contactless laser vibrometers. Generally, they can operate at different distances from the test bench (between 125 mm and 100 m, for example), with high resolution and the possibility of multiplying the number of measurements if necessary. However, its cost is still prohibitive depending on the context in which it is used. The experimental measurements conducted in this Thesis and presented in Chapters 4, 5 and 6, consider response measurements acquired by laser vibrometers as references.

Piezoelectric sensors are also an alternative for vibration monitoring (SILVA, 2018). Moreover, with advances in computing power, there is a growing use of Digital Image Correlation (DIC) and high-speed camera to capture and reconstruct the motion of oscillating systems (BRØNS *et al.*, 2020; ANDRÉ *et al.*, 2021; CHABRIER *et al.*, 2021). As pointed by Chen, Escalera Mendoza and Griffith (2021), image-processing techniques have the advantage to operate well in a wide dynamic range and the possibility to measure low-frequency vibrations, but in contrast, their use has limitations to measure very high-frequency vibrating modes.

2.2.3 Excitation devices

Excitation devices are important components in experimental setups. Regarding the analysis of jointed structures, to achieve the measurement of frequency response functions (FRFs) or to achieve backbone tracking, it is necessary to use a proper excitation device. In linear modal analysis, the most popular devices are impact hammers (BRAKE *et al.*, 2014), see Fig. 9(d). No permanent connection with the structure is the main advantage of

these excitation devices. The vibration signal they generate has a high-frequency content and a relatively low excitation amplitude. There is also limited control over the applied force, which depends on the hammer tip and the hammer mass. In the context of bolted structures, where the appearance of nonlinear behavior depends directly on the extent to which the lap-joint is stressed, their use may not be recommended to visualize nonlinear effects.

Vibration shakers (Fig. 9(e)) are adequate (tools) to obtain a very controlled frequency content and higher magnitudes (SCHEEL *et al.*, 2018). There are drawbacks in its use, such as the need to ensure that the transmitted force is undirectional (the use of flexible drive rods can mitigate these effects), as well as the change in dynamics of the structure to which the shaker is attached due to its impedance. Tang, Brennan and Gatti (2018) investigated the shaker-structure interaction by means of the dynamic stiffness method. The authors have found that when the shaker operates in current mode, i. e., when the current supplied to the shaker is kept constant, the force applied to the mechanical system under analysis is dependent on both the dynamic stiffness of the shaker and the dynamic stiffness of the structure. Even so, because of the possibilities of providing frequency-controlled signals, applications discussed in the Thesis make use of shakers.

It is interesting to point out that some works are trying to propose exotic excitation devices such as coils or piezoelectric devices to couple the advantages of both hammers and shakers (PEYRET; DION; CHEVALLIER, 2016; HUYNH; DANG; KIM, 2018). For example, the use of these devices embedded in the structure to provide the excitation force ensures a negligible impedance modification on the system response when the excitation signal stops.

2.2.4 Excitation design

As mentioned in the introduction, several excitation types are commonly used to study dynamic behavior. The impact test is widespread and practical for measuring frequency response functions. This kind of excitation is not subject to the mass and stiffness effects of the shaker attachment, and it is helpful for linear structures. The input power spectrum is broadband, and it can excite a wide frequency range (BRAKE *et al.*, 2014; AVITABILE, 2015). It is also an interesting type of excitation to infer information from the effect of components external to the testing structure related to boundary conditions and instrumentation, as investigated by Smith *et al.* (2015) in a series of testing scenarios

involving the BRB benchmark. However, exciting nonlinearities through impact testing is a difficult task. Nevertheless, recent works have explored the transient response for the nonlinear model updating of bolted jointed structures (LACAYO; ALLEN, 2019; YUAN; REN; ZHANG, 2019).

Still, regarding excitation techniques useful for modal analysis, the random excitation signals have a fundamental role due to their practical implementation of exciting the structure with varying amplitude and also reaching a wide frequency range. However, when considering this excitation type for identifying nonlinear systems and depending on the nonlinearity severity, the nonlinear effects in the system's output may be mistaken for noise disturbances. This may be a limitation of random excitations in dealing with nonlinear systems (CAUGHEY, 1959; SCHOUKENS; LJUNG, 2019).

One of the main advantages of using controlled periodic excitations lies in selecting a frequency range. It is possible to characterize, locate, and quantify the nonlinear distortions on the system's response. Sweeping sine tests provide an attractive, cost-effective ratio between the magnitude of excitation level and testing time (GLOTH; SINAPIUS, 2004). However, as clarified by Dion, Chevallier and Peyret (2013), for weakly damped natural modes, the sweep rate shall be appropriately chosen to avoid modulations between natural frequencies and excitation ones. Special attention must also be given to step-sine, and stop-sine tests, commonly used for mode isolation through force appropriation methods, jump-up and jump-down testing for characterization of nonlinearities, harmonic component analysis, among other applications (PEETERS; KERSCHEN; GOLINVAL, 2011c; TANG *et al.*, 2016; SCHEEL *et al.*, 2018). When compared with sweeping sine tests, both step and stop-sine may require a long testing time.

Figure 10 presents a compilation of the excitations strategies here discussed, as well as a comparison between each excitation in the time-frequency domain. Of course, several variants exist for each excitation technique, for instance, burst-random, multi-sine, and so on. However, the main idea behind this section is to present, among several excitation types, which one may provide the most accurate excitation in the context of our study. Further discussion on this subject is found in Worden and Tomlimson (2001), Ewins (2009).

Figure 10 – Comparison between different excitation types.

Input	Time-Frequency	Benefits	Disadvantages
Impact Test 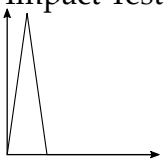	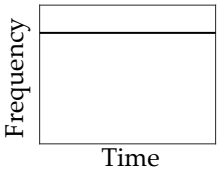	• Practical and fast testing; • Broadband excitation.	• Difficult to excite nonlinearities.
Stop-Sine 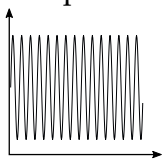	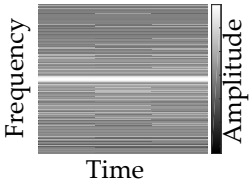	• Single frequency excitation; • Highlight harmonics in system response.	• Narrow-banded spectrum.
Sweep Sine 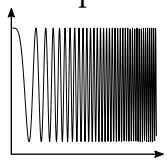	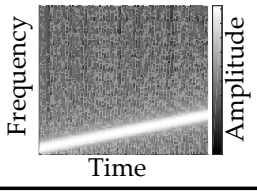	• Ajustable frequency band; • Ajustable sweep rate.	• Modulations between resonant frequencies and excitation ones.
Step-Sine 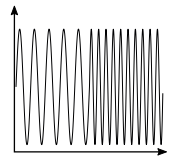	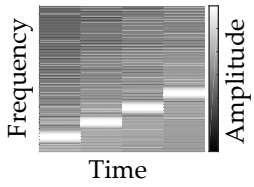	• Ajustable frequency band; • Jump-up and jump-down testing; • Steady-state response.	• Long time testing; • Amplitude control.
Random 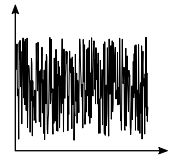	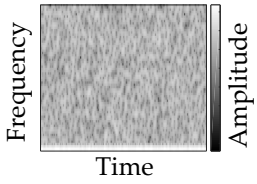	• Broadband excitation; • Linear modal testing.	• Difficult to excite nonlinearities.

Source: Teloli *et al.* (2022).

2.3 MODELING JOINT CONTACTS

One of the main limitations of models that attempt to describe in detail the contact interface at joints lies in the difficulty of measuring parameters on a small scale, making these representations liable to epistemic uncertainties due to, *inter alia*, simplifying assumptions made during parameter calibration, the subjectivity in the modeling framework and data paucity (BEER; FERSON; KREINOVICH, 2013). Nonetheless, the presence of epistemic uncertainties is ‘‘unavoidable by necessity’’, since the cost-benefit of making approximations is reflected in reducing the elapsed time to perform computational calculations. Thus, to ponder the role of uncertainties (aleatoric and epistemic) on

computational models of joints and motivated by the multidisciplinary nature of the issue, a new field in mechanical engineering has recently been proposed. So-called tribomechadynamics (BRAKE; KRACK; SCHWINGSHACKL, 2020), this research area has the objective of integrating aspects of tribology (FANTETTI *et al.*, 2019), contact mechanics (BRAKE, 2014; DREHER *et al.*, 2021), and structural and nonlinear dynamics to predict the nonlinear response of a jointed structure with frictional interfaces.

No matter how regular, smooth, and flat the surfaces are, from the nano and micro length of scale view, there will always exist asperities. In the tribology field, there are constitutive contact models to describe the stress-strain relationship between rough surfaces. These models are derived from the Hertz contact theory (HERTZ, 1882; JOHNSON; JOHNSON, 1987), which was first proposed to describe the usual contact of elastic solids that represent each asperity individually by spherical bodies. Then, to take into account tangential contact, which is responsible for micro slip motion between bodies, Mindlin (1949) proposed a model that reduces the contact problem by considering normal and tangential displacements between a sphere and a plane. Unlike the classical laws of friction, which define that below a threshold value, i.e., a static frictional force, there is no relative motion between bodies and consequently no energy dissipation (BOWDEN; BOWDEN; TABOR, 2001), Mindlin (1949) showed that energy dissipation and nonlinear damping behavior already start in partial slip regimes. Figure 11 illustrates a schematic representation of the stress distribution present in contact regions investigated by Mindlin (1949). Two contact zones are present: the stick zone and the slip zone. When the tangential force T applied on the interfaces in contact increases, the diameter $2c$ of the stick zone decreases until the tangential force reaches an upper threshold $T_c = \mu N_0$ (it follows the Coulomb friction law), in which μ is the friction coefficient and N_0 is the normal force applied, such that, from this point on, $c = 0$ and the surface reaches the macro-slip phase.

There are several approaches that have been expanded to represent rough surfaces in contact. One can refer to statistical models, in which probability density functions are proposed to describe the distribution of asperities over a rough surface (GREENWOOD; WILLIAMSON, 1966; ERITEN; POLYCARPOU; BERGMAN, 2010), or even deterministic models that calculate the actual contact area by integrating the asperities over the contact surface (OLOFSSON; HAGMAN, 1997; ZHAO *et al.*, 2016; ZHAO *et al.*, 2021). Figure 12 illustrates the fretting contact of nominally flat rough surfaces investigated by Eriten, Polycarpou and Bergman (2010). In such an approach, one surface is assumed flat, whereas, for the equivalent rough surface, each asperity is treated as spheres of

Figure 11 – Schematic illustration of stress distribution described by the Mindlin model (MINDLIN, 1949) between a sphere and a plane regarding (a) the contact area and (b) the contact between a sphere and a plane under the influence of the tangential force. In both figures, $2c$ and $2c$ are the stick zone diameter and the surface diameter, respectively; $\mu\sigma_0$ and τ represent are the stress due to the normal and tangential loads, respectively.

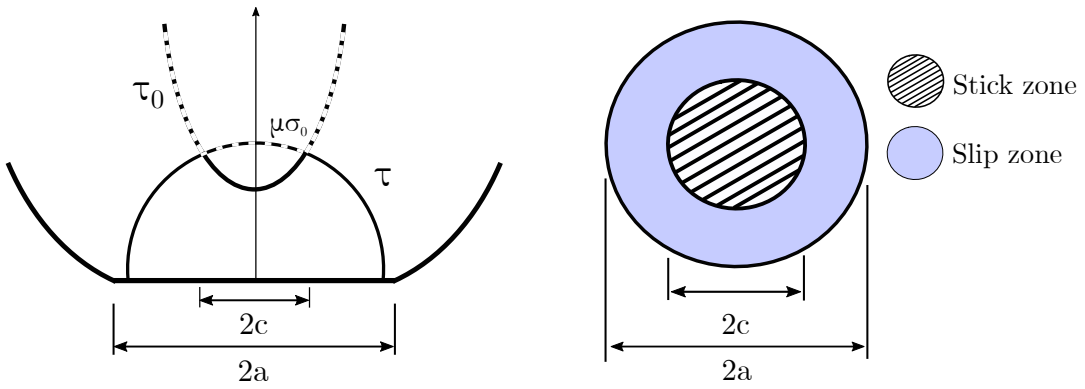

(a) Stress distribution at contact interface.

(b) Contact between sphere and plane.

Source: Adapted from Peyret *et al.* (2017).

the equal radius with randomly distributed heights $\pi(z)$. The asperities are assumed uniformly distributed over the nominal contact area and, since the problem is treated by the sphere-plane representation, the Mindlin model is used. These constitutive models can be implemented into discretization methods, as the FE method, to describe the contact mechanics in bolted joints (BOGRAD *et al.*, 2011; LI; HAO, 2021). As already mentioned, problems involving the interface zone at the nano and micro-scale are beyond the scope of this Thesis, but the interested reader will find comprehensive reviews on the subject in Johnson and Johnson (1987), Brake (2018a), Bouchaala, Dion and Peyret (2018) and Meurdefroid (2020).

Figure 12 – Schematic illustration of fretting contact of nominally flat rough surfaces investigated by Eriten, Polycarpou and Bergman (2010), in which z exemplifies the asperity height.

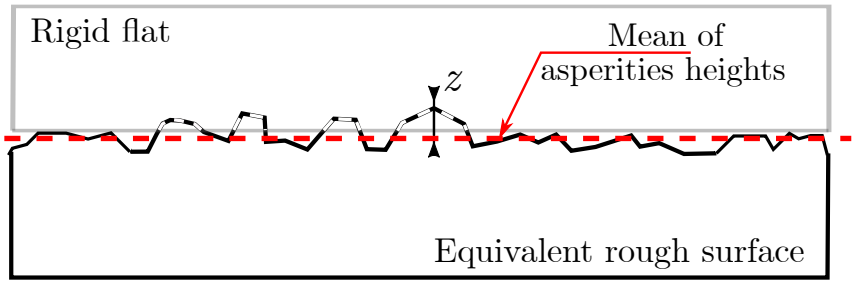

Source: Adapted from Eriten, Polycarpou and Bergman (2010)

General-purpose FE software offer tools for modeling contact in bolted structures, including the possibility to adjust normal contact influenced by compressive loads applied by bolts, as well as tangential contact induced by dynamic loads that induce slip between surfaces (SEGALMAN *et al.*, 2009). Penalty (WILLNER; GAUL, 1970; GWINNER; BROSOWSKI, 1989), Lagrange multipliers (BARAFF, 1993) and augmented Lagrangian (SIMO; LAURSEN, 1992) models, for instance, can be used to enforce contact constraints, whereas the frictional motion is generally modeled by the Coloumb friction law (GAUL; NITSCHE, 2001). To ensure good fidelity to the sliding motion, which occurs in a length scale of μm, FE-based models require refinement of their mesh, especially in the region around the contact interface. Due to the complex nonlinear behavior, the prediction of the dynamic response of bolted joints is computationally expensive or even prohibitive depending on the level of the model's detail.

At this point, although not directly related to the modeling of contact interfaces[1], it is worth mentioning some solutions available to speed up the calculation of FE-based model responses. Proposed initially by Festjens, Chevallier and Dion (2013), the quasi-static modal analysis (QSMA) consists of calculating the frequency and damping curves as a function of the total mechanical energy related to the mode of interest (modal backbone curves) from the quasi-static response of an assembled structure, which avoids traditional problems involved in calculating responses in the time and frequency domains. Simply put, the method initially estimates a specific vibration mode of a structure on a linear modal basis (monolithic state) and then extracts the corresponding nodal displacements. Then the mode of interest's displacement is transformed into inertial forces that are applied as a distributed load to the structure with joints. The stationary solver present in FE software is responsible for calculating the quasi-static nonlinear response of the model up to a given maximum strain amplitude, i. e. until a maximum amplitude of the distributed load. Based on Masing's rules, this initial loading path is then used to extrapolate the entire hysteresis cycle present in the restoring force × displacement plane. These rules will be covered in detail in Appendix A. Since the enclosed area by a hysteresis curve is equivalent to the dissipated energy per cycle and the nonlinear response curves were calculated in the quasi-static regime, one can estimate the effective damping and the instantaneous natural frequency of the mode of interest to construct the frequency-energy plot (FEP) and the damping-energy plot (DEP). In practical terms, the approximations made by the QSMA algorithm lead to the reduced computational effort since there is

[1]In fact, FE analysis involves macroscopic scale geometries. But due to the modeling aspects of contact interfaces related to the micro-scale length, this approach is investigated throughout this section.

also no need to compute transient regimes. Recent works advance the evaluation of the robustness of the algorithm for different sets of model properties in commercial FE codes, or also by comparing the amplitude-dependent frequency and damping predictions made by QSMA in FE-based models with experimental measurements of actual structures (JEWELL *et al.*, 2020; ZARE; ALLEN, 2021). It is important to stress that Masing's rules are a simplifying assumption and may not be satisfied depending on the application, thus invalidating the use of the QSMA algorithm.

In parallel, there exist simplified ways to represent joint interfacial elements in a discrete analysis context that comprise low computational cost and/or accuracy in predictions. By far, beam elements are the simplest available representation of joints. These approximations are physically driven by the essential nonlinear features present in the global behavior of joints, e.g., decreasing of resonant frequencies as the excitation amplitude increases, usually using phenomenological models coupled in combination with parallel/series stiffness elements and generic mass and damping matrices to formulate the hysteretic relationship between the restoring force and displacement. The energy dissipation mechanism of bolted joints during the vibration regime is also taken into account. Song (2004) proposed the adjusted Iwan beam element, a two-dimensional element to describe the elastic-plastic hysteresis characteristics present in transverse and rotational displacements of assembled structures by means of an Iwan model. Figure 13 puts the linear elastic element (a) and the Iwan element (b) in contrast, where the internal forces acting on the element $V_1 = f(\Delta_1, h_1)$ and $V_2 = -f(\Delta_1, h_1)$ become a function of the strain Δ associated with the Iwan models. Subsequent works have explored similar formulations (FESTJENS; CHEVALLIER; DION, 2014; YUAN; REN; ZHANG, 2019; WANG; XU, 2020), including the analog adjusted LuGre beam element proposed by Jaumouillé, Sinou and Petitjean (2010). Ahmadian and Jalali (2007b) described an assembled structure through the Euler-Bernoulli beam formulation, in which the joint is approximated by a lumped interface model containing a combination of nonlinear stiffness and damping elements to capture the softening phenomenon due to slip motion.

Segment-to-segment contact elements are generally formulated into the thin layer or zero-thickness element (ZTE) theories. Both formulations, which were initially developed for the geomechanics field to model soil-structure interactions (SHARMA; DESAI, 1992), have proven to be suitable for describing contact in joints (BOGRAD *et al.*, 2011). They reduce the computational cost in a FE analysis since the bodies that share the interface are assumed to remain in a contact condition, and there is no need to implement search algorithms to enforce contact constraints. The thin layer element consists of modeling the

Figure 13 – Schematic illustration of the (a) linear elastic element and the (b) Adjusted Iwan element. In both figures, V and M are the shear forces and bending moments, respectively; each element contains 2-DoF, Θ and u, which are the rotation angle and the vertical deflection, respectively; k is the stiffness; l and h are the length and height of the beam element.

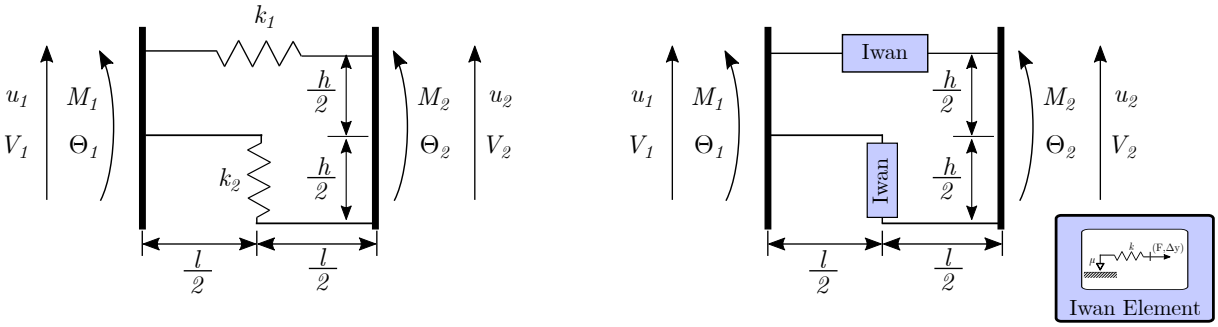

(a) Linear elastic element. (b) Adjusted Iwan element.

Source: Adapted from Song (2004).

contact between two interfaces by a continuous element with minimal but finite thickness to regularize rigid contacts. These elements may assume a linear elastic constitutive form (MAYER; GAUL, 2007), or even a thin layer model represented by the nonlinear stress-strain curve of the contact zone to emulate the slip motion in bolted joints (IRANZAD; AHMADIAN, 2012). Figure 14(a) depicts an arbitrary thin layer model, in which the tangential forces $\overrightarrow{T}$ produce shear stress τ in the layer. By experimentally estimating the contact area A, the tangential force $\overrightarrow{T}$, and an approximation for the lap joint stiffness, it is possible to derive the remaining model values (BOGRAD *et al.*, 2011). Zero thickness elements (ZTE), in turn, establish an interfacial element (two four-node quadrilateral elements, $1-2-3-4$ and $5-6-7-8$, which face each other) with arbitrary constitutive laws to describe the small global relative displacement between two segments (MAYER; GAUL, 2007). Figure 14(b) illustrates a ZTE with emphasis on the $\xi \times \eta$ tangential plane with respect to the normal direction n. To illustrate, there are applications that include three-dimensional contact law based on Jenkin elements to incorporate separation, stick and slip effects into the model (SÜSS; WILLNER, 2015), as well as frameworks that employ rough contact theory to establish fundamental constitutive relationships with parameters estimated from micro-scale surface scans (BALAJI; CHEN; BRAKE, 2020).

Introduced by Segalman (2006), whole joint approximations reduce the degrees-of-freedom (DoFs) of the contact interface by adopting constitutive models with a number of measurable quantities to account for critical nonlinear physics at the joint. In a FE context, such an approach is created by constraining all the DoFs on each side of the

Figure 14 – Schematic illustration of: (a) thin layer element, in which G, τ and φ are the shear modulus, stress and angle; A is the contact area; d and u are the layer thickness and relative displacement, respectively. (b) ZTE, in which $\xi \times \eta$ is the tangential plane natural coordinate and n is the normal direction.

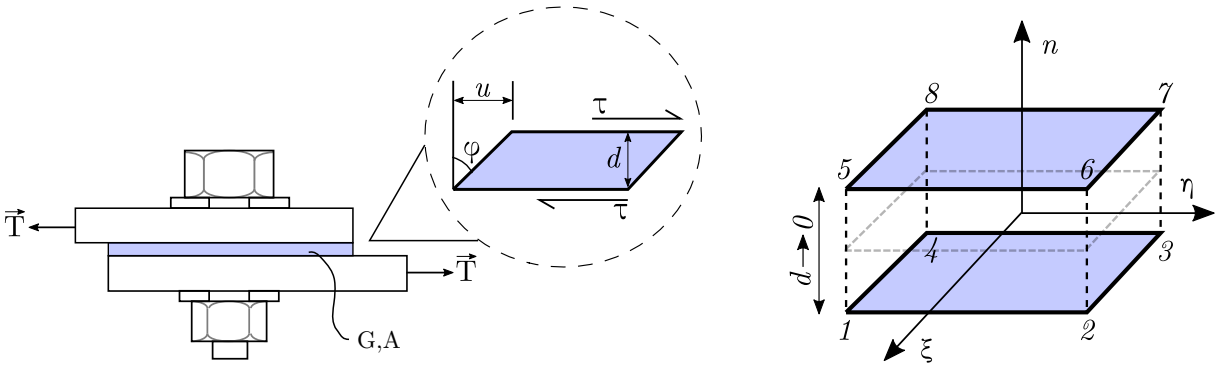

(a) Schematic of a thin layer element.

(b) Schematic of a ZTE.

Source: Adapted from (a) Bograd *et al.* (2011) and (b) Balaji, Chen and Brake (2020).

interface to a single virtual node (may be referenced as averaging multi-point constraint) composed by a nonlinear constitutive element with tunable parameters, as illustrated in Fig. 15(a). Among several candidates, Iwan element stands out as the constitutive model chosen for modeling micro and macroslip in the contact interface (SEGALMAN *et al.*, 2015; NAJERA-FLORES; KUETHER, 2020; LACAYO *et al.*, 2019; LACAYO; ALLEN, 2019). This results in low-order models that can be integrated by time-domain solvers to compute responses to impulsive excitations, for instance. However, some drawbacks are present in this formulation.

In the case of a bolted structure with many joints, it becomes difficult to evaluate the contribution of each joint in the global nonlinear behavior through experimental measurements (this contribution will depend on the vibrating mode that stresses more or less the area around the joint, contact pressure distribution over the surface, among other attributes challenging to be isolated for each joint location), reflecting in an additional challenge to calibrate the parameters of constitutive models that compose the virtual nodes (LACAYO; DEANER; ALLEN, 2017). Moreover, whole-joint representations may be inaccurate in describing the contact interface, being limited to displacements that ensure weak nonlinear behavior. To minimize part of this problem and investigate alternatives to remove sources of epistemic uncertainties inherent in the modeling procedure, Balaji and Brake (2019) introduced a three-patch formulation to model the lap-joint of the BRB benchmark under different design choices (different lengths and). In this

formulation, the contact interface is divided into five whole joint patches connected by virtual nodes with Iwan elements, such that the pairs comprising the ‘‘external patches’’, i.e., referring to the two external bolts in Fig. 6(d), are assumed identical by symmetry. By doing this, the complexity in the optimization procedure of the model parameters is reduced.

Figure 15 – Schematic illustration of (a) whole joint element; (b) node-to-node element, in which k_T and k_n are the tangential and normal stiffness, N_0 is the normal force and μ is the friction coefficient.

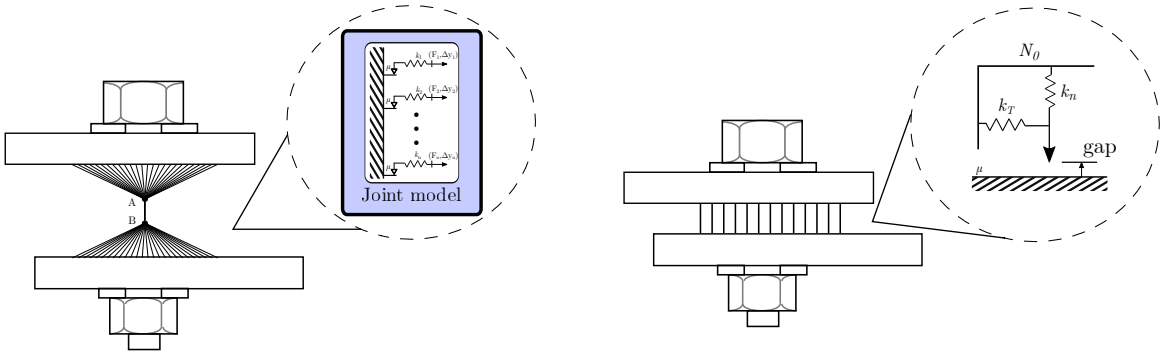

(a) Schematic of a whole joint element.

(b) Schematic of a node-to-node element.

Source: Adapted from (a) Segalman (2006) and (b) Petrov and Ewins (2003).

First proposed by Petrov and Ewins (2003) to model nonlinear frictional vibrations of bladed disks (PESARESI *et al.*, 2017; YUAN *et al.*, 2021) and then expanded to deal with jointed structures (ARMAND *et al.*, 2018), node-to-node contact elements consider that each node at the interface is coupled with a corresponding node, such that the relative displacement leading to stick-slip motion is modeled in normal and tangential directions, as depicted in Fig. 15(b) for a 2D application. In summary, each contact element describes the motion in 3D, consisting of two Jenkins elements in the tangential direction (2D-Jenkins element) and a spring element oriented in the normal direction. All these elements are connected to a frictional Coulomb slider to emulate stick-slip transitions, as well as contact-separation transitions (PETROV; EWINS, 2003; ARMAND *et al.*, 2018). Thus, each contact element is given as a function of the parameters friction coefficient, initial normal load, tangential, and normal contact stiffness elements, which can be extracted from experimental measurements (SCHWINGSHACKL; PETROV; EWINS, 2012). When compared to whole joint approximations, node-to-node contact formulations offer the highest accuracy in the nonlinear analysis of joints, but in trade-off, they are computationally more expensive.

To minimize the computational cost involved in models formed by node-to-node

contacts, a nonlinear analysis code has been proposed, so-called FORSE (FOrced Response SuitE). As already mentioned, meshes regarding the geometry of ''linear''[1] models that will include node-to-node contacts are built-in general-purpose FE software. Then, after substructuring the problem assembling friction interface forces, the FORSE algorithm expands the steady-state response of the nonlinear algebraic system into multi harmonic components via Fourier series representation (ARMAND *et al.*, 2018). Represented in the frequency domain through the Fourier coefficients, the nonlinear system is solved using the alternating frequency-time (AFT) procedure (CAMERON; GRIFFIN, 1989; SALLES *et al.*, 2011). In the context of bolted joints and as an alternative to reduce the connection nodes in the description of the BRB benchmark, Lacayo *et al.* (2019) proposed the node-to-node joint model using partitioning of the contact region via Voronoi polygon calculation, such that each polygon assumes the sum of normal forces per unit area. According to the authors, the simplified representation of the contact area accelerated the computational calculations without compromising the model's fidelity through the results achieved.

To better illustrate the constitutive models discussed throughout this section, Appendix A provides a brief review on static and dynamic models for describing hysteresis.

2.4 MODELING GLOBAL NONLINEAR BEHAVIOR

In a bolted joint structure, the nonlinear effects are directly related to the loads imposed in the region around the joints. This implies that not all vibrating modes of a structure will exhibit nonlinear behavior, only those that lead motion in a more pronounced manner at the interface with friction. In this scenario and for applications where the contact area modeling is not of utmost importance, assuming a representation that is based on matrices or meshes extracted from finite element geometries may represent an unrequired computational cost.

The concept of nonlinear modes is helpful for the dynamic characterization of mechanical systems, in which the contributions related to nonlinear normal modes (NNMs) stand out. The NNMs are the nonlinear counterpart of the normal linear modes (LNMs) (ROSENBERG, 1960; SHAW; PIERRE, 1993), having some distinctions in their properties, such as violation of the superposition principle and amplitude-dependent resonant frequencies (curved modal lines), but also similarities as the invariance principle (KING; VAKAKIS, 1994; KERSCHEN *et al.*, 2009). In general, NNMs have the purpose

[1] Simply put, the constitutive matrices of these models do not include contact-related elements; these are added later in external numeric computing platforms, such as Matlab or Python.

of extracting modal backbones and branches (internal resonances) of modal interactions in an FEP, which offers the possibility of interpreting the nonlinear behavior of mechanical systems as the vibration energy level increases (PEETERS *et al.*, 2009; RENSON; KERSCHEN; COCHELIN, 2016).

To evaluate a specific nonlinear mode in isolation, it is necessary to ensure its extraction during experimental testing. Success in achieving this task depends on the characteristic of the input signal adopted, which should have restricted frequency content near the resonance region of interest (see subsection 2.2.4), the existence of low modal coupling (light modal density and modes well-spaced) and the higher-order harmonics of the mode of interest do not coincide with other vibrating modes, which relies on the severity of the nonlinearity. Thus, for the NNMs extraction, the use of experimental modal analysis (EMA) techniques is adopted, including phase resonance testing (also known as force appropriation). Obtaining the NNMs from this test consists of two steps: first, the structure under analysis is driven to a monophase periodic motion in quadrature with excitation, indicating that an NNMs is well isolated; then, the external excitation force is turned off, and from the NNM free decay, the evolution of the frequency and modal curves is identified (PEETERS; KERSCHEN; GOLINVAL, 2011b; PEETERS; KERSCHEN; GOLINVAL, 2011a).

Besides the robust theoretical background, the framework of NNMs is only well-defined for conservative systems or slightly damped systems at least and include only nonlinearities in stiffness. This restricts its applicability for dealing with bolted joints, a type of system where both frequency and damping are dependent on vibration energy. To analyze nonlinear modes[1] of nonconservative autonomous systems, Krack (2015) proposed the extended periodic motion concept (EPMC). The approach consists of capturing nonlinear modes through periodic dynamics under either near-resonant harmonic forcing or self-excitation by negative modal damping. Practically speaking, the periodic dynamics are induced by an excitation source that drives the system to resonance and introduces an artificial negative damping term that compensates the nonconservative forces, i.e., mass-proportional velocity is feedback-controlled as an excitation force to the system. By performing this procedure, modal characteristics are directly obtained (energy dependence of modal frequency and damping ratio). The EPMC has been validated considering several numerical applications, and among them is a friction-damped rod, illustrating that the

[1]The term *nonlinear modes* is adopted by the Krack (2015) instead of NNMs, since the term ‘‘Normal’’ derives from the property of orthogonality between modes, which is held only for symmetric conservative systems.

method is also valid for bolted joint applications.

Then, based on the EPMC definition, Scheel *et al.* (2018) proposed a phase resonance approach similar to that discussed earlier for NMMs to extract the nonlinear modes of structures undergoing the nonlinear dissipation process. To isolate the periodic motion of a nonlinear mode of interest, the authors considered the phase-locked loop (PLL) feedback-controller, which is to adjust the excitation frequency until the fundamental harmonic force component finds the frequency where the system response at the driving point is in phase resonance. One of the advantages of this method is its feasibility in an experimental context, as only a single-point single-frequency force appropriation is necessary to isolate a nonlinear mode. However, although it seeks resonant frequencies separately at each input force level, the excitation is harmonic (similar to step-sine tests), and the time required to reach a steady-state regime can be high. The method was then used to investigate the evolution of modal backbones in different assembled structures, including a Gaul resonator (SCHEEL *et al.*, 2018), the BRB benchmark (SCHEEL *et al.*, 2020) and the Rubber system, a cantilever beam that permits to vary the joint's position (SCHEEL; WEIGELE; KRACK, 2020).

Another way to reconstruct the global dynamics of nonlinear modes in bolted structures is through lumped models in the form of single-degree-of-freedom (SDoF) oscillators. In most cases, this class of reduced-order models (ROMs) has discrete nonlinearity terms that are adopted based on a physical understanding (phenomenological approximations) of the source of the nonlinear behavior (EWINS; WEEKES; Delli CARRI, 2015). The restoring force comprises these nonlinear terms, which assume the form of functionals taking into account measurable quantities of motion, such as velocity and displacement[1], to emulate nonlinear phenomena observed in joints, as the presence of multiple harmonics in the response signal, hysteresis on the restoring force × displacement plane and softening effects.

Due to the characteristics of these SDoF oscillators, which often have the restoring force driven by hysteresis models (e.g., Iwan, Bouc-Wen and Dahl models)[2] featuring non-smoothness, multiple solutions, and rate-dependent or -independent memory effects, the process of estimating the parameters that constitute these models restricts the use of conventional nonlinear system identification (NSI) techniques (KERSCHEN *et al.*, 2006),

[1] In practice, due to the availability of measurement instruments, usually one quantity is acquired, either acceleration, velocity, or even displacement, and the others are estimated by numerical integration/derivation.

[2] Note that the same constitutive models presented earlier in the context of modeling local joint behavior are also helpful in describing global nonlinear dynamics.

including approximations based on the restoring force surface method, Volterra series expansions through the harmonic probing algorithm or even perturbation methods if no smoothing procedure is employed.

Contributions to the identification of SDoF oscillators for describing frictional effects in bolted structures have been proposed. Eriten *et al.* (2013) developed a NSI methodology that consists of first performing experimental modal analysis by means of an impact hammer on a bolted structure to extract resonance frequencies and damping ratios. Subsequently, for appropriate impact levels that ensured prominent nonlinear behavior, the empirical mode decomposition (EMD) in combination with the Hilbert transform was applied to the response time series to extract sets of intrinsic modal oscillators. These, in turn, when compared with the extracted linear characteristics, allowed deducing the evolution of the nonlinear damping and how it affected the dynamics of the bolted beam for the excitation levels investigated. Apart from that, one of the main aspects discussed by the authors lies in the investigation under which conditions one can assume the assumption of uncoupled modes, allowing the approximation of each structural mode from SDoF oscillators. The authors showed that energy transfer between modes is negligible either when resonance frequencies are far apart from each other and between their respective harmonics or for weak nonlinearities.

From the foundations presented by Eriten *et al.* (2013), other work has explored the possibility of approximating each structural mode of bolted structures with nonlinear constitutive models. Segalman *et al.* (2015), for instance, discussed the idea of modal Masing models, which consists of approximating each nonlinear mode of an assembled plate specimen by joint-based modal models under the central hypothesis that the nonlinear modal forces encode only the deformation history of just one mode. A similar extension of this method was proposed by Deaner *et al.* (2015), which used modal Iwan models to individually reproduce the vibration modes of the Sumali beam (see Fig. 8(b)). For each nonlinear mode, a set of Iwan model parameters was identified to capture the evolution of the stiffness and damping of the structure at different input amplitudes. More recently, Roettgen and Allen (2017) explored the applicability of modal Iwan models to predict the dynamics of a catalytic converter system, a test rig that has joints as the source of its nonlinearities.

It is in the proposition of SDoF oscillators and NSI methodologies for describing the dynamics of bolted structures that some contributions of the Thesis lie. SDoF approximations combine relatively lower complexity when compared to FE representations, for

example, and are pretty representative for real engineering applications, allowing proof of concept for new identification strategies such as those presented in this dissertation. However, it is important to point out that there are disadvantages to using this approach. Overall, these models are not able to represent interactions that occur at the micro-scale, only the influence that the whole nonlinear restoring force has on a given vibrating mode. For this reason, parameters related to these models are often non-physical.

As will be discussed in Chapters 3 and 4, one of the main advantages in Bouc-Wen models may also be one of its main pitfalls. The parameters of this model can be combined in infinite ways to generate different hysteresis loops, and for this reason, there can be sets of parameters that result in the same outputs. Thus, to minimize the range of possible solutions to the model for applications involving parameter estimation, analytical approximations become a valuable tool in the white-box modeling framework.

The analysis of the frequency curves of isolated nonlinear modes provides qualitative indications about the system behavior (where are the resonance frequencies, what is their dependence with respect to different input amplitude levels, presence of the jump phenomenon, among others). However, how can one get clues about the influence that the tightening torque has on the behavior of a bolted structure in qualitative terms from these curves? Analysis on modal parameters, although not a valid concept in nonlinear systems, still provides interesting indications about different forms of behavior, but without a direct estimation of the nonlinear forces governing the motion. In this context, Chapter 5 introduces the Duffing-Van der Pol model that, through the analysis of its parameters estimated in an HBM-based methodology (another example that analytical approximations can be useful), enables quantitative inquiry on how different contact pressures influence the nonlinearities in the Orion beam.

Finally, as will be discussed in Chapter 6, black-box approaches face difficulties in describing systems in the presence of hysteresis, usually associated with the model structure, which must be carefully selected to reproduce the memory effect of hysteresis, and difficulty in validating these models for input conditions other than those used in the training phase. Thus, analyzing the first nonlinear vibrating mode of the BERT benchmark through the GP-NARX model is a necessary step for proof of concept that these models can be used to reproduce bolted structures in more general and challenging applications.

2.5 STATE-OF-THE-ART OVERVIEW

This Chapter introduced a brief state-of-the-art review, covering topics related to joint architecture by analyzing benchmarks available in the literature, the inherent presence of uncertainty in these structures since contact-related aspects are a source of epistemic uncertainty in their vibration behavior (see the results presented in subsection 5.4.2, for example), and discussions on a joint design that improve structural damping are also covered. From the point of view of designing experimental setups, the Chapter brings discussions on issues for selecting boundary conditions and vibration sensing, and also types of excitation signal that are suited for exploring nonlinear behavior in joints. Note that although these investigations have been done taking bolted structure applications as an example, such practices are also valid for other nonlinear systems.

Finally, issues related to bolted joint models are addressed from local modeling and global modeling perspectives. It is at these standpoints that the complexity (and also the attractiveness) involved in these structures stands out, as although some of the model approaches are constituted of common characteristics, the massive majority of these models have their own parameters to be estimated or hypothetically assumed, be it friction coefficient values, asperities distribution, pressure in the contact area, phenomenological model parameters for SDoF oscillators, among several others. It is clear that there is still no single approach that provides solutions to all problems, but rather approaches that are more convenient for specific applications and how much computational effort is at hand to calculate the responses of numerical models.

3 ON THE APPLICATION OF FREQUENCY DOMAIN TECHNIQUES FOR HYSTERESIS MODELS

Describing hysteresis models with a closed-form solution is challenging due to some pitfalls regarding the non-smooth and memory effect mechanisms that do not permit, for example, to apply frequency domain approximations. Thus, this Chapter brings forward new ways to approximate the hysteresis loops based on smoothing procedures, either by using smooth nonlinear operators or truncated Taylor series.

The Chapter begins by presenting the procedures required to turn it possible to derive analytical approximations of the higher-order FRFs for hysteretic oscillators. Section 3.1 shows the assumptions used to develop the smooth bounding functions that compose a smooth nonlinear operator. These bounding functions, in turn, aim to reproduce the loading and unloading regime of the restoring force individually in systems possessing the RIH property. Next, the applicability of the procedure is assessed on a Bouc-Wen oscillator. Section 3.2, in turn, introduces the Volterra theory and the harmonic probing method employed to derive the analytical expressions for the higher-order FRFs. Next, section 3.3 presents the numerical application of the suggested approach for the Bouc-Wen model benchmark proposed by Noël and Schoukens (2016b) at the Workshop on Nonlinear System Identification Benchmarks. The results presented in this subject were published in Teloli and Silva (2019).

Notwithstanding, another way to smooth oscillators with hysteresis is then addressed. From some theoretical foundations investigated during the proposition of the smooth nonlinear operator, it was found in section 3.1.2 the possibility of approximating the hysteretic restoring force of a Bouc-Wen oscillator by piecewise nonlinear expressions and then expanding them as explicit functions of displacement by the Taylor series approach. Thus, having the background to smooth the Bouc-Wen model, section 3.4

brings forward the harmonic balance method (HBM) and particularities involving its application to approximate hysteretic systems. These results were published in Miguel, Teloli and Silva (2020). Finally, section 3.4.3 presents a numerical application of HBM on the Bouc-Wen benchmark already investigated in the context of the higher-order FRFs.

Finally, since both frequency domain methodologies presented throughout the Chapter are numerically tested on the same hysteretic oscillator, section 3.5 proposes a comparison between the methods, assessing their respective advantages and disadvantages. Section 3.6 closes the Chapter with partial conclusions.

3.1 ON SMOOTH NONLINEAR OPERATOR

Nonlinear operators can be used to describe non-smooth systems or even singular functions (GUO; YANG; PAN, 2006; GIRI *et al.*, 2013; NASER; IKHOUANE, 2015; HUANG *et al.*, 2018). Giri *et al.* (2014) demonstrated that effects of backlash presented in non-smooth oscillators could be approached through Wiener models by applying beforehand a piecewise smooth operator. Radouane *et al.* (2017) assume a similar procedure to analyze a hysteretic system modeled by a Bouc-Wen oscillator. Martins and Aguirre (2016) discussed sufficient conditions to identify autoregressive models for rate-independent hysteretic systems to reproduce multiple solutions in the polynomial model by considering a single-input and single-output (SISO) Hammerstein model, which uses a multi-input and single-output (MISO) deterministic NARX block. It is essential to point out that all these bounding functions or structures do not try to propose new physical models but rather to extend methods and techniques to deal with non-smooth systems. In addition, the present paper relates the Bouc-Wen parameters to the polynomial coefficients that compose the bounding functions, as it is shown in 3.1.2.

3.1.1 Nonlinear operator

Some assumptions need to be made. First, a system with hysteresis that carries the bounded-input bounded-output (BIBO) property when excited by a harmonic input $u(t) = A\cos(\omega t)$ bounded between amplitudes $-\infty < -A \leq u(t) \leq A < \infty$ will produce on the displacement × restoring force plane a hysteresis loop delimited by the enclosed area $ABCD$ (VISINTIN, 2013), as is shown in Fig. 16(a).

The excitation $u(t)$ belongs to the class of $T-$periodic input signals (IKHOUANE; RODELLAR, 2007) and presents a periodic loading-unloading regime defined in a period

Figure 16 – Example of hysteresis loop in time continuous domain for a bounded loading-unloading input. – – – is the loading output and – the unloading output.

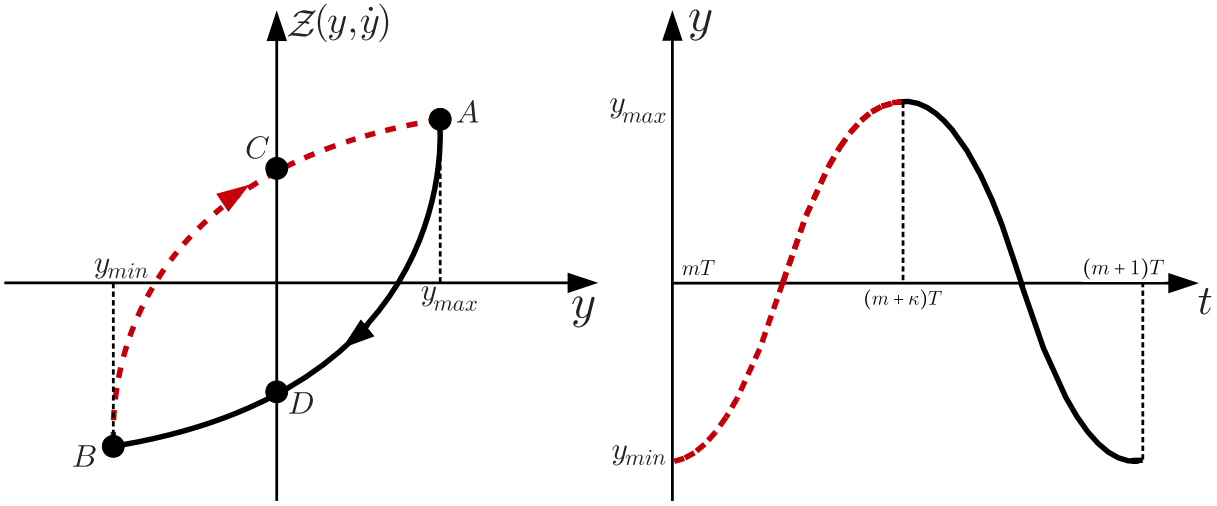

(a) Hysteresis loop. (b) Hysteretic response.

Source: Teloli and Silva (2019).

$T \in \mathbb{R}^+$. Thus, the output from the hysteretic system $-\infty < y_{\min} \leq y(t) \leq y_{\max} < \infty$ moves along two different paths. When $\dot{u}(t) > 0$ the output $y(t)$ is subjected to the load regime in the interval $y^{\uparrow}(t) \in [y(t+mT), \quad y(t+(m+\kappa)T)]$ and the pair $(\mathcal{Z}, y)$ moves along the path BCA. On the other hand, when $\dot{u}(t) < 0$, the system is in the unloading regime in the interval $y^{\downarrow}(t) \in [y(t+(m+\kappa)T), \quad y(t+(m+1)T)]$ and the pair $(\mathcal{Z}, y)$ moves along ADB, where $\kappa = \frac{1}{2}$ is a time constant and $m \in \mathbb{Z}^+$ is the number of oscillation cycles. This second remark was well discussed by Radouane *et al.* (2017) for defining the hysteretic loop assumption. Furthermore, systems where the restoring force $\mathcal{Z}$ encodes the hysteresis depending only on the $y_{\min} \leq y(t) \leq y_{\max}$ excursion interval are called rate-independent hysteretic systems. The Bouc-Wen, Duhem, Presaich, Prandtl-Ishlinkiĭ models, etc. exhibit this property (HASSANI; TJAHJOWIDODO; DO, 2014).

From the description of the loading-unloading paths on the hysteresis loop, it is possible to propose the bounding functions making use of the Weierstrass approximation theorem (JEFFREYS; JEFFREYS, 1999), which defines if $f(x)$ is a continuous function defined in the interval $[A, B]$ and, if an approximation error $\epsilon > 0$ exists, then a polynomial form $P(x)$ in $[A, B]$ exists such that:

$$|f(x) - P(x)| < \epsilon \quad \forall\, x \in [A, B], \tag{1}$$

Assuming that the load and unload regime cycles on the hysteresis loop can be

interpreted individually, one can propose a particular function for each regime by encoding its nonlinear dynamic to transform a hysteretic system into an equivalent piecewise smooth problem.

Then, let $\mathscr{F}^{\uparrow}[y(t)]$ and $\mathscr{F}^{\downarrow}[y(t)]$ be continuous bounding functions along the interval $y_{\min} \leq y(t) \leq y_{\max}$ to describe properly the load and unload regimes, respectively. Based on the Weierstrass approximation theorem, the functions $\mathscr{F}^{\uparrow}[y(t)]$ and $\mathscr{F}^{\downarrow}[y(t)]$ can be written as (GIRI *et al.*, 2014):

$$\mathscr{F}[y(t)] : \begin{cases} \mathscr{F}^{\uparrow}[y(t)] = f_0 + f_1 y(t) + \cdots + f_n y^n(t) & \text{for} \quad \operatorname{sign}(\dot{u}(t)) \geq 0, \\ \mathscr{F}^{\downarrow}[y(t)] = d_0 + d_1 y(t) + \cdots + d_n y^n(t) & \text{for} \quad \operatorname{sign}(\dot{u}(t)) \leq 0, \end{cases} \tag{2}$$

where $f_0 + f_1 + \cdots + f_n$ and $d_0 + d_1 + \cdots + d_n$ are the coefficients that compose the bounding functions. Furthermore, the continuity relation between these functions must be guaranteed to provide a smooth transition between the cycles:

$$\begin{aligned} \mathscr{F}^{\uparrow}[y(t+mT)] &= \mathscr{F}^{\downarrow}[y(t+mT)], \\ \mathscr{F}^{\uparrow}[y(t+(m+\kappa)T)] &= \mathscr{F}^{\downarrow}[y(t+(m+\kappa)T)] \quad \forall \ t. \end{aligned} \tag{3}$$

After establishing the existence of bounding functions, the next section presents how to rewrite the coefficients $f_0 + f_1 + \cdots + f_n$ and $d_0 + d_1 + \cdots + d_n$ as a function of the hysteretic system described by the Bouc-Wen model.

3.1.2 Application example on the Bouc-Wen oscillator

The classic phenomenological oscillator model proposed by Bouc (1967) and expanded by Wen (1976) to describe a single-degree-of-freedom system with hysteresis is given by:

$$m\ddot{y}(t) + c\dot{y}(t) + ky(t) + \mathcal{Z}(y, \dot{y}) = u(t), \tag{4}$$

$$\dot{\mathcal{Z}}(y, \dot{y}) = \alpha\dot{y}(t) - \beta\left(\gamma|\dot{y}(t)||\mathcal{Z}(y, \dot{y})|^{\nu-1}\mathcal{Z}(y, \dot{y}) + \delta\dot{y}(t)|\mathcal{Z}(y, \dot{y})|^{\nu}\right), \tag{5}$$

where m [kg] is the mass, c [Ns/m] is the viscous damping, k [N/m] is the linear stiffness, α [N/m], β, γ [m^{-1}], δ [m^{-1}] and ν are the Bouc-Wen parameters. In addition, $\ddot{y}$, $\dot{y}$ and y are the acceleration [m/s^2], velocity [m/s] and displacement [m], respectively, for an excitation input u [N]. The term $\mathcal{Z}(y, \dot{y})$ represents the hysteretic force that is described

by the ordinary differential equation $\dot{\mathcal{Z}}(y, \dot{y})$. Unfortunately, few research works have used white-box modelling to derive analytical solutions for the Bouc-Wen model, and contributions still lack in the literature.

Okuizumi and Kimura (2004) examined the response from a Bouc-Wen oscillator through the multiple scales method to verify the stability of the solutions by visualizing the trajectories on the phase plane. The idea behind the method lies in smoothing the hysteresis loop by expanding the restoring force using power series through multiple scales. Ikhouane and Rodellar (2005) proposed the analytical characterization of the limit cycle that occurs in the Bouc-Wen oscillator for a periodic input by using its normalized version and instrumental functions that can describe the effect of parameters of the model on the hysteresis loop. Laxalde, Thouverez and Sinou (2006) examined the usefulness of a nonlinear hysteretic absorber described by a Bouc-Wen model, which was used as a dissipation source of the vibratory energy. The periodic solutions predicted by the averaging strategy open the possibility of establishing some designing criteria to optimize energy dissipation. Other works use equivalent linearization to achieve analytic expressions for the oscillator response, such as Shen, Golnaraghi and Heppler (2005), who used the averaging method to obtain the response of a suspension system with a magnetorheological damper, and Jalali (2014), who proposed an alternative linearized approach to deal with weakly hysteretic systems.

The use of the Volterra series and the harmonic probing method in equations (4) and (5) is not possible due to the presence of absolute values. However, the smooth bounding functions $\mathscr{F}^{\uparrow}[y(t)]$ and $\mathscr{F}^{\downarrow}[y(t)]$ can be well represented by the Volterra series, since their representation are convergent. In this way, the interest in proposing the nonlinear operator is to explore the possibility of the higher-order FRFs describing systems with hysteresis in addition to being parametrized by the Bouc-Wen parameters.

The shape of the hysteresis loop changes according to the model parameters and more details are given by (IKHOUANE; RODELLAR, 2005; MALDONADO, 1987; WONG; NI; KO, 1994; IKHOUANE; HURTADO; RODELLAR, 2007). Dividing the equation (5) by $\dot{y}$:

$$\begin{aligned} \frac{d\mathcal{Z}}{dy} &= \alpha - \beta\left(\frac{\gamma\,|\dot{y}|\,|\mathcal{Z}|^{\nu-1}\,\mathcal{Z}}{\dot{y}} + \delta\,|\mathcal{Z}|^{\nu}\right), \\ \Rightarrow \quad \frac{d\mathcal{Z}}{dy} &= \alpha - \beta\,|\mathcal{Z}|^{\nu}\left[\operatorname{sgn}(\dot{y}\mathcal{Z})\,\gamma + \delta\right]. \end{aligned} \tag{6}$$

If $\mathcal{Z} = 0$, the slope of the restoring force is α implying that the parameter α can be associated equivalently with the linear stiffness k when the oscillator is subjected to null initial conditions. Moreover, it is important to point out that β is responsible for the hysteresis effects, γ in turn, whose values are always greater than zero for real systems, is the parameter that controls the hysteretic relationship between $\mathcal{Z}$ and y. Finally, the combination of $(\pm\gamma + \delta)$ characterizes the hardening or softening behavior in the hysteresis loop (BABER; WEN, 1981).

The explicit time integration of equation (6) with $\nu = 1$ divides the hysteresis loop of the Bouc-Wen model into four different intervals on the force × displacement plan between the signs of $\dot{y}$ and $\mathcal{Z}$. Figure 17(a) exemplifies, in the restoring force × displacement plane, the hysteresis loop produced by a Bouc-Wen model when subjected to a bounded harmonic input $u(t) = A\cos(\omega t)$, defined in a period $T \in [0\ \frac{2\pi}{\omega}]$, whereas Fig. 17(b) depicts an exemplifying output. The hysteretic restoring force $\mathcal{Z}(y, \dot{y})$ is a multi-valued function according to the excursion interval of the pair $(\mathcal{Z}, y)$, which can move along the path ACD when $\dot{u} < 0$, otherwise it moves on the path DBA for $\dot{u} > 0$; these excursion intervals define the loading and unloading regime cycles, respectively, on the hysteresis loop.

Figure 17 – Illustrative example of the hysteresis loop. —— represents unloading regime of motion whereas —— represents the loading one.

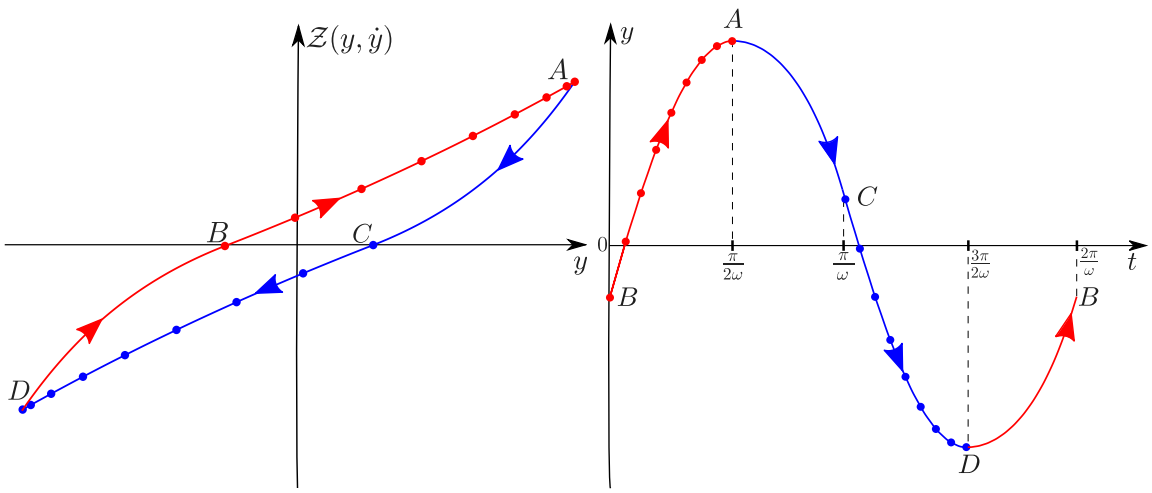

(a) Hysteresis loop of a hysteretic model. (b) Exemplifying hysteretic output.

Source: Teloli *et al.* (2021).

The equations of each interval are given by:

- path AC: $\dot{y} \leqslant 0, \mathcal{Z} \geqslant 0$

$$\mathcal{Z}_1 = \frac{\alpha}{\beta(\delta-\gamma)}\left(1-e^{-\beta(\delta-\gamma)(y-y_0)}\right), \tag{7}$$

- path CD: $\dot{y} \leqslant 0, \mathcal{Z} \leqslant 0$

$$\mathcal{Z}_2 = -\frac{\alpha}{\beta(\delta+\gamma)}\left(1-e^{\beta(\delta+\gamma)(y-y_0)}\right), \tag{8}$$

- path DB: $\dot{y} \geqslant 0, \mathcal{Z} \leqslant 0$

$$\mathcal{Z}_3 = -\frac{\alpha}{\beta(\delta-\gamma)}\left(1-e^{\beta(\delta-\gamma)(y+y_0)}\right), \tag{9}$$

- path BA: $\dot{y} \geqslant 0, \mathcal{Z} \geqslant 0$

$$\mathcal{Z}_4 = \frac{\alpha}{\beta(\delta+\gamma)}\left(1-e^{-\beta(\delta+\gamma)(y+y_0)}\right), \tag{10}$$

where y_0 is the displacement at $\mathcal{Z} = 0$. The loading regime of the hysteresis cycle is described by the pair $(\mathcal{Z}_3, \mathcal{Z}_4)$, whereas that the unload pair is $(\mathcal{Z}_1, \mathcal{Z}_2)$. The transition between each restoring force path is continuous, exemplifying $\mathcal{Z}_4\left(y(\frac{\pi}{2\omega}), \dot{y}(\frac{\pi}{2\omega})\right) = \mathcal{Z}_1\left(y(\frac{\pi}{2\omega}), \dot{y}(\frac{\pi}{2\omega})\right)$ where this continuity relation is valid on all time interval, and the hysteresis loop is symmetric in relation to the coordinate $(\frac{y_{\max}+y_{\min}}{2}, 0)$ on the y and $\mathcal{Z}$ axes, respectively. Under these conditions, the bounding functions need to have the same structure for load and unload cycles, which means that the coefficients with the same subscript have equal absolute values, i. e., $f_0 = d_0, f_1 = d_1, \ldots f_n = d_n$.

For conditions where the hysteresis force is weak, each of these piecewise functions that compose the restoring force equations (7)-(10) can be smoothed by a functional expansion through the Taylor series approach around the displacement y_0:

$$\mathcal{Z}_1 \approx \frac{\alpha}{\beta\,(\delta-\gamma)}\left(1-\left[\sum_{n=0}^{\infty}\frac{[-\beta(\delta-\gamma)]^n\,(y-y_0)^n}{n!}\right]\right), \tag{11}$$

$$\mathcal{Z}_2 \approx -\frac{\alpha}{\beta\,(\delta+\gamma)}\left(1-\left[\sum_{n=0}^{\infty}\frac{[\beta(\delta+\gamma)]^n\,(y-y_0)^n}{n!}\right]\right), \tag{12}$$

$$\mathcal{Z}_3 \approx -\frac{\alpha}{\beta\,(\delta-\gamma)}\left(1-\left[\sum_{n=0}^{\infty}\frac{[\beta(\delta-\gamma)]^n\,(y+y_0)^n}{n!}\right]\right), \tag{13}$$

$$\mathcal{Z}_4 \approx \frac{\alpha}{\beta\,(\delta+\gamma)}\left(1-\left[\sum_{n=0}^{\infty}\frac{[-\beta(\delta+\gamma)]^n\,(y+y_0)^n}{n!}\right]\right), \tag{14}$$

Although there exist other available methods to approach the piecewise restoring forces through polynomial functions, the Taylor series provides the necessary condition for expanding the polynomial coefficients as a function of the physical parameters and,

in addition, the series guarantees satisfying results using only a few terms, as will be addressed in this Chapter with the higher-order FRFs and HBM as well.

Although the more terms included in the Taylor series, the more significant the precision of the polynomial form for the hysteresis loop will be; the conditions addressed in this work with the smooth nonlinear operator deliver perfectly acceptable results assuming the first three orders $n = 3$. Thus, the bounding functions $\mathscr{F}^{\downarrow}[y(t)]$ and $\mathscr{F}^{\uparrow}[y(t)]$ are given according to the order used in the Taylor series approach, yielding:

$$\mathscr{F}^{\uparrow}[y(t)] = \lambda_0 + \lambda_1 y(t) - \lambda_2 y^2(t) + \lambda_3 y^3(t) \quad \text{for} \quad \text{sign}\left(\dot{u}(t)\right) \geq 0, \tag{15}$$

$$\mathscr{F}^{\downarrow}[y(t)] = -\lambda_0 + \lambda_1 y(t) + \lambda_2 y^2(t) + \lambda_3 y^3(t) \quad \text{for} \quad \text{sign}\left(\dot{u}(t)\right) \leq 0. \tag{16}$$

where λ_0 [N], λ_1 [N/m], λ_2 [N/m^2] and λ_3 [N/m^3] are the bounding function coefficients. Also, each coefficient is responsible for describing many features of the hysteresis loop, for instance, λ_0 provides the multiple solutions to the nonlinear operator, λ_1 is the slope of the restoring force and finally, λ_2 and λ_3 give the hardening or softening stiffness characteristics to the model. Comparing equations (11)-(14), the $\mathscr{F}^{\downarrow}[y(t)]$ is used to approach the pair $\mathcal{Z}_1$ and $\mathcal{Z}_2$, which describes the paths AC and CD, whereas the $\mathscr{F}^{\uparrow}[y(t)]$ function is responsible for the other ones. Finally, the motion equation using the proposed nonlinear operator is given by:

$$m\ddot{y}\left(t\right) + c\dot{y}\left(t\right) + ky\left(t\right) + \mathscr{F}[y(t)] = u\left(t\right), \tag{17}$$

The coefficients of the polynomial form are computed by minimizing an error function described by (CHATTERJEE, 2010a):

$$E(\lambda_0, \lambda_1, \lambda_2, \lambda_3) = \int_{-Y}^{y_0} \left\{\mathcal{Z}_2 - \mathscr{F}^{\downarrow}[y(t)]\right\}^2 dy + \int_{y_0}^{Y} \left\{\mathcal{Z}_1 - \mathscr{F}^{\downarrow}[y(t)]\right\}^2 dy, \tag{18}$$

subjected to:

$$\frac{\partial E}{\partial \lambda_i} = 0, \quad \text{for} \quad i = 0, 1, 2, 3. \tag{19}$$

which results in the following expressions:

$$\lambda_0 = \frac{\alpha y_0}{16}\left(3\beta\delta Y + 8\beta\gamma y_0 - 16\right), \tag{20}$$

$$\lambda_1 = \alpha, \tag{21}$$

$$\lambda_2 = \frac{\alpha\beta}{16Y}\left(8\beta\delta^2 Y y_0 + 8\beta\gamma^2 Y y_0 + 15\beta\delta\gamma y_0^2 - 8\gamma Y - 15\delta y_0\right), \tag{22}$$

$$\lambda_3 = \frac{\alpha\beta}{96Y^5}\left(\begin{array}{c}16\beta\delta^2 Y^5 + 70\beta\delta\gamma Y^4 y_0 - 70\beta\delta\gamma Y^2 y_0^3 - 35\delta Y^4 + \\ 105\delta Y^2 y_0^2 - 105\delta y_0^4\end{array}\right). \tag{23}$$

where $Y = |y_{\min}| = |y_{\max}|$. These equations are valid only for harmonic excitations that ensure a weak hysteretic force and when the force × displacement plane draws a single loop (minor-loops require at least two-input conditions (BISWAS; CHATTERJEE, 2018)). Furthermore, despite the application illustrated on a Bouc-Wen model, the approach proposed could be used to deal with other hysteretic systems with the rate-independent property.

3.2 VOLTERRA SERIES AND THE HARMONIC PROBING METHOD

The mathematical theory behind the Volterra series was introduced by the Italian mathematician Vito Volterra in a paper dating back to 1887[1] and consists of an analogy to Taylor series described by an integro-differential functional mapping to represent continuous and stable nonlinear systems with finite memory (VOLTERRA, 1959; DOYLE; PEARSON; OGUNNAIKE, 2002). The popularization of the Volterra series for the design and analysis of nonlinear systems in the engineering field started with the work of Wiener (1942), whose contribution lies in applying such functional series to nonlinear circuit analysis. Since then, a wide variety of results involving the Volterra series can be found in different areas of the literature, involving topics ranging from biomedical engineering, fluid dynamics, process control to digital signal processing and mechanical engineering (CHENG *et al.*, 2017).

The Volterra series is a generalization of the well-known impulse response functions (IRFs), and can be used to describe the relationship between the input and output in nonlinear systems through the concept of multidimensional convolutions (SCHETZEN, 1980). For multi-input and single-output (MISO) systems, the functional of the Volterra

[1] Vito Volterra's (⋆1860, †1940) original work is entitled as *''Sopra le funzioni che dipendono da altre funzioni''*, initially published in the author's native language.

series in continuous time domain is given by the following mapping with the multi-inputs $u_1(t) + u_2(t) + \cdots + u_j(t)$:

$$\begin{aligned} y(t) &= \sum_{\eta=1}^{\infty} y_\eta(t) = \underbrace{\sum_{p=1}^{j} \int_{\mathbb{R}^1} h_1^{(u_p)}(\tau_1) u_p(t-\tau_1) d\tau_1}_{=y_1(t)} \\ &+ \underbrace{\sum_{p=1}^{j}\sum_{k=1}^{j} \int_{\mathbb{R}^2} h_2^{(u_p,u_k)}(\tau_1,\tau_2) u_p(t-\tau_1) u_k(t-\tau_2) d\tau_1 d\tau_2}_{=y_2(t)} \\ &+ \sum_{p=1}^{j}\sum_{k=1}^{j}\sum_{l=1}^{j} \int_{\mathbb{R}^3} h_3^{(u_p,u_k,u_l)}(\tau_1,\tau_2,\tau_3) \times \\ &\qquad \underbrace{u_p(t-\tau_1) u_k(t-\tau_2) u_l(t-\tau_3) d\tau_1 d\tau_2 d\tau_3}_{=y_3(t)} \\ &\quad \text{and higher-order contributions.} \end{aligned} \tag{24}$$

where $y_1(t)$, $y_2(t)$ and $y_3(t)$ are the polynomial contributions that compose the nonlinear response $y(t)$. The most interesting property of this formulation relies on the possibility of decomposing the total response of a nonlinear system into its linear $y_1(t)$ and nonlinear components $y_2(t) + y_3(t) + \ldots$ (RUGH, 1991). Note that the linear component is written as the classical convolution integral. Each polynomial contribution of $\eta-$order is given by :

$$\begin{aligned} y_\eta(t) &= \sum_{p=1}^{j}\sum_{k=1}^{j}\cdots\sum_{n=1}^{j} \int_{\mathbb{R}^\eta} h_\eta^{(u_p,u_k,\ldots,u_n)}(\tau_1,\tau_2,\ldots,\tau_\eta) \\ &\times \prod_{i=1}^{\eta} u_p(t-\tau_1) u_k(t-\tau_2)\ldots u_n(t-\tau_\eta) d\tau_1 d\tau_2 \ldots d\tau_\eta, \end{aligned} \tag{25}$$

The term $h_\eta^{(u_p,u_k,\ldots,u_n)}(\tau_1,\tau_2,\ldots,\tau_\eta)$ is called direct or cross Volterra kernel related to the j^{th} input. In order to simplify the notation it is assumed that:

$$\int_{\mathbb{R}^\eta} = \int_{\mathbb{R}\times\mathbb{R}\times\ldots\mathbb{R}} = \underbrace{\int_{-\infty}^{\infty}\int_{-\infty}^{\infty}\cdots\int_{-\infty}^{\infty}}_{\eta\text{th order}}.$$

Despite the fact that most physical systems are described in continuous time (integral representation), part of the implementations of the method are done in the discrete domain. Conventional discrete-time Volterra kernels (summation representation) are beyond the scope of the Thesis, but the interested reader will find contributions on the

subject in work already published under the supervision of this Thesis advisor (SHIKI, 2016; SCUSSEL, 2017; VILLANI, 2019).

The estimation of each contribution for a MISO system involves a large number of parameters that occur over-parametrization. However, these kernels can be constructed in a symmetric way, which reduces the number of terms to be calculated (TOMLINSON; MANSON; LEE, 1996), i. e., the term $h_\eta^{(u_1,u_2,\ldots,u_m)}(\tau_1,\tau_2,\ldots,\tau_\eta)$ is considered identical for all the input permutations, for instance $h_2^{(u_1,u_2)}(\tau_1,\tau_2) = h_2^{(u_2,u_1)}(\tau_1,\tau_2)$. Then, assuming $m = 2$ the contributions are given by:

$$
\begin{aligned}
y_1(t) &= y_1^{(u_1)}(t) + y_1^{(u_2)}(t), \\
\Leftrightarrow \quad & y_1(t) = \int_{\mathbb{R}^1} h_1^{(u_1)}(\tau_1)u_1(t-\tau_1)d\tau_1 + \\
& \int_{\mathbb{R}^1} h_1^{(u_2)}(\tau_1)u_2(t-\tau_1)d\tau_1, \qquad (26) \\
y_2(t) &= y_2^{(u_1,u_1)}(t) + y_2^{(u_2,u_2)}(t) + y_2^{(u_1,u_2)}(t) \\
\Leftrightarrow \quad & y_2(t) = \int_{\mathbb{R}^2} h_2^{(u_1,u_1)}(\tau_1,\tau_2)u_1(t-\tau_1)u_1(t-\tau_2)d\tau_1 d\tau_2 + \\
& \int_{\mathbb{R}^2} h_2^{(u_2,u_2)}(\tau_1,\tau_2)u_2(t-\tau_1)u_2(t-\tau_2)d\tau_1 d\tau_2 + \\
& 2\int_{\mathbb{R}^2} h_2^{(u_1,u_2)}(\tau_1,\tau_2)u_1(t-\tau_1)u_2(t-\tau_2)d\tau_1 d\tau_2 \qquad (27) \\
+ \quad & \text{higher-order contributions.}
\end{aligned}
$$

The higher-order FRFs, as well as the linear FRFs, provide an interesting insight into the dynamical properties of nonlinear systems in the frequency domain (JING; LANG; BILLINGS, 2008). It is important to point out that since the higher-order FRFs are known, these functions can be used to describe the system output for any input with a well-known mathematical expression. The multi-dimensional Fourier transform of the Volterra kernels for multi-inputs can be calculated by (WORDEN; MANSON; TOMLINSON, 1997; SWAIN; BILLINGS, 2001):

$$
\mathcal{H}_\eta^{(u_p,u_k,\ldots,u_n)}(\omega_1,\omega_2,\cdots,\omega_\eta) = \int_{\mathbb{R}^\eta} h_\eta^{(u_p,u_k,\ldots,u_n)}(\tau_1,\tau_2,\ldots,\tau_\eta) \times \prod_{i=1}^{\eta} e^{-j\omega_i\tau_i} d\tau_1 d\tau_2 \ldots \tau_\eta. \qquad (28)
$$

Bedrosian and Rice (1971) proposed the harmonic probing method to derive the analytical expressions of the higher-order FRFs, having only as a requirement the knowledge of the motion equations of the systems of interest, such as the traditional

white-box modelling. For a three-tone input given by:

$$u(t) = A\cos\omega_1 t + B\cos\omega_2 t + C\cos\omega_3 t,$$
$$\Rightarrow u(t) = \frac{A(e^{j\omega_1 t} + e^{-j\omega_1 t})}{2} + \frac{B(e^{j\omega_2 t} + e^{-j\omega_2 t})}{2} + \frac{C(e^{j\omega_3 t} + e^{-j\omega_3 t})}{2}, \tag{29}$$

the generalized expression for the contributions mapping of $\eta-$order is written as (CHATTERJEE; VYAS, 2004):

$$y_\eta(t) = \frac{1}{2^\eta} \sum_{N+M+L=\eta} A^N B^M C^L \left(C^\eta_{p,q,r,s,v,\varpi}\right) \mathcal{H}^{p,q,r,s,v,\varpi}_\eta(\omega) e^{j(N\omega_1 + M\omega_2 + L\omega_3)t}, \tag{30}$$

where p, q, r, s, v and ϖ are integer values and

$$C^\eta_{p,q,r,s,v,\varpi} = \frac{\eta}{p!q!r!s!v!\varpi!}, \tag{31}$$

$$\mathcal{H}^{p,q,r,s,v,\varpi}_\eta(\omega) = \mathcal{H}_\eta(\underbrace{\omega_1,\ldots,\omega_1}_{p \text{ times}}, \underbrace{-\omega_1,\ldots,-\omega_1}_{q \text{ times}}, \underbrace{\omega_2,\ldots,\omega_2}_{r \text{ times}}, \underbrace{-\omega_2,\ldots,-\omega_2}_{s \text{ times}},$$
$$\underbrace{\omega_3,\ldots,\omega_3}_{v \text{ times}}, \underbrace{-\omega_3,\ldots,-\omega_3}_{\varpi \text{ times}}). \tag{32}$$

Regarding the application of Volterra's theory under the higher-order kernels framework to approximate systems with hysteresis, few contributions have been presented. Ran, Xiao and Hu (2014) proposed simplifying assumptions that allowed to smooth the restoring force of a hysteretic system modeled by the Bouc-Wen model by using the Taylor series, but the hysteretic loop was not reproduced. Manson and Worden (2016) explored the possibility of considering the non-smooth system as a combination of smooth systems to develop a Volterra series representation for such models. That method aims to rewrite motion equations by removing the hysteretic effect using a switch between the smoothed submodels. Unfortunately, it was also not possible to represent the hysteresis loop analytically using the Volterra series since the switching procedure among the submodels includes a nonexistent transient component in the total output.

With the generalized series response established for a multi-input case, the solution proposed by this dissertation to enable the use of Volterra theory in systems with hysteresis consists of applying the harmonic probing algorithm directly to the motion equation (17) of the equivalent system that has the nonlinear operator.

3.2.1 Higher-order frequency response functions applied on the nonlinear smooth operator

The equivalent system with hysteresis defined in equation (17) carries the change between the bounding functions according to sign $[\dot{u}(t)]$, which can be approximated well by a square wave with the same period of $\dot{u}(t)$. Thus, equation (17) can be rewritten as:

$$m\ddot{y}(t) + c\dot{y}(t) + ky(t) + \underbrace{u_0(t) + \lambda_1 y(t) + \varrho y^2(t) + \lambda_3 y^3(t)}_{=\mathscr{F}[y(t)]} = u(t), \tag{33}$$

where the term $u_0(t) = \lambda_0 \Phi[\dot{u}(t)]$, with $\Phi[\dot{u}(t)] \approx \text{sign}[\dot{u}(t)]$, is considered as an additional input applied to the equivalent system and ϱ is defined as $\varrho = \lambda_2$ $(\varrho = -\lambda_2)$ for $\text{sgn}[\dot{u}(t)] < 0$ $(\text{sgn}[\dot{u}(t)] > 0)$.

Since the nonlinear operator has terms up to the cubic order, it is used $m = 3$ contributions to compute the higher-order FRFs. More than three contributions could be used to predict the output, but the complexity to compute other higher-order FRFs kernels is increased. Fortunately, as highlighted by Lin and Ng (2018) (LIN; NG, 2018), the use of the first three Volterra kernels has been suitable to deal with polynomial nonlinearities similar to that presented in the equation (33), as well as in practical engineering problems (SHIKI; SILVA; TODD, 2017).

The discontinuity that occurs with $\varrho y^2(t)$ directly impacts on the calculation of the second order Volterra contribution in the time domain; however, as pointed out in section 3.2.2 the discontinuity can be overcome. The changes on $\Phi[\bullet]$ can be described by Fourier series:

$$\begin{aligned}
& u_0(t) = \lambda_0 \underbrace{\sum_{k=1}^{N_s} \frac{4\sin\{[1+2(k-1)]\,\omega t\}}{[1+2(k-1)]\,\pi}}_{=\Phi[\dot{u}(t)]}, \\
\Leftrightarrow \quad & u_0(t) = \frac{j2\lambda_0}{\pi} \underbrace{\sum_{k=1}^{N_s} \left(\frac{e^{-j[1+2(k-1)]\omega t} - e^{j[1+2(k-1)])\omega t}}{1+2(k-1)} \right)}_{=\Phi[\dot{u}(t)]}, \\
\Rightarrow \quad & u_0(t) = \sum_{k=1}^{N_s} A_k \left(e^{j[1+2(k-1)])\omega t} - e^{-j[1+2(k-1)]\omega t} \right),
\end{aligned} \tag{34}$$

where

$$A_k = -\frac{j2\lambda_0}{\pi + 2(k-1)\pi}, \tag{35}$$

and ω is the excitation frequency [rad/s], N_s is the number of terms used by the Fourier series and $j = \sqrt{-1}$. This approximation states that: if N_s tends to ∞, then $\Phi[\dot{u}(t)]$ must tends to sign$[\dot{u}(t)]$. Thus, for a single-tone input $u(t) = Ae^{j\omega t}$ the following additional input is assumed with $N_s = 2$:

$$u_0(t) = A_1 e^{j\omega t} + A_2 e^{j3\omega t}. \tag{36}$$

The calculation of the higher-order FRF is carried out by assuming the probing harmonic inputs:

$$u_1 = Ae^{j\omega t}, \tag{37}$$

$$u_2 = A_1 e^{j\omega t}, \tag{38}$$

$$u_3 = A_2 e^{j3\omega t}, \tag{39}$$

based on the generalized response contributions, the probing expressions of displacement, velocity and acceleration for the first order $y_1(t)$ contribution are:

$$\begin{aligned} y_1 &= A\mathcal{H}_1^{(u_1)}(\omega)e^{j\omega t} + A_1\mathcal{H}_1^{(u_2)}(\omega)e^{j\omega t} + A_2\mathcal{H}_1^{(u_3)}(3\omega)e^{j3\omega t}, \\ \dot{y}_1 &= j\omega A\mathcal{H}_1^{(u_1)}(\omega)e^{j\omega t} + j\omega A_1\mathcal{H}_1^{(u_2)}(\omega)e^{j\omega t} + j3\omega A_2\mathcal{H}_1^{(u_3)}(3\omega)e^{j3\omega t}, \\ \ddot{y}_1 &= -\omega^2 A\mathcal{H}_1^{(u_1)}(\omega)e^{j\omega t} - \omega^2 A_1\mathcal{H}_1^{(u_2)}(\omega)e^{j\omega t} - (3\omega)^2 A_2\mathcal{H}_1^{(u_3)}(3\omega)e^{j3\omega t}, \end{aligned} \tag{40}$$

by substituting the responses into equation (33), and equating the terms $Ae^{j\omega t}$, $A_1e^{j\omega t}$, $A_2e^{j3\omega t}$ provides:

$$\mathcal{H}_1^{(u_1)}(\omega) = \mathcal{H}_1^{(u_2)}(\omega) = \mathcal{H}_1(\omega) \Leftrightarrow \mathcal{H}_1(\omega) = \frac{1}{-m\omega^2 + j\omega c + (k + \lambda_1)}, \tag{41}$$

$$\mathcal{H}_1^{(u_3)}(3\omega) = \mathcal{H}_1(3\omega) \Leftrightarrow \mathcal{H}_1(3\omega) = \frac{1}{-m(3\omega)^2 + j3\omega c + (k + \lambda_1)}. \tag{42}$$

The kernel expression $\mathcal{H}_1(\omega)$ corresponds to the linear FRF, where $\omega_n = \sqrt{(k + \lambda_1)m^{-1}}$. The first order contribution $y_1(t)$ holds the superposition principle and, for this reason,

its kernel $\mathcal{H}_1^{(u_3)}(3\omega)$ presents resonance frequency at $3\omega = \omega_n \Rightarrow \omega = \omega_n/3$ due to the harmonic from the input signal $e^{j3\omega t}$. Furthermore, the kernels that have been derived by the single-tone inputs $u_1 = Ae^{j\omega t}$ and $u_2 = A_1 e^{j\omega t}$ will always show equal expressions for both inputs, for instance $\mathcal{H}_2^{u_1,u_1}(\omega_1,\omega_2) = \mathcal{H}_2^{u_2,u_2}(\omega_1,\omega_2) = \mathcal{H}_2^{u_1,u_2}(\omega_1,\omega_2)$. For this reason, the kernel superscripts are omitted as well as the computation of the kernels that arise from the input u_2.

The mapping performed through the nonlinear contributions in the frequency domain requires that the kernel transforms contains a sum of frequency components $(\omega_1 + \omega_2)$ and $(\omega_1 + \omega_2 + \omega_3)$ for the second and third order contributions, respectively. Moreover, the algorithm developed by Worden, Manson and Tomlinson (1997) computes the higher-order kernels to analyze separately each term that composes the contribution $y_\eta(t)$. This procedure uses a significant reduction of the mathematical effort to obtain the kernels. The probing inputs to estimate the second order direct-kernels are given by:

$$u_1 = Ae^{j\omega_1 t} + Ae^{j\omega_2 t}, \tag{43}$$

$$u_3 = A_2 e^{j3\omega_1 t} + A_2 e^{j3\omega_2 t}, \tag{44}$$

then, the responses $y_2^{(u_1,u_1)}$, $\dot{y}_2^{(u_1,u_1)}$ and $\ddot{y}_2^{(u_1,u_1)}$ are:

$$\begin{aligned}
y_2^{(u_1,u_1)} &= A\mathcal{H}_1(\omega_1)e^{j\omega_1 t} + A\mathcal{H}_1(\omega_2)e^{j\omega_2 t} + 2A^2\mathcal{H}_2(\omega_1,\omega_2)e^{j(\omega_1+\omega_2)t},\\
\dot{y}_2^{(u_1,u_1)} &= j\omega_1 A\mathcal{H}_1(\omega_1)e^{j\omega_1 t} + j\omega_2 A\mathcal{H}_1(\omega_2)e^{j\omega_2 t} +\\
&\qquad j2(\omega_1+\omega_2)A^2\mathcal{H}_2(\omega_1,\omega_2)e^{j(\omega_1+\omega_2)t},\\
\ddot{y}_2^{(u_1,u_1)} &= -\omega_1^2 A\mathcal{H}_1(\omega_1)e^{j\omega_1 t} - \omega_2^2 A\mathcal{H}_1(\omega_2)e^{j\omega_2 t} -\\
&\qquad 2(\omega_1+\omega_2)^2 A^2\mathcal{H}_2(\omega_1,\omega_2)e^{j(\omega_1+\omega_2)t},
\end{aligned} \tag{45}$$

substituting the expressions (45) into equation (33) and equating the terms $A^2 e^{j(\omega_1+\omega_2)t}$ the second order Volterra direct-kernel is given by:

$$\mathcal{H}_2(\omega_1,\omega_2) = -\varrho\mathcal{H}_1(\omega_1)\mathcal{H}_1(\omega_2)\mathcal{H}_1(\omega_1+\omega_2). \tag{46}$$

Applying the previous procedure with the outputs $y_2^{(u_2,u_2)}$, $\dot{y}_2^{(u_2,u_2)}$ and $\ddot{y}_2^{(u_2,u_2)}$ yields:

$$\mathcal{H}_2(3\omega_1,3\omega_2) = -\varrho\mathcal{H}_1(3\omega_1)\mathcal{H}_1(3\omega_2)\mathcal{H}_1(3\omega_1+3\omega_2). \tag{47}$$

To obtain the simplified mapping for the second order Volterra cross-kernel, the probing is performed with the inputs $u_1 = Ae^{j\omega_1 t}$ e $u_2 = A_2 e^{j3\omega_2 t}$. Thus, the output probing expression is given by:

$$\begin{aligned}
y_2^{(u_1,u_2)} &= A\mathcal{H}_1(\omega_1)e^{j\omega_1 t} + A_2\mathcal{H}_1(3\omega_2)e^{j3\omega_2 t} + 2AA_2\mathcal{H}_2(\omega_1, 3\omega_2)e^{j(\omega_1+3\omega_2)t}, \\
\dot{y}_2^{(u_1,u_2)} &= j\omega_1 A\mathcal{H}_1(\omega_1)e^{j\omega_1 t} + j3\omega_2 A_2\mathcal{H}_1(3\omega_2)e^{j3\omega_2 t} + \\
&\qquad j2(\omega_1 + 3\omega_2)AA_2\mathcal{H}_2(\omega_1, 3\omega_2)e^{j(\omega_1+3\omega_2)t}, \\
\ddot{y}_2^{(u_1,u_2)} &= -\omega_1^2 A\mathcal{H}_1(\omega_1)e^{j\omega_1 t} - (3\omega_2)^2 A\mathcal{H}_1(3\omega_2)e^{j3\omega_2 t} - \\
&\qquad 2(\omega_1 + 3\omega_2)^2 AA_2\mathcal{H}_2(\omega_1, 3\omega_2)e^{j(\omega_1+3\omega_2)t}.
\end{aligned} \tag{48}$$

The cross-kernel expression is:

$$\mathcal{H}_2(\omega_1, 3\omega_2) = -\varrho\mathcal{H}_1(\omega_1)\mathcal{H}_1(3\omega_2)\mathcal{H}_1(\omega_1 + 3\omega_2). \tag{49}$$

All the second-order kernel expressions result in a three-dimensional plot figure. For this reason, the analysis of the surfaces is a difficult task, which can be overcome considering only the leading diagonal of the higher-order FRFs, since it provides the key features of the resonance peaks. For $\omega_1 = \omega_2 = \omega$, the leading diagonals are expressed as:

$$\mathcal{H}_2(\omega, \omega) = -\varrho\mathcal{H}_1^2(\omega)\mathcal{H}_1(2\omega), \tag{50}$$

$$\mathcal{H}_2(3\omega, 3\omega) = -\varrho\mathcal{H}_1^2(3\omega)\mathcal{H}_1(6\omega), \tag{51}$$

$$\mathcal{H}_2(\omega, 3\omega) = -\varrho\mathcal{H}_1(\omega)\mathcal{H}_1(3\omega)\mathcal{H}_1(4\omega). \tag{52}$$

As can be seen, all the second-order kernels are dependent on the loading-unloading cycles that occur along the hysteresis loop since these kernels are affected by the changes on the parameter ϱ. When represented in time domain, the contribution $y_2(t)$ must be split into $y_2^{\downarrow}(t)$ and $y_2^{\uparrow}(t)$ derived by the kernels computed with $\varrho > 0$ and $\varrho < 0$, respectively. The harmonic interactions that occur between the frequency components from the inputs are clear in the cross-kernel $\mathcal{H}_2(\omega, 3\omega)$, which shows sub-harmonics at frequencies of 3ω and 4ω.

The third-order direct-kernels are derived from following probing inputs:

$$u_1 = Ae^{j\omega_1 t} + Ae^{j\omega_2 t} + Ae^{j\omega_3 t}, \tag{53}$$

$$u_3 = A_2 e^{j3\omega_1 t} + A_2 e^{j3\omega_2 t} + A_2 e^{j3\omega_3 t}, \tag{54}$$

then, the output probing expression $y_3^{(u_1,u_1,u_1)}$ is given by:

$$\begin{aligned} y_3^{(u_1,u_1,u_1)} = A\mathcal{H}_1(\omega_1)e^{j\omega_1 t} + A\mathcal{H}_1(\omega_2)e^{j\omega_2 t} + A\mathcal{H}_1(\omega_3)e^{j\omega_3 t} + \\ 2A^2\mathcal{H}_2(\omega_1,\omega_2)e^{j(\omega_1+\omega_2)t} + 2A^2\mathcal{H}_2(\omega_1,\omega_3)e^{j(\omega_1+\omega_3)t} + \\ 2A^2\mathcal{H}_2(\omega_2,\omega_3)e^{j(\omega_2+\omega_3)t} + 6A^3\mathcal{H}_3(\omega_1,\omega_2,\omega_3)e^{j(\omega_1+\omega_2+\omega_3)t}, \end{aligned} \tag{55}$$

where the responses $\dot{y}_3^{(u_1,u_1,u_1)}$ and $\ddot{y}_3^{(u_1,u_1,u_1)}$ are the first and second derivatives of $y_3^{(u_1,u_1)}$ with respect to time. Substituting the response terms into equation (33), the algebraic expression for $\mathcal{H}_3(\omega_1,\omega_2,\omega_3)$ is given by equating the terms $A^3e^{j(\omega_1+\omega_2+\omega_3)t}$:

$$\begin{aligned} \mathcal{H}_3(\omega_1,\omega_2,\omega_3) = \mathcal{H}_1(\omega_1)\mathcal{H}_1(\omega_2)\mathcal{H}_1(\omega_3)\mathcal{H}_1(\omega_1+\omega_2+\omega_3) \times \\ \left[\frac{2\varrho^2}{3}\left\{\mathcal{H}_1(\omega_1+\omega_2)+\mathcal{H}_1(\omega_1+\omega_3)+\mathcal{H}_1(\omega_2+\omega_3)\right\}-\lambda_3\right]. \end{aligned} \tag{56}$$

The third-order direct-kernel obtained through the probing with $y_3^{(u_2,u_2,u_2)}$, $\dot{y}_3^{(u_2,u_2,u_2)}$ and $\ddot{y}_3^{(u_2,u_2,u_2)}$ is:

$$\begin{aligned} \mathcal{H}_3(3\omega_1,3\omega_2,3\omega_3) = \mathcal{H}_1(3\omega_1)\mathcal{H}_1(3\omega_2)\mathcal{H}_1(3\omega_3)\mathcal{H}_1(3\omega_1+3\omega_2+3\omega_3) \times \\ \left[\frac{2\varrho^2}{3}\left\{\mathcal{H}_1(3\omega_1+3\omega_2)+\mathcal{H}_1(3\omega_1+3\omega_3)+\mathcal{H}_1(3\omega_2+3\omega_3)\right\}-\lambda_3\right]. \end{aligned} \tag{57}$$

The third-order cross-kernel transform is derived with the probing inputs $u_1 = Ae^{j\omega_1 t} + Ae^{j\omega_2 t}$ and $u_3 = A_2e^{j\omega_3 t}$. These inputs generate the following response expression:

$$\begin{aligned} y_3^{(u_1,u_1,u_3)} = A\mathcal{H}_1(\omega_1)e^{j\omega_1 t} + A\mathcal{H}_1(\omega_2)e^{j\omega_2 t} + A_2\mathcal{H}_1(3\omega_3)e^{j3\omega_3 t} + \\ 2A^2\mathcal{H}_2(\omega_1,\omega_2)e^{j(\omega_1+\omega_2)t} + 2AA_2\mathcal{H}_2(\omega_1,\omega_3)e^{j(\omega_1+3\omega_3)t} + \\ 2AA_2\mathcal{H}_2(\omega_2,\omega_3)e^{j(\omega_2+3\omega_3)t} + 6A^2A_2\mathcal{H}_3(\omega_1,\omega_2,3\omega_3)e^{j(\omega_1+\omega_2+3\omega_3)t}, \end{aligned} \tag{58}$$

substituting $y_3^{(u_1,u_1,u_3)}$ and its derivatives into (33) produces the FRF expression:

$$\begin{aligned} \mathcal{H}_3(\omega_1,\omega_2,3\omega_3) = \mathcal{H}_1(\omega_1)\mathcal{H}_1(\omega_2)\mathcal{H}_1(3\omega_3)\mathcal{H}_1(\omega_1+\omega_2+3\omega_3) \times \\ \left[\frac{2\varrho^2}{3}\left\{\mathcal{H}_1(\omega_1+\omega_2)+\mathcal{H}_1(\omega_1+3\omega_3)+\mathcal{H}_1(\omega_2+3\omega_3)\right\}-\lambda_3\right]. \end{aligned} \tag{59}$$

Moreover, the third-order cross-kernel from the contribution $y_3^{(u_1,u_3,u_3)}$ is given by:

$$\mathcal{H}_3(\omega_1,3\omega_2,3\omega_3) = \mathcal{H}_1(\omega_1)\mathcal{H}_1(3\omega_2)\mathcal{H}_1(3\omega_3)\mathcal{H}_1(\omega_1+3\omega_2+3\omega_3)\times \left[\frac{2\varrho^2}{3}\left\{\mathcal{H}_1(\omega_1+3\omega_2)+\mathcal{H}_1(\omega_1+3\omega_3)+\mathcal{H}_1(3\omega_2+3\omega_3)\right\}-\lambda_3\right]. \tag{60}$$

The algebraic expression of the third-order kernels can be reduced considering only the leading diagonals, expressed as

$$\mathcal{H}_3(\omega,\omega,\omega) = \mathcal{H}_1^3(\omega)\mathcal{H}_1(3\omega)\left[2\varrho^2\mathcal{H}_1(2\omega)-\lambda_3\right], \tag{61}$$

$$\mathcal{H}_3(3\omega,3\omega,3\omega) = \mathcal{H}_1^3(3\omega)\mathcal{H}_1(9\omega)\left[2\varrho^2\mathcal{H}_1(6\omega)-\lambda_3\right], \tag{62}$$

$$\mathcal{H}_3(\omega,\omega,3\omega) = [\mathcal{H}_1(\omega)]^2\mathcal{H}_1(3\omega)\mathcal{H}_1(5\omega)\left\{\frac{2\varrho^2[2\mathcal{H}_1(4\omega)+\mathcal{H}_1(2\omega)]}{3}-\lambda_3\right\}, \tag{63}$$

$$\mathcal{H}_3(\omega,3\omega,3\omega) = \mathcal{H}_1(\omega)[\mathcal{H}_1(3\omega)]^2\mathcal{H}_1(7\omega)\left\{\frac{2\varrho^2[2\mathcal{H}_1(4\omega)+\mathcal{H}_1(6\omega)]}{3}-\lambda_3\right\}. \tag{64}$$

All the kernels described by equations (61)–(64) show that the term ϱ^2 is always greater than zero, which indicates that the third-order kernels are independent of the regime cycles and maintains the same framework. Moreover, the presence of sub-harmonics in the third-order kernels is more pronounced. For instance, the cross-kernel $\mathcal{H}_3(\omega,3\omega,3\omega)$ shows sub-harmonics at frequencies 3ω, 4ω, 6ω and 7ω. This analysis is simple to carry out when the leading diagonal is known.

3.2.2 Total response in time domain

The output response of the system with hysteresis (33) described analytically by the Volterra series up to third-order contributions is given by:

$$y(t) = y_1(t)+y_2(t)+y_3(t), \tag{65}$$

splitting the second-order contribution according to the loading-unloading cycles:

$$y_2(t) = \frac{1+\Phi[\dot{u}(t)]}{2}y_2^{\uparrow}(t)+\frac{1-\Phi[\dot{u}(t)]}{2}y_2^{\downarrow}(t), \tag{66}$$

where $\Phi[\dot{u}(t)]$ is used to ensure a smooth transition between each load regime. Thus, the polynomial contributions of the total response $y(t)$ described by Volterra series are

calculated considering the following input:

$$u(t) = \frac{A(e^{j\omega t} + e^{-j\omega t})}{2}, \tag{67}$$

$$u_0(t) = A_1(e^{j\omega t} - e^{-j\omega t}) + A_2(e^{j3\omega t} - e^{-j3\omega t}), \tag{68}$$

the contributions are given by:

$$\begin{aligned} y_1(t) &= \frac{A}{2}\mathcal{H}_1(\omega)e^{j\omega t} + A_1\mathcal{H}_1(\omega)e^{j\omega t} + A_2\mathcal{H}_1(3\omega)e^{j3\omega t} \\ &+ \text{complex conjugates,} \end{aligned} \tag{69}$$

$$\begin{aligned} y_2^{\uparrow}(t) &= \frac{A^2}{2}\mathcal{H}_2(\omega,-\omega) - 2A_1^2\mathcal{H}_2(\omega,-\omega) - 2A_2^2\mathcal{H}_2(3\omega,-3\omega) + \\ &\frac{A^2}{4}\mathcal{H}_2(\omega,\omega)e^{j2\omega t} + A_1^2\mathcal{H}_2(\omega,\omega)e^{j2\omega t} + A_2^2\mathcal{H}_2(3\omega,3\omega)e^{j6\omega t} + \\ &AA_1\mathcal{H}_2(\omega,\omega)e^{j2\omega t} + AA_2\mathcal{H}_2(-\omega,3\omega)e^{j2\omega t} + AA_2\mathcal{H}_2(\omega,3\omega)e^{j4\omega t} - \\ &A_1A_2\mathcal{H}_2(-\omega,3\omega)e^{j2\omega t} + A_1A_2\mathcal{H}_2(\omega,3\omega)e^{j4\omega t} \\ &+ \text{complex conjugates,} \end{aligned} \tag{70}$$

$$y_2^{\downarrow}(t) = -y_2^{\uparrow}(t) \tag{71}$$

$$\begin{aligned} y_3(t) &= \frac{3A^3}{8}\mathcal{H}_3(\omega,\omega,-\omega)e^{j\omega t} - 3A_1^3\mathcal{H}_3(\omega,\omega,-\omega)e^{j\omega t} + \\ &\frac{3A^2A_1}{4}\mathcal{H}_3(\omega,\omega,-\omega)e^{j\omega t} + \frac{3A^2A_2}{4}\mathcal{H}_3(-\omega,-\omega,3\omega)e^{j\omega t} - \\ &\frac{3AA_1^2}{2}\mathcal{H}_3(-\omega,-\omega,3\omega)e^{j\omega t} - 3AA_2^2\mathcal{H}_3(\omega,-3\omega,3\omega)e^{j\omega t} + \\ &3A_1^2A_2\mathcal{H}_3(-\omega,-\omega,3\omega)e^{j\omega t} - 6A_1A_2^2\mathcal{H}_3(\omega,-3\omega,-3\omega)e^{j\omega t} + \\ &\frac{A^3}{8}\mathcal{H}_3(\omega,\omega,\omega)e^{j3\omega t} + A_1^3\mathcal{H}_3(\omega,\omega,\omega)e^{j3\omega t} - \\ &3A_2^3\mathcal{H}_3(3\omega,3\omega,-3\omega)e^{j3\omega t} + \frac{3A^2A_1}{4}\mathcal{H}_3(\omega,\omega,\omega)e^{j3\omega t} + \\ &\frac{3A^2A_2}{2}\mathcal{H}_3(-\omega,\omega,3\omega)e^{j3\omega t} + \frac{3AA_1^2}{2}\mathcal{H}_3(\omega,\omega,\omega)e^{j3\omega t} - \\ &6A_1^2A_2\mathcal{H}_3(\omega,-\omega,3\omega)e^{j3\omega t} + \frac{3A^2A_2}{4}\mathcal{H}_3(\omega,\omega,3\omega)e^{j5\omega t} + \\ &\frac{3AA_2^2}{2}\mathcal{H}_3(-\omega,3\omega,3\omega)e^{j5\omega t} + 3A_1^2A_2\mathcal{H}_3(\omega,\omega,3\omega)e^{j5\omega t} - \\ &3A_1A_2^2\mathcal{H}_3(-\omega,3\omega,3\omega)e^{j5\omega t} + \frac{3AA_2^2}{2}\mathcal{H}_3(\omega,3\omega,3\omega)e^{j7\omega t} + \\ &3A_1A_2^2\mathcal{H}_3(\omega,3\omega,3\omega)e^{j7\omega t} + A_2^3\mathcal{H}_3(3\omega,3\omega,3\omega)e^{j9\omega t} \\ &+ \text{complex conjugates.} \end{aligned} \tag{72}$$

Remark 1. Although the harmonics present in the contributions $y_2^{\uparrow}(t)$ and $y_2^{\downarrow}(t)$ are from even order such as $e^0, e^{2\omega t}, e^{4\omega t}$ and $e^{6\omega t}$, the multiplication in equation (66) by $\Phi[\dot{u}(t)]$ causes odd harmonics $e^{\omega t}, e^{3\omega t}, e^{5\omega t}$, and so on, to appear. Hence, the harmonic of higher order generated by $y_2(t)$ must also be in $y_3(t)$, otherwise, the odd harmonics generated does not match those in the response of the oscillator. To meet this condition, the number of terms N_s to approximate $\Phi[\dot{u}(t)]$ needs to be the same as the one used to compute the input $u_0(t)$.

The main advantage in estimating the higher-order FRFs is the dependence that they have on the physical parameters of the system and its linear FRF. Another interesting aspect is that the Volterra kernels provide an approximate overview in the frequency domain about the nonlinear behavior occurring in the oscillator with hysteresis for the applied input condition. Thus, as long as the higher-order FRFs and the Volterra series are convergent, the outputs in the time and frequency domain provide a unique mapping from the system dynamics, a characteristic that the short-time Fourier transform has for non-stationary systems.

3.3 NUMERICAL APPLICATION OF THE HIGHER-ORDER FRFs

With the analytical higher-order FRFs derived from the system composed of the nonlinear operator, this section aims to explore the applicability of these expressions to describe a hysteretic benchmark with a dynamic nonlinearity well approximated by a Bouc-Wen model and recently proposed by Noël and Schoukens (2016b) at the Workshop on Nonlinear System Identification Benchmarks. Although the white-box methods have improved their applicability to complex nonlinear systems, the main contributions in the literature for the Bouc-Wen model or even for the proposed benchmark are with gray-box and black-box approaches. For instance, Noël *et al.* (2017) used a framework based on black-box identification to deal with the hysteresis effect without the requirement of a specific physical model. The algorithm procedure consists of identifying polynomial nonlinear state-space (PNLSS) models fitted under multi sine excitation. Then, to reduce the high number of terms required to identify the PLNSS model, Esfahani *et al.* (2018) proposed using the canonical polyadic decomposition, which rewrites the univariate polynomials in linear combinations of states and inputs.

From the perspective of grey-box modeling, Worden *et al.* (2018) provided an

identification scheme to obtain the Bouc-Wen model parameters based on an evolutionary optimization algorithm. The procedure has also addressed issues about the good choice of excitation inputs and reference models. In addition, Bajrić and Høgsberg (2018) used stochastic output-only subspace methods to identify the poles of an equivalent linear damper model parametrized according to the excitation amplitude, frequencies, and benchmark model parameters. Furthermore, the work provides interesting physical insight about the benchmark behavior under different forcing conditions since the equivalences considered to construct the linear system was based on intrinsic characteristics from slow and fast motion regimes of the Bouc-Wen oscillator.

The Bouc-Wen benchmark model parameters are shown in Tab 2 and were selected according to Noël and Schoukens (2016b). First, this section starts with a numerical example of the nonlinear operator shown in the motion equation (17) to describe a hysteretic system. Thus, through the higher-order FRFs framework applied to the nonlinear operator, the analytical output from the system with hysteresis is calculated and compared to the output obtained by the numerical integration with 4^{th} order Runge-Kutta method. The Volterra contributions and the higher-order kernel surfaces are also provided.

Table 2 – Bouc-Wen benchmark parameters.

m [kg]	c [Ns/m]	k [N/m]	α [N/m]	β	γ [m^{-1}]	δ [m^{-1}]	ν
2	10	5×10^4	5×10^4	1×10^3	0.8	-1.1	1

Source: Noël and Schoukens (2016b).

3.3.1 Numerical example of the nonlinear operator

Some numerical simulations are carried out to evaluate the nonlinear operator proposed to describe hysteretic systems. All simulations with the benchmark presented in this work used a sampling frequency equal to 750 Hz and $N = 2^{14}$ samples with the parameters listed in Tab. 2. The numerical integration was solved through the 4^{th} order Runge-Kutta method with a variable time step. A convergence analysis based on the terms selected to be used in the Taylor series expansion considering a varying number of terms from the Fourier series is carried out to illustrate that the framework of the nonlinear operator, defined in equation (17), is suitable to deal with the Bouc-Wen benchmark. The error is calculated by the Normalized Mean Square Error (NMSE) [%]

between the responses from the Bouc-Wen oscillator and the system in (17):

$$\text{NMSE} = 100 \times \frac{\|\mathcal{Z}(t) - \mathscr{F}[y(t)]\|_2}{\|\mathcal{Z}(t)\|_2}\%. \tag{73}$$

Figure 18 – Convergence analysis of the nonlinear operator representing the hysteretic restoring force of the Bouc-Wen benchmark. ■ represents $N_s = 1$, ■ represents $N_s = 2$, ■ represents $N_s = 3$ and ■ is for $N_s = 4$.

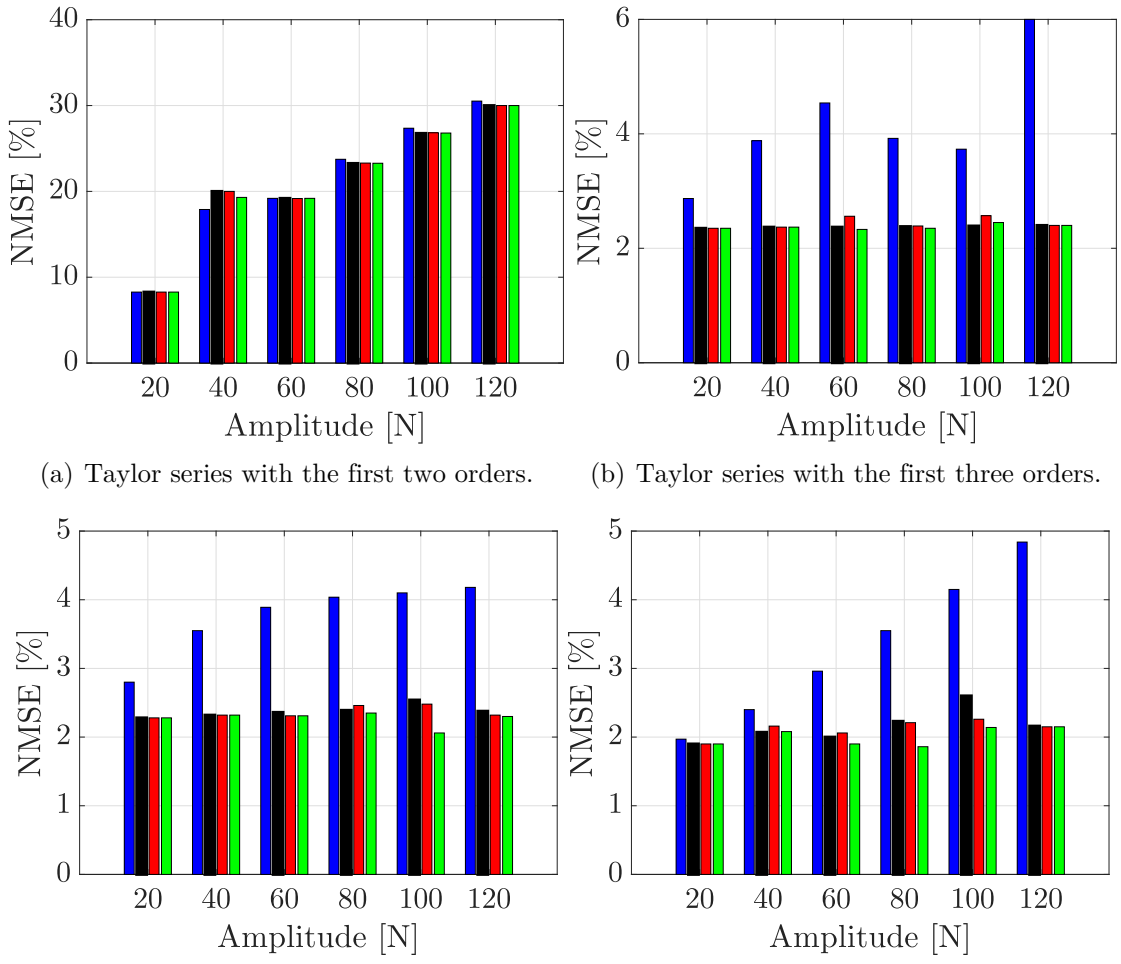

(a) Taylor series with the first two orders.

(b) Taylor series with the first three orders.

(c) Taylor series with the first four orders.

(d) Taylor series with the first five orders.

Source: Teloli and Silva (2019).

Figure 18 depicts four different cases of the NMSE in function of the excitation amplitudes considering a quasi-static harmonic input $u(t) = A\cos(2\pi t)$. Regardless of the number of terms used in the Fourier series are used, the NMSE in Figure 18(a) indicates that the nonlinear operator fails to describe the hysteretic restoring force when it assumes less than three terms in the Taylor series expansion. For expansions from the 3rd order on, Figures 18(b)-(d) show that the nonlinear operator reaches the convergence, with values below of 2.5%, if $N_s \geq 2$. In conclusion, since the framework of the nonlinear operator provides an interesting, cost-effective ratio between accuracy and algebraic complexity of

the higher-order FRFs, the third-order polynomial form in the bounding functions with $N_s = 2$ is adequate to describe and reproduce the benchmark hysteresis loop.

Figure 19 shows the simulated response of the Bouc-Wen model described in section 3.1.2 considering a quasi-static harmonic input with amplitude of $A = 120$ N selected based on (NOËL; SCHOUKENS, 2016b). Under this excitation condition, the model with RIH property draws a single hysteresis loop bounded between loading and unloading regions. The restoring force obtained through numerical integration of the equations (4) and (5) is plotted in Fig. 19(a) by considering null initial conditions. Figure 19(b) shows the restoring force × displacement graphic, where it is possible to note that the continuous hysteresis loop is bounded over the output amplitudes $[-Y, Y]$ and the symmetric loading and unloading regimes of the restoring force.

Figure 19 – Comparison between the restoring forces obtained from the Bouc-Wen oscillator and through the nonlinear operator. – – – for the Bouc-Wen's response and – • – is for the nonlinear operator. The NMSE obtained is 2.15% and the dissipated energy of both hysteretic loops is ≈ 42.35 N.mm.

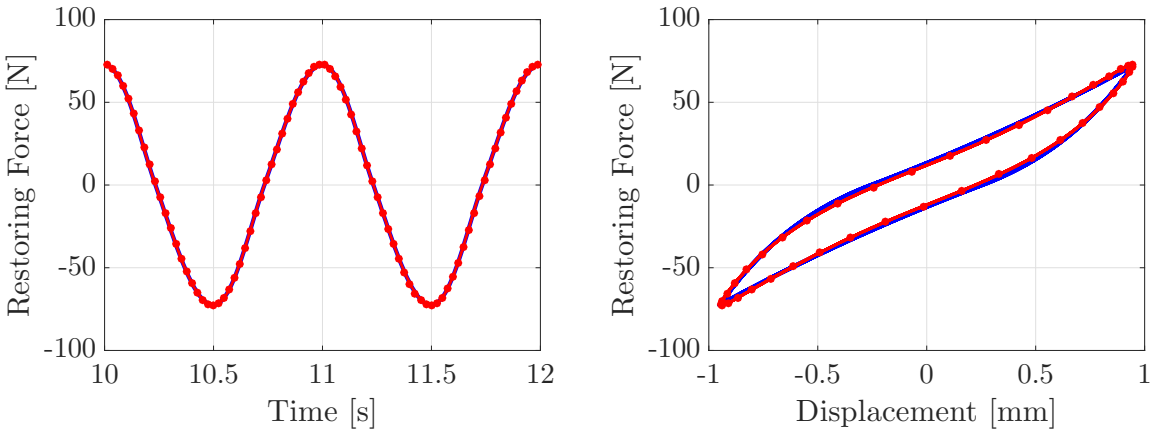

(a) Restoring force response.

(b) Hysteresis loop.

Source: Teloli and Silva (2019).

The displacement amplitudes Y and y_0 obtained are 0.9502 mm and 0.2536 mm, respectively. These two amplitudes were used to compute the bounding functions coefficients through the equations (20), (21), (22) and (23). The absolute values obtained are $\lambda_0 = 13.88$ N, $\lambda_1 = 5 \times 10^4$ N/m, $\lambda_2 = 1.0941 \times 10^7$ N/m^2 and $\lambda_3 = 3.0665 \times 10^{10}$ N/m^3. By solving numerically the motion equation (17), the equivalent restoring force from the nonlinear operator is able to reproduce the force $\mathcal{Z}(y, \dot{y})$ properly, as can been seen in Fig. 19(a). Furthermore, the enclosed area of the hysteresis loops depicted in Fig. 19(b) is almost the same for both restoring forces, which means that these systems have the same energy dissipation [Nmm].

3.3.2 Bouc-Wen benchmark

A harmonic quasi-static input $u(t) = A\cos(2\pi t)$ with amplitude of $A = 40$ N was used and the system outputs were obtained through numerical integration of the motion equations (4) and (5) based on the 4^{th} order Runge-Kutta method. For quasi-static input conditions, the selected amplitude $A = 40$ N reproduces a weak hysteresis loop. Amplitudes of $Y = 0.3641$ mm and $y_0 = 0.0445$ mm were obtained to compute the coefficients λ_0, λ_1, λ_2 and λ_3 used in the higher-order FRFs.

The parameters m, c, k and α from Tab. 2 were used to calculate the kernels $\mathcal{H}_1(\omega)$ and $\mathcal{H}_1(3\omega)$ over a frequency range of $0 - 71.30$ Hz with an incremental step of 0.046 Hz. Figure 20 shows the first order FRF both in terms of its magnitude (Fig. 20(a)) and phase (Fig. 20(b)). The resonance peaks are 35.58 and $\frac{35.6}{3}$ Hz, which means that the resonances occur at ω_n, which is associated with the linear dynamic of the model, and at $3\omega = \omega_n \Rightarrow \omega = \frac{\omega_n}{3}$, associated with the third order harmonic from the additional input.

Figure 20 – Frequency Response Functions. -- represents the kernel $\mathcal{H}_1(\omega)$, whereas --●-- is for the kernel $\mathcal{H}_1(3\omega)$.

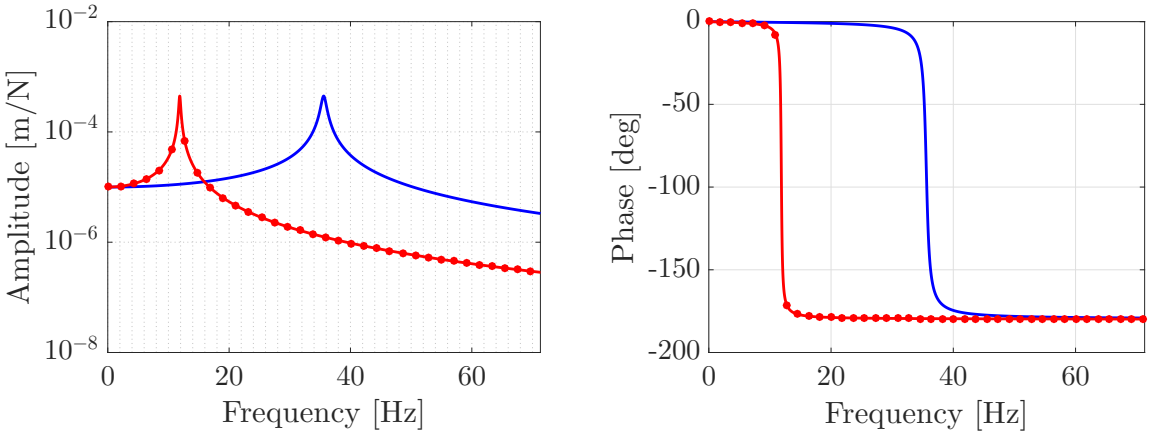

(a) Amplitude.

(b) Phase.

Source: Teloli and Silva (2019).

In the case of an equivalent system that does not hold the principle of superposition, its response presents the frequency components from the input as well as multiple harmonics from the nonlinear behavior. The interactions between the system presents' frequency components are clear in the second and third-order FRFs equations, with components of 5ω, 6ω, and 7ω order, among others. Thus, Figures 21 and 23 show the magnitude and phase surface of each kernel, whereas Figures 22 and 24 are their leading diagonal.

Figures 21(a)-(b) present the surfaces from $\mathcal{H}_2(\omega_1, \omega_2)$ on the components ω_1 and ω_2,

whereas Figures 22(a)-(b) show the leading diagonal in $\omega_1 = \omega_2 = \omega$, where $f_1 = \frac{\omega_1}{2\pi}$ and $f_2 = \frac{\omega_2}{2\pi}$. These plots evidence the resonance peaks at 35.58 and 17.79 Hz ($2\omega = \omega_n$), which refer to the linear and secondary resonances. Although the total output does not have quadratic components, the FRF framework provides knowledge about the bounding functions nonlinearity. Furthermore, the changes in λ_2 influence on the phase plot, as shown in Figure 22, whereas the surfaces depicted in Fig. 21 exemplify only the second order FRFs that have $\lambda_2 > 0$.

Figures 21(c)-(d) illustrate the second-order cross-kernel surfaces that highlight the interaction between frequency components with the inputs. Additionally, Figures 22(c)-(d) show the amplitude and phase of the leading diagonals, thus evidencing the main resonance at 35.58 and the secondary resonances at 11.86 and 8.89 Hz, corresponding to the harmonics of $3\omega = \omega_n$ and $4\omega = \omega_n$, respectively. Finally, the plot of surfaces in Figures 21(e)-(f) with their leading diagonals in 22(e)-(f) shows the direct kernel calculated with the additional input evidencing the resonance peaks at 11.86 and 5.93 Hz ($6\omega = \omega_n$), which is an interaction that the third-order harmonic input holds in the second order kernel.

The framework of the third-order kernels plotted in Figure 23 shows surfaces on the frequency components ω_1, ω_2 and sliced at $\omega_3 = \frac{\omega_n}{3}$. Visualizing the presence of sub-harmonics and resonance peaks, as well as phase jumps in these surfaces, is not trivial, and it needs the support of each leading diagonal, which is plotted in Figure 24. All the third-order kernels have in their leading diagonal, depicted as amplitude and phase plots, weak resonances in secondary sub-harmonics, indicating quadratic nonlinearities' influence on these kernels. Nevertheless, the peaks with major amplitude are regarded as tertiary sub-harmonics, highlighting the domain of cubic nonlinearity over the frequency response. Although the calculation of kernels was carried out for a specific input condition, their framework in the frequency domain will remain the same for other conditions, experiencing changes only concerning their amplitudes, since the first-order kernels still maintain the same values due to the linear physical parameters.

Having the higher-order FRFs, the analytical polynomial contributions $y_1(t)$, $y_2(t)$ and $y_3(t)$ are estimated in time domain through the equations (69)–(72) with frequency $\omega = 2\pi$. Figure 25 presents a comparison between the output generated by numerical integration and the analytical one, which demonstrates a good match between the results. Figure 26 shows a close-up view of the response spectrum over a frequency range of $0 - 8$ Hz, evidencing the excitation frequency at 1 Hz and also the third, fifth, and seventh-order harmonics at 3, 5 and 7Hz, respectively. Welch's periodogram with a rectangular

Figure 21 – Second-order Volterra kernels.

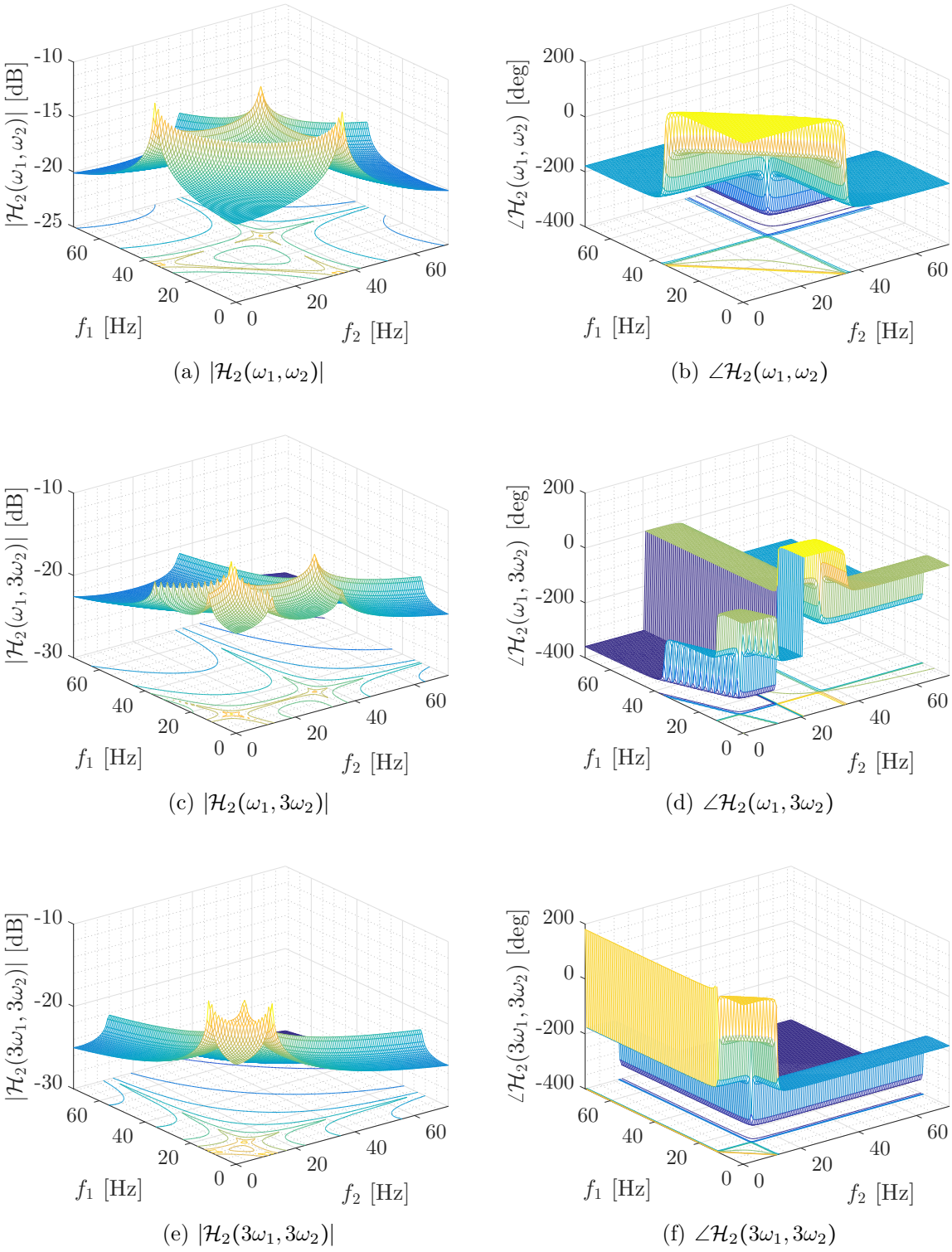

(a) $|\mathcal{H}_2(\omega_1,\omega_2)|$ (b) $\angle\mathcal{H}_2(\omega_1,\omega_2)$

(c) $|\mathcal{H}_2(\omega_1,3\omega_2)|$ (d) $\angle\mathcal{H}_2(\omega_1,3\omega_2)$

(e) $|\mathcal{H}_2(3\omega_1,3\omega_2)|$ (f) $\angle\mathcal{H}_2(3\omega_1,3\omega_2)$

Source: Teloli and Silva (2019).

window over a frequency range of $0-70$ Hz was used to attain this. The Volterra model can reproduce up to the fifth-order harmonic component (5 Hz), but more terms in the

Figure 22 – Leading diagonals of the second-order Volterra kernels. -- represents the kernels with $\lambda_2 > 0$, whereas --●-- is for the kernels that have $\lambda_2 < 0$.

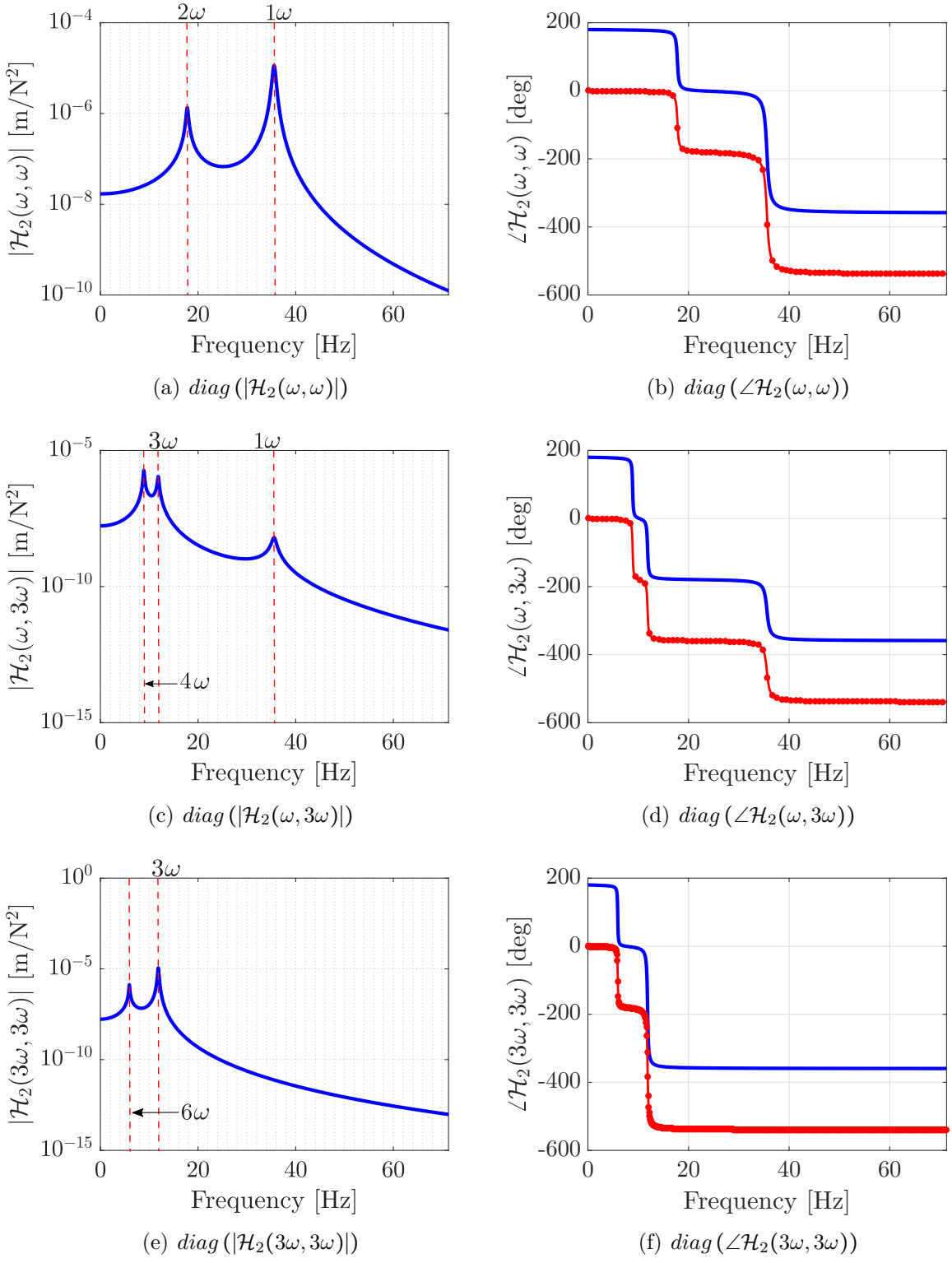

Source: Teloli and Silva (2019).

series expansion are necessary to predict higher-order components. However, the number of terms included in this work is sufficient to deal with the Bouc-Wen model subjected

Figure 23 – Third-order Volterra kernels.

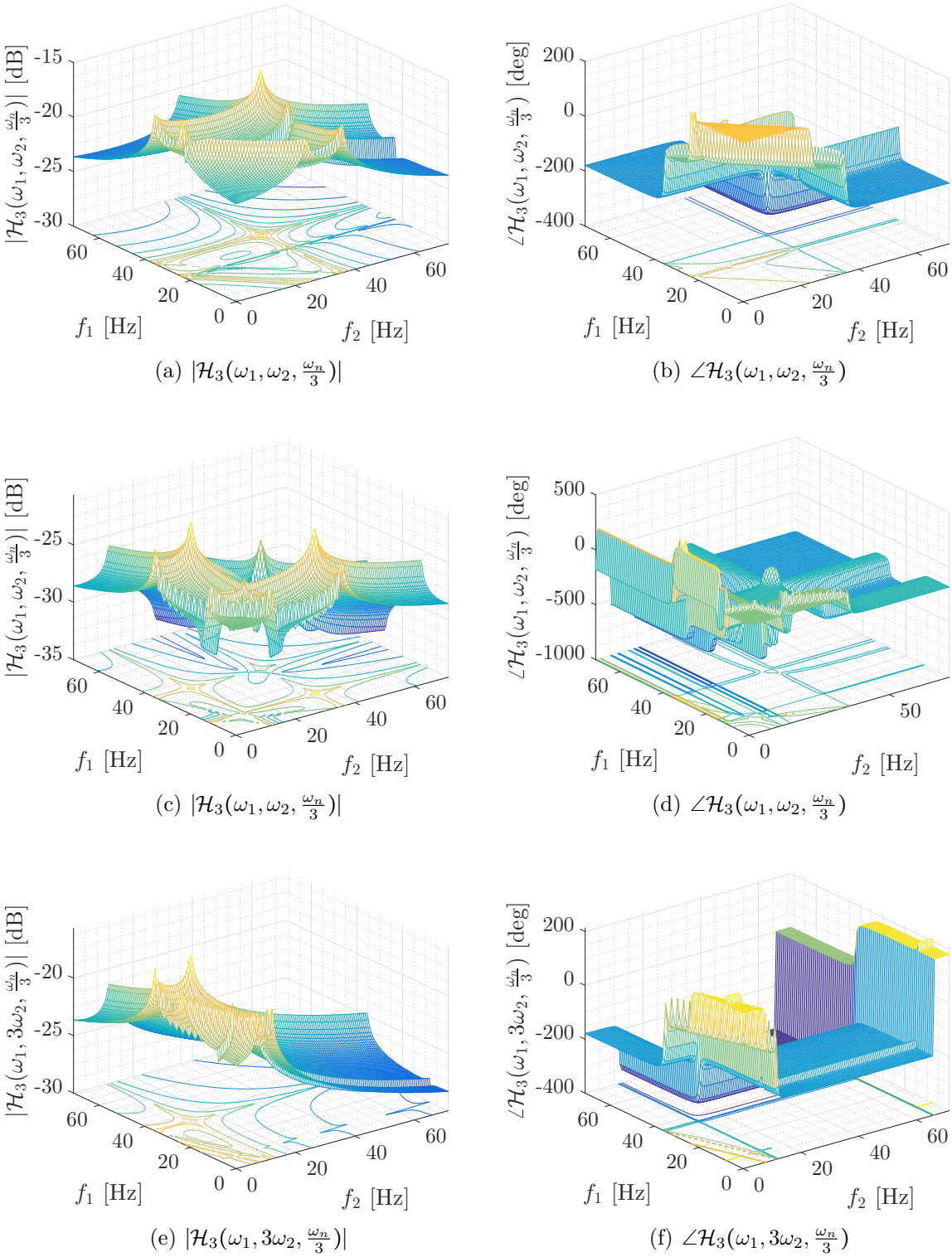

(a) $|\mathcal{H}_3(\omega_1,\omega_2,\frac{\omega_n}{3})|$

(b) $\angle\mathcal{H}_3(\omega_1,\omega_2,\frac{\omega_n}{3})$

(c) $|\mathcal{H}_3(\omega_1,\omega_2,\frac{\omega_n}{3})|$

(d) $\angle\mathcal{H}_3(\omega_1,\omega_2,\frac{\omega_n}{3})$

(e) $|\mathcal{H}_3(\omega_1,3\omega_2,\frac{\omega_n}{3})|$

(f) $\angle\mathcal{H}_3(\omega_1,3\omega_2,\frac{\omega_n}{3})$

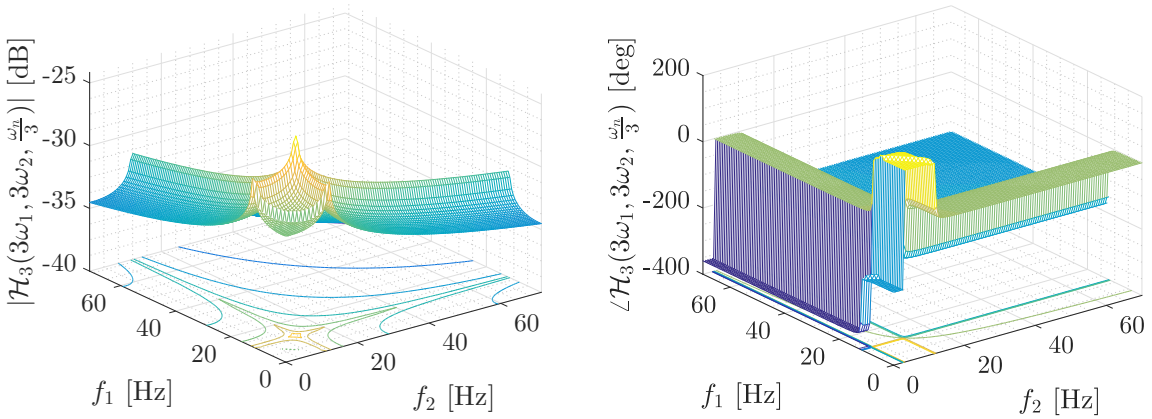

(g) $|\mathcal{H}_3(3\omega_1, 3\omega_2, \frac{\omega_n}{3})|$ (h) $\angle\mathcal{H}_3(3\omega_1, 3\omega_2, \frac{\omega_n}{3})$

Source: Teloli and Silva (2019).

to weak excitation inputs.

The nonlinear contributions $y_2(t) + y_3(t)$ oscillate with a phase shift compared to the linear contribution, which highlights the nonlinear damping that arises from the hysteresis effect. Even with the presence of the second-order contribution $y_2(t)$, the total response of the Volterra model has only odd harmonics, as discussed in Remark 3.1. In addition, Fig. 27 depicts the linear and nonlinear contributions of the total response in time domain (Fig. 27(a)) and each output spectrum (Fig. 27(b)), which is a demonstration of Remark 3.1, since the second-order contribution has components at 1, 3 and 5 Hz, as well as the third-order contribution. With the influence of the additional input, the linear output $y_1(t)$ has components at 1 and 3 Hz.

The odd harmonics presented in the response spectrum are not enough to conclude if the analytical output describes well the hysteresis loop since other nonlinearities could show the same behavior (KOVACIC; BRENNAN, 2011). Figure 28 shows the comparison between the smoothed hysteresis loop obtained with the Volterra model and by numerical integration, whose loops dissipate 2.61% Nmm and 2.5% Nmm respectively, demonstrating that the analytical response is able to reproduce with a reasonable agreement the Bouc-Wen oscillator hysteresis loop.

Figure 29 illustrates the hysteresis loop obtained through the Volterra model for different forcing amplitudes and the same excitation frequency. In the case of low amplitude with $A = 1$ N, as plotted in Figure 29(a), the analytical output can reproduce the hysteresis loop with a good match which is almost closed and the restoring force is linear. However, when the input amplitude gets higher, as seen in Figure 29(b) with

A = 60 N, the Volterra model starts presenting convergence problems; for instance, the dissipated energy by the analytical model is 4.52 Nmm, whereas the value of 3.75

Figure 24 – Leading diagonals of the third-order Volterra kernels.

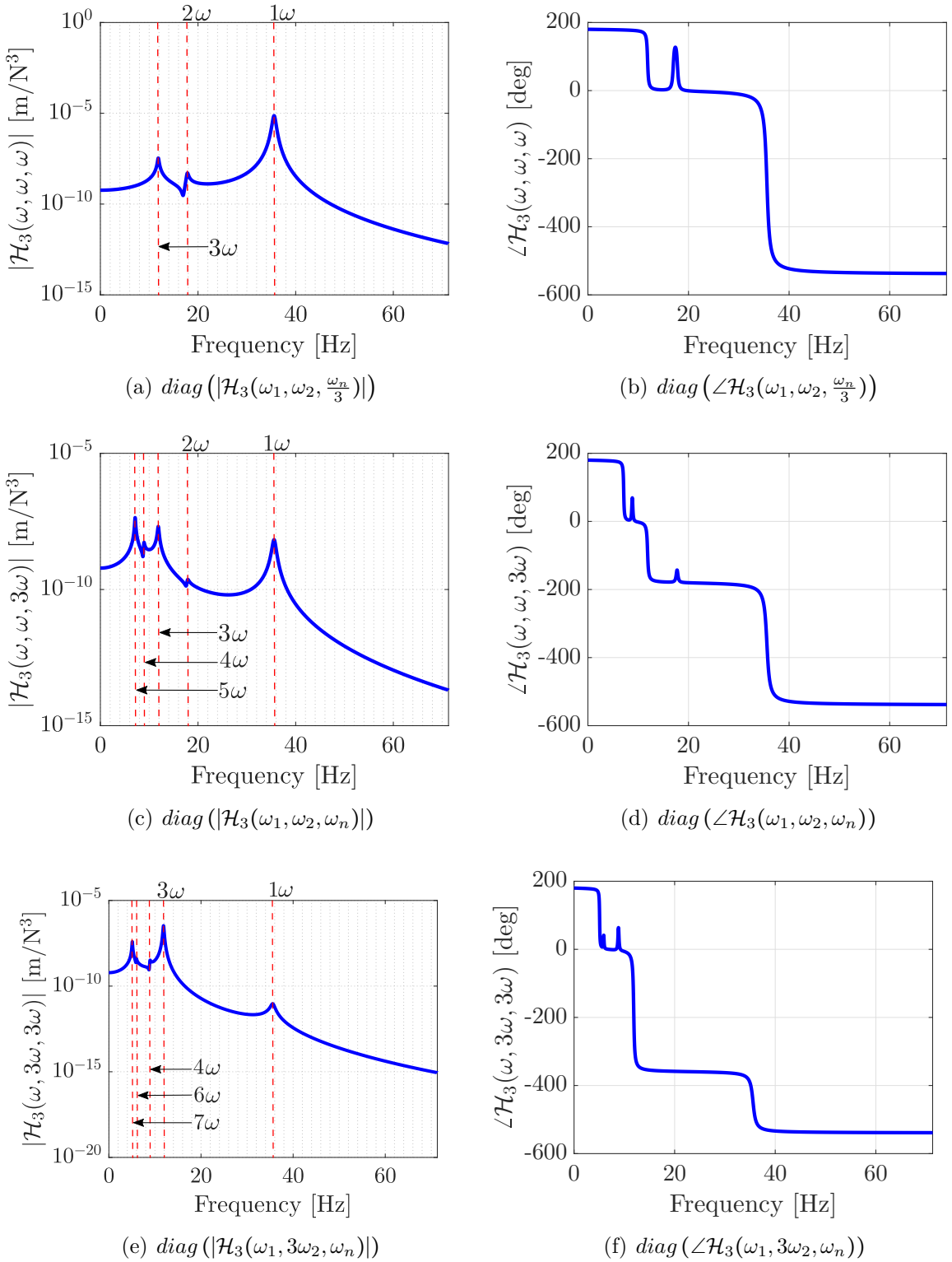

(a) $diag\left(|\mathcal{H}_3(\omega_1,\omega_2,\frac{\omega_n}{3})|\right)$

(b) $diag\left(\angle\mathcal{H}_3(\omega_1,\omega_2,\frac{\omega_n}{3})\right)$

(c) $diag\left(|\mathcal{H}_3(\omega_1,\omega_2,\omega_n)|\right)$

(d) $diag\left(\angle\mathcal{H}_3(\omega_1,\omega_2,\omega_n)\right)$

(e) $diag\left(|\mathcal{H}_3(\omega_1,3\omega_2,\omega_n)|\right)$

(f) $diag\left(\angle\mathcal{H}_3(\omega_1,3\omega_2,\omega_n)\right)$

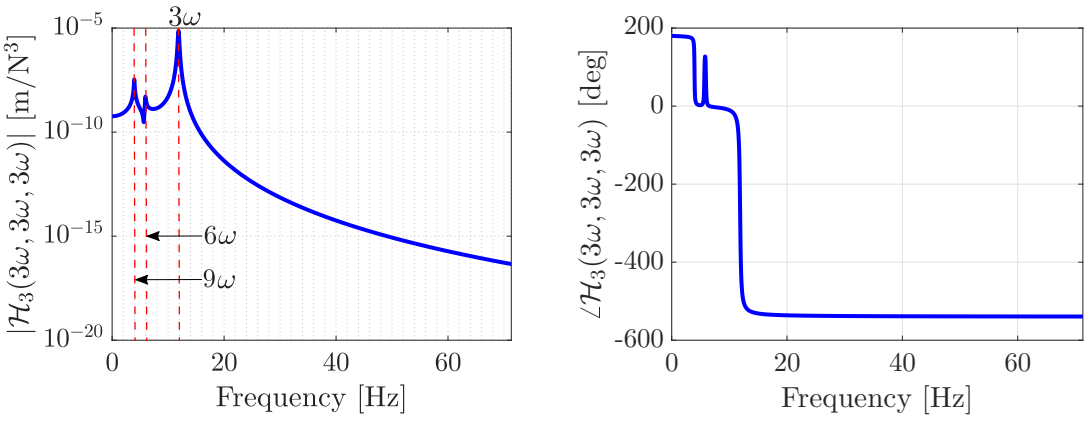

(g) $diag\left(|\mathcal{H}_3(3\omega_1, 3\omega_2, \omega_n)|\right)$ (h) $diag\left(\angle|\mathcal{H}_3(3\omega_1, 3\omega_2, \omega_n)|\right)$

Source: Teloli and Silva (2019).

Figure 25 – Output of the identified Volterra model in a close-up view over 6 – 18 seconds. – represents the response of the Bouc-Wen oscillator by numerical integration and • is the response of the proposed Volterra model. The value of NMSE computed between the outputs is 2.7%.

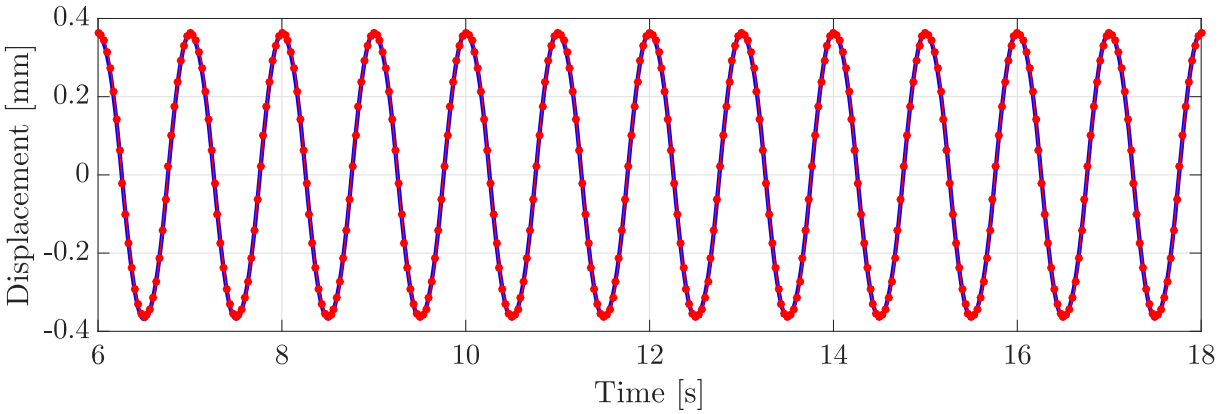

Source: Teloli and Silva (2019).

Nmm is obtained from the numerical integration. Although the mathematical framework helps overcome difficulties in representing discontinuities and multiple solutions on the hysteresis loop, the Volterra series is adequate to describe hysteretic systems under weak excitation amplitudes and conditions hysteresis loop is almost closed. The methodology presented in this work can be an alternative tool of an algorithm to perform a modal analysis on a hysteretic system.

Finally, Figure 30 shows the comparison between the response amplitudes estimated through numerical integration and by Volterra model for a sweep sine test with constant input amplitude of A = 20 N over a normalized frequency range $\frac{\omega}{\omega_n} \in [0.1\ 1.6]$. The proposed smooth nonlinear operator has quadratic terms that are taken into account to

Figure 26 – Comparison between the outputs spectrum. – represents the output spectrum simulated from the Bouc-Wen and • is the spectrum predicted by the proposed Volterra model.

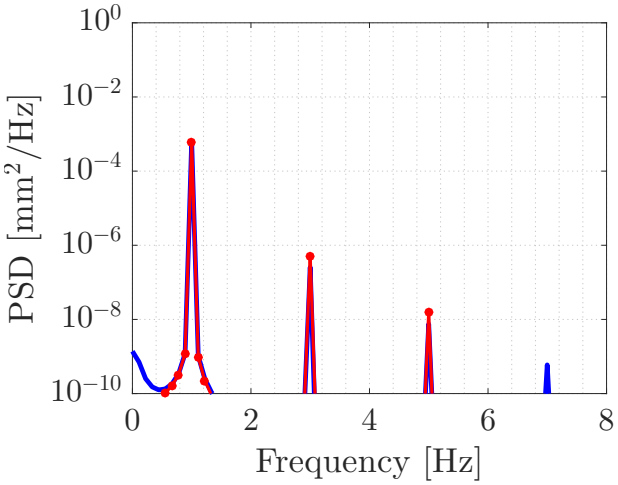

Source: Teloli and Silva (2019).

Figure 27 – Representation of the Volterra model contributions. –, $y_1(t)$; –•–, $y_2(t)$ and –▲–, $y_3(t)$

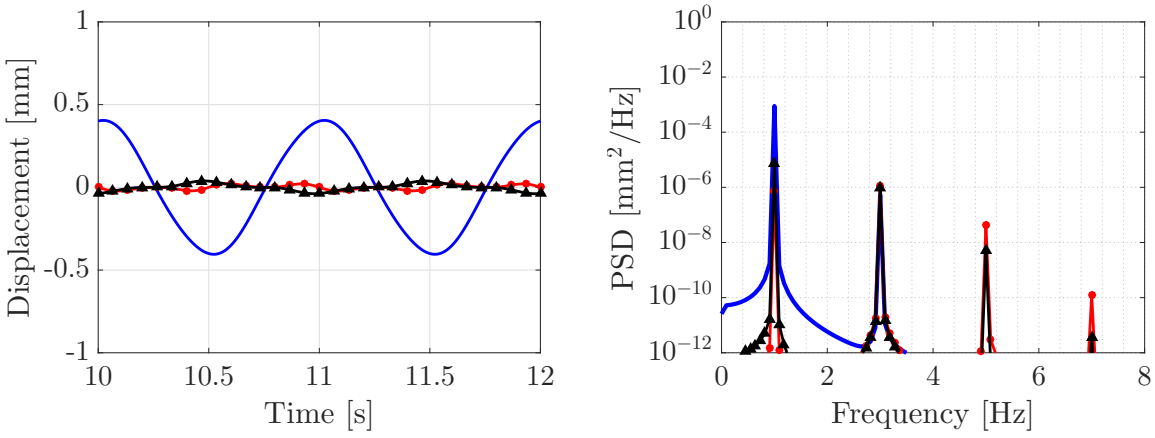

(a) Contributions. (b) Outputs spectrum

Source: Teloli and Silva (2019).

compute the second-order kernels and, for this reason, the amplitude of the second-order contributions increase when $\frac{\omega}{\omega_n} = 0.5$, whereas the Bouc-Wen output does not present this sub-harmonic. In addition, around the linear resonance frequency range $\frac{\omega}{\omega_n} \in [0.75 \;\; 1.2]$, the analytical Volterra model is absolutely inaccurate. The result clearly details that the response predicted by the Volterra model is only suitable for a narrow-banded input condition.

Figure 28 – Comparison between the hysteresis loop responses with excitation amplitude of $A = 40$ N. – represents the restoring force of the Bouc-Wen model and • is the restoring force estimated through the Volterra model output.

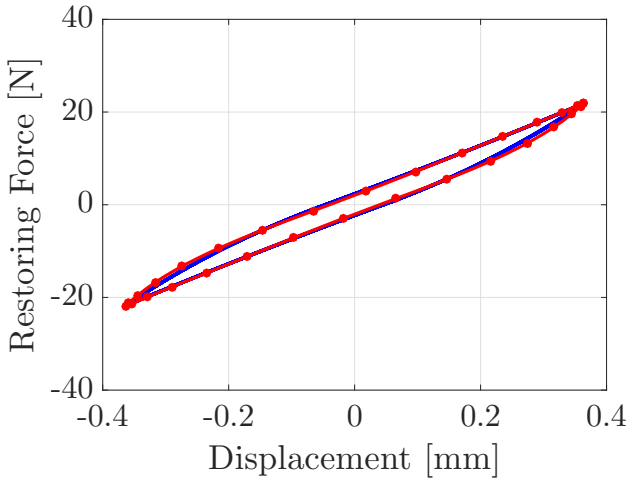

Source: Teloli and Silva (2019).

Figure 29 – Bouc-Wen hysteresis loop for different forcing amplitudes. – represents the restoring force calculated through numerical integration and • is the restoring force by the Volterra model output.

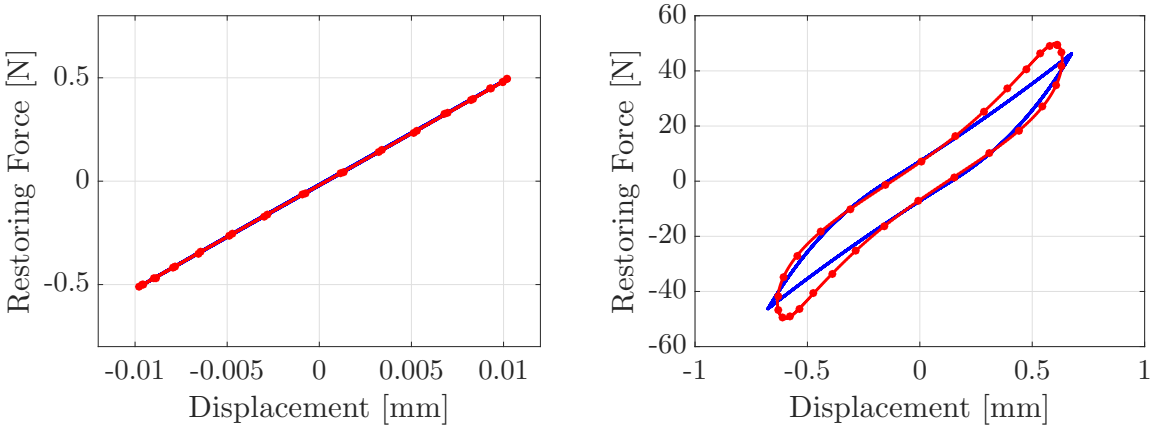

(a) Low amplitude level of $A = 1$ N.

(b) High amplitude level of $A = 60$ N.

Source: Teloli and Silva (2019).

Figure 30 – Comparison between the response amplitudes for a sweep sine input. – represents the numerical response from the Bouc-Wen and • is the spectrum predicted by the proposed Volterra model.

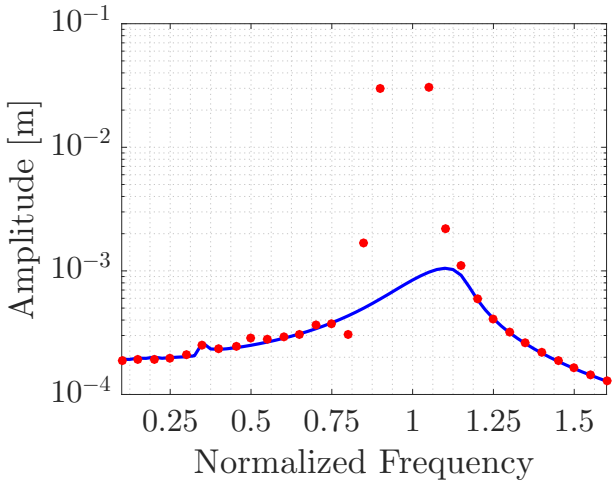

Source: Teloli and Silva (2019).

3.4 HARMONIC BALANCE METHOD

As previously mentioned, there are different alternatives to approximate the output of nonlinear systems by analytical descriptions (NAYFEH, 2008; SILVA; COGAN; FOLTÊTE, 2010; SCUSSEL; SILVA, 2017) when a mono-harmonic input is applied to a nonlinear system, usually due to the presence of higher-order harmonics as a result of existing nonlinearities, its response exhibits waveform distortions. Thus, the fundamental premise of the HBM is to represent the system response through the Fourier series, projecting the higher-order harmonic components on a sine and cosine basis as an *ansatz* to solve the problem. In the context of constitutive models with hysteresis, harmonic balance variants provide a proper tool for dealing with non-smooth nonlinearities. Krack and Gross (2019) presented a comprehensive review of HBM-based tools and how to solve harmonic balance equations.

Basically, there are two different strategies for obtaining an approximation of the response of nonlinear systems via HBM, the so-called numerical approximations, and analytical approximations. Regarding the former, there are contributions through continuation algorithms that can automatically calculate the progress of the solution given a frequency interval in which it is desired to obtain the frequency response curves of a particular system. The continuation methods are divided into the prediction step (e.g., secant method, tangent method, or Lagrange polynomial method), which consists in predicting an initial estimate of solution of an algebraic system of equations[1], followed by a correction step (e.g., Newton method, Moore-Penrose method or pseudo-arclength method), which consists of improving this estimate until the desired solution is found, given a convergence criterion. The advantage related to these methodologies is in the possibility of tracking the resonance frequencies of the system under different excitation conditions, with the capability of estimating the different branches present in the frequency response curves, even those unstable ones where the system may present multiple solutions in the region near the jump phenomenon. It is important to emphasize that these methodologies do not necessarily depend on prior knowledge of the constitutive equations of the system under analysis, but only on the estimation of the Fourier coefficients of its response, either in the time or frequency domain. These approaches are already established in the literature and have been investigated in different contexts, such as in the approximation of a Bouc-Wen oscillator (WONG; NI; KO, 1994; NI; KO; WONG, 1998), to solve the LuGre model (JAUMOUILLÉ; SINOU; PETITJEAN, 2010), dealing with systems whose damping is

[1]The ansatz usually form a system of algebraic equations to solve in terms of the Fourier coefficients.

generated due to dry friction (KRACK, 2015), among others.

Concerning analytical approximations, which consist in obtaining closed-form solutions for the Fourier coefficients from the knowledge of motion equations, there is a limitation in applying Fourier series to models with hysteresis since the non-smoothness present in part of these models establishes a restrictive condition in forming the balance equations, because it does not permit the explicit expansion of hysteretic forces in terms of the displacement, as is the case for the Bouc-Wen oscillator. Consequently, a smoothing procedure should be performed before deriving the analytical solutions by the harmonic balance technique. In this scenario, the piecewise smooth equations (11)-(14) derived by the Taylor series approach paves the way for using the HBM.

The section proceeds with the general idea of HBM applied to a smooth oscillator with polynomial nonlinear stiffness term and then discussed the particularities of applying the method on systems with a hysteresis.

3.4.1 General Harmonic Balance Method

The system analyzed here to exemplify the harmonic balance method is the symmetric Duffing oscillator with a smooth stiffness nonlinearity (KOVACIC; BRENNAN, 2011):

$$m\ddot{y}(t) + c\dot{y}(t) + ky(t) + \underbrace{k_3 y^3(t)}_{=\mathscr{F}_{nl}(y)} = u(t), \tag{74}$$

where $\mathscr{F}_{nl}(y)$ [N] is the nonlinear restoring force. The ansatz of the nonlinear system when subjected to a harmonic input $u(t) = A\sin(\omega t)$ is assumed to be written as a Fourier series:

$$y(t) = a_0 + \sum_{n=1}^{M_k} \left[a_n \cos(n\omega t) + b_n \sin(n\omega t) \right], \tag{75}$$

where a_n and b_n are the coefficients of the series and M_k corresponds to the number of harmonics considered to approach the desired solution. After substituting the series of $y(t)$ in the motion equation (74), the nonlinear restoring force is also formulated as the Fourier series:

$$\mathscr{F}_{nl}(y) = \frac{\mathcal{A}_0}{2} + \sum_{n=1}^{M_k} \left[\mathcal{A}_n \cos(n\omega t) + \mathcal{B}_n \sin(n\omega t)\right], \tag{76}$$

where $\mathcal{A}_n$ and $\mathcal{B}_n$ are the coefficients of the series of the restoring force. As the term $\mathscr{F}_{nl}(y)$ is continuous over all the oscillation period established in $[0, \frac{2\pi}{\omega}]$, the classical Fourier analysis can properly expand it (WORDEN; TOMLIMSON, 2001; SILVA *et al.*, 2009; BUSSETTA; SHIKI; SILVA, 2017):

$$\mathcal{A}_n = \frac{\omega}{\pi} \int_0^{\frac{2\pi}{\omega}} \mathscr{F}_{nl}(t) \cos(n\omega t) dt, \tag{77}$$

$$\mathcal{B}_n = \frac{\omega}{\pi} \int_0^{\frac{2\pi}{\omega}} \mathscr{F}_{nl}(t) \sin(n\omega t) dt. \tag{78}$$

Substituting equations (75)--(78) into the motion equation (74) yields:

$$\begin{aligned} A\sin(\omega t) &= -m\omega^2 \left\{\sum_{n=1}^{M_k} n^2 \left[a_n \cos(n\omega t) + b_n \sin(n\omega t)\right]\right\} \\ &+ c\omega \left\{\sum_{n=1}^{M_k} n \left[-a_n \sin(n\omega t) + b_n \cos(n\omega t)\right]\right\} \\ &+ k\left\{a_0 + \sum_{n=1}^{M_k} \left[a_n \cos(n\omega t) + b_n \sin(n\omega t)\right]\right\} \\ &+ \frac{\mathcal{A}_0}{2} + \sum_{n=1}^{M_k} \left[\mathcal{A}_n \cos(n\omega t) + \mathcal{B}_n \sin(n\omega t)\right]. \end{aligned} \tag{79}$$

Balancing the equal harmonic terms from equation (79) results in the following system of equations:

$$
\begin{aligned}
&\underbrace{\sum_{n=1}^{M_k}\left[-m\left(\omega n\right)^2 a_n + c\left(n\omega\right) b_n + k a_n + \mathcal{A}_n\right] = 0}_{\text{cosine terms}} \\
&\underbrace{-m\left(\omega\right)^2 b_1 - c\omega a_1 + b_1 k + \mathcal{B}_1}_{\text{first order sine terms}} = A \\
&\underbrace{\sum_{n=2}^{M_k}\left[-m\left(\omega n\right)^2 b_n - c\left(n\omega\right) a_n + k b_n + \mathcal{B}_n\right] = 0}_{\text{sine terms}} \\
&\underbrace{k a_0 + \frac{\mathcal{A}_0}{2}}_{\text{remaining terms}} = 0.
\end{aligned}
\tag{80}
$$

Thus, it is demanded to solve all the series coefficients that minimize the set of equations in (80). There are constraints to handle this task, e. g., a particular frequency range where multiple solutions exist. Here, the Newton-Raphson method is utilized for solving equation (80).

3.4.2 Particularities of the harmonic balance method for hysteretic system

As discussed before, the method can be realized directly in a smooth nonlinear system since the restoring force is continuous on the oscillation period (VIRGIN, 1988; DONESCU; VIRGIN; WU, 1996). However, the piecewise smooth equations from the Bouc-Wen model require modifications in the Fourier approach, meaning to describe each restoring force term properly in its right time intervals. In sum, the harmonic balance generates an average hysteretic restoring force based on splitting the coefficients of the series $\mathcal{A}$ and $\mathcal{B}$ according to the valid oscillation period of $\mathcal{Z}_1(y,\dot{y})$, $\mathcal{Z}_2(y,\dot{y})$, $\mathcal{Z}_3(y,\dot{y})$ and $\mathcal{Z}_4(y,\dot{y})$. The particularities involved in this model are similar to the strategy required to deal with the Coulomb friction law, which decomposes the friction force into the stick and slip intervals (KIM; PERKINS, 2003).

Fourier analysis of Bouc-Wen model

The hysteretic restoring force of the Bouc-Wen model was split into four motion intervals, where each of them is valid on a quarter of the total oscillation period, as exposed in Fig. 17. Then, the general expression of the average restoring force in steady-

state is constituted as:

$$\mathcal{Z} = \sum_{n=1}^{M_k} \left[\mathcal{A}_n \cos(n\omega t) + \mathcal{B}_n \sin(n\omega t) \right], \tag{81}$$

where the Fourier expansion of the coefficients is given by:

$$\mathcal{A}_n = \frac{\omega}{\pi} \left(\begin{array}{l} \int_0^{\frac{\pi}{2\omega}} \mathcal{Z}_1 \cos(n\omega t) dt + \int_{\frac{\pi}{2\omega}}^{\frac{\pi}{\omega}} \mathcal{Z}_2 \cos(n\omega t) dt + \\ \\ \int_{\frac{\pi}{\omega}}^{\frac{3\pi}{2\omega}} \mathcal{Z}_3 \cos(n\omega t) dt + \int_{\frac{3\pi}{2\omega}}^{\frac{2\pi}{\omega}} \mathcal{Z}_4 \cos(n\omega t) dt \end{array} \right), \tag{82}$$

$$\mathcal{B}_n = \frac{\omega}{\pi} \left(\begin{array}{l} \int_0^{\frac{\pi}{2\omega}} \mathcal{Z}_1 \sin(n\omega t) dt + \int_{\frac{\pi}{2\omega}}^{\frac{\pi}{\omega}} \mathcal{Z}_2 \sin(n\omega t) dt + \\ \\ \int_{\frac{\pi}{\omega}}^{\frac{3\pi}{2\omega}} \mathcal{Z}_3 \sin(n\omega t) dt + \int_{\frac{3\pi}{2\omega}}^{\frac{2\pi}{\omega}} \mathcal{Z}_4 \sin(n\omega t) dt \end{array} \right). \tag{83}$$

The Bouc-Wen hysteresis loop is symmetric regarding each regime of motion. Consequently, the Fourier terms related to asymmetric motion are null.

3.4.3 Numerical application for the Bouc-Wen model

The Bouc-Wen model parameters are displayed in Tab. 2. Before starting to derive analytical expressions for the coefficients of the series, some numerical simulations are handled to establish how many terms are required to expand the equations (11)--(14) using the Taylor series approach. The bar graph in Figure 31 shows the normalized mean square error (NMSE) between the hysteresis loop approached by Taylor series expansion with regard the loop obtained through numerical integration of equations (1)-(2) considering the 4^{th} order Runge-Kutta method with variable time step.

The error analysis provides a convergence criterion for selecting the order of the Taylor series approach, which can describe adequately the numerically integrated hysteresis loop, considering different excitation amplitudes for a quasi-static harmonic input $u(t) = A\sin(2\pi t)$ and varying the number of terms n. From Fig. 31, it can be concluded

that upper than $n = 4$ terms the Taylor series expansion reaches the convergence, with the NMSE values above 2.5%. Figure 32 shows a direct comparison between the hysteretic restoring force numerically integrated, and the paths $\mathcal{Z}_1$, $\mathcal{Z}_2$, $\mathcal{Z}_3$ and $\mathcal{Z}_4$ expanded using $n = 4$ terms in the Taylor series approach for the input amplitude of $A = 160$ N.

Figure 31 – Comparative error between different numbers of terms used in the Taylor series for approaching the hysteresis loop of the Bouc-Wen model. ■ represents $n = 2$ terms, ■ represents $n = 3$ terms, ■ represents $n = 4$ terms and ■ represents $n = 5$ terms.

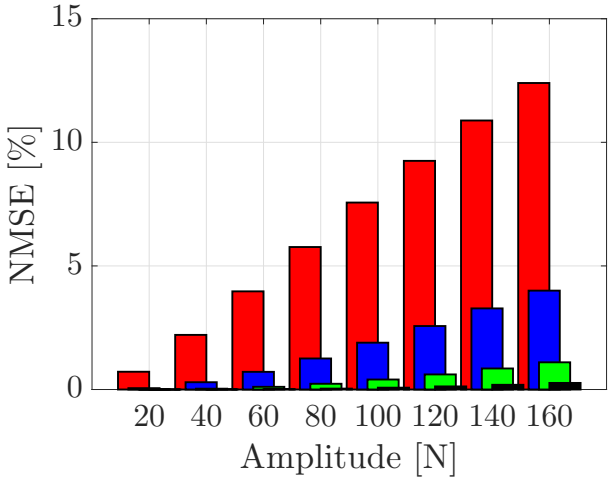

Source: Miguel, Teloli and Silva (2020).

Figure 32 – Comparison between the hysteretic restoring forces of the Bouc-Wen model obtained from numerical integration of equations (4)-(4) and through the four different paths approached by the Taylor series. ▬ is the $\mathcal{Z}(y, \dot{y})$ term response by numerical integration, whereas --■-- represents $\mathcal{Z}_1$, --●-- represents $\mathcal{Z}_2$, --■-- represents $\mathcal{Z}_3$ and --●-- is $\mathcal{Z}_4$.

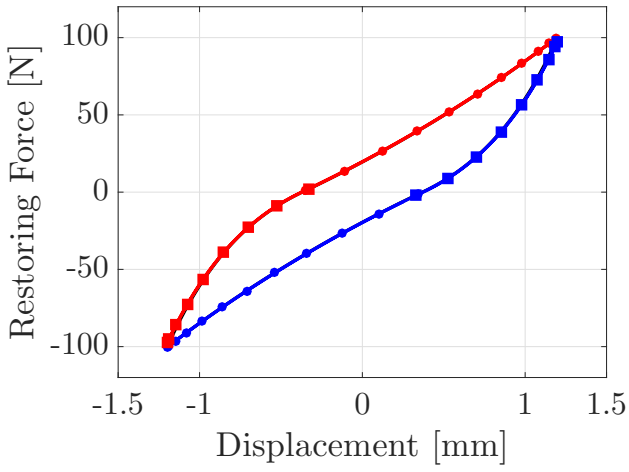

Source: Miguel, Teloli and Silva (2020).

As observed, four terms in the Taylor series are enough to approach the hysteresis loop of the model benchmark properly under a high level of excitation amplitude, providing a close match within the responses and enclosing the same area of the hysteresis loop obtained by numerical integration, which is ≈ 83.1 mJ per cycle. Although $n = 4$ terms provide good results, it is necessary to point out that n may change according to the shape of the hysteretic curve, keeping in mind that the higher the complexity in a hysteresis curve, the more terms need to be included. Having defined the framework of the piecewise hysteretic restoring force, the next step is to propose trial responses and later to compute the coefficients of the Fourier series using the Newton-Raphson method.

The frequency response curves obtained analytically and through numerical integration are shown in Figure 33. The curves were estimated with a constant amplitude input $A = 10$ N over a normalized frequency range $\frac{\omega}{\omega_n} \in [0.1 \quad 1.8]$, examining as trial solutions for applying the harmonic balance method the fundamental harmonic ($M_k = 1$) and the sum of the fundamental plus the third harmonic ($M_k = 3$). The resonance frequency shifts up due to the hardening characteristic of the hysteretic restoring force, with the analytical responses capturing the jump phenomena between different amplitude solutions. Around the jump resonant region, $\frac{\omega}{\omega_n} \in [1.125 \quad 1.25]$, the choice of the initial conditions for estimating the coefficients of the harmonic components by the Newton-Raphson method require to be handled carefully. Moreover, the trial solution regarding the fundamental and third harmonic can predict well the subharmonic at frequency $\omega = \frac{\omega_n}{3}$, whereas only the fundamental harmonic cannot, as observed in Figure 33(b).

Figure 34 presents the normalized mean square error between the integrated numerical solution and the analytical responses for all the frequency intervals. The error decreases on almost all the frequency spectrum for using the fundamental and the third harmonic as a trial solution, whereas only the first harmonic deviates from that calculated by the numerical integration. Also, the error achieves maximum values around the jump region because the integrated numerical solution does not reproduce the jump effect.

Figure 35 shows the hysteresis loop for different forcing conditions to assess the accuracy of the analytical solution with the fundamental and the third harmonic in predicting the Bouc-Wen response. It was considered three levels of amplitude 10, 20 and 40 N, applied for two different excitation frequencies of $\omega = \frac{\omega_n}{3}$ and $\omega = \omega_n$. The hysteresis loops predicted analytically through different amplitudes at $\omega = \frac{\omega_n}{3}$ shown in the Figs. 35(a), 35(c) 35(e) present substantially the same enclosed area, for instance, the dissipated energy from both the hysteresis loops in Figure 35(e) is ≈ 3.35 mJ per period of oscillation.

Figure 33 – Comparison between the frequency response curves of the Bouc-Wen model obtained with numerical integration and through harmonic balance method considering an input level of 10N. ··· is the numerical integrated response, whereas −− is the fundamental harmonic and ▬ is the fundamental added to the third harmonic.

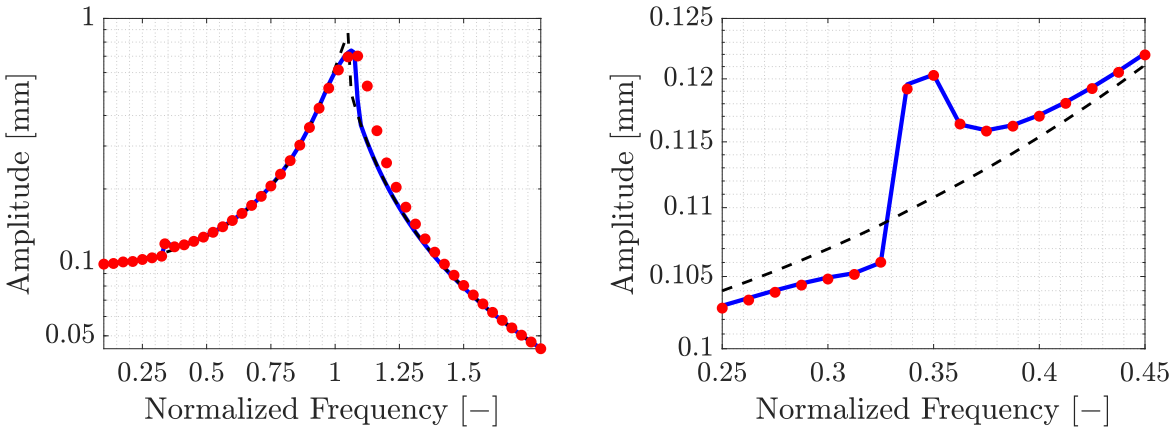

(a) Frequency response curve. (b) Zoom in the subharmonic $\omega = \frac{\omega_n}{3}$.

Source: Miguel, Teloli and Silva (2020).

Figure 34 – Normalized mean square error between the numerical integrated solution and the analytical responses. −− is the error between the fundamental harmonic and the numerical integrated curve, whereas ▬ is the error derived from the fundamental harmonic added to the third harmonic. The straight line ····· corresponds to the threshold error value of 5%.

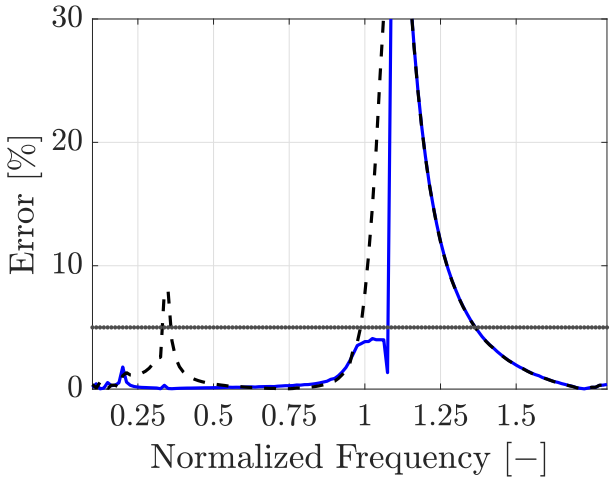

Source: Miguel, Teloli and Silva (2020).

Figures 35(b), 35(d) 35(f) show the comparison between both analytical and numerical loops when the excitation frequency is at $\omega = \omega_n$. For all cases with this excitation frequency, the area contained by the analytic hysteresis loop is smaller, for instance, in Figure 35(f) the analytic loop dissipates ≈ 72.4 mJ per period of oscillation, whereas the

integrated numerical one corresponds to ≈ 87.9 mJ. Generally speaking, although there exist differences between the responses, the analytical solution is more conservative and, for this reason, it could help design purposes. Finally, Figures 36 and 37 exemplify the responses in the time domain of the Figs. 35(e) and 35(f), respectively.

Figure 35 – Direct comparison between the hysteresis loop obtained by numerical integration and through the harmonic balance method considering different forcing conditions applied on the Bouc-Wen oscillator. ····· is the numerical integrated response, whereas ▬ corresponds to the analytical response.

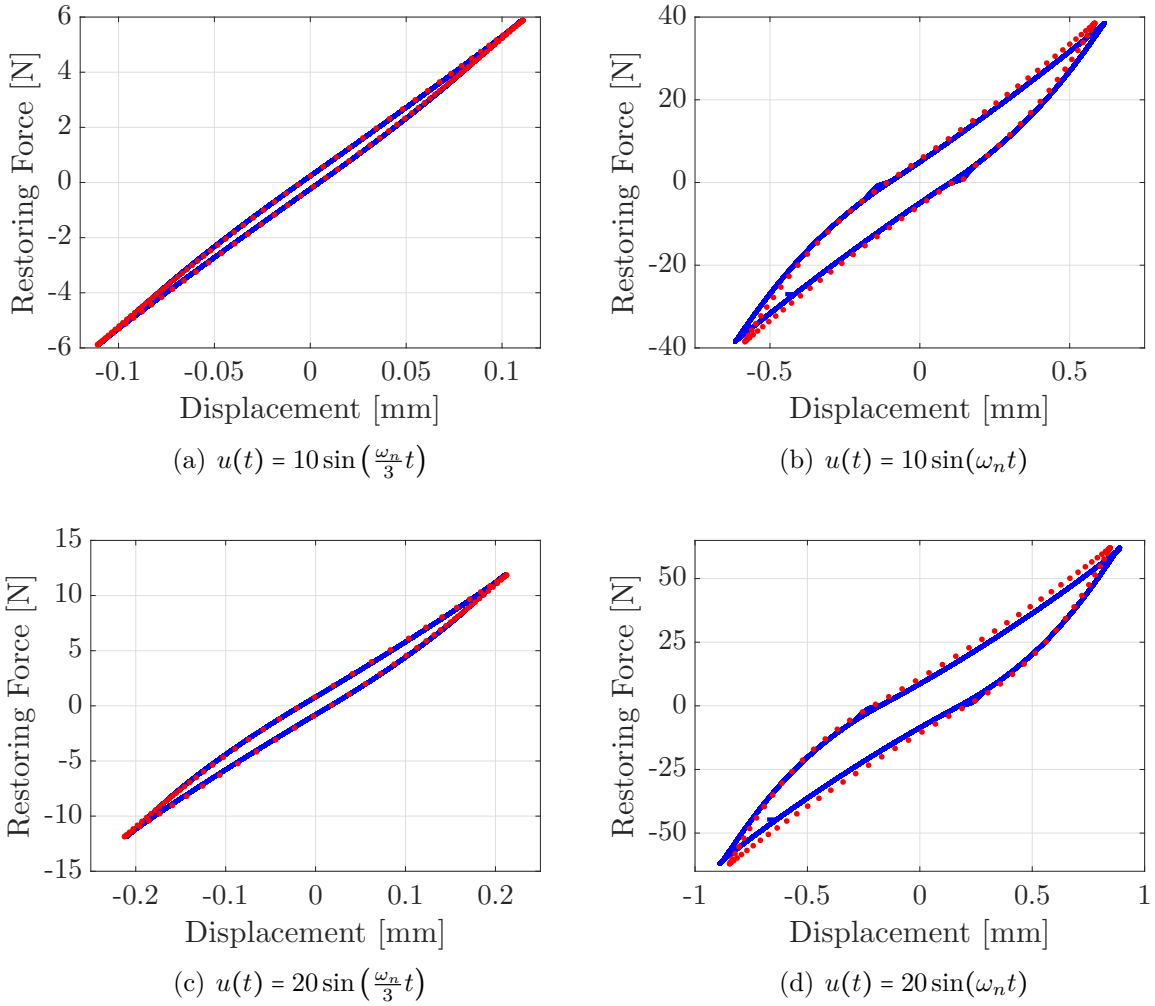

(a) $u(t) = 10\sin\left(\frac{\omega_n}{3}t\right)$ (b) $u(t) = 10\sin(\omega_n t)$

(c) $u(t) = 20\sin\left(\frac{\omega_n}{3}t\right)$ (d) $u(t) = 20\sin(\omega_n t)$

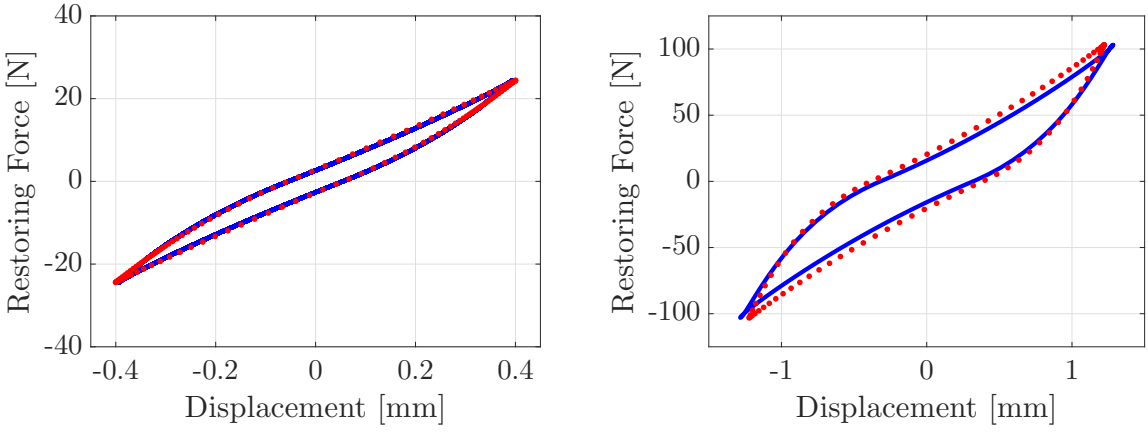

(e) $u(t) = 40\sin\left(\frac{\omega_n}{3}t\right)$ (f) $u(t) = 40\sin(\omega_n t)$

Source: Miguel, Teloli and Silva (2020).

Figure 36 – Output identified by the harmonic balance method considering as input $u(t) = 40\sin\left(\frac{\omega_n}{3}t\right)$, in zoom between 11.15 and 11.5 seconds. ····· is the integrated numerical response, whereas ▬ corresponds to the analytical response.

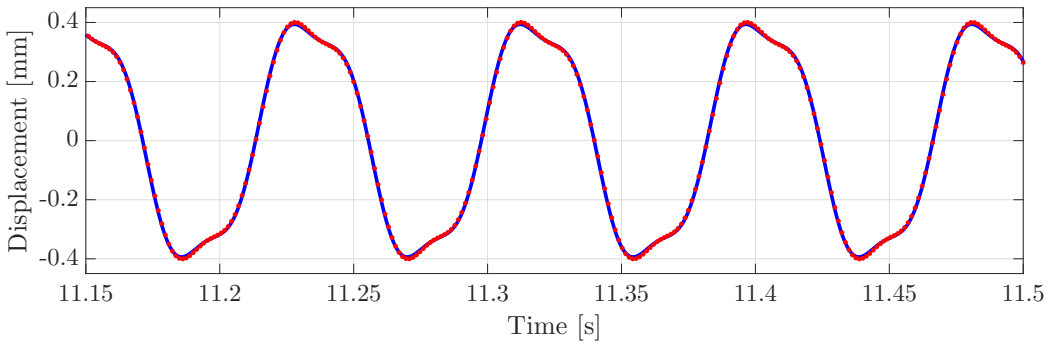

Source: Miguel, Teloli and Silva (2020).

Figure 37 – Output identified by the harmonic balance method considering as input $u(t) = 40\sin(\omega_n t)$, in zoom between 11.15 and 11.5 seconds. ····· is the integrated numerical response, whereas ▬ corresponds to the analytical response.

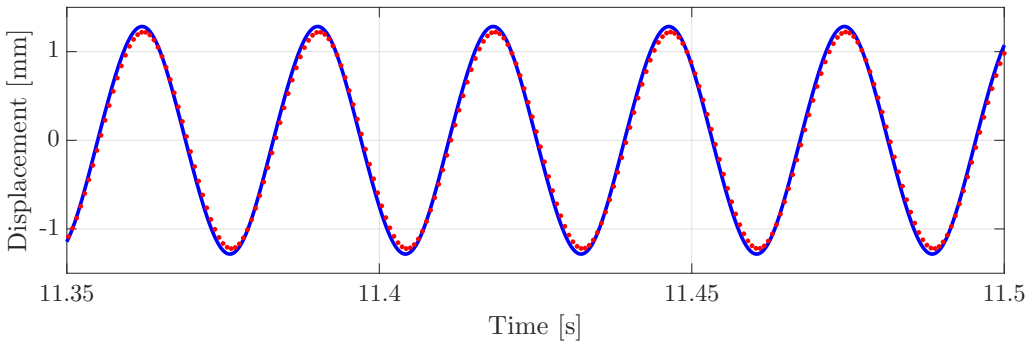

Source: Miguel, Teloli and Silva (2020).

3.5 COMPARISONS BETWEEN FREQUENCY DOMAIN TECHNIQUES

Regarding the use of the Volterra series, although the results obtained here allow the hysteresis loop for narrow-banded input conditions to be represented analytically, to the best of our knowledge, the possibility of describing an analytical hysteresis loop approached by the Volterra model was not demonstrated in previous works.

In general, the functional series has convergence problems in regions near resonance frequencies, even for oscillator models with the polynomial type of nonlinearity. Discussions on convergence problems of the Volterra series have already been covered in the literature, verifying that approximations by higher-order FRFs are valid for systems with weak nonlinearity or with input conditions that ensure weak nonlinear behavior (PENG; LANG, 2007).

However, for input and frequency conditions, the series exhibits convergence; the higher-order FRFs framework provides concise algebraic equations, with the potential to verify how the parameters of a model interfere with its nonlinear behavior, as seen in the expressions of the Volterra kernels for the oscillator with hysteresis. Besides this frequency domain representation, another advantage present in the Volterra theory is evaluating each nonlinear contribution on the total time response. As will be seen in the next Chapter, this framework is an interesting NSI procedure suitable for applications involving bolted joints.

The HBM, in turn, presents the possibility of predicting the response of the Bouc-Wen oscillator in a region where the Volterra series approximation is not capable, which is in the vicinity of the resonance frequency. Another advantage presented by HBM lies in the possibility of performing the Fourier analysis directly on piecewise equations of the hysteretic restoring force without the need to employ a nonlinear operator, which minimizes approximation errors during the smoothing procedure (see the NSME values in Figs. 18 and 31, for example).

On the other hand, the algebraic expressions resulting from Fourier analysis are not straightforward and require the Newton-Raphson solver's use, which is sensitive to the initial guess conditions, to obtain the series coefficients.

3.6 CONCLUDING REMARKS

The first part of this Chapter was dedicated to the use of the Volterra series to represent hysteretic systems based on the analytical higher-order FRFs estimated through the harmonic probing method. Initially, the polynomial form's existence of bounding functions was discussed to approximate independently each loading regime that occurs along the hysteresis loop. Combining these functions into an equivalent system allowed the application of the harmonic probing method for multi-input systems and derived expressions for the higher-order FRFs. The proposed methodology includes the hysteresis memory effect in the output predicted through the Volterra model by considering an additional input that depends on the input signal rate of change and guarantees multiple solutions to the analytical higher-order FRFs. The effectiveness of the proposed solution was tested using a benchmark involving the Bouc-Wen model. The results obtained show that for narrow-banded input conditions with weak excitation amplitudes, the Volterra series can provide an adequate analytical approximation. Furthermore, with representation proposed using Volterra kernels, it is possible to identify all the parameters from the higher-order FRFs using experimental data, as will be shown hereinafter.

Afterward, the Chapter presented an analytical strategy applied to the Bouc-Wen model through the harmonic balance method. First, the framework to rewrite the hysteretic restoring forces as piecewise smooth functions was performed using a simple Taylor series approach to expand them as explicit displacement functions. Further, the central particularities to use the harmonic balance method and then to determine balancing equations to calculate the Fourier series coefficients were discussed. As each piecewise expression is valid only at a specific frequency interval, the Fourier series has to be integrated by parts producing an average hysteretic restoring force based on splitting the coefficients of the series. Finally, a numerical application was proposed to examine the accuracy of the proposed closed-form solutions. The harmonic balance method could predict the frequency response curve of the Bouc-Wen oscillator and predict the hysteresis loop of the system. Besides, the analytical solution could be an adequate alternative to obtain the steady-state response quickly and practically.

Although there is criticism of using higher-order FFR methods and the harmonic balance method to analytically describe systems with hysteresis in the literature, both approaches proffered a new and straightforward way to approach the Bouc-Wen. Notably, the smoothing procedures presented in this chapter can also be applied to other models with hysteresis. Regarding the Volterra series, the framework could turn into an

alternative tool to perform nonlinear modal analysis on a hysteretic system, which will be covered in the next Chapter. From the HBM point of view, one possibility is to extend the method for problems involving FE-based models and model updating with experimental data from practical engineering problems which present weak hysteresis. Also, expanding the algorithm of the harmonic balance method for MDoF systems, the methodology could be a welcome alternative to analyze the nonlinear modes of hysteretic systems. All these points can be addressed in further works.

4 HIGHER-ORDER FREQUENCY RESPONSE FUNCTIONS FOR STRUCTURES ASSEMBLED BY BOLTED JOINTS: AN EXPERIMENTAL APPLICATION

Frequency domain formulations are advantageous in dealing with assembled structures. One topic of interest involves identifying the evolution of resonance frequencies and damping ratios according to excitation amplitudes, the so-called ‘‘modal backbone’’ curves. Peyret, Dion and Chevallier (2016) developed a framework for tracking experimental backbones involving a clamped-clamped beam with transverses interfaces subject to friction and partial slip. The authors post-processed the modal damping and resonance frequencies related to the first bending mode using the extended Kalman filter. Based on the concept of nonlinear modes, Scheel *et al.* (2018) developed a force appropriation technique, which considers steady-state response periods for extracting resonance frequencies and damping ratios considering isolated modes. Then, these modal parameters are used for constructing the modal backbone curve. Alternatively to these curves, frequency-domain methods are often used for predicting the nonlinear behavior of assembled structures. Jaumouillé, Sinou and Petitjean (2010) proposed an adaptive harmonic balance method to compute higher-order harmonic amplitudes of a bolted joint structure. Claeys *et al.* (2016a) implemented the harmonic balance method with continuation and condensation algorithms to predict the nonlinear vibrational response of an experimental setup that includes frictional elements. Lacayo *et al.* (2019) put forward a frequency-domain solver, which is based on a multi-harmonic balance approach, for capturing the slight amplitude-dependency behavior of a bolted lap joint structure.

The frequency-domain techniques are also helpful in parameter estimation procedures. In this context, the multidimensional Fourier transform of the Volterra Kernels is a possible approach to apply. On the one hand, the framework of the higher-order FRFs

is suitable for applications involving parameter estimation on polynomial nonlinearities (CHATTERJEE; VYAS, 2003; CHATTERJEE, 2010a; LIN; NG, 2018). On the other hand, however, there is a lack of contributions related to parameter estimation of hysteretic systems. Recently, Teloli and da Silva (TELOLI; SILVA, 2019) introduced a new approach for harmonic probing of hysteretic systems through a nonlinear smooth operator. In a pioneering way, the authors predicted using closed-form solutions the output of a Bouc-Wen oscillator after rewriting the loading and unloading regimes of the hysteresis loop through smooth operators, which are based on the Taylor series procedure.

In this Chapter, we use a stochastic version of this Bouc-Wen model to reconstruct a probabilistic hysteresis loop of the first vibrating mode of an experimental cantilever beam formed of two aluminum beams assembled by a bolt connection data variation related to the presence of uncertainties in the measurement process. It is essential to point out that the hysteretic model is not used to describe directly the frictional forces in contact interfaces, but rather the whole restoring forces related to the mode of interest. Thus, the Bouc-Wen model stands out for accommodating a wide range of hysteresis loops in the restoring force *versus* displacement plane (IKHOUANE; RODELLAR, 2007). Additionally, it is argued that this model can represent any Iwan's model, which is the most widely used model for modeling jointed structures, just by selecting its parameters accurately (BRAKE, 2018c). Finally, it is worth mentioning the work of Oldfield et al. (OLDFIELD; OUYANG; MOTTERSHEAD, 2005), which brings forward a Bouc-Wen model for producing the hysteresis loop generated by synthetic data of a finite element model involving three components in the assembled configuration. However, the fact that the Bouc-Wen parameters are non-physical turns the parameter identification process into a challenging task if not appropriately conducted and justifies why their use for capturing the dynamic behavior in jointed structures is still modest (ISMAIL; IKHOUANE; RODELLAR, 2009).

Thus, concerning the parameter identification scheme to compute the Bouc-Wen parameters, this Chapter proposes a procedure formulated into a white-box Bayesian modeling framework and considers, as an essential step in the complete identification process, the use of higher-order FRFs derived by Teloli and da Silva (TELOLI; SILVA, 2019). The advantage of using the Volterra kernels at this identification scheme lies in the possibility of visualizing, with physical meaning, the influence of the nonlinear parameters on the system output through the Volterra contributions. The main contribution of this work lies in proposing a new parameter estimation procedure in reduced numerical probabilistic models for representing the dynamics of bolted joint structures by propagating

uncertainties in the coefficients that control the hysteresis loop. Moreover, although this work investigates the first vibrating mode of a structure which carries complex nonlinear effects, the identification strategy here proposed may be suitable for dealing with hysteretic systems that potentially allow the use of smoothing procedures, such as the bit-rock interaction of a drill string (REAL *et al.*, 2019) or even as a formulation in the parametric reduced-order models of jointed structures (FESTJENS; CHEVALLIER; DION, 2013; FESTJENS; CHEVALLIER; DION, 2014).

Toward this background, the parametric identification strategy proposed here includes, firstly, identifying the underlying linear model using conventional modal techniques. Then, the higher-order FRFs are used to calibrate the Bouc-Wen parameters with independent experimental realizations with probing tests. After the Markov Chain Monte Carlo (MCMC) Metropolis-Hastings algorithm, the probability density function (PDF) of each random variable is updated. Once calibrated, the computational model is evaluated, and its dynamical behavior is compared with experimental measurements from the bolted structure. For covering all these steps, the Chapter's outline is: section 4.1 starts presenting a complete description of the parameter estimation procedure proposed. Then the section goes on the Bayesian inference strategy, describing the MCMC/Metropolis-Hastings algorithm to update the random variables. Next, section 4.3 presents an experimental application of the identification procedure for identifying an assembled structure by bolted joints, exemplifying the applicability of the stochastic Bouc-Wen oscillator in representing the linear and nonlinear behavior of the experimental test-bench structure. Since this model is not commonly used to represent bolted joints, comparing with Iwan's model, this paper shows that the Bouc-Wen model operates well, assuming the available experimental data. Finally, section 4.4 reports the final remarks and the next steps for future work.

4.1 ON THE PARAMETER ESTIMATION PROCEDURE

Before going further, equations from the previous Chapter are recalled. The SDoF Bouc-Wen model used in this Chapter is given by:

$$\ddot{y}(t) + 2\zeta\omega_n\dot{y}(t) + \tilde{k}y(t) + \mathcal{Z}(y,\dot{y}) = \tilde{u}(t), \tag{84}$$

$$\dot{\mathcal{Z}}(y,\dot{y}) = \alpha\dot{y}(t) - \gamma|\dot{y}(t)|\,|\mathcal{Z}(y,\dot{y})|^{\nu-1}\mathcal{Z}(y,\dot{y}) - \delta\dot{y}(t)|\mathcal{Z}(y,\dot{y})|^{\nu}, \tag{85}$$

where ω_n is the resonance frequency, ζ is the damping ratio, $\tilde{k}$ is a normalized stiffness coefficient and $\ddot{y}(t)$, $\dot{y}(t)$ and $y(t)$ are the acceleration, velocity and displacement, respectively, of the hysteretic oscillator when subjected to an input $\tilde{u}(t)$, whereas $\mathcal{Z}(y, \dot{y})$ is the hysteretic restoring force that obeys the differential term $\dot{\mathcal{Z}}(y, \dot{y})$; α, γ, δ and ν are the Bouc-Wen parameters. For this work, $\nu = 1$.

This equivalent version of the oscillator is preferred because of the explicit dependency on ω_n and ζ in equation 84, which are parameters that can be extracted through conventional EMA procedures. By doing this, estimating the parameters responsible for the nonlinear behavior through the framework of the higher-order FRFs becomes significantly less cumbersome.

Applying the concept of bounding functions $\mathscr{F}^{\downarrow}[y(t)]$ and $\mathscr{F}^{\uparrow}[y(t)]$ to reproduce the different paths present in the restoring force × displacement plane of the oscillator in (84)-(85) and assuming the first three orders $n = 3$ in the Taylor series approach for each path, yields the following expressions:

$$\lambda_0 = \frac{\alpha y_0}{16}\left(3\delta Y + 8\gamma y_0 - 16\right), \tag{86}$$

$$\lambda_1 = \alpha, \tag{87}$$

$$\lambda_2 = \frac{\alpha}{16Y}\left(8\delta^2 Y y_0 + 8\gamma^2 Y y_0 + 15\delta\gamma y_0^2 - 8\gamma Y - 15\delta y_0\right), \tag{88}$$

$$\lambda_3 = \frac{\alpha}{96Y^5}\left(\begin{array}{c}16\delta^2 Y^5 + 70\delta\gamma Y^4 y_0 - 70\delta\gamma Y^2 y_0^3 - 35\delta Y^4 + \\ 105\delta Y^2 y_0^2 - 105\delta y_0^4\end{array}\right), \tag{89}$$

where λ_0 [Nkg^{-1}], λ_1 [Nkg^{-1}/m], λ_2 [Nkg^{-1}/m^2] and λ_3 [Nkg^{-1}/m^3] are the bounding function coefficients, $Y = |y_{\min}| = |y_{\max}|$ for symmetric hysteresis loops and y_0 is a threshold displacement. Once again, these equations are valid only for harmonic excitations that ensure a weak hysteretic force and when the force × displacement plane draws a single loop.

The switch between bounding functions occurs according to sign$[\dot{\tilde{u}}(t)]$ and thus, an equivalent system with hysteresis is proposed:

$$\ddot{y}(t) + 2\zeta\omega_n\dot{y}(t) + ky(t) + \underbrace{u_0(t) + \lambda_1 y(t) + \varrho y^2(t) + \lambda_3 y^3(t)}_{=\mathscr{F}[y(t)]} = \tilde{u}(t), \tag{90}$$

where $\mathscr{F}[y(t)]$ is the nonlinear operator responsible for encoding the hysteretic characteristics smoothly, and ϱ is defined as $\varrho = \lambda_2$ ($\varrho = -\lambda_2$) for $\text{sign}\left[\dot{\tilde{u}}(t)\right] < 0$ $\left(\text{sign}\left[\dot{\tilde{u}}(t)\right] > 0\right)$. Additionally, for a single-tone input $\tilde{u}(t) = Ae^{j\omega t}$, the term $u_0(t) = \lambda_0 \Phi[\dot{\tilde{u}}(t)]$, which is considered as an additional input applied to the equivalent system, is given by:

$$u_0(t) = \frac{j2\lambda_0}{\pi} \underbrace{\sum_{k=1}^{2} \left(\frac{e^{-j[1+2(k-1)]\omega t} - e^{j[1+2(k-1)])\omega t}}{1+2(k-1)} \right)}_{=\Phi[\dot{\tilde{u}}(t)]}, \tag{91}$$

where $\Phi[\dot{\tilde{u}}(t)]$ is the complex exponential Fourier series up to the second term.

This equivalent version of the oscillator in (84)-(85) was preferred because of the explicit dependency on ω_n and ζ, which are parameters that can be extracted through conventional EMA procedures.

Having introduced the necessary theoretical background, the outline of the identification procedure is explained as follows:

- *Step 1. Data acquisition:*

In principle, this step involves experimental measurements considering controlled vibration tests. The following input signals were considered: white-noise signal with low excitation amplitude to estimate parameters related to the linear regime of motion. Second, probing testing signals were considered to generate the experimental higher-order FRFs. Finally, sweeping sine tests were acquired for verification and testing of the proposed Bouc-Wen oscillator.

- *Step 2. Linear regime of motion:*

This step identifies the underlying linear model. It starts with a modal testing procedure to identify the parameters ω_n and ζ. To accomplish that, the line-fit method (MAIA; SILVA, 1997) is applied on the experimental FRF, which is estimated when the system is subjected to a white noise input with a low excitation level.

The framework of the higher-order FRFs requires the knowledge of the first-order Volterra kernel, which corresponds to the conventional FRF. Having computed the

parameters ω_n and ζ, the first-order Volterra kernel is estimated:

$$\mathcal{H}_1(\omega) = \frac{1}{-\omega^2 + j2\omega\zeta\omega_n + \omega_n^2}. \tag{92}$$

- *Step 3. Nonlinear regime of motion:*

This step covers the calibration of nonlinear parameters based on the higher-order FRFs for hysteretic systems. It is introduced through the following sub-steps: *3.1. Harmonic filtering*, *3.2. Third-order kernel computation*, and *3.3. Updating parameters*. However, before proceeding, the important characteristics of the framework involving the higher-order FRFs are addressed.

For conditions where the hysteresis loop is almost closed $(y_0 \approx 0)$, the coefficients related to the opening and closening of the loop are null, i. e. $\lambda_0 = \lambda_2 = 0$, whereas the remaining terms result in:

$$\lambda_1 = \alpha, \tag{93}$$

$$\lambda_3 = \frac{16\alpha\delta^2}{96} - \frac{35\alpha\delta}{96Y}. \tag{94}$$

These equations attend the characteristics of the Bouc-Wen model since they are not a function of the parameter γ, which is responsible for the opening and closening of the hysteresis loop. Thus, under the condition $(y_0 \approx 0)$, the equivalent nonlinear system is rewritten as:

$$\ddot{y}(t) + 2\zeta\omega_n\dot{y}(t) + (\tilde{k} + \alpha)y(t) + \lambda_3 y^3(t) = \tilde{u}(t). \tag{95}$$

Since the nonlinear system in equation (95) has terms up to the cubic order, it is used $\eta = 3$ contributions to compute the higher-order FRFs (LIN; NG, 2018; TELOLI; SILVA, 2019; VILLANI *et al.*, 2020). Thus, applying the harmonic probing method to map the three-dimensional kernel in frequencies ω_1, ω_2 and ω_3, the derived higher-order FRF yields:

$$\mathcal{H}_3(\omega_1, \omega_2, \omega_3) = -\mathcal{H}_1(\omega_1)\mathcal{H}_1(\omega_2)\mathcal{H}_1(\omega_3)\mathcal{H}_1(\omega_1 + \omega_2 + \omega_3)\lambda_3. \tag{96}$$

An alternative way to simplify the algebraic complexity of the higher-order FRFs

consists of analyzing only their leading diagonal by letting $\omega_1 = \omega_2 = \cdots = \omega_\eta = \omega$. The leading diagonals encode the main characteristics of the kernels, such as the sub-harmonic resonances and, additionally, the use of this formulation is suitable for calculating response outputs or even estimating nonlinear parameters (LIN; NG, 2018). Thus, the leading diagonal of the third-order Volterra kernel in Eq. (96) is given by:

$$\begin{aligned} &\mathcal{H}_3(\omega,\omega,\omega) = -\mathcal{H}_1(\omega)\mathcal{H}_1(\omega)\mathcal{H}_1(\omega)\mathcal{H}_1(\omega+\omega+\omega)\lambda_3, \\ &\quad \Leftrightarrow \mathcal{H}_3(\omega,\omega,\omega) \equiv \mathcal{H}_3(\omega) = -\mathcal{H}_1^3(\omega)\mathcal{H}_1(3\omega)\lambda_3, \end{aligned} \tag{97}$$

where the dependence of the kernel $\mathcal{H}_3(\omega,\omega,\omega)$ on the first-order kernel $\mathcal{H}_1(\omega)$ highlights that the previous step is essential to the advance of the identification procedure. Nevertheless, the kernel expression in (97) indicates the presence of sub-harmonic in the third-order kernel at frequency 3ω. Furthermore, to simplify excessive mathematical notation bearing in mind that the kernel in Eq. (97) depends only on the frequency component ω, it is considered the equivalent notation $\mathcal{H}_3(\omega,\omega,\omega) \equiv \mathcal{H}_3(\omega)$.

– *Step 3.1. Harmonic filtering:*

Considering a harmonic excitation of frequency ω, the response output of the equivalent nonlinear system from Eq. 48 can be written through the Volterra series representation using $\eta = 3$ contributions (CHATTERJEE; VYAS, 2003):

$$y(t) = |Y(\omega)|\cos(\omega t + \phi_1) + |Y(3\omega)|\cos(3\omega t + \phi_3), \tag{98}$$

where $|Y(\omega)|$ and $|Y(3\omega)|$ are the amplitudes related to the first and third-order harmonic amplitudes, respectively, whereas the respective phases are given by $\phi_1 = \angle Y(\omega)$ and $\phi_3 = \angle Y(3\omega)$. The harmonic amplitudes can be filtered out from the total experimental response using, for instance, the Fourier filtering.

– *Step 3.2. Third-order kernel computation:*

By truncating the higher-order components at the third-order harmonic amplitude, the kernel $\hat{\mathcal{H}}_3^{\text{exp}}(\omega)$ is estimated by (CHATTERJEE; VYAS, 2003):

$$\hat{\mathcal{H}}_3^{\text{exp}}(\omega) \approx \frac{4Y(3\omega)}{\tilde{A}^3}, \tag{99}$$

For experimental measuring of the kernel $\hat{\mathcal{H}}_3^{\text{exp}}(\omega)$ following the assumption that $y_0 \approx 0$, it is necessary to select correctly a frequency range where the harmonic amplitude

is distinctly measurable. Based on the methodology proposed by Chatterjee and Vyas (2003) (CHATTERJEE; VYAS, 2003), which developed an iterative estimation procedure through the higher-order FRFs, the third-order harmonic component should be measured around a set of frequencies close to the sub-harmonic component $3\omega = \omega_n$, i. e., $\omega = \frac{\omega_n}{3}$, where the harmonic $Y(3\omega)$ is the most prominent.

Jointed structures carry the amplitude-dependent nonlinearity, having a significant evolution of the frictional dissipation in the vicinity of resonance frequencies, where the structure experiences the highest response amplitudes. Since the amplitude response around the sub-harmonic $\omega = \frac{\omega_n}{3}$ assumes smaller values in comparison with the amplitude in the vicinity of ω_n, the assumption of considering the hysteresis almost closed $y_0 \approx 0$ is an adequate approximation. The results in section 4.3.2 exemplify the harmonic amplitudes measured experimentally.

– *Step 3.3. Updating parameters:*

The updating of parameters α and δ is carried out considering the experimentally measured kernel $\hat{\mathcal{H}}_3^{\text{exp}}(\omega)$:

$$\hat{\mathcal{H}}_3^{\text{exp}}(\omega) = -\mathcal{H}_1^3(\omega)\mathcal{H}_1(3\omega)\underbrace{\left(\frac{16\alpha\delta^2}{96} - \frac{35\alpha\delta}{96Y}\right)}_{=\lambda_3}, \tag{100}$$

where the Bayesian inference strategy, which is addressed in section 4.2, updates the estimative of such parameters.

The advantage of using the Volterra series at this identification step lies in the possibility of visualizing, with physical meaning, the influence of the nonlinear parameters on the system output through the Volterra contributions. Additionally, the propagation of uncertainties through the analytical formulation of the third-order kernel reduces the computational effort for the Bayesian identification.

- *Step 4.* Model Verification:

This step conducts the updating, verification, and validation of the nonlinear model. The fourth step of the proposed strategy aims to identify the last parameter, γ, which controls the opening of the hysteresis loop when the jointed structure operates under a nonlinear regime of motion. Since this is the parameter that remains to be identified, it is estimated through the calibration of the integrated numerical output of the proposed

Bouc-Wen model in terms of the experimental output of the jointed structure. Finally, the model verification is performed by comparing the response of the identified model with experimental measurements, whereas the validation occurs comparing the experimental hysteresis loop with the estimated one.

4.2 BAYESIAN INFERENCE STRATEGY

We employ the Bayesian framework to infer information about the system parameters. In this framework, prior knowledge is updated with experimental data, statistical envelopes can be obtained for the identified parameters and the model response, and it is possible to compute correlation among the variables. The procedure considers that: (1) the parameters to be identified are modeled as random variables $\boldsymbol{\theta} \in \mathbb{R}^N$, and the system observations are also random $\mathscr{D}$; (2) a prior probability density function is assigned to the random vector (composed of random variables), and a likelihood function is obtained from some hypotheses of the process; (3) the solution lies in updating the prior density function based on a set of data observations $\mathscr{D}$ from the system or structure in interest, which converts an *a priori* density function into *a posteriori* one $\pi(\boldsymbol{\theta}|\mathscr{D})$ (GREEN; WORDEN, 2015; CASTELLO; RITTO, 2016).

In this sense, having $\mathscr{D}$ and $\boldsymbol{\theta}$ as random variables, the posterior density function is given based on the Bayes' theorem:

$$\pi(\boldsymbol{\theta}|\mathscr{D}) = \frac{\pi(\mathscr{D}|\boldsymbol{\theta})\pi(\boldsymbol{\theta})}{\pi(\mathscr{D})}, \tag{101}$$

where $\pi(\boldsymbol{\theta}|\mathscr{D})$ is the updated posterior probability density function given the system observations $\mathscr{D}$, $\pi(\mathscr{D}|\boldsymbol{\theta})$ is the likelihood function, $\pi(\boldsymbol{\theta})$ is the prior probability density function containing evidences for candidate model parameters, whereas $\pi(\mathscr{D})$ is a normalizing constant that ensures $\pi(\boldsymbol{\theta}|\mathscr{D})$ is a probability density function with integral equal to unity. It is noteworthy that, if a Uniform prior probability density function $\pi(\boldsymbol{\theta})$ is chosen, the posterior probability density function is proportional to the likelihood function, such that $\pi(\boldsymbol{\theta}|\mathscr{D}) \propto \pi(\mathscr{D}|\boldsymbol{\theta})$.

Assuming that the fluctuations in the system response are related to the measurement process, the measurement data $\mathscr{D}$ are described as:

$$\mathscr{D} = \mathscr{D}^{\mathcal{M}}(\boldsymbol{\theta}) + \boldsymbol{\varepsilon}, \tag{102}$$

where $\mathscr{D}^{\mathcal{M}}(\boldsymbol{\theta})$ corresponds to model $\mathcal{M}$ predictions, given a set of parameters $\boldsymbol{\theta}$, and $\boldsymbol{\varepsilon} \sim \mathcal{N}(\mathbf{0}, I\sigma_{\varepsilon}^2)$ is a random noise vector $\boldsymbol{\varepsilon} \in \mathbb{R}^N$ with covariance $I\sigma_{\varepsilon}^2$, where I is the identity matrix, i.e., we are assuming and additive decorrelated Gaussian noise. Based on equation (102), the analytical expression of the likelihood function yields:

$$\pi(\mathscr{D}|\boldsymbol{\theta}) \propto \exp\left(-\frac{1}{2}\frac{(\mathscr{D} - \mathscr{D}^{\mathcal{M}}(\boldsymbol{\theta}))^T (\mathscr{D} - \mathscr{D}^{\mathcal{M}}(\boldsymbol{\theta}))}{\sigma_{\varepsilon}^2}\right), \tag{103}$$

and a common point estimate θ^* is the *maximum a posteriori probability* (MAP):

$$\theta^* = arg\max_{\theta \in \mathcal{K}} \pi(\theta^*|\mathscr{D}), \tag{104}$$

where $\mathcal{K}$ denotes the domain constrained by the uniform prior distribution $\pi(\theta)$, i.e., $\mathcal{K} = [(1-\Delta)\theta^*, (1+\Delta)\theta^*] \equiv [\boldsymbol{\theta}_{\min}, \boldsymbol{\theta}_{\max}]$.

Toward this background, the parameters $\theta^* = \{\zeta, k, \alpha, \delta, \gamma\}^T$ for modelling the jointed structure are set as the random variables with an Uniform prior probability density function; $\mathscr{D}$ consists of experimental measurements acquired from the jointed structure at *Step 1.*; *Step 2.* provides an initial estimate for ω_n and ζ; $\mathscr{D}^{\mathcal{M}}(\boldsymbol{\theta})$ is given according to *Steps 3.* and *4.* respectively, which results in the following likelihood expressions:

$$\pi(\mathscr{D}|\{\zeta, \alpha, \delta\}^T) \propto \exp\left(\frac{-\left\|\mathcal{H}_3(\{\zeta, \alpha, \delta\}^T; \omega) - \hat{\mathcal{H}}_3^{\exp}(\omega)\right\|^2}{2\sigma^2}\right), \tag{105}$$

$$\pi(\mathscr{D}|\gamma) \propto \exp\left(\frac{-\left\|y(\gamma; t) - \hat{y}^{\exp}(t)\right\|^2}{2\sigma^2}\right), \tag{106}$$

where $\mathcal{H}_3(\{\zeta, \alpha, \delta\}^T; \omega)$ and $y(\gamma; t)$ are the leading diagonal of third-order kernel and the output response, respectively, both predicted through the computational model, whereas $\hat{\mathcal{H}}_3^{\exp}(\omega)$ and $\hat{y}^{\exp}(t)$ are experimental measurements. Once the prior density function is Uniform, and we are assuming an additive Gaussian noise, the MAP (104) produce the

same value as the least squares estimate.

Although the Bayesian paradigm has a solid theoretical basis for evaluating the likelihood function, it does not specify by itself methods for obtaining the posterior efficiently, primarily when the model is defined by a combination of parameters with different distributions sampled simultaneously. Due to this fact, there is an auxiliary algorithm in the literature from the family of Monte Carlo methods that are useful to avoid high-dimensional integration, the so-called Markov Chain Monte Carlo (MCMC)/Metropolis-Hastings (GAMERMAN; LOPES, 2006; ROBERT; CASELLA, 2010), which is used to generate samples. The random variables $\boldsymbol{\theta}$ are limited to the interval $[\boldsymbol{\theta}_{\min}, \boldsymbol{\theta}_{\max}]$, whose current state is symmetrically normalized as $\boldsymbol{\theta}' = (1-\mathbb{X})\boldsymbol{\theta}_{\min} + \mathbb{X}\boldsymbol{\theta}_{\max}$, and $\mathbb{X}$ is a random variable $\in [0,1]$. The MCMC/Metropolis Hastings is illustrated in the following:

Algorithm 1: MCMC/Metropolis-Hastings for parameter identification.

Set the counter $i = 1$;
Set a first candidate $\mathbb{X}_{\mathbf{0}} = \{0.5, 0.5, \ldots, 0.5\}^{\mathrm{T}}$;
Define σ_p, Δ and n_s ;
while $i < n_s$ **do**
    Generate a candidate $\mathbb{Y} \sim \mathcal{N}(\mathbb{X}_{\boldsymbol{i-1}}, \sigma_s)$;
    Interpolate the value $\boldsymbol{\theta} = \mathbb{Y}(1+\Delta)\theta^* + (1-\mathbb{Y})(1-\Delta)\theta^*$;
    Interpolate the value $\boldsymbol{\theta}'_{\mathbb{X}_{\boldsymbol{i-1}}} = \mathbb{X}_{\boldsymbol{i-1}}(1+\Delta)\theta^* + (1-\mathbb{X}_{\boldsymbol{i-1}})(1-\Delta)\theta^*$;
    Generate $\mathcal{C} \sim \mathcal{U}(0,1)$;
    if $\mathcal{C} \leq \mathcal{L}\{\boldsymbol{\theta}\}/\mathcal{L}\left\{\boldsymbol{\theta}'_{\mathbb{X}_{\boldsymbol{i-1}}}\right\}$ **then**
        Accept candidate $\mathbb{X}_{\boldsymbol{i}} = \mathbb{Y}$;
    else
        Reject candidate $\mathbb{X}_{\boldsymbol{i}} = \mathbb{X}_{\boldsymbol{i-1}}$;
    Set $i = i + 1$;

From the Algorithm 1, $\mathbb{X}_{\mathbf{0}} \in \mathbb{R}^N$ is the first candidate centered at the prior distribution, $\mathbb{X} \in \mathbb{R}^{n_s \times n}$ is the matrix that contains the n_s sets of n parameters accepted by the algorithm to compose the posterior distributions. The operator $\mathcal{L}(\bullet)$ evaluates the likelihood function, equations (105)-(106) in this work for the set $\boldsymbol{\theta}$, originated from the interpolation of the vector $\mathbb{Y}$, which each element belongs to the range $[0,1]$, between the boundaries of the domain $\mathcal{K}$. Only 90% of the Monte Carlo simulations n_s are considered in the final stationary Markov chain (burn-in of 10%), and the value of the random walk step σ_p is chosen such that the acceptance rate is about 50%.

Finally, Figure 38 summarizes the strategy proposed along the section, depicting each

step into a flowchart representation.

Figure 38 – Flowchart of the estimation procedure. *Step (1)* provides experimental measurements for each next step. *Step (2)* computes values for ω_n and ζ and provides prior knowledge about them; in *Step (3)*, after computing the experimental third-order kernel, the PDFs of $\{\zeta, \alpha, \delta\}^T$ are updated, including the PDF $\pi(\zeta)$ because of the uncertainty regarding experimental visualizations on the parameter, whereas ω_n is held at the mean value; estimated MAP of $\{\zeta, \alpha, \delta, \omega_n\}^T$ are used to construct the computational model in *Step (4)* and update $\pi(\gamma)$, then to evaluate and to validate the constructed model.

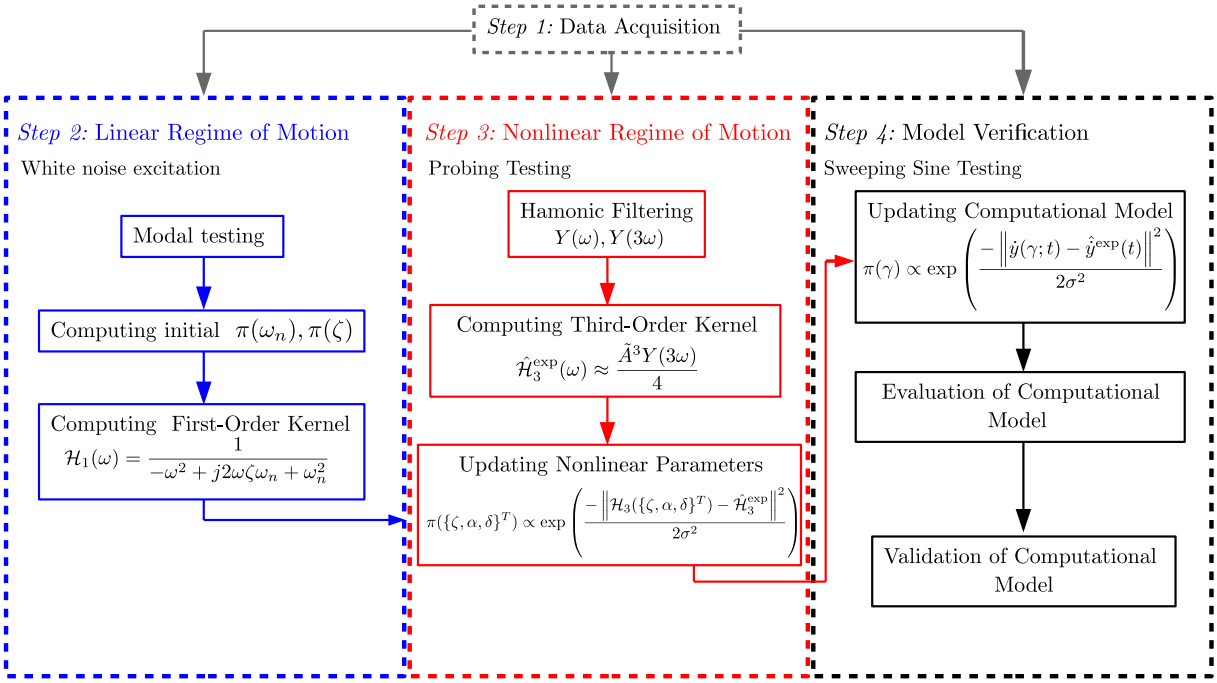

Source: Teloli *et al.* (2021).

4.3 EXPERIMENTAL APPLICATION

4.3.1 Experimental setup

The identification problem tackled may be stated as follows: the experimental test rig is nonlinearly dependent on excitation amplitude, presenting the well-known softening effect of friction joints. The structure presents data variation related to the presence of uncertainties in the measurement process. The experimental measurements were conducted through different days, and only the tightening torque in the joint connection was controlled after each experimental realization. Once the general aspects of the identification problem have been discussed, this subsection focus on describing the experimental setup.

Figure 39 presents the jointed structure investigated. The test rig is formed of two aluminum beams, each one with dimensions of $270 \times 25.4 \times 6.35$ mm and assembled by a bolted-joint connection with a tightening torque of 5 Nm. The joint is connected by two M6 bolts. The excitation of the structure was conducted by a Modal Shop 2400E shaker located at 85 mm from the clamped end of the cantilever beam to minimize shaker-structure interaction (PEETERS; KERSCHEN; GOLINVAL, 2011b). It is worth noting that although a clamped condition is assumed in the region near to the shaker, no additional experimental measurements have been performed to verify this assumption. For the clamp, two M6 bolts were used. The alignment of the structure was checked with respect to its axis parallel to the ground.

Figure 39 – Experimental setup and the schematic representation illustrating the cantilever beam which carries a bolted joint connection.

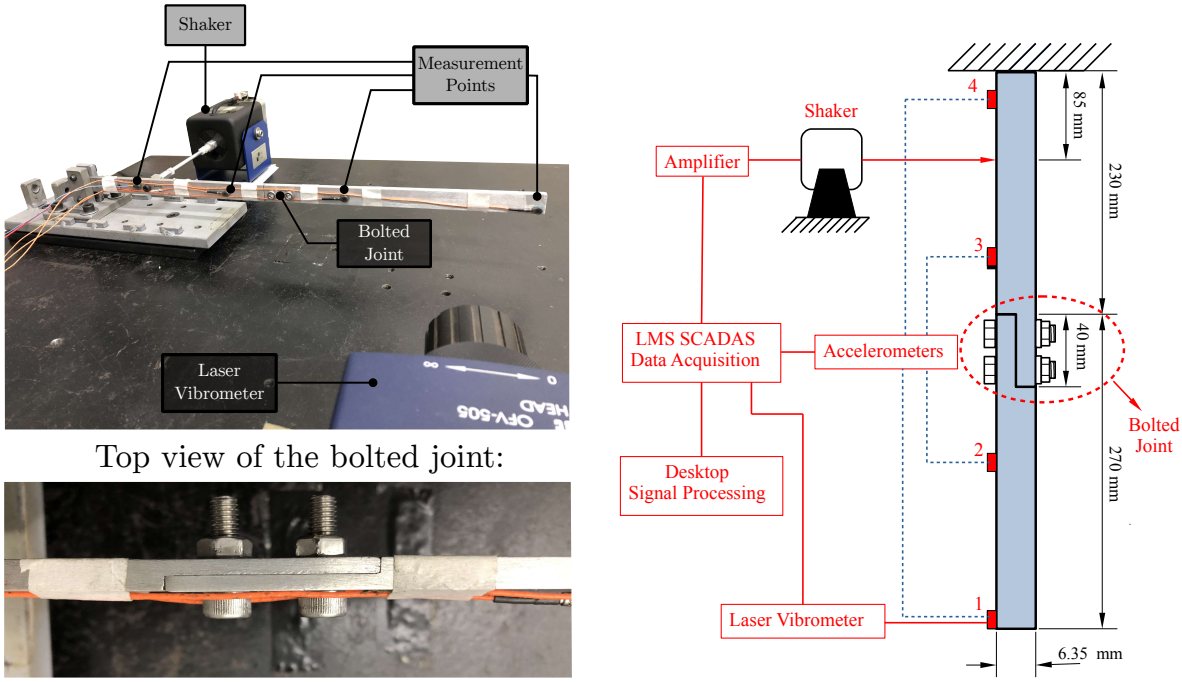

(a) Experimental setup (b) Schematic top view of the experimental setup.

Source: Teloli *et al.* (2021).

Due to observability purposes for modeling the first vibrating mode of the structure, the system output was measured at the beam's free end, using a laser vibrometer Polytec®OFV-525/5000S. The data acquisition system was the LMS SCADAS. The structure was excited using different levels of input amplitude 0.05 V (low), 0.10 V (medium) and 0.20 V (high). This paper regards the voltage supplied by the shaker amplifier as the excitation signal since it is easier to keep this signal constant over a frequency range. The same strategy was used in Villani *et al.* (2019). All signals were

measured with a sampling frequency of 1024 Hz.

Figure 40(a) illustrates the receptance calculated during a sweeping sine test from 0 to 40 Hz (around the first mode), collected with 16384 samples and burst of 50%, regarding different input levels supplied in the shaker amplifier. On the receptance, it is worthy of remark that the FRF starts to exhibit distortions and shifts in the resonant peak as the input force level increases. Further, Figure 40(b) depicts a zoom on the frequency response curve for a stepped sine test from 3 up to 23 Hz, which indicates that the resonant frequency decreases when the forcing amplitude increases, revealing the bolted joint softening operation. For capturing this nonlinear behavior, the Bouc-Wen model parameters must accomplish the condition $0 < \gamma \leqslant \delta$.

Figure 40 – Frequency response plots for different excitation amplitudes: —— for low amplitude level (0.05 V), △ for medium amplitude level (0.10 V), and ∘ for high amplitude level (0.20 V).

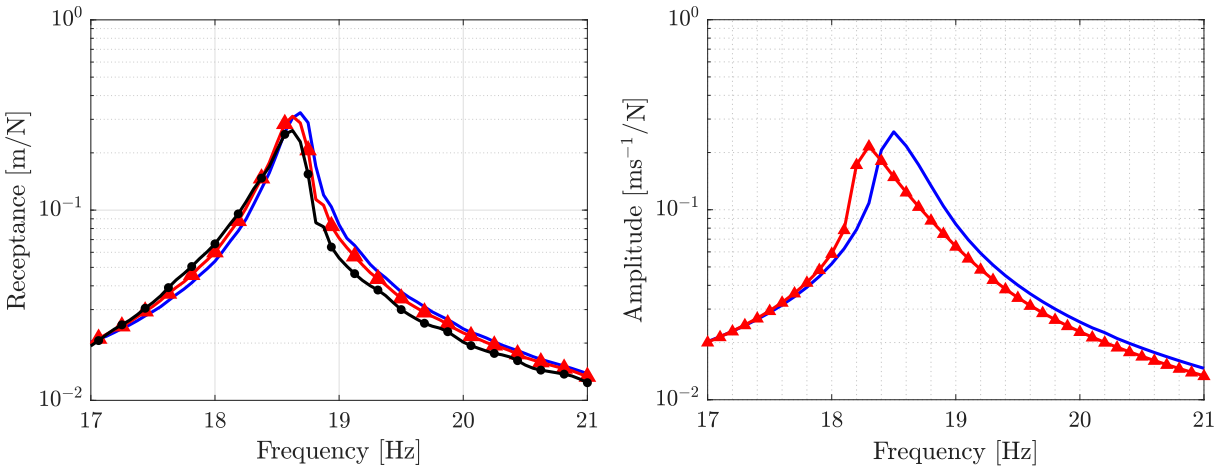

(a) Magnitude plot of the receptance.

(b) Experimental frequency response curve for a stepped sine test.

Source: Teloli *et al.* (2021).

Figure 41 exemplifies the data fluctuation considering several experimental measurements with 99% of statistical confidence bands. This figure demonstrates that even with a small confidence band variation, it is necessary to create a stochastic model to encode the observed variations in experimental realizations. It should be stressed that the Fig. 41(b) corresponds to the same excitation conditions from the receptance plot in Fig. 40(a) denoted by the circ marker ∘.

Figure 41 – Variation of the Frequency Response Function calculated for different excitation amplitudes with 99% of confidence bands. ▓ represents the confidence bands, whereas — is the mean values.

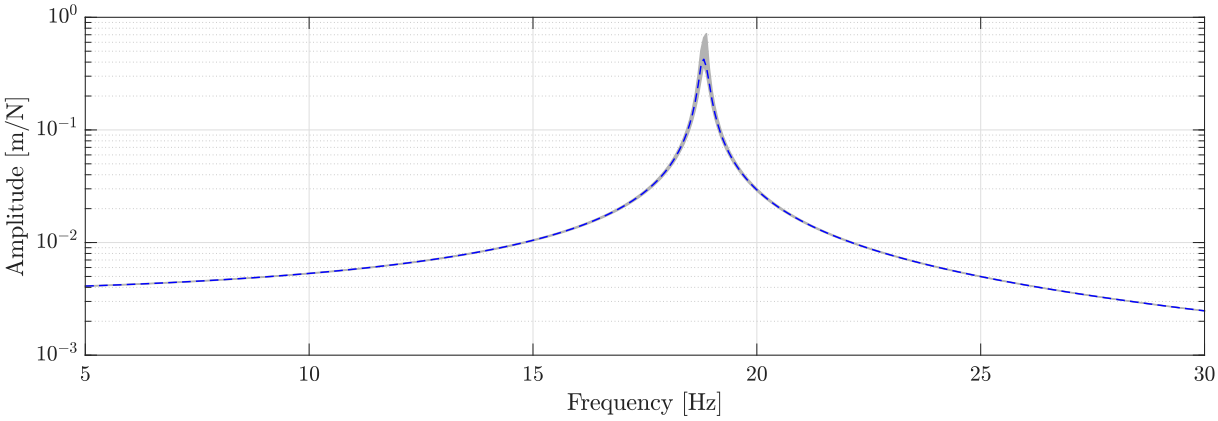

(a) Low level of excitation amplitude (0.05 V).

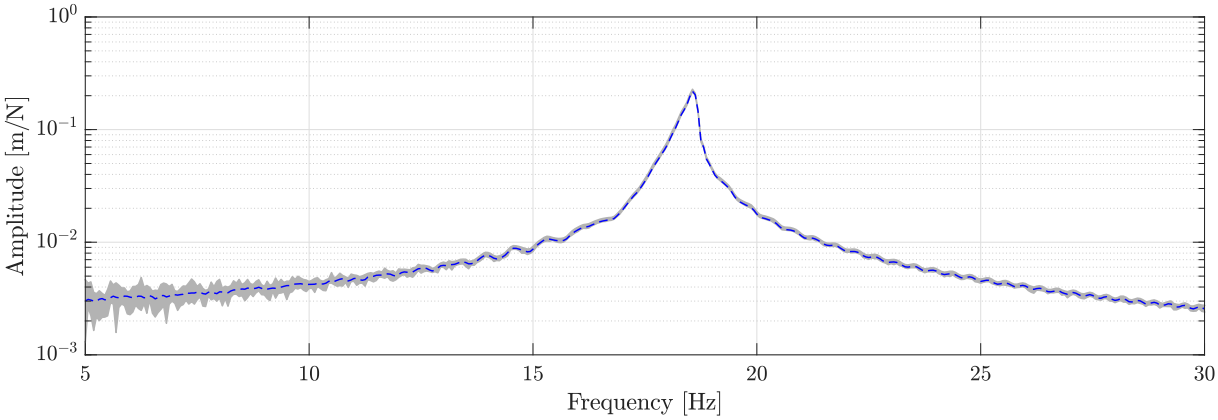

(b) High level of excitation amplitude (0.20 V).

Source: Teloli *et al.* (2021).

4.3.2 Identification of the stochastic Bouc-Wen model

Based on the identification steps in Fig. 38, this subsection is presented as follows:

- *Step 2. Linear regime of motion:*

Figure 41(a) represents the FRF obtained experimentally used for extracting the system modal parameters considering a white noise as input signal with low excitation amplitude (0.05 V). Under this operating condition, the system behaves linearly. The mean values were μ_{ω_n} = 18.80 Hz and μ_ζ = 0.39%, whereas the coefficient of variation (CV), defined as standard deviation over the mean of the random variables, is 0.176% and 24.75%, respectively, implying that the uncertainty on the damping ratio is more

significant than in the resonance frequency. Therefore, in this scenario, the resonance frequency will be held at the mean value of 18.80 Hz for the next identification step, whereas the posterior probability density function of ζ will be computed through the Metropolis-Hastings algorithm.

- *Step 3. Nonlinear regime of motion:*

For the identification *Step 3.1.*, Figure 42 exemplifies a set of harmonic amplitudes extracted from the structure response around the sub-harmonic $\omega_n/3$ using Fourier filter. Note that around the selected frequencies of $[5, 5.5, 6, 6.5, 6.75]$ Hz, considering a probing input with an amplitude level of 0.15 V to compute the leading diagonal of the third-order Volterra, the harmonic component $Y(3\omega)$ is prominent and measurable. The probing signals were collected with 65536 samples to ensure that the harmonic components are extracted during the steady-state condition. As summarized in *Step 3.2.*, the third-order harmonics are considered for computing the experimental third-order kernel.

Figure 42 – Harmonic Amplitude filtered from the system output. $\triangle$ for $Y(3\omega)$ and $*$ represents the $Y(\omega)$ amplitude.

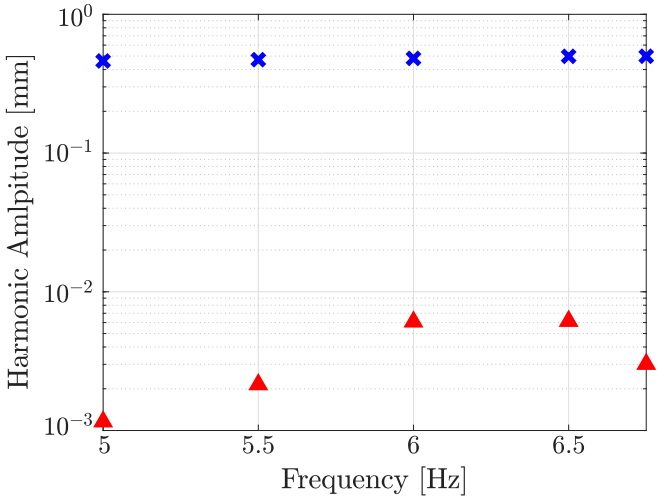

Source: Teloli *et al.* (2021).

For updating the random variables $\boldsymbol{\theta} = \{\zeta, \alpha, \delta\}^T$ in *Step 3.3.*, the prior PDF is set to Uniform assuming as limits $\boldsymbol{\theta}_{\min} = \{0.352\%, 424.31, 272.80\}^T$ and $\boldsymbol{\theta}_{\max} = \{0.528\%, 589.61, 409.92\}^T$, and then the updated PDF is computed simulating a Markov Chain. In addition, it is important to point out that the prior PDF to ζ is set Uniform such that the previous results identified from *Step 2.* do not bias the updating at this step. The interval for each parameter was based on initial results considering the sequential

quadratic programming (SQP) algorithm (GILL; WONG,) as an optimization procedure for minimizing the objective function:

$$\min J(\{\zeta, \alpha, \delta\}^T) = \left\| \mathcal{H}_3(\{\zeta, \alpha, \delta\}^T; \omega) - \hat{\mathcal{H}}_3^{\exp}(\omega) \right\|^2, \tag{107}$$

subject to:

$$\begin{aligned} 0 < \alpha \leqslant \omega_n^2 \ \text{ and } \ \alpha + k = \omega_n^2, \\ 0 < \delta \leqslant 500. \end{aligned} \tag{108}$$

For estimating the Markov Chain, it was assumed $\sigma = 6.8092 \times 10^{-9}$, which is calculated based on the covariance matrix of 8 experimental measurements collected at each selected frequency, and $\sigma_p = 2.5108 \times 10^{-3}$ such that the acceptance rate of the chain was $\sim 50\%$. The statistics of the parameters were estimated considering Monte Carlo simulations with 850 samplings. The convergence concerning the number of samplings was estimated considering a function which depends on the leading diagonal of the Volterra kernel:

$$conv(n_s) = \frac{1}{n_s} \sum_{i=1}^{n_s} \int_B \left\| \mathcal{H}_3^i(\omega) \right\|^2 d\omega, \tag{109}$$

where $\mathcal{H}_3^i$ corresponds to the i^{th} calculated realization of the Volterra kernel in the Markov Chain, and B is the integration domain. Figure 43 exhibits the convergence test performed.

Figures 44(a), 44(b) and 44(c) show the prior Uniform PDF of ζ, α and δ together with the updated (posterior) PDF, respectively. Special attention should be given to Figure 44(c), which shows that ζ has a completely different PDF than the first one estimated. Besides, it is interesting to note that both PDF of the damping ratio and the δ parameter exhibit bimodal behavior. The characteristic of these PDFs shows that the Bayesian inference paradigm is robust to the presence of multiple possible solutions for the Bouc-Wen model, in which a deterministic approach is not capable of dealing. Additionally, the prior PDF for each parameter starts with a CV $\sim 28\%$, whereas the CVs based on the posterior PDFs and given in Table 3 present lower values. Table 3 also shows that the MAP estimator is very close to the mean values for each parameter.

An alternative way to quantify how much information is lost concerning the prior

Figure 43 – Convergence test applied in the third-order Volterra kernel.

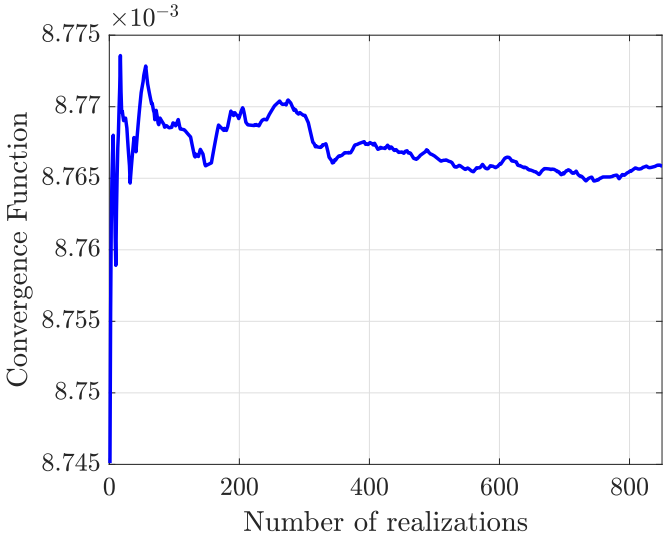

Source: Teloli *et al.* (2021).

Table 3 – MAP estimator, mean value μ and CV for each random variable.

Parameter	MAP estimator	μ	CV(%)
ζ	0.446%	0.444%	0.57
α	491.36 [N/mkg^{-1}]	497.40 [N/mkg^{-1}]	0.98
δ	341	340.21	0.98

Source: Teloli *et al.* (2021).

PDF is computing the Kullback-Leibler (KL) Divergence (HERSHEY; OLSEN, 2007). The KL divergence measures the similarity between two PDFs and is helpful to analyze which PDF provides a better representation of the experimental observations. For each posterior PDF at this step, the divergence values are around $D_{kl}(\text{posterior}||\text{prior}) \approx 0.36$, which indicates that for all cases, the posterior PDFs have added a considerable amount of information in comparison with the Uniform one.

Figure 45 depicts the leading diagonal of the calibrated third-order Volterra kernel with 99% of statistical bands, evidencing that the analytical kernel can capture the data variation in experimental measurements.

- *Step 4. Model verification:*

The *Step 4.* of the identification procedure starts estimating the γ parameter. At this stage, once the CVs of the parameters identified earlier are low ~ 1%, they were held fixed at their mean values $\{\zeta, \alpha, \delta\}^T = \{0.444\%, 497.40, 320.21\}^T$, just as the resonance frequency. Thus, the prior PDF is also set to Uniform assuming the interval $\gamma_{\min} = 17$

Figure 44 – PDF of the random variables $\boldsymbol{\theta} = \{\zeta, \alpha, \delta\}^T$. In (a), – – – represents the PDF estimated after modal analysis, whereas in (a), (b) and (c), - - - is the Uniform PDF and —— is the posterior one.

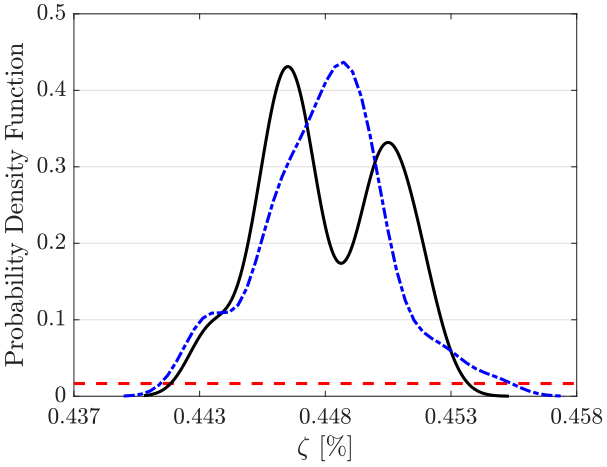

(a) PDF of the random variable ζ.

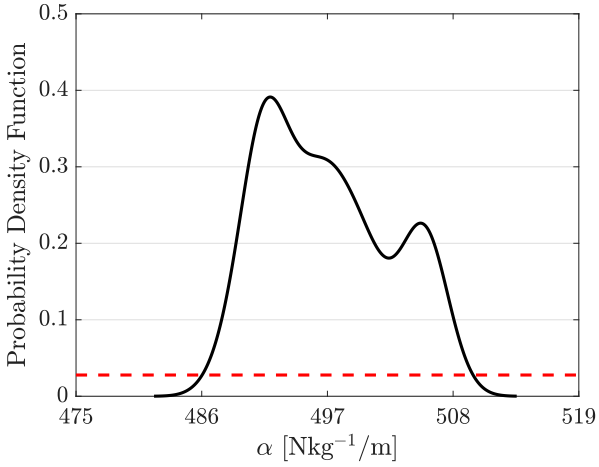

(b) PDF of the random variable α.

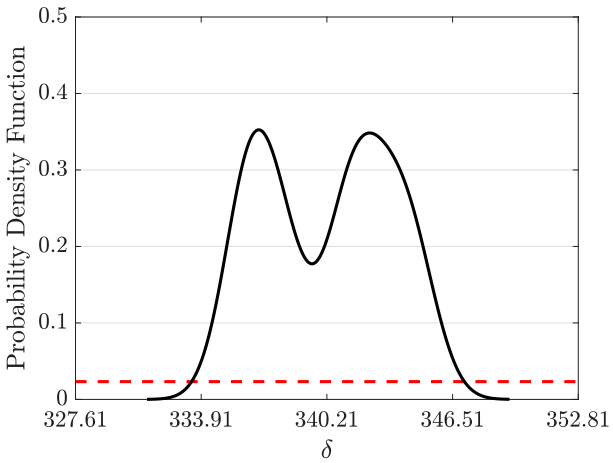

(c) PDF of the random variable δ.

Source: Teloli *et al.* (2021).

and $\gamma_{\max} = 41$ based on initial observations performed on the following objective function solved through the SQP algorithm:

$$\min J(\gamma) = \frac{\left\| \hat{\ddot{y}}^{\exp}(t) - \ddot{y}(\gamma; t) \right\|}{\left\| \hat{\ddot{y}}^{\exp}(t) - \text{mean}(\hat{\ddot{y}}^{\exp}(t)) \right\|}, \tag{110}$$

subject to:

$$0 < \gamma \leqslant \delta, \tag{111}$$

where $[y(\gamma; t) \;\; \dot{y}(\gamma; t) \;\; \ddot{y}(\gamma; t)]^T$ are obtained through a numerical integration scheme with

Figure 45 – Comparison between the leading diagonal of the third-order Volterra kernel estimated versus the experimental data. ■ represents the 99% model response confidence bands, — is the model response mean and • represents three experimental realizations.

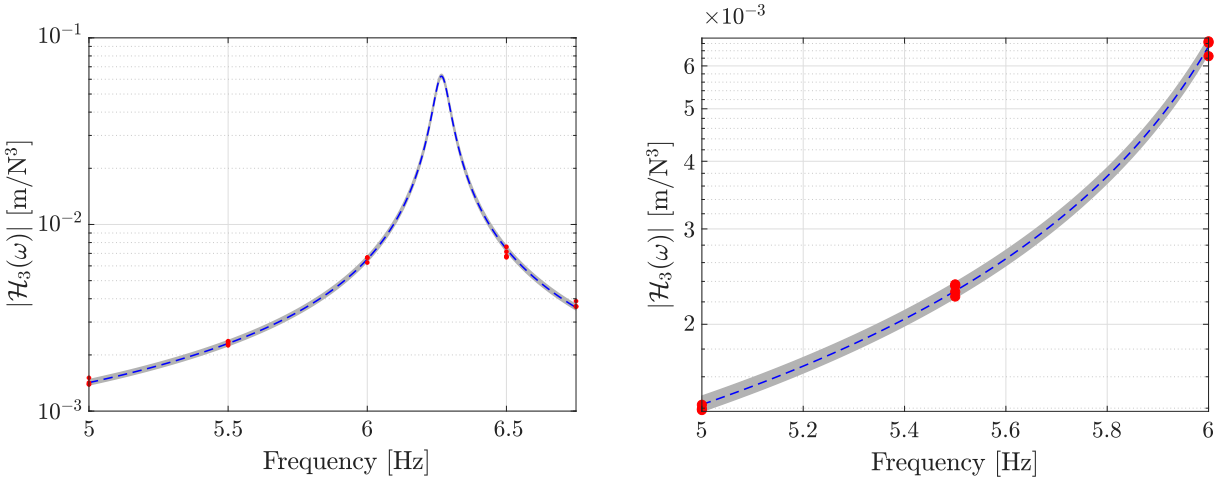

(a) Third-order Volterra kernel. (b) Zoom between 5 and 6 Hz.

Source: Teloli *et al.* (2021).

the 4$^{\text{th}}$order Runge-Kutta method and variable time-step, whereas the collected testing data (velocity vibration signal measured by the laser vibrometer Figure 39) $\hat{y}^{\text{exp}}(t)$ for this step is based on a sweeping sine test around the first vibrating mode, from 0 to 40 Hz, with an amplitude level of 0.20 V supplied in the shaker amplifier.

For estimating the posterior PDF of γ parameter, the Markov Chain was computed assuming $\sigma = 1.26{\times}10^3$, which is based on the covariance of 48 experimental measurements, and $\sigma_p = 0.025$, ensuring an acceptance rate also around 50%. Besides, the statistics of γ were also estimated considering Monte Carlo simulations with 850 samplings. For this step, the convergence was estimated based on equation (109) and the numerically integrated velocity of the Bouc-Wen model considering a high level of excitation amplitude.

Figure 46 presents a comparison between the prior and posterior PDFs of γ parameter. Similar to what happened in the previous step, the posterior PDF also enclosed a great amount of information around the mean, providing a mean value of $\mu_\gamma = 32.84$, whereas the MAP estimated $\gamma^* = 33.01$. The CV of the posterior PDF is greater than in previous cases, being 10.20% but lower than the CV of the prior PDF, which starts ~ 28%. Further, the KL divergence for the γ parameter is $D_{kl}(\text{posterior}||\text{prior}) = 1.236$, which means that in this specific case, the information lost by using the Uniform approximation is greater than in the other ones.

For evaluation of the stochastic Bouc-Wen model, Figure 47 presents a comparison

Figure 46 – PDF of the random variable γ. - - - represents the prior PDF, whereas —— is the posterior one.

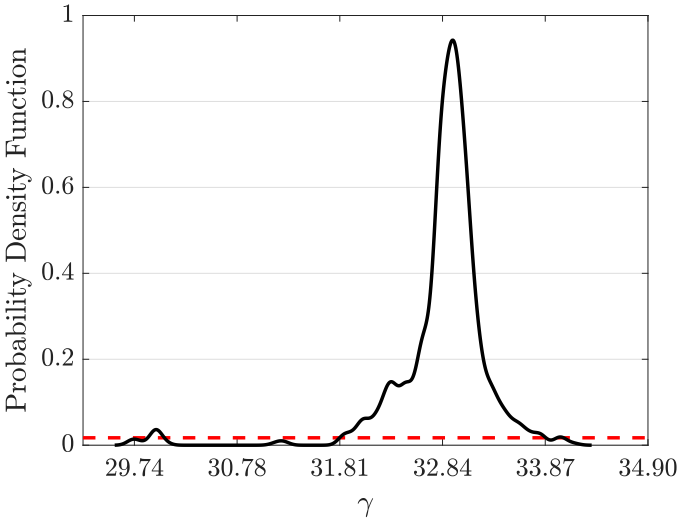

Source: Teloli *et al.* (2021).

Figure 47 – Comparison between the frequency response functions estimated from the numerical Bouc-Wen versus the experimental data around the first vibrating mode. ■ represents the 99% model response confidence bands, —— is the model response mean and • represents three experimental realizations.

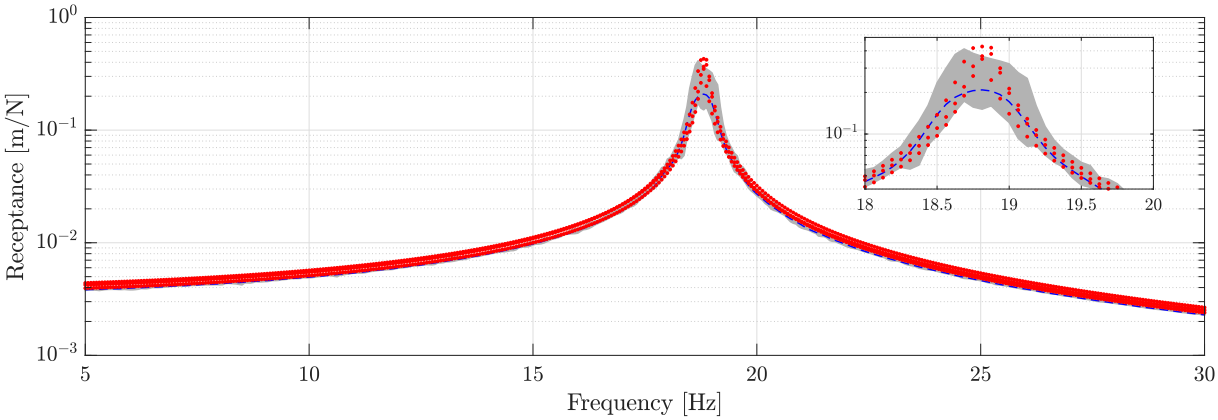

Source: Teloli *et al.* (2021).

between the FRF reproduced by the Bouc-Wen with 99% of statistical bands and three FRFs obtained experimentally considering white-noise excitation at the low amplitude level. As well as the experimental receptance, the computational one also presents more significant uncertainty related to the damping.

Figures 48 and 49 illustrate the predicted response of the numerical model with 99% of statistical confidence bands in comparison with experimental data for a sweeping sine test with low and high excitation amplitude, respectively. The narrow confidence bands feature the applied computational model, which represents well the experiment under

Figure 48 – Comparison between the frequency response functions estimated from the numerical Bouc-Wen model versus the experimental data around the first vibrating mode. ▩ represents the 99% model response confidence bands, — is the model response mean and • represents three experimental realizations.

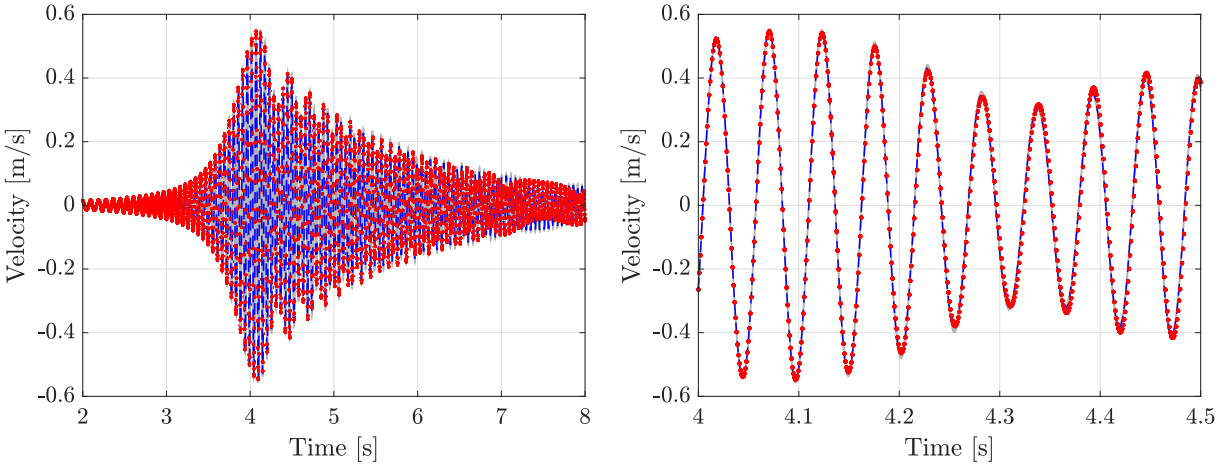

(a) Response output. (b) Response zoom between 4 and 4.5 seconds.

Source: Teloli *et al.* (2021).

Figure 49 – Verification and validation of the Bouc-Wen model for high excitation amplitude (0.20 V) considering a sweeping sine test. ▩ represents the 99% model response confidence bands, — is the model response mean and • represents three experimental realizations.

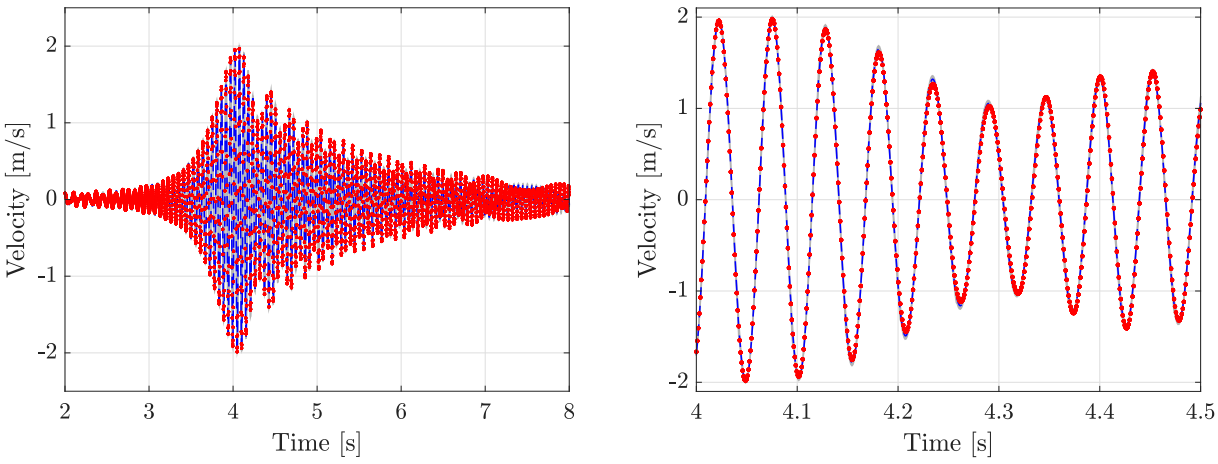

(a) Response output. (b) Response zoom between 4 and 4.5 seconds.

Source: Teloli *et al.* (2021).

analysis.

Finally, Figure 50 exhibits the measured and the predicted hysteresis loops for different amplitudes applied in the shaker. In all cases, both hysteretic cycles enclose substantially the same area on the restoring force *versus* displacement plane, producing an adequate prediction for the experimental tests. This figure evidences that the Bouc-Wen

model can accommodate enough accuracy of the experimental test bench. In addition, Figure 50(a) shows that for a maximum displacement of ~ 4.8 mm, the hysteresis loop is almost closed, which exemplifies that the assumption made during the *Step (3)* is reasonable, since the maximum displacement amplitude in Figure 42 is about ~ 0.8 mm.

Figure 50 – Comparison between the identified hysteresis loop through the Bouc-Wen versus experimental data for several excitation amplitudes. ▬ represents the 99% model response confidence bands, — is the model response mean and • represents three experimental realizations.

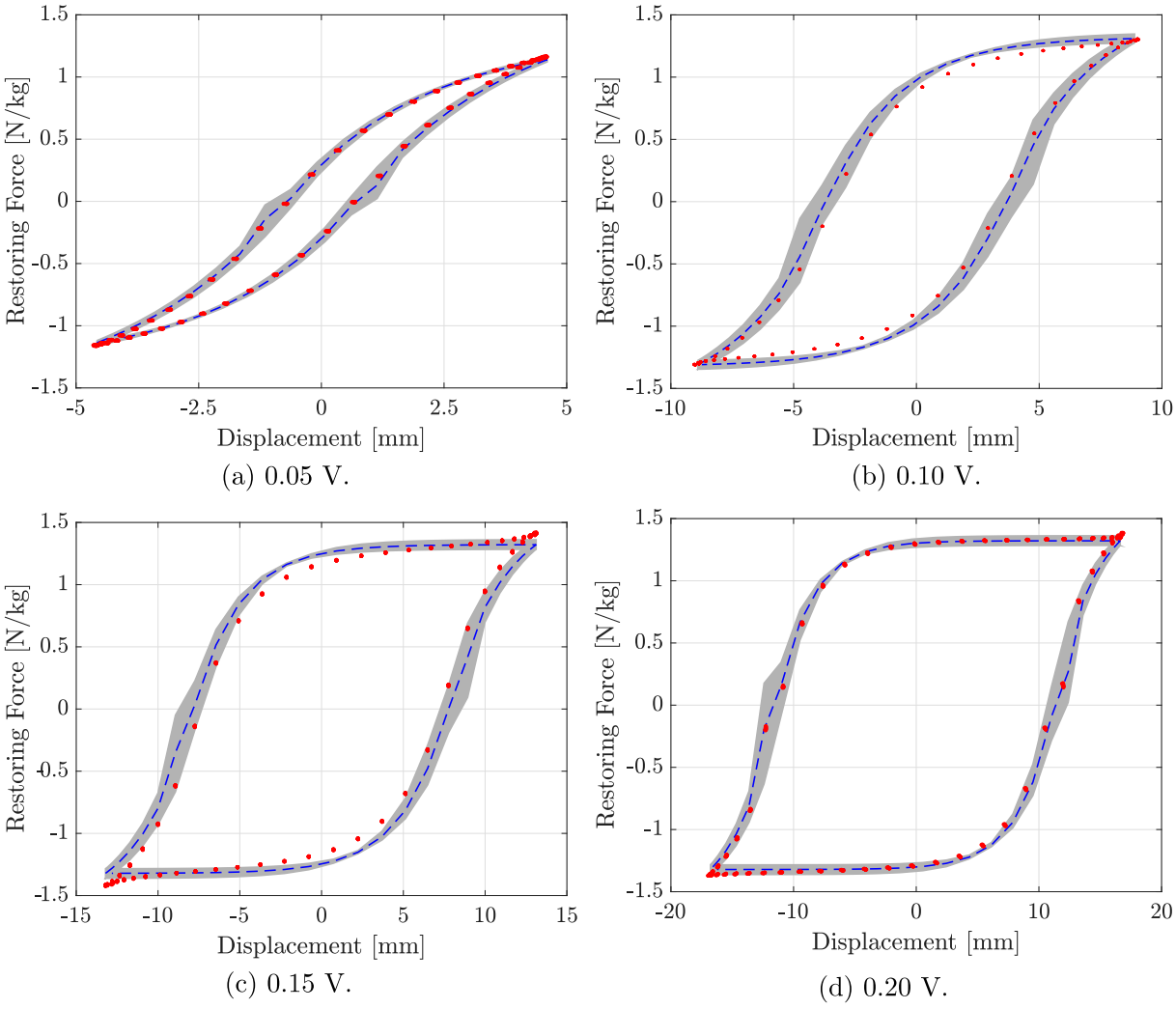

Source: Teloli *et al.* (2021).

4.4 CONCLUDING REMARKS

This Chapter proposes a procedure to identify structures that have jointed connections based on a four-step algorithm. The identification procedure was applied to an experimental setup under a nonlinear regime of motion due to the frictional contact between different structural components. This work considers the white-box modeling of a Bouc-Wen model to capture the jointed structure's dynamical behavior. A set of

preliminary experimental tests have shown fluctuations in the system response. Therefore, a Bayesian inference strategy for updating the model parameters was employed. The Bayesian strategy presented in this paper could be used directly to identify the complete Bouc-Wen model, just setting all parameters to update in *Step (4)*, which carries similar particularities to the Worden and Hensman (2012) work. However, the higher-order FRFs was fundamental for nonlinear parameter estimation, providing a clear physical meaning about the structure behavior and conducted with traditional experimental tests.

The results of the stochastic Bouc-Wen model indicate that the computational model can provide an adequate description of assembled structures by bolt connection. In an uncertain scenario, the model can reproduce the fluctuations related to the damping ratio, which were also visualized in the experimental FRF. The computational hysteretic loops carry a full confidence band around the displacement y_0, especially in Figure 50(a), where the hysteresis loop is almost closed. Despite this, it was possible to predict the output of the jointed structure cons with a good agreement during several excitation amplitudes.

Importantly, the approach adopted in this chapter adopts the use of linear damping in the proposed Bouc-Wen equivalent model, such that the evolution of the nonlinear dissipative characteristics of the BERT benchmark are captured through the hysteresis restoring force. Thus, due to approach adopted, the model becomes limited for excitation forces with values higher than those used during the model parameter calibration procedure. Thus, targeting industrial applications where nonlinear dissipation-related behaviors become more pronounced, the model needs to be modified to take this damping amplitude dependency into account. Notwithstanding, the identification framework, especially in *Step. 3*, needs to be modified to consider several excitation amplitudes while updating the damping parameter.

Finally, this work is a natural extension of the methodology developed by Teloli and da Silva (2019) (TELOLI; SILVA, 2019), exploring the advantages of using the Volterra series as an alternative tool to perform the nonlinear parametric estimation. Although the benchmark addressed here is a controlled experimental laboratory setup, and still far from complex industrial cases, this paper presents the use of both higher-order FRFs and the Bouc-Wen model as effective alternatives to deal with problems involving experimental bolted joints with data fluctuation, which is an original contribution to literature. In future work, additional experiments will be collected to test the identification procedure in an even more uncertain scenario involving different tightening torque conditions and assembly/disassembly of jointed structures. This is a challenging issue that includes

several variabilities on the response of the structure. Future works will also focus on using the Bouc-Wen parameters for modeling the contact interfaces in whole-joint element models of assembled structures. To accomplish this task, modifications on the hysteretic model are expected to accommodate the non-local memory effects present in frictional forces according to the pre-sliding and sliding regimes of motion.

The next Chapter introduces the Orion beam, with description of its nonlinear behavior and focus on the vibration mode that stresses the lap-joint most pronouncedly. In contrast to the BERT benchmark that was identified by considering a single torque condition applied to the bolts, the Orion beam discusses the influence that different values of the tightening torque have on its dynamic behavior.

5 EXPERIMENTAL TESTING OF DYNAMICALLY EXCITED JOINTED STRUCTURES

In the academic field, one of the main ways to evaluate the influence that bolted joints have on structural dynamics is through benchmark systems. In addition to providing experimental data to test modeling strategies, these systems also provide insights into loading conditions, experimental practices, dissipation mechanisms in standard joints, nonlinear effects from micro-scale interactions, and other aspects of analysis. In this context, the Chapter proposes the Orion beam benchmark, an assembly configuration in which connecting bolts play different structural functions. Contact patches have been added at each bolt connection to retain the contact between both beams in a small area, minimizing uncertainties on the structure's response and enhancing the repeatability between measurements. The central bolt is dedicated to ''static'' functions to ensure structural integrity and resist dynamic loads without substantial stiffness changes. The external bolts, in turn, perform ''damping'' functions to increase energy dissipation due to frictional contact, in which the torque preload can be set without changing the nominal frequency. Thus, the Orion beam presents the benefit of amplitude attenuation without significant losses in the contact stiffness, which paves the way for proposing new control techniques in jointed structures by combining vibration amplitude attenuation and bolt preload.

First, section 5.1 introduces the Orion beam's design, the experimental setup, and considerations regarding experimental measurements. Next, section 5.2 presents a complete description of the real-time feedback controller designed for this work to control the excitation force as frequency changes during step-sine tests to overcome limitations regarding amplitude control. Afterward, section 5.3 introduces the underlying linear structure, in which the frequency response functions of the beam are assessed considering the patches perfectly glued (monolithic state) and estimated after applying a low-amplitude white noise excitation. Under these experimental conditions, it is also

possible to evaluate the experimental setup, clamp conditions, the influence of the shaker-structure coupling, whether the bending modes are correctly isolated, among other aspects of the experiment. Next, section 5.4 presents the experimental results of the Orion beam around the vibrating mode most affected by the presence of nonlinearities, discussing the repeatability of measurements, influences of the tightening torque, and impact of several excitation amplitudes on the structure behavior based on a single-point measurement. Based on single-point measurements, a single-degree-of-freedom (SDoF) Duffing-Van der Pol oscillator is introduced in section 5.5 to fit the characteristics present in the frequency response curves of the lap-joint structure around the vibrating mode of interest. Finally, section 5.6 reports the final remarks, expected contributions of the Orion beam for the joint structures' community, and proposes the next steps for future work.

5.1 THE ORION BEAM

This section starts presenting the Orion beam's design to minimize the effects that the tightening torque has on contact stiffness and, at the same time, to maximize the damping effects due to friction dissipation. The experimental setup, experimental protocol, and vibration sense are also addressed.

The idea behind the new lap-joint configuration lies in highlighting the damping that results from friction effects, which are retained on the contact interface rather than stiffness changes. The lap-joint consists of two assembly duraluminium beams with dimensions of $200 \times 30 \times 2$ [mm] and connected by three M4 bolts spaced along a length 30 mm, as depicted in Fig. 51. A washer is placed under each screw and nut. There are contact patches at each bolt connection to retain the contact between both beams in a small area. These patches consist of a square of 12×12 mm with an extra thickness of 1 mm. To minimize residual stresses due to the manufacturing process, which may induce stress-stiffening alterations due to internal loads, the beams were manufactured using the electrical discharge machining (EDM) process, providing mechanical precision on the components without any distortions. The thinner design enhances the conformability of the jointed interface and provides more superior repeatability of the measurements if the experiment is appropriately controlled (see subsection 5.4.2). The Orion beam suggests an assembly configuration that associates bolts dedicated to ''static'' functions and those performing ''damping'' functions. This ensures a significant increase in the structural damping without degrading the structural stiffness.

Figure 51 – (a) Lap-joint 3D model CAD, which highlights the three contact patches, present only in one beam. (b) Patches beam picture. The central patch without friction marks because of the fully tightening, the external patch with friction marks because of the light tightening. (c) Lap-joint drawings CAD (lengths are in mm) - 2 beams, two clamp holes Ø4 mm, one excitation hole Ø5 mm, three contact patches.

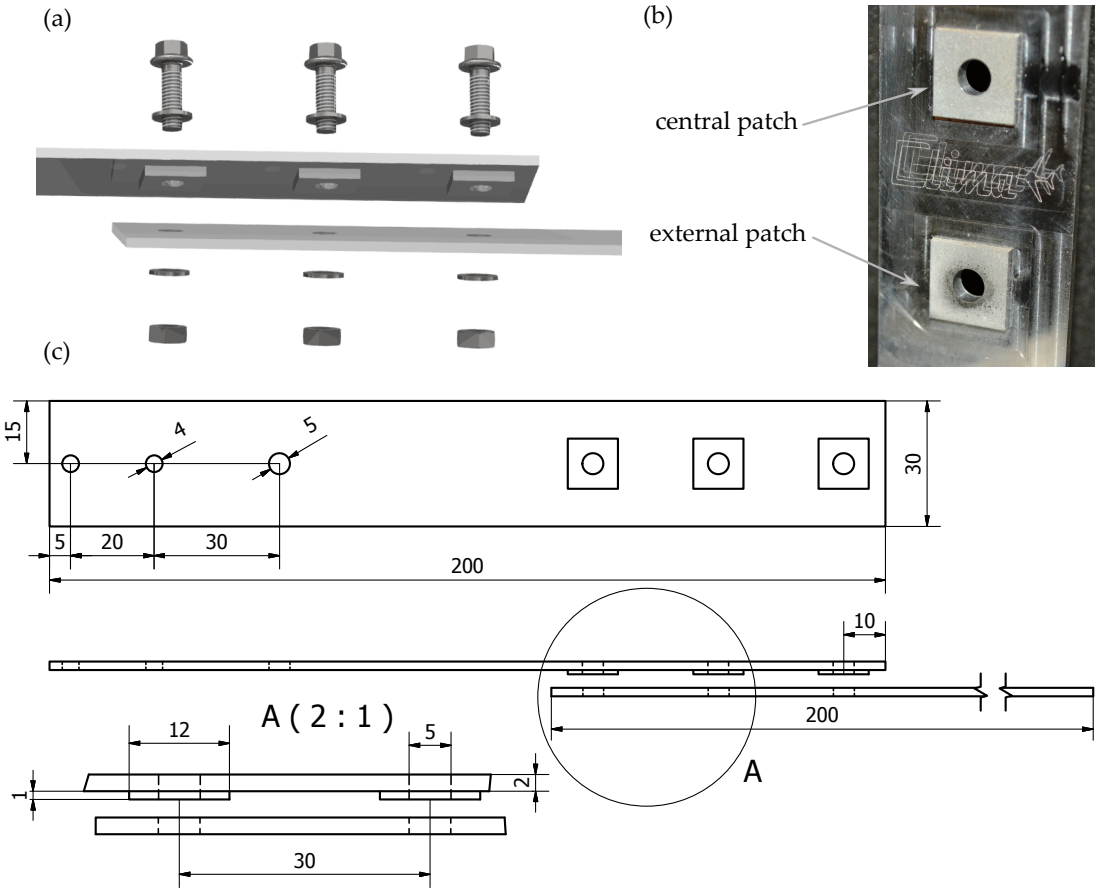

Source: Teloli *et al.* (2022).

The central bolt's preload is maintained, ensuring the appropriately tighten condition and then warranting its static function. In contrast, the tightening torque of the external bolts is variable for each testing condition to examine its influence on the structure's response. Figure 51(b) represents the patches after the experimental testing campaign. Note that there exist black traces on the external patch. From this qualitative point of view, the macro-scale observations indicate the influence of the friction actuating on the external patch, whereas at the central patch where the bolt is fully tightened, there are no visible traces due to the frictional contact. Besides the three connections and contact patches on the interface, there are two holes of Ø4 mm dedicated to clamping purposes and one hole of Ø5 mm for the shaker/stinger attachment to the testing beam. Details about the clamping procedure shall be mentioned herein.

5.1.1 Experimental setup

The experimental setup is shown in Fig. 52 consists of a lap-joint structure with dimensions of $370 \times 30 \times 2$ [mm], a load cell PCB 288D01, an electromagnetic Modal Shop shaker (Model K2004E01), a 3D scanning laser, NI9234 hardware for data acquisition. For all measurements, the beam with the contact patches is completely clamped on one side. Thus, to minimize uncertainties related to the stiffness in the boundary condition (RITTO; SAMPAIO; AGUIAR, 2016), a length of 30 mm is glued and screwed into a massive steel block.

The excitation is performed by the shaker placed near the clamped end and placed on the beam's centerline to avoid exciting torsional modes and to reduce the shaker-structure interaction (PEETERS; KERSCHEN; GOLINVAL, 2011c). A threaded nylon rod stinger is used. To avoid the effect of gravity as well as the presence of torsional modes on the vibrational behavior of the beam once bending modes are in interest, the structure is positioned vertically with its neutral line perpendicular to the ground.

Figure 52 – Experimental setup picture.

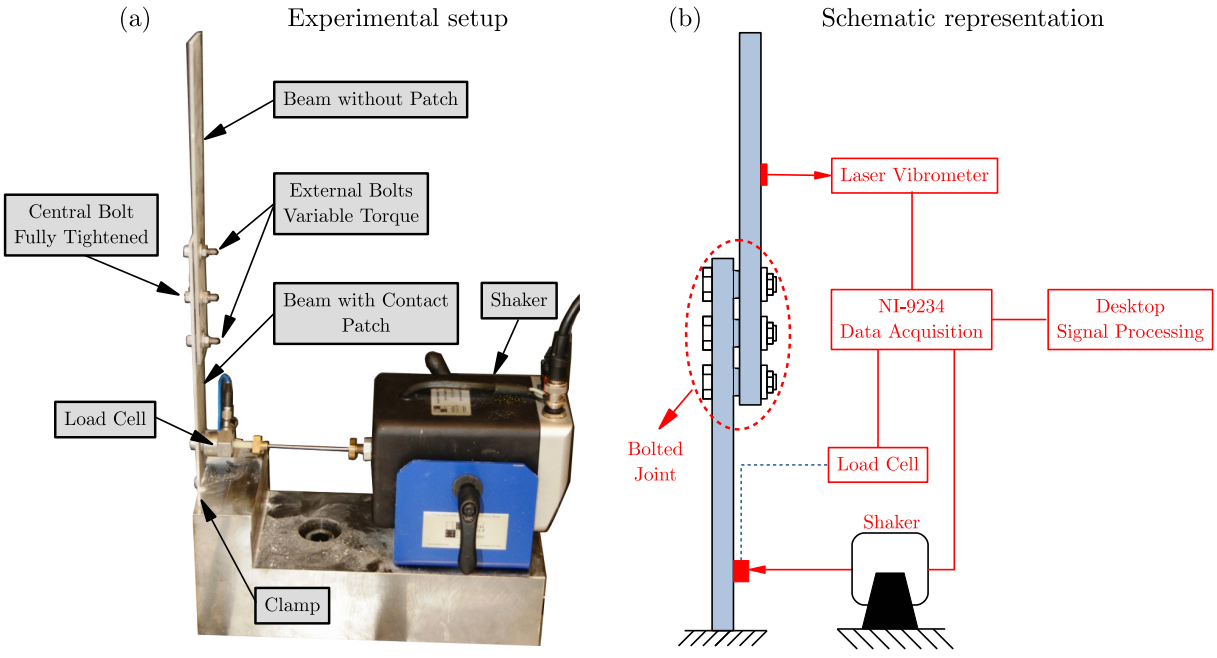

Source: Teloli *et al.* (2022).

For the assembly procedure, we follow the three-step protocol: firstly, to guarantee the alignment between both beams, two-axis are inserted in the external holes; then, the central bolt is fully tightened with a torque of 80 cNm; finally, both axes are removed, and the external bolts are thus tightened. The tightening torques applied on the external

bolts are 10 cNm, 20 cNm, 30 cNm, and 80 cNm, to observe their influence on the structure's response. This screw ensures the stiffness of the assembly during the tests. The tightening torque at the central bolt was checked after each experimental run using a Lindstorm MA500-1 torque wrench.

Before the experimental campaign started, the force applied from each tightening torque was measured with a Futek LTH300 donut load cell. Table 4 presents the associated force and the equivalent joint pressure of each torque condition and the coefficient of variation λ [%], defined as the standard deviation over the mean of the variable after several tests. The force ranges from 136 N (10 cNm) to 877 N (80 cNm), equivalent to contact pressures of 0.94 MPa and 6.09 MPa, respectively. These values correspond to typical mean joint pressure values applied in practice (between 5 Pa and 200 MPa) (BOGRAD; SCHMIDT; GAUL, 2008). Although the maximum torque value considered is far from the upper limit used in practice, its value was satisfactory for the application investigated, with respect to the excitation level considered. Further, note that the variation around low torque values is more notable, which highlights the complexities of dealing with jointed structures, once even the tightening torque carries uncertainties in its values.

Table 4 – Associated force and the equivalent joint pressure for each tightening torque applied and its coefficient of variation.

Torque [cNm]	Force [N]	Pressure [MPa]	λ [%]
10	136.42	0.94	7.35
20	260.61	1.80	7.09
30	384.75	2.97	8.31
80	877.17	6.09	4.45

Source: Teloli *et al.* (2022).

The choice of the torque values in Tab. 4 was supported by preliminary studies involving the lap-joint in the glued condition (monolithic structure). The variation in terms of stiffness and damping between the glued and 80 cNm preload is not expressive, as will be seen in subsection 5.4.4. Thus, this value was set as the upper limit. In contrast, the $10, 20$, and 30 cNm values applied to the contact patches indicate that there is a trade-off between increased damping and reduced joint pressure, without significant changes in stiffness.

5.1.2 Vibration sensing

The signal response has to be acquired in a less invasive manner to conduct the experimental tests as well as possible. The accelerometers are efficient as measuring instruments, but the wires may introduce uncertainties or errors in the measurements in terms of bias (SMITH *et al.*, 2015), especially for lightweight structures. A wireless accelerometer can be used to mitigate this problem, but the sensor mass may also induce uncertainties. In this context, the measurements are performed using the contactless Polytec vibrometer PSV-500 with a 3D scanning laser. Its working distance is between 125 mm and 100 m. Its minimum resolution is 10 nanometers per second.

Two measurement types will be presented. Firstly, a complete laser scanning spans the whole structure through 195 sensing points distributed on the Orion beam surface. The scanning provides global structure behavior and allows obtaining experimental eigenvalues and eigenvectors. Then, to highlight the nonlinear behavior of the structure according to the excitation amplitude as well as to evaluate the influences of the tightening torque, only one measurement point is kept positioned at a distance of 30 mm from the upper external patch center, which makes it easier to conduct a more significant number of measurements involving several torque conditions and excitation amplitudes, thus reducing the elapsed time between experimental tests. Figure 52(b) illustrates a schematic representation of the experimental apparatus.

5.2 EXCITATION DESIGN

A shaker conducted the excitation of the structure placed 30 mm from the clamped end of the Orion beam (Fig. 52) to minimize the shaker-structure interaction. Initially, for preliminary tests with the global scan of the assembled structure, a frequency-controlled white noise between 10 Hz and 2000 Hz with low excitation amplitude was applied. It is essential to point out that, at this excitation condition, the structure's underlying linear model can be estimated.

There is an effort in the literature to propose experimental practices for dynamic analysis and the development of predictive dynamic models that is also related to excitation design. Ewins, Weekes and Delli CARRI (2015) introduced a modal testing framework for validating structural models that is useful when establishing experimental test procedures involving nonlinear analysis. The primary task of identifying a nonlinear feature is subdivided into the detection of early signals of nonlinearity, characterization

of the physical origins of nonlinear effects, location of the source of nonlinearity, and quantification of the strength of nonlinearity. It is emphasized that the sequence in which these steps are presented need not necessarily be followed if there is a fundamental understanding of the dynamic system under analysis.

Extending this framework to the implementation of experimental tests on the Orion beam, the lap-joint of the structure is the source of the nonlinear behavior. Once the aspects of the location of nonlinearities have been discussed, the next step is to detect which vibrating modes present early signs of nonlinear features. Then, the best alternative to characterize how the tightening of the external bolts influences the dry friction effects on the system's response is conducting step-sine tests around resonant frequencies to isolate nonlinear modes. Once that features involving friction and micro-slip behavior exhibit a degree of amplitude dependence, the structure is subject to several excitation amplitudes to quantify the strength of nonlinearity. In this regard, one of the main problems faced by step-sine tests is the difficulty in controlling the amplitude of the excitation force, especially in the vicinity of the resonances due to the force drop-off phenomenon (PERES; BONO; BROWN, 2010). One way to observe this if a load cell is not available to inspect the force response is through the presence of saw tooth effects in peak amplitudes of frequency curves.

There are possibilities to reduce/eliminate limitations in the amplitude control of the applied force. Shaker amplifiers can operate in current mode, in which the output voltage is adjusted to maintain the required current at the amplifier output. In this scenario, the force generated by the shaker is constant (proportional to the current supplied) but divided into two parts: one part excites the shaker itself, and the other excites the structure. As a consequence, the force applied to the beam is dependent on the dynamic stiffness of the shaker and the dynamic stiffness of the structure (TANG; BRENNAN; GATTI, 2018). Thus, to overcome these limitations and achieve a constant excitation amplitude as the frequency changes, the root means square (RMS) values of the applied force measured directly by the load cell were controlled using a real-time feedback controller. Figure 53 depicts the block diagram of the controller designed for performing the feedback control and integrating software and measurement hardware. Although the algorithm was used for amplitude control of the excitation force, other kinematic quantities can be considered, such as acceleration measurements. The following script algorithm is executed:

1. The algorithm starts by defining the following parameters: increment and frequency

range, desired excitation amplitude, the initial supply voltage of the shaker, the time duration of the test and sampling frequency;

2. The acquisition board converts the control signal, which is the voltage for supplying the exciter, from digital to analog. It then sends it to the shaker that contains an amplifier. During the vibrational testing, the load cell or the accelerometer measures the signal that corresponds to the applied force/acceleration by the shaker. Now, reversely, the acquisition hardware converts the output signal of the sensor and sends the measured voltage to the acquisition software;

3. The software converts the measured voltage to force or displacement and estimates its RMS value. The error ε between the experimental RMS $\hat{F}$ [N] and the desired one F [N] is calculated:

$$\varepsilon = \frac{|\hat{F} - F|}{F} \tag{112}$$

Then, based on the error, the new voltage amplitude A_N [V] used to supply the shaker is corrected according to the voltage value A_{N-1} [V] from the last iteration following the simple controller design:

Algorithm 2: Amplitude correction.

```
Define convergence criteria: (ε_max, N_max) ;
if 1 − ε/1.5 ⩽ 0 then
    A_N = 0.1 A_{N−1} ;
    else if 1 − ε/1.5 ⩾ 0 then
        A_N = 2 A_{N−1} ;
if N > N_max then
    break;
end;
u(t) = A_N cos(ω_i t);
```

where $\varepsilon_{\max}$ denotes the maximum acceptable error and $N_{\max}$ is the stop criterion based on the number of iterations until reaching the convergence; $u(t)$ [V] is the control signal and ω_i corresponds to the i^{th} excitation frequency during the step-sine testing. For this work, $\varepsilon_{\max}$ = 2% and $N_{\max}$ = 20. This simple algorithm is inspired on the bang-bang logic, in which the control law has two control positions

(just as the bang-bang scheme) restricted to lower or upper limits for actuating. Each position is defined based on the error, which determines the magnitude of the voltage that must be applied to the shaker. The controller at position $1 - \frac{\varepsilon}{1.5} \geqslant 0$ considers a case where the applied voltage signal is further away from the desired one, whereas the position $1 - \frac{\varepsilon}{1.5} \leqslant 0$ reduces that value considerably to rest exactly around the desired error;

4. The acquisition board reads the control signal and sends it to the shaker;

5. The real-time controller returns to the second step and restarts the controlling system while the error between the experimental RMS amplitude and the desired one is greater than $\varepsilon_{\max}$;

6. The excitation frequency is increased. The voltage amplitude of the previous increment updates the value of the initial voltage supplied in the shaker.

Figure 53 – Block diagram of the feedback controller of the excitation force. The current excitation force is compared to the desired one (setpoint), and the error is calculated. Then, the controller evaluates at which position of the control law it is must actuate. The voltage control signal is converted and applied to the shaker, which excites the Orion beam. The load cell measures the force applied and feeds back their values so it can be compared to the setpoint once again, and the process is restarted.

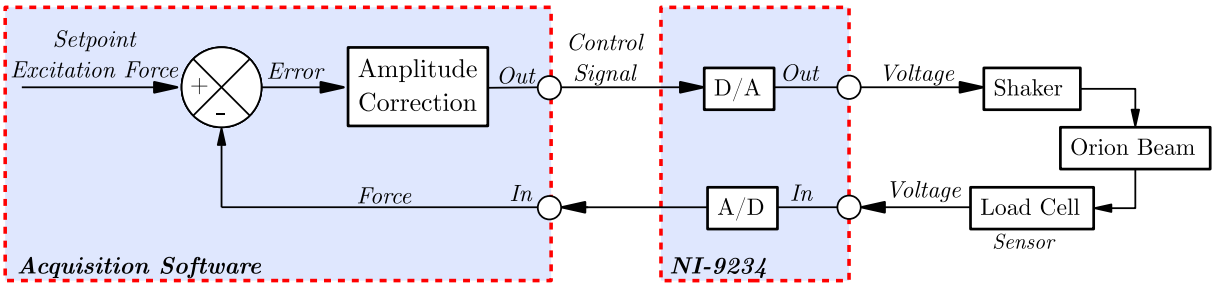

Source: Teloli *et al.* (2022).

Figure 54 exemplifies the need for considering the amplitude control during step-sine tests. In this case, a low amplitude level of 10 mN is desired around the frequency ranging from 1700 to 1775 Hz. Note that the supplied voltage in the shaker amplifier from Fig. 54(a) reaches peak values around the vicinity of resonance (see Fig. 10) to keep a constant force amplitude, as illustrated in Fig. 54(b). Still, in Fig. 54(b), the excitation amplitude lies within the maximum acceptable error, with values around 9.8 mN and 10.2 mN. Finally, Fig. 54(c) illustrates the iterations until convergence for each frequency increment. The real-time controller presents more iterations for the first excitation frequency, in which the user sets the initial voltage amplitude and in the vicinity of the

Figure 54 – Representative example of the real-time controller actuating on the excitation amplitude.

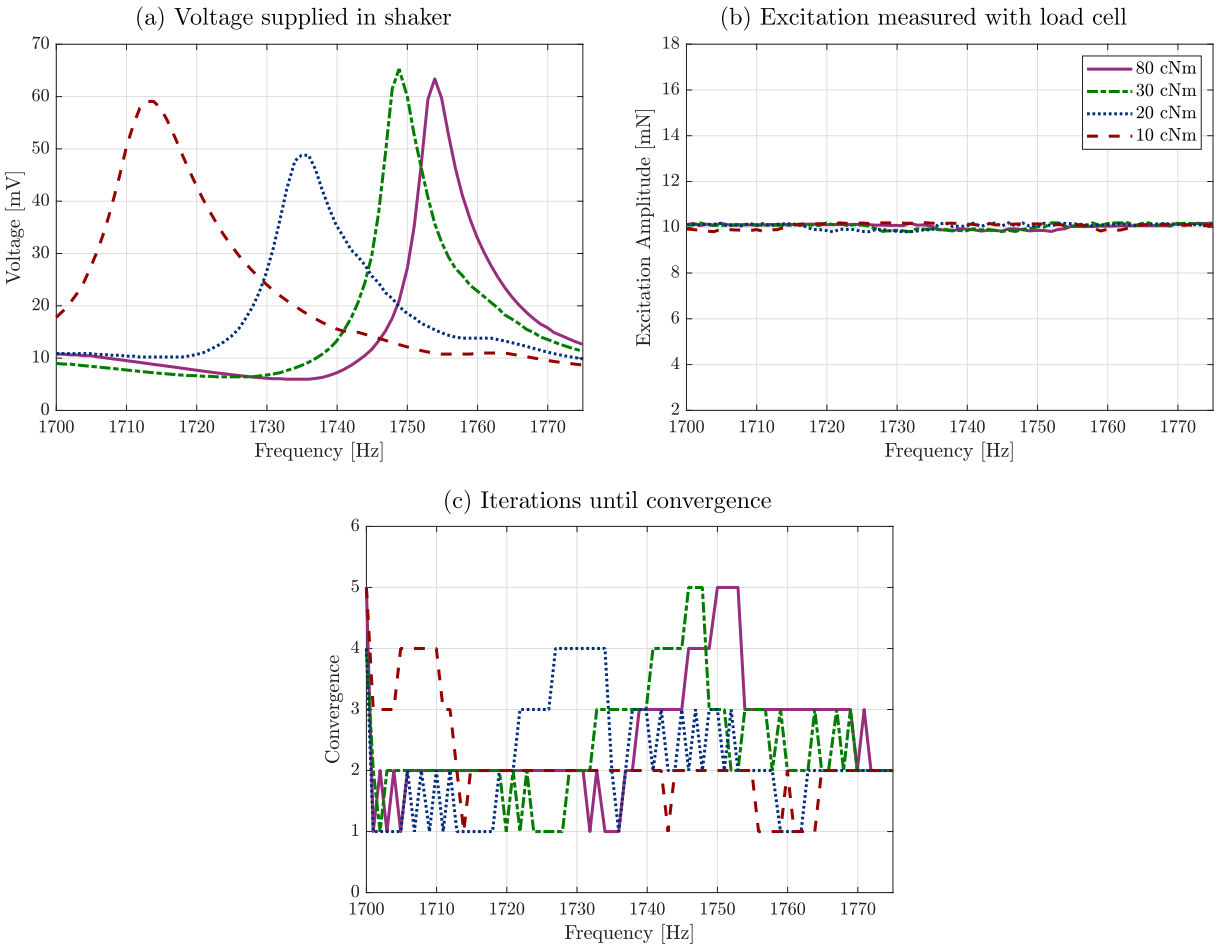

Source: Teloli *et al.* (2022).

resonance frequency. The proposed controller exhibits satisfactory performance for the conditions examined in this work, providing the amplitude control with a small number of iterations. Likewise, the control strategy presents limitations related to supplying high voltage values in the shaker amplifier for conditions where it drives the control to its upper bound. To avoid problems related to the voltage supply required to maintain the force constant, Catalfamo *et al.* (2016) investigated the acceleration amplitude control in the BRB, taking measurements close to the shaker driving point. The advantage in considering acceleration as a reference in a control strategy lies in the fact that resonance regions promote higher acceleration amplitudes to the whole structure, thus requiring lower current supply to the shaker. It is stressed that the algorithm presented can also be redefined to control another physical variable of interest, such as using acceleration measurements close to the driving point.

The controlled RMS force values were $10, 50, 100, 150, 200$, and 250 mN, whereas the

maximum excitation amplitude was selected to keep the structural integrity. For reaching these forcing values, the shaker's voltages are distant from its maximum acceptable input voltage range.

5.3 UNDERLYING LINEAR STRUCTURE

This section presents the Orion beam's preliminary results, starting with the white noise excitation. Figure 55(a) presents the frequency response function of the Orion beam considering the patches perfectly glued, which represents the monolithic state, and estimated after applying a low-amplitude white noise excitation (63.45 mN RMS) band-limited between 10 Hz and 2000 Hz. Six bending modes, corresponding to the first 19.38 Hz, second 122.5 Hz, third 289.38 Hz, fourth 723.8 Hz, fifth 922.5 Hz and sixth 1758 Hz modes were identified in the FRF data. The measurements indicate a low mode coupling (light modal density) in the frequency range around the 1st, 2nd, 3rd, and 6th modes. Note the presence of the first torsional mode (546.30 Hz) between the third and fourth bending modes, but even so, its response amplitude is lower than the other modes shown in the FRF. The 4th and 5th modes are relatively close, in a frequency range with considerable modal density due to the presence also of torsional effects on the 5th vibrating mode, which is probably caused by undesired moments at the driving point the random excitation.

Figure 55(b) exemplifies the modes predicted experimentally considering 195 sensing points on the Orion beam's surface. Note that the energy delivered by the white noise excitation around the first bending mode was not enough to visualize the beam vibrating uniformly. The visualization of the fifth mode, in turn, presents a contribution of the torsional mode. Nevertheless, the beam velocity in the vicinity of the clamped region is nearly zero for all modes, which confirms the clamping procedure's effectiveness.

The third and sixth bending modes present modal shapes that promote a pronounced deformation around the lap joint. Due to this reason, these modes were potential candidates to investigate the nonlinear behavior induced by friction effects as well as the contribution of the tightening torque in the system's response. Therefore, a preliminary analysis based on the step-sine tests is conducted to highlight the amplitude-dependent effect.

The following section starts by presenting the third vibration mode. It then focuses on the frequency response curves around the sixth bending mode considering several tighten-

Figure 55 – FRF velocity from the experimental result.

(a) Bending modes

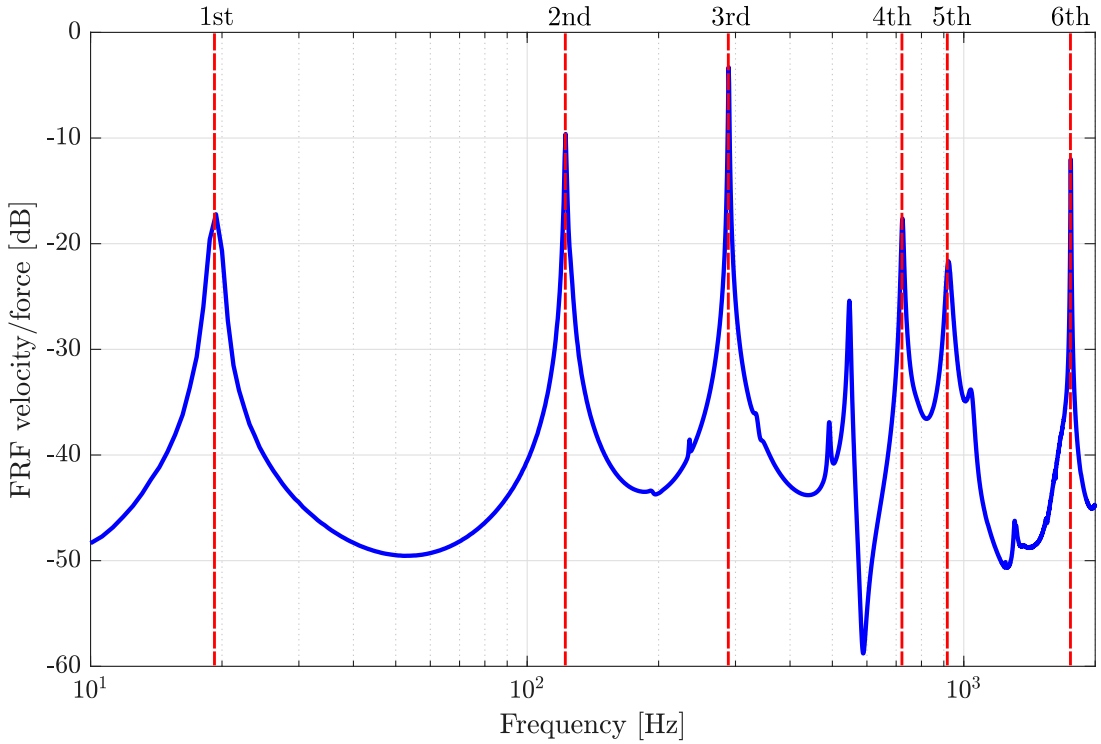

(b) Illustration of the bending modes of the Orion beam

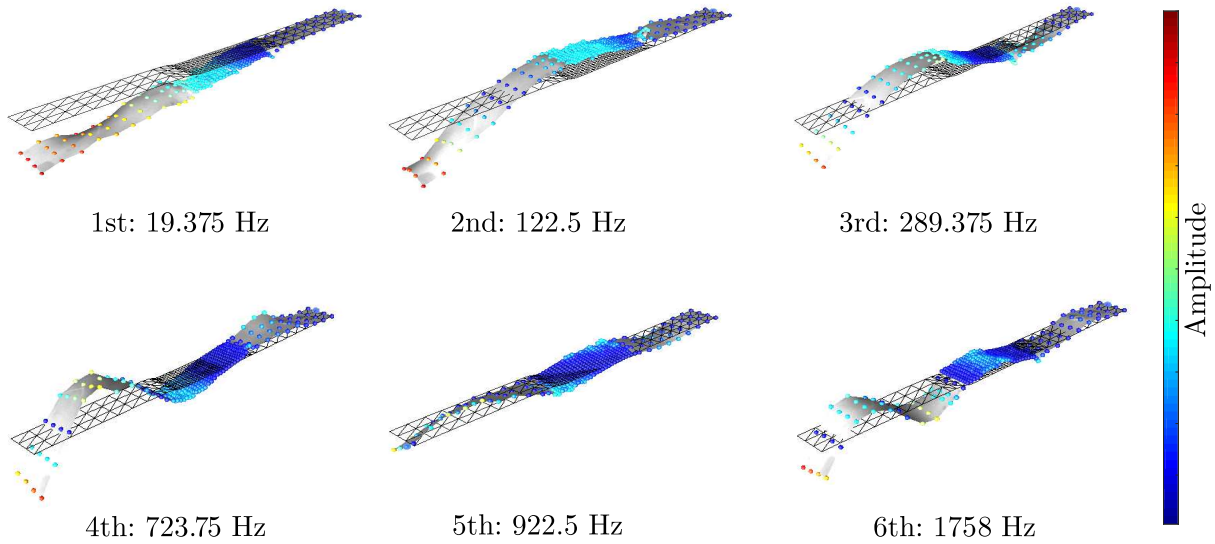

Source: Teloli *et al.* (2022).

ing torques and excitation amplitudes, as after preliminary analysis considering harmonic excitations, it was found that the latter mode is the most affected by nonlinearity.

5.4 ON THE ORION BEAM'S RESPONSE

All the frequency curves presented subsequently correspond to the one-point measurement (see Fig. 52), which provides proper observability on the bending modes of interest. The excitation force is feedback-controlled following the block diagram previously presented in Fig. 53. The following parameters are defined: step-sine with a time 5.12 seconds in steady-state motion at each step; and a sampling frequency of 25.6 kHz.

Moreover, three representative quantities are investigated: the resonance frequency f_n [Hz], the peak amplitude of the frequency response curves $A_{\max}$ [dB] and the half-power bandwidth at -3dB Δ_{BW} [Hz]. These parameters indirectly estimate the evolution of the structure's damping and stiffness, providing the necessary understanding of Orion benchmark behavior when subjected to the external variables of excitation level and tightening torque.

5.4.1 On the third vibrating mode's response

The preliminary frequency response curves related to the 3rd mode are illustrated in Fig. 56 by considering two tightening torque conditions, 20 and 80 cNm, and several excitation amplitudes, 10 mN to 200 mN. In those curves, step-sine tests are starting at 280 Hz up to 300 Hz with a frequency increment of 0.3901 Hz. It is worth noting that the central bolt is located close to the nodal point for this vibrating mode, and thus, the influence of external bolts is enhanced.

For low excitation amplitudes, the resonance frequencies for both torque conditions, i.e., 289.1 Hz for 80 cNm and 287.9 for 20 cNm, are close to the resonance visualized for the glued condition during tests with random excitation. Although the softening effects can be visualized under these preloads as the excitation amplitude increases, the special feature of the frequency curves is the amplitude attenuation. Figure 57 presents the shift in f_n, $A_{\max}$ and -3 dB Δ_{BW} parameters. In Fig. 57(b), for a torque condition of 80 cNm, note that the peak amplitudes vary from -1.1 dB to -10.24 dB as the excitation increases, representing an absolute amplitude attenuation of 89%, whereas for 20 cNm, there is a similar trend from -2.55 dB to -10.39 dB, but with an attenuation of 75%. The increase of the -3 dB Δ_{BW} bandwidth related to the excitation amplitude, as illustrated in Fig. 3 for both torque conditions, highlights the influence of the frictional effects on the structural damping due to the external patches, which can have their preload adjusted without

significantly changing the nominal frequency of the structure, as seen in Fig. 57(a).

Figure 56 – Nonlinear behavior of the Orion lap-joint around 280 and 300 Hz for different torques (80 cNm and 20 cNm) distinguished by different colors, and for multiple excitation level (10 mN to 200 mN) distinguished by different line types and gradient color.

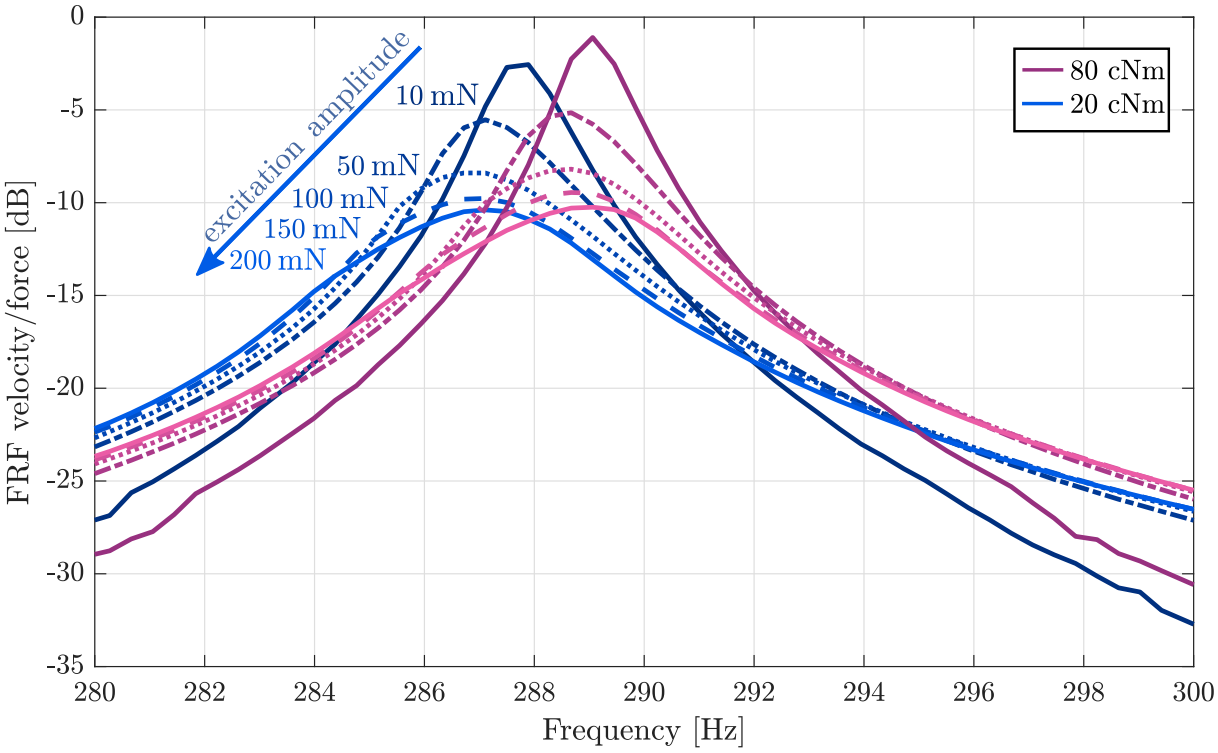

Source: Teloli *et al.* (2022).

The investigations conducted in this section are only to introduce a preliminary analysis of the Orion beam's behavior and highlight the different roles played by the bolts in the structure's response. The frequency changes are negligible since the central patch is close to a nodal point, and the energy dissipation can be mainly attributed to the external patches. The advantage of dealing with the other mode compared to the one presented in this section is the possibility of subjecting the three contact patches to similar displacements, highlighting nonlinear effects related to softening stiffness. This paper's following sections present a detailed discussion on the 6th bending mode from different perspectives outlined after experimental tests.

Figure 57 – Nonlinear behavior of the Orion lap-joint around 280 and 300 Hz for different torques (80 cNm and 20 cNm) distinguished by different colors, and for multiple excitation level (10 mN to 200 mN) distinguished by different line types and gradient color.

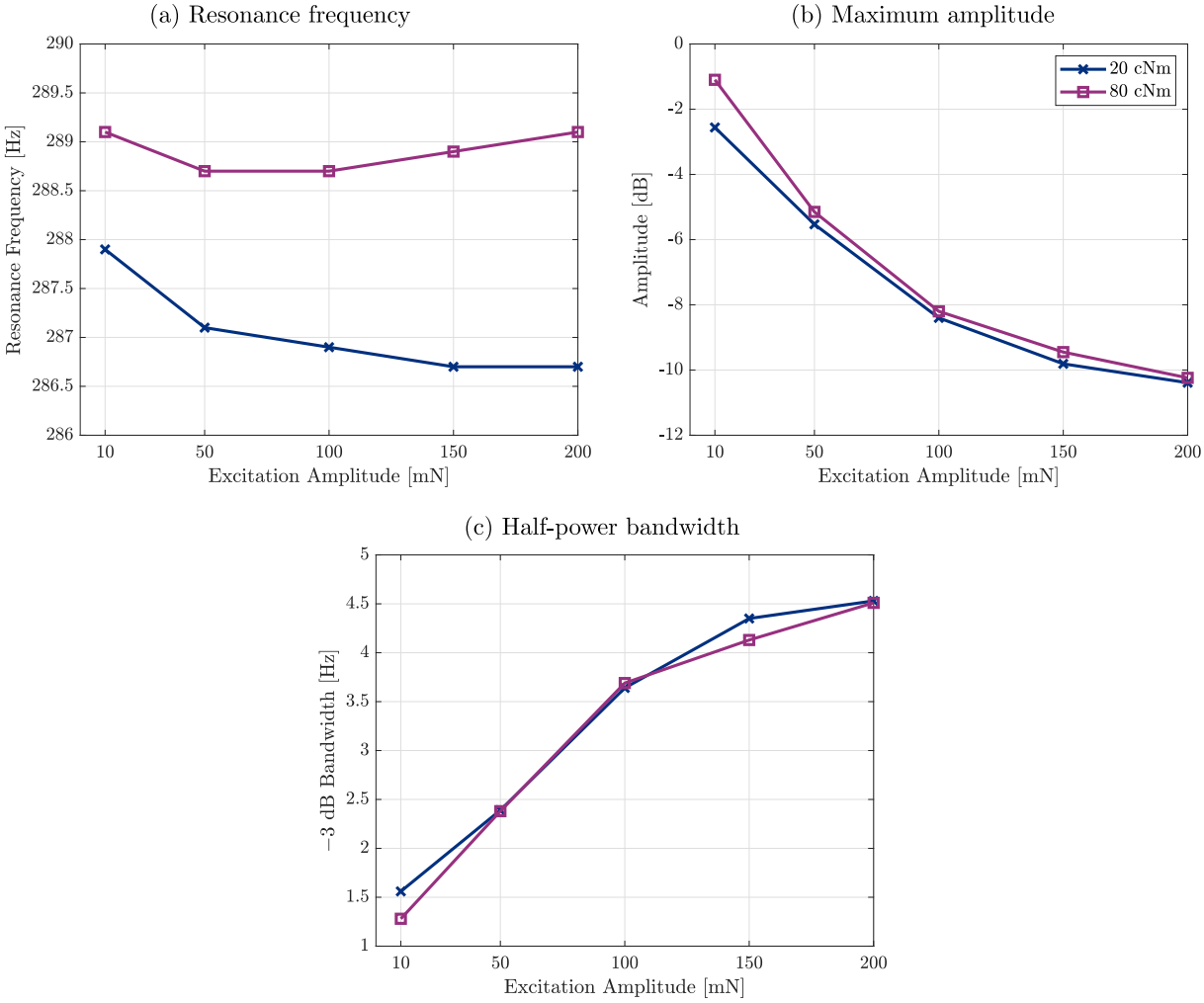

Source: Teloli *et al.* (2022).

5.4.2 Measurements repeatability

This subsection aims to provide the degree of uncertainties of the results by studying the stability of the assembly and the repeatability of the measurements. This section tries to respond to the question: ‘‘How much can we trust the experimental measurements?" With the ambition, people could use these data to validate their numerical models.

The Orion beam is built with thin components and has the contact interface concentrated at each patch. Thus, due to the small area at each bolt, the lap-joint connection occurs only under the pressure cone (MASUKO; ITO; YOSHIDA, 1973). Recently, Brake, Schwingshackl and Reuß (2019) presented an extensive study about the variability and repeatability of the BRB benchmark considering several modifications on the interface

of the beams. One of the profiles investigated has small contact pads at the lap joint, similar to the Orion beam design. Although the conditions observed by the authors are related to the linear behavior, the repeatability of the small pad system is significantly higher than the nominal BRB design (BRAKE *et al.*, 2014). Furthermore, recent research results, including Brake, Schwingshackl and Reuß (2019), have indicated that reducing the contact area to the pressure cones should reduce the uncertainty in the structure response once the frictional dissipation is more negligible (GOYDER; IND; BROWN, 2013; DOSSOGNE *et al.*, 2017).

In this context, to verify whether the Orion beam ensures repeatability among several experimental measurements, two sides are then studied: the tightening/loosening of the bolts in different orders and the complete tightening of the upper beam (the one without patches, see Fig. 52). Then, based on several assemblies and disassemblies of the lap-joint, the mean values μ, standard deviation σ, and coefficient of variation λ [%], are estimated. Besides, as the analysis presented by Brake, Schwingshackl and Reuß (2019), the repeatability analysis through this subsection also addresses nonlinearities in the structure behavior.

Figure 58 presents the frequency response curve of the structure considering a tightening torque of 80 cNm and two excitation amplitudes of 10 mN (low-level) and 250 mN (high-level) controlled by the feedback algorithm. All step-sine tests conducted for the mode of interest start at 1660 Hz up to 1780 Hz with a frequency increment of 1 Hz. The data variation represented by the figure appears due to seven experimental realizations. Furthermore, after each run, the lap-joint is completely disassembled and then reassembled. Table 5 summarizes the obtained results for the testing conditions. Note that, at the excitation amplitude of 10 mN, λ values for the parameters f_n, $A_{\max}$ and Δ_{BW} are higher than the ones obtained at 250 mN. This may be explained by the fact that the energy delivered for high excitation levels is higher than the low amplitudes, minimizing uncertainties related to the measurement procedure. Additionally, for both excitation amplitudes, the variation λ of the parameters $A_{\max}$ and Δ_{BW} presents higher values than the f_n variation, which is associated mainly to the stiffness of the jointed structure. The structure exhibits considerable repeatability at 80 cNm, even considering a high excitation amplitude. As investigated by Dossogne *et al.* (2017), these results are expected for designs that have small contact areas, like the Orion beam, since the uncertainties on the contact pressure are reduced, and the torque of 80 cNm leads to a significant preload.

Figure 58 – Repeatability of the measurements for seven experimental runs in frequency response curves considering a tightening torques of 80 cNm and excitation amplitudes of 10 mN (solid line ——) and 250 mN (dash line – –); —— represents the mean value for 7 lap-joint disassemblies, see Table 5.

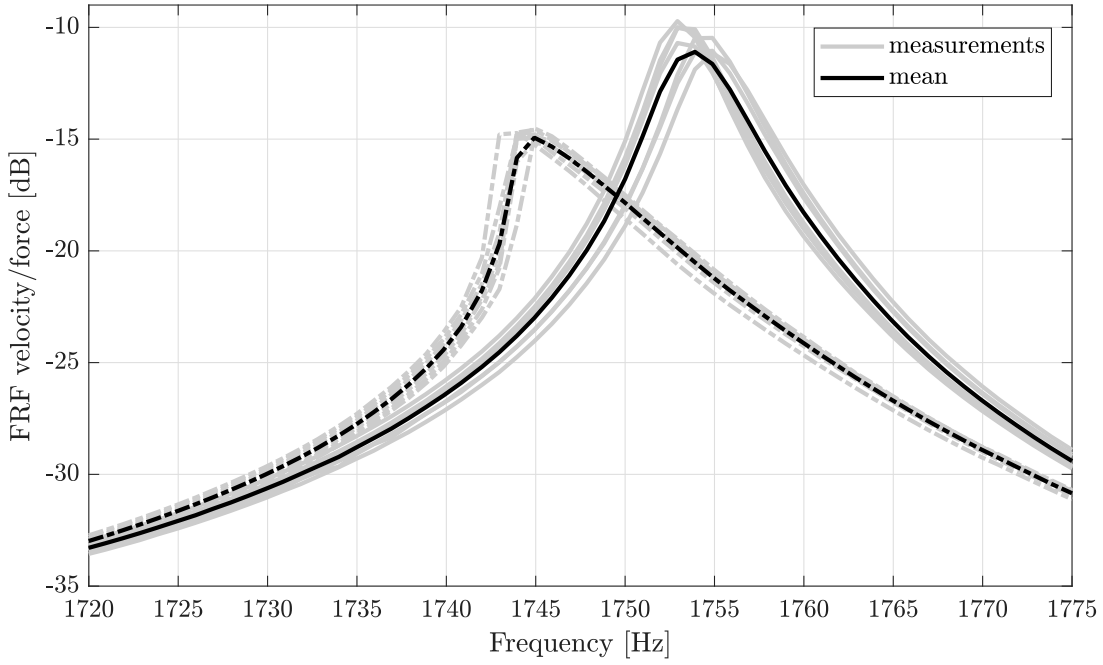

Source: Teloli *et al.* (2022).

Table 5 – Repeatability of the measurements for seven experimental runs with disassembly of the lap-joint and considering a tightening torque of 80 Nm at two excitation amplitudes of 10 mN (low-level) and 250 mN (high-level). Mean values (μ), standard deviations (σ) and coefficients of variation (CV) of the parameters f_n, $A_{\max}$ and Δ_{BW}, see Fig. 58.

	10 mN			**250 mN**		
80 cNm	μ	σ	λ [%]	μ	σ	λ [%]
f_n	1753.71 Hz	0.86 Hz	0.05	1744.55 Hz	0.51 Hz	0.03
$A_{\max}$	-10.45 dB	0.55 dB	5.26	-14.80 dB	0.22 dB	1.48
Δ_{BW}	4.76 Hz	0.32 Hz	6.72	6.59 Hz	0.30 Hz	4.55

Source: Teloli *et al.* (2022).

To investigate the variability induced by changes in the tightening torque, Fig. 59 presents several measurements considering a tightening torque of 20 cNm and the low level of excitation amplitude 10 mN. Figure 59(a) presents the frequency response curves of four experimental runs after complete disassembly, whereas Fig. 59(b) also depicts four experimental realizations, but considering tightening/loosening of the bolts. The changes between the testing conditions are evident: all the coefficients of variance on the structure with disassembly are higher than the ones without disassembly, especially for the parameters $A_{\max}$ and Δ_{BW}. These results indicate that when the tightening torque

assumes lower values, even with the structure operating linearly, the reassembly process significantly changes the patches' contact surface profile. This process consequently increases the variability of the system's responses. Additionally, a direct comparison between the tightening torques of 20 cNm and 80 cNm, both at low excitation level, shows that the λ values of f_n, $A_{\max}$ and Δ_{BW} for 20 cNm are higher than the ones for 80 cNm. The low excitation amplitude allows observing only the impact of the tightening torque in the structure's response. Considering this, Table 4 provides an intuitive justification of why that happens once the variations around low torque values (10, 20, and 30 cNm) are more significant than for the highest preload (80 cNm). Misalignment of the contact region, even when adopting an assembly protocol, can also influence the response of the structure.

Figure 59 – Repeatability of the measurements in frequency response curves considering a tightening torque of 20 cNm and low excitation amplitude 10 mN. Figure 59(a) represents the measurements with the complete disassembly of the lap-joint (solid-lines), whereas Fig. 59(b) depicts the measurements without the disassembly, but with tightening/loosening of the bolts (——), see Table 6.

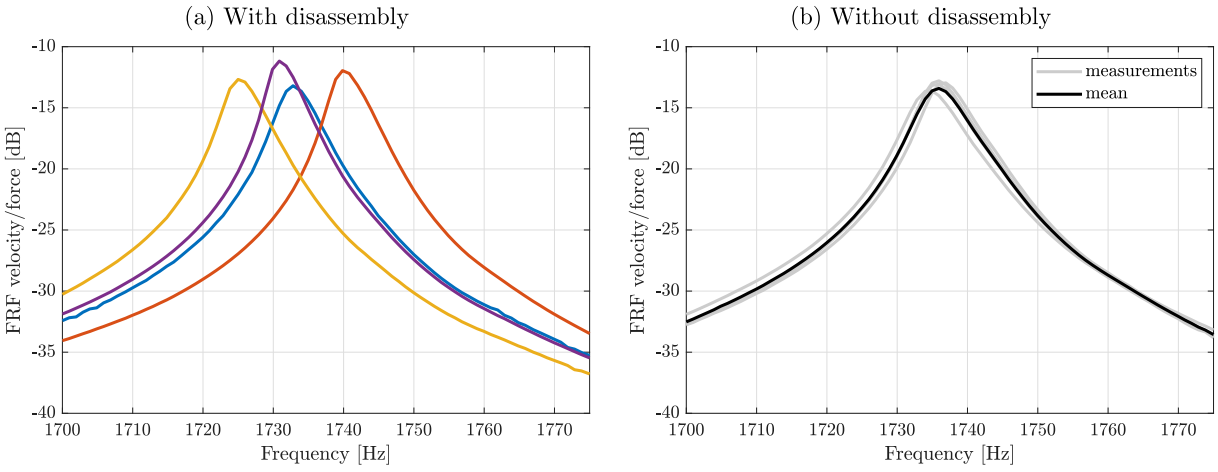

Source: Teloli *et al.* (2022).

As pointed Ewins (2016), joints are a source of epistemic uncertainty in structural dynamics, with emphasis on the fact that the order of tightening bolts can yield different static configurations to the system. From the modeling point of view, predicting these deviations could become a potential issue. Testing runs without complete disassembly may be proposed to mitigate this problem. Figure 59(b) shows that the loosening/tightening of the bolts and the order in which the bolts are tightened have almost no impact on the dynamic behavior.

On the one hand, another opportunity is to measure the tightening torque at the bolt during the experimental campaign, just employing strain gauges at the screw head.

Table 6 – Repeatability of the measurements considering a tightening torque of 20 cNm and an excitation level of 10 mN. Mean values (μ), standard deviations (σ) and coefficients of variation (CV) of the parameters f_n, $A_{\max}$ and Δ_{BW}; for four measurements with the disassembly of the lap-joint and 4 measurements without the disassembly, but considering tightening/loosening of the bolts in different orders, see Fig. 59.

	With disassembly			**Without disassembly**		
20 cNm	μ	σ	λ [%]	μ	σ	λ [%]
f_n	1732.16 Hz	6.11 Hz	0.35	1735.66 Hz	0.91 Hz	0.05
$A_{\max}$	-12.26 dB	0.87 dB	7.09	-13.10 dB	0.36 dB	2.75
Δ_{BW}	6.17 Hz	0.61 Hz	9.88	7.83 Hz	0.43 Hz	5.49

Source: Teloli *et al.* (2022).

Measuring this parameter may be desirable to detect mechanisms for frictional energy dissipation within a connected surface and be helpful in reducing epistemic uncertainty as direct measurements on contact mechanics become available. On the other hand, the reliability of the patches' functions, i. e., the static and damping functions, are based on the pressure distribution on interfaces considering various tightening conditions. Thus, this analysis, together with information about the tightening torque in experimental campaigns, will provide not only more extraordinary insight into the appearance of black traces on external patches, as seen in Fig. 51(b), but also how repeatability relates to interactions on the contact surface of the Orion beam.

5.4.3 On the influence of the tightening torque

Tests were conducted at a low excitation amplitude (10 mN) to highlight only the tightening torque's influence on the Orion benchmark. The frequency response curves considering several preload conditions are depicted in Fig. 60. Two characteristics stand out in this figure: the decrease in the resonance frequency when the tightening torque also decreases, showing that the lap-joint inevitably softens the total rigidity of the system; a greater attenuation of the vibration amplitude for lower tightening values, indicating that the damping patches lead to greater energy dissipation. Table 7 evaluates the impact of the tightening torque on the parameters f_n, $A_{\max}$, Δ_{BW}. The results in Table 7 also indicate that there exists a similar trend between the frequency attenuation band Δ_{BW} and the tightening torque since energy dissipation processes also influence this parameter. The frequency response curves considering several preload conditions are depicted in Fig. 60. Two characteristics stand out in this figure: the decrease in the resonance frequency when the tightening torque also decreases, showing that the lap-joint inevitably softens

the total rigidity of the system; a greater attenuation of the vibration amplitude for lower tightening values, indicating that the damping patches lead to greater energy dissipation. Table 7 evaluates the impact of the tightening torque on the parameters f_n, $A_{\max}$, Δ_{BW}. The results in Table 7 also indicate that there exists a similar trend between the frequency attenuation band Δ_{BW} and the tightening torque since energy dissipation processes also influence this parameter.

Figure 60 – Torque impact at 10 mN excitation level.

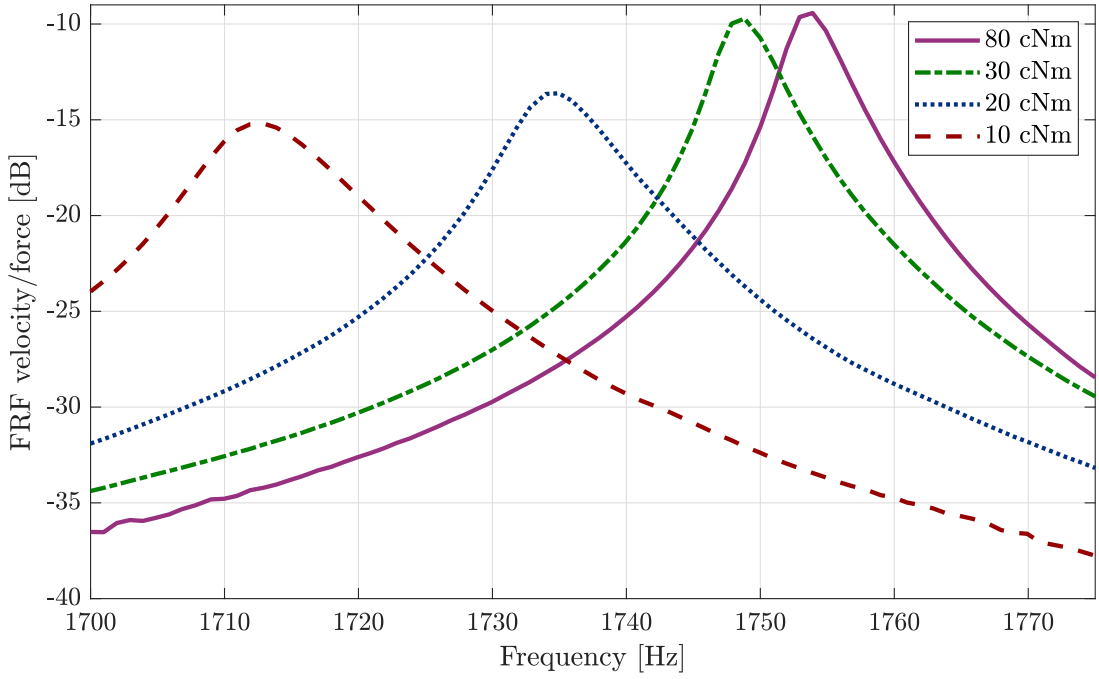

Source: Teloli *et al.* (2022).

The peak amplitudes vary from -9.40 dB for 80 cNm to -14.30 dB for 10 cNm, representing an absolute amplitude attenuation of 52%. The resonance frequency also changes, from 1754 Hz for 80 cNm, to 1714 Hz for 10 cNm. However, the frequency changes are small (2.28 %) compared with variations in amplitude. This feature indicates that, even for conditions where the structure presents a behavior without early signs of nonlinearity in the frequency response curve, it is possible to attenuate vibration amplitudes without significantly compromising the structure's stiffness by controlling the contact in the patches. Although the recent work developed for the BRB benchmark (BRAKE; SCHWINGSHACKL; REUSS, 2019) discusses the influence of several design parameters, including modifications on the contact surface, roughness tests, among others, the contribution sought by the Orion beam is new and ponders about the possibility of exploring the benefits that a lap-joint may offer for damping purposes without compromising the structural integrity.

Table 7 – Torque impact at 10 mN excitation level.

Torque [cNm]	f_n [Hz]	$A_{\max}$ [dB]	Δ_{BW} [Hz]
10	1714	-14.28	9.90
20	1735	-13.62	8.43
30	1749	-9.71	5.18
80	1754	-9.43	4.97

Source: Teloli *et al.* (2022).

5.4.4 On the influence of the excitation amplitudes

After tests involving the influence of the tightening torque on the structure's behavior, this section aims to assess the nonlinear effects on the Orion beam's response when subjected to different excitation amplitudes.

Figure 61 shows the frequency response curves in terms of amplitude (Fig. 61(a)) and phase (Fig. 61(b)) of the Orion beam considering six excitation levels at the tightening torque of 10 cNm. As several lap-joint benchmarks, the Orion beam presents amplitude-dependent nonlinearities. One of the most prominent characteristics in the frequency *versus* amplitude plot is the resonant frequency decreasing as the excitation level increases, e.g., decreasing from 1713 Hz to 1695 Hz for the excitation amplitudes of 10 and 250 mN, respectively. This so-called softening effect occurs, especially in jointed structures, due to the partial slippage on the joint interface, which reduces the contact stiffness (SEGALMAN, 2010; FESTJENS; CHEVALLIER; DION, 2013). Moreover, it should also be stressed that peak amplitudes have a clear trend of reducing their values when the excitation level increases, which indicates the amplitude-dependence of the damping on the structure displacement. For the frequency increment of 1 Hz, the Orion beam does not present jump-up frequencies in step-sine tests. Additionally, even for high excitation levels, the frequency response curves do not exhibit the dropout effect around the resonant frequencies, which shows the effectiveness of the feedback controller applied.

Figure 62 summarizes the Orion lap joints nonlinear behavior around the sixth bending mode according to excitation levels and torques. The softening effect is present in all assembly conditions. Although the glued state also shows variations in the resonance frequency, the structure's behavior is only moderately altered. The frequency decreases by 3 Hz from low to high excitation amplitudes, representing a variation of 0.17%. The joint pressure is high in this condition, and the linearity assumption sufficiently represents the system's behavior. For a torque level of 80 cNm and excitation force at 10 mN, the changes in frequency and peak amplitudes concerning the glued condition are not

Figure 61 – Excitation level impact at 10 cNm torque.

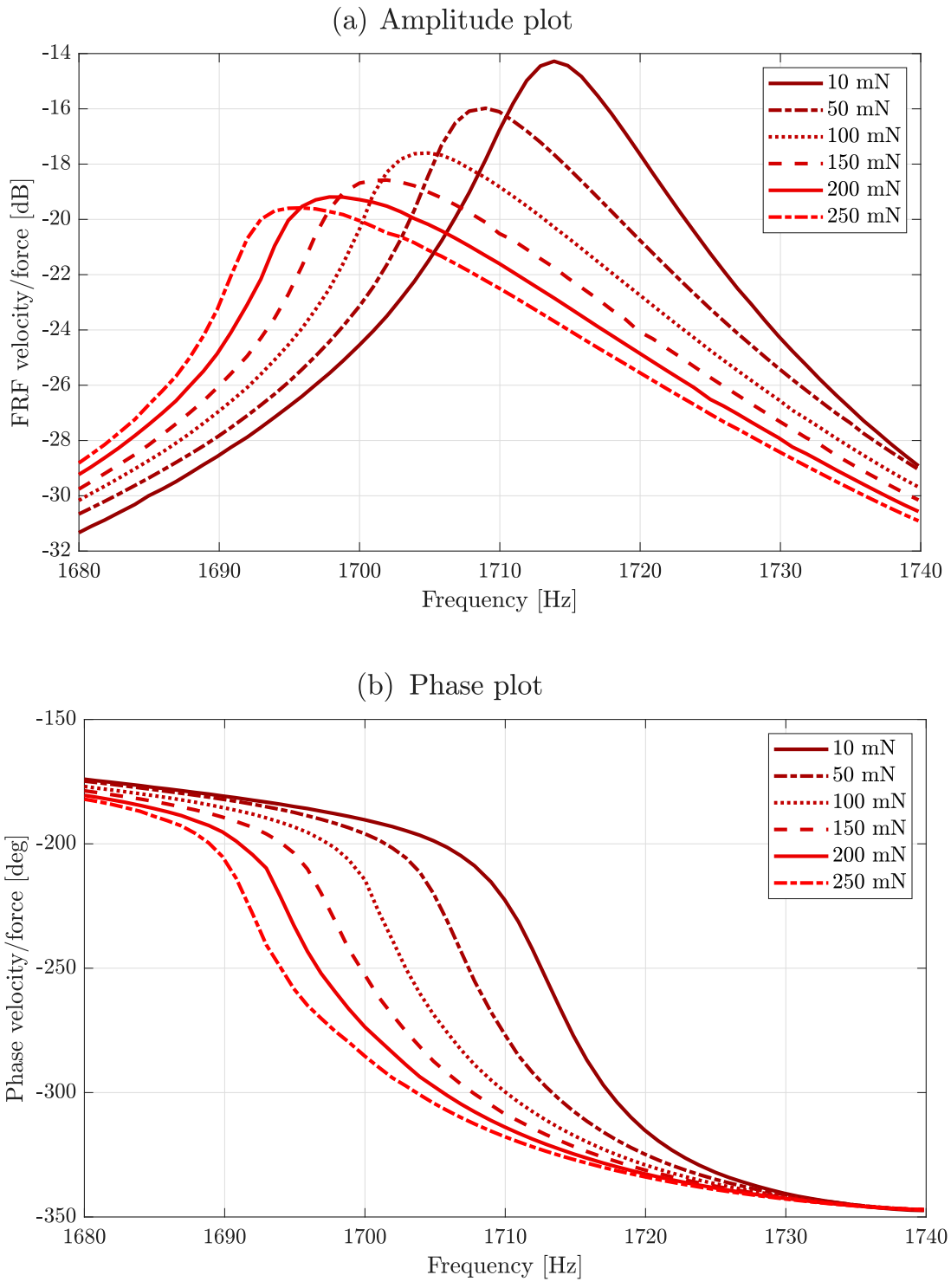

Source: Teloli *et al.* (2022).

expressive, a shift of 4 Hz in frequency, and an absolute difference between peaks of 0.21 dB, respectively. One can see that torque values above 80 cNm could have been selected, but there would be no substantial changes regarding resonant frequencies at low excitation amplitudes.

Furthermore, through these frequency response curves that combine several conditions, one of the main issues involving modeling lap-joints arises. There is a superposition between the response curves, which is difficult for modeling differences if a law to describe the tightening torque is not taken into account. Therefore, studies that consider a multi-scale analysis to capture the evolution of the frictional effects over time and frequency are still developed (BALAJI; CHEN; BRAKE, 2020).

To clarify how excitation and torque contribute to each frequency response, Fig. 63 depicts the variations on the parameters f_n, $A_{\max}$, Δ_{BW}. The Orion beam allows distinguishing properly how the external variables influence the analyzed parameters. For instance, Fig. 63 (a) shows the evolution of the resonance frequency versus excitation amplitude considering several tightening torques. In this figure: the observed values of resonance frequencies are slightly higher as the tightening torque increases; the frequency shift from low (10 mN) to high (250 mN) excitation amplitudes has more prominent values for low preload (10 cNm) with an absolute difference of 19 Hz, whereas for high torque values the variation is 9 Hz.

Figure 62 – Nonlinear behavior of the Orion lap-joint around 1665 and 1775 Hz for different torques (80 cNm, 30 cNm, 20 cNm, and 10 cNm) distinguished by different colors, and for multiple excitation level (10 mN to 250 mN) distinguished by different line types and gradient color. The greyscale curves show the behavior of a glued assembly.

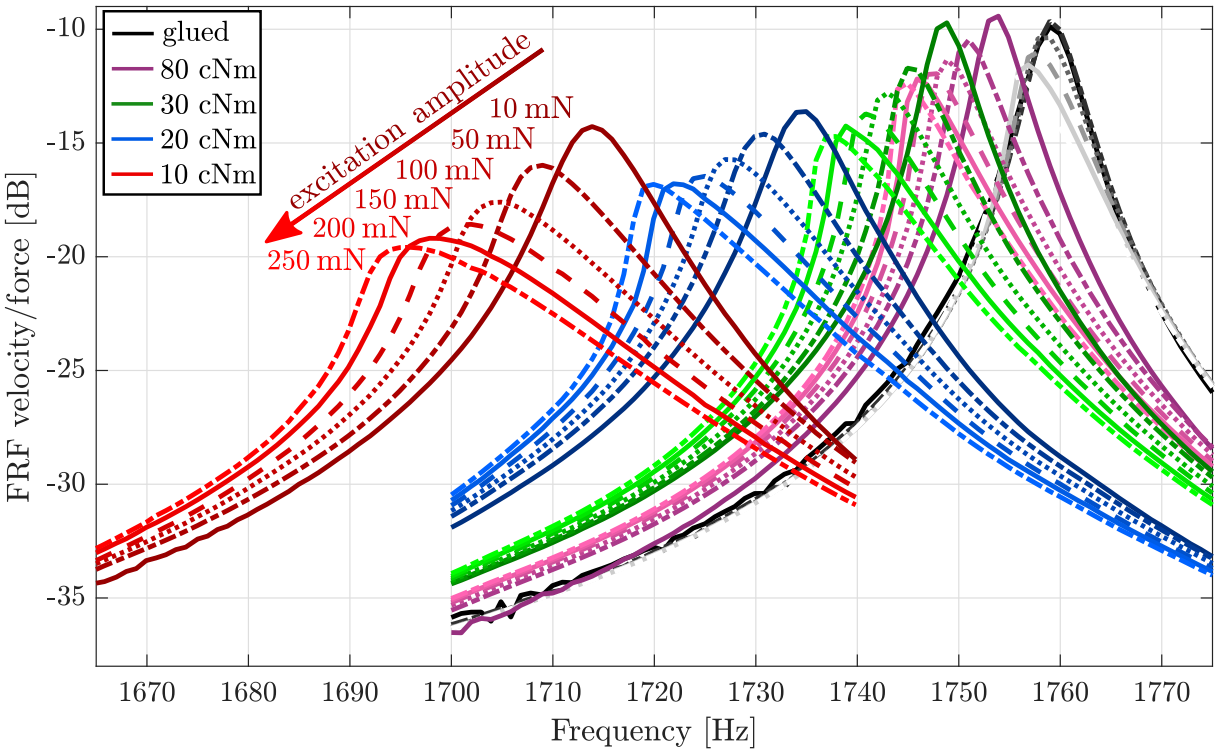

Source: Teloli *et al.* (2022).

Figure 63(c) depicts the evolution of the Δ_{BW} parameter. The −3 dB bandwidth is an estimator that works well in damping, i.e., for linear systems. Nevertheless, it is a popular indicator for people who study vibrations, but one must be careful about what it means.

In the investigations carried out in this work, two mechanisms cause the bandwidth to evolve: energy dissipation by friction and structure softening. Frictional energy dissipation leads to an asymptotic evolution of the vibration attenuation when full slip occurs. But this condition was never reached during testing. The loss of stiffness acts as a softening nonlinearity. It leads to the peak being laid down on the left and the bandwidth being widened if the damping is sufficient. If the damping is not sufficient concerning the softening effect, the bandwidth no longer increases and may even decrease. This happens with 20, 30, 80 cNm tightening torques above the 200 mN amplitude. When both increase simultaneously, the bandwidth increases continuously. This is the case for the 10 cNm torque. Moreover, the estimation of the half-power bandwidth is sensitive to the frequency increment adopted during the step-sine tests. Thus, since the $A_{\max}$ parameter is the reference for computing the half-power bandwidth, its results may show small discrepancies.

Table 8 presents a comparison between the relative variations that the parameters of resonance frequency and amplitude attenuation undergo between the condition of the lowest excitation amplitude (10 mN) to the highest (250 mN). The variations in the response amplitude are relatively more significant than the variations observed in the resonance frequency. As expected, the friction effects on the Orion beam are more pronounced in amplitude attenuation than in stiffness changes.

Table 8 – Variations of Δf_n and $\Delta A_{\max}$ in absolute values.

Torque [cNm]	$\lvert\Delta f_n\rvert$ [%]	$\lvert\Delta A_{\max}\rvert$ [%]
10	1.1	31.18
20	0.86	51.49
30	0.68	23.72
80	0.50	38

Source: Teloli *et al.* (2022).

This beam is intended to be an academic benchmark for the joints community, in which the frictional effects promoted by contact patches are used to improve damping. It is supposed that, when considering higher joint pressures and consequently reduction of micro-slip behavior, the response of the structure would be close to the behavior exhibited by the glued condition. However, the Orion beam paves the way for what could be

Figure 63 – Analysis of the Orion beam around 1665 and 1775 Hz. Torque and level impact on (a) the natural frequency, (b) the maximum amplitude and (c) the half-power bandwidth.

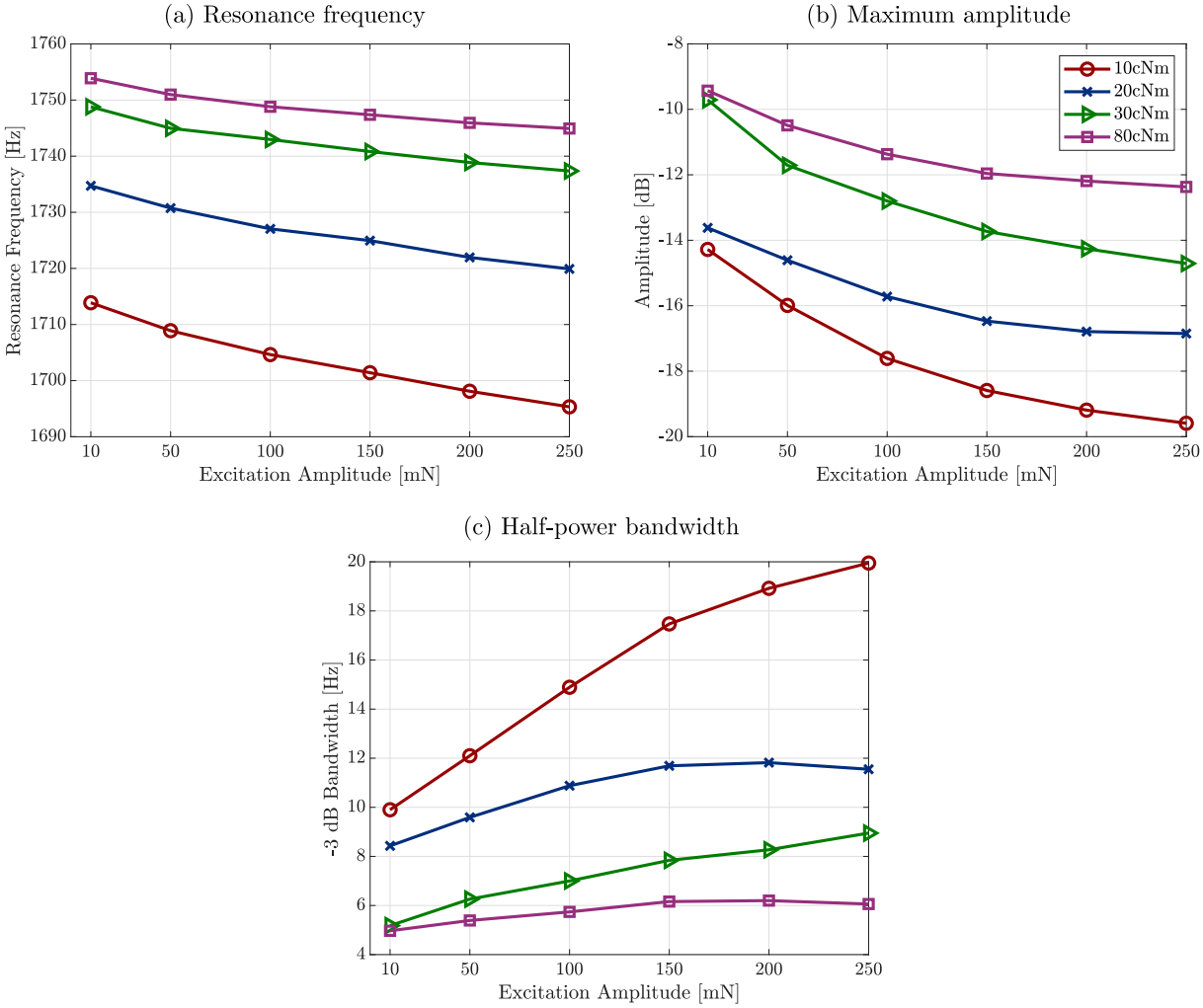

Source: Teloli *et al.* (2022).

explored in jointed structures in terms of taking advantage of the damping intrinsic to these systems without compromising stiffness in applications where amplitude attenuation is of utmost importance, for instance, designing optimization of bolted structures to act as tuned vibration dampers with dry friction damping.

5.5 EVALUATION OF DUFFING VAN-DER POL OSCILLATOR FOR DESCRIBING THE ORION BEAM'S RESPONSE

This section investigates the feasibility of proposing an SDoF model to describe the single-point measurements discussed above around the 6th bending mode of the

Orion beam. Based on the nonlinear amplitude-dependent characteristics observed experimentally in the structure's response, an analytical Duffing-Van der Pol oscillator is considered (MASRI *et al.*, 2004). It is argued that the presence of terms related to both nonlinear damping and nonlinear stiffness can describe the effects of amplitude attenuation and decrease resonance frequencies due to multiple levels of excitation.

The SDoF Duffing-Van der Pol oscillator is given by:

$$m\ddot{q}(t) + c\dot{q}(t) + kq(t) + \underbrace{\beta_n \dot{q}(t) q(t)^2}_{\text{nonlinear damping}} + \underbrace{\alpha_n q(t)^3}_{\text{nonlinear stiffness}} = F(t), \tag{113}$$

where m [kg], c [Ns/m] and k [N/m] are the equivalent mass, damping and stiffness coefficients, respectively, whereas β_n [Ns/m^3] and α_n [N/m^3] are coefficients responsible to project the nonlinear restoring forces on physical basis. Additionally, it is important to point out that the model is not used to directly describe the frictional forces in contact interfaces, but rather the generalized restoring forces that actuate the mode of interest.

Keeping in mind that steady-state measurements were acquired after step-sine tests applied in the resonance frequencies' vicinity, an identification technique is proposed. The methodology is developed into a harmonic balance framework considering a first-order harmonic as a solution:

$$q(t) = \underbrace{j\left(\mathcal{Q} - \overline{\mathcal{Q}}\right)}_{=q_s} \sin(\Omega t) + \underbrace{\left(\mathcal{Q} + \overline{\mathcal{Q}}\right)}_{=q_c} \cos(\Omega t), \tag{114}$$

where q_s and q_c are the harmonic coefficients, $\mathcal{Q}$ and $\overline{\mathcal{Q}}$ are the fundamental harmonic amplitude and its complex conjugate, respectively, measured at the frequency Ω. Once that the fundamental harmonic component at the excitation frequency is the most prominent, providing a way to capture the main characteristics present in the frequency response curves from Fig. 62. Substituting equation (114) into equation (113) and balancing the harmonic terms:

$$(-m\Omega^2 + k)q_s - c\Omega q_c - \frac{\beta_n \Omega}{4}\left(q_c^3 - q_c q_s^2\right) + \frac{3\alpha_n}{4}\left(q_s^3 + q_c^2 q_s\right) = F_e, \tag{115}$$

$$(-m\Omega^2 + k)q_c + c\Omega q_s + \frac{\beta_n \Omega}{4}\left(q_s^3 - q_s q_c^2\right) + \frac{3\alpha_n}{4}\left(q_c^3 + q_s^2 q_c\right) = 0. \tag{116}$$

Given equations (115)-(116), the model parameters are estimated by:

$$\begin{Bmatrix} m \\ c \\ k \\ \beta_n \\ \alpha_n \end{Bmatrix} = \begin{bmatrix} -\Omega^2 q_s & -\Omega q_c & q_s & \frac{\Omega}{4}\left(q_c^3 - q_c q_s^2\right) & \frac{3}{4}\left(q_s^3 + q_c^2 q_s\right) \\ -\Omega^2 q_c & \Omega q_s & q_c & \frac{\Omega}{4}\left(q_s^3 - q_s q_c^2\right) & \frac{3}{4}\left(q_c^3 + q_s^2 q_c\right) \end{bmatrix}^{+} \begin{Bmatrix} F_e \\ 0 \end{Bmatrix}, \tag{117}$$

where $(\bullet)^{+}$ denotes the pseudo-inverse matrix, the parameters are estimated over each torque condition's excitation band frequency. It is worth mentioning the work of Jalali, Ahmadian and Mottershead (2007), which identified a set of parameters used to describe a nonlinear jointed structure through the harmonic balance framework. However, different from the formulation proposed here, which identifies the whole set of parameters present in the model equation based on harmonic components, Jalali, Ahmadian and Mottershead (2007) considered the nonlinear restoring force's computation for each excitation frequency.

The main idea is to identify a unique set of SDoF Duffing-Van der Pol parameters for each tightening torque condition to track the evolution of the equivalent stiffness and damping and thus furnishing a better physical insight into the influence of tightening torque on the system's behavior over a wide range of excitations amplitude.

Table 9 presents the set of parameters calibrated considering the glued condition, whereas Fig. 64 shows the evolution of calibrated parameters as a function of several tightening torque conditions. To emphasize the variations of m, c, k, α_n, and β_n when the preload varies, the identified values of glued condition (Table 9) are considered a reference and then used as normalization scale for other conditions.

Table 9 – Model parameters considering the glued condition for all excitation amplitudes.

m [kg]	c [Ns/m]	$k \times 10^7$ [N/m]	$\beta_n \times 10^{11}$ [Ns/m^3]	$\alpha_n \times 10^{15}$ [N/m^3]
0.0917	2.7946	1.1204	1.4862	-2.0090

Source: Teloli *et al.* (2022).

Based on the estimated parameters, some indicators can be stressed out. On the one hand, note that the equivalent coefficients of mass and stiffness are decreasing as a function of the tightening torque in Fig. 64(a). The formulation employed in equation 113 is equivalent to the representation of uncoupled reduced-order models, which is usually considered to describe full order Finite Element (FE) models but written on the physical

Figure 64 – Evolution of calibrated parameters as function of several tightening torque conditions.

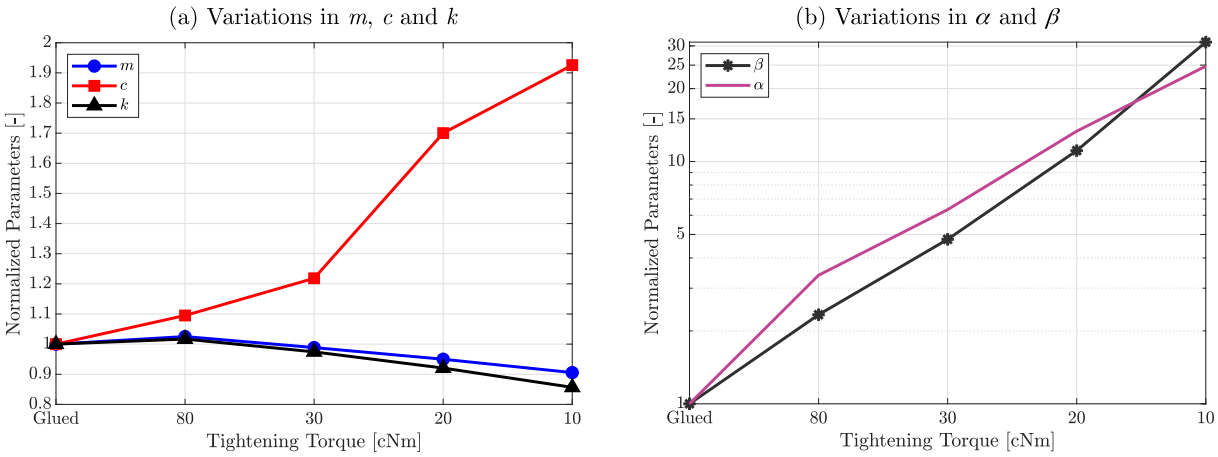

Source: Teloli *et al.* (2022).

basis (FESTJENS; CHEVALLIER; DION, 2014). Notwithstanding the foregoing, the equivalent comparison can also be proposed: $m \equiv \Phi^T \mathbf{M} \Phi$ and $k \equiv \Phi^T \mathbf{K} \Phi$. Assuming the mass matrix constant, whereas the modal mass changes according to the applied torque level, one can note that the mode shapes change. The shape changes are small considering the numerical values and, therefore, validate assumptions made in previous numerical works, which consider that contact nonlinearities alter the mode shapes (FESTJENS; CHEVALLIER; DION, 2013; FESTJENS; CHEVALLIER; DION, 2014). Additionally, the experimental tests used to calibrate the model were performed consecutively without disassembly of the setup. On the other hand, the equivalent damping coefficient almost doubled its value from the glued condition to the preload of 10 cNm, detaching that although m and k are sensitive to preload values changes, it is possible to increase damping, preserving the structural stiffness.

Figure 64(b) depicts the evolution of β_n and α_n for different torque values. These parameters are the projection of nonlinear forces that actuate in the 6th vibrating mode and show a significant increase in nonlinear terms' contribution to the structure's behavior for tightening torques far from the monolithic condition. Moreover, negative values of cubic stiffness α_n are expected once Fig. 62 indicates that the structure presents softening effects.

Figure 65 exhibits a comparison between the predicted frequency response curves for several torque conditions *versus* the experimental ones for a excitation level of 200 mN. Despite its simplicity, the Duffing-Van der Pol model proposed could reproduce with a satisfactory agreement with the experimental measurements. Table 10 presents

the Duffing-Van der Pol model's evaluation through the normalized mean square error (NMSE) between the predicted responses and the experimental measurements for different torque conditions and multiple excitation levels. Note that the model could reproduce better the measurements for the conditions glued and 80 cNm, since for high preload values, the structure behavior is moderately altered by the presence of nonlinear effects. Despite the differences between the model and experimental measurements, the results have demonstrated that the excitation design could uncouple the bending mode, allowing the SDoF nonlinear model to reproduce the dynamics of the Orion beam present in the frequency response curves properly. Additionally, the identification strategy has proven to operate well, assuming the available experimental data from a single-point measurement.

Figure 65 – Comparison between the frequency response curves predicted by the Duffing-Van der Pol model (dashed lines — —) *versus* experimental measurements (solid lines ———) for different torques (Glued, 80 cNm, 30 cNm, 20 cNm and 10 cNm) considering an excitation amplitude of 200 mN.

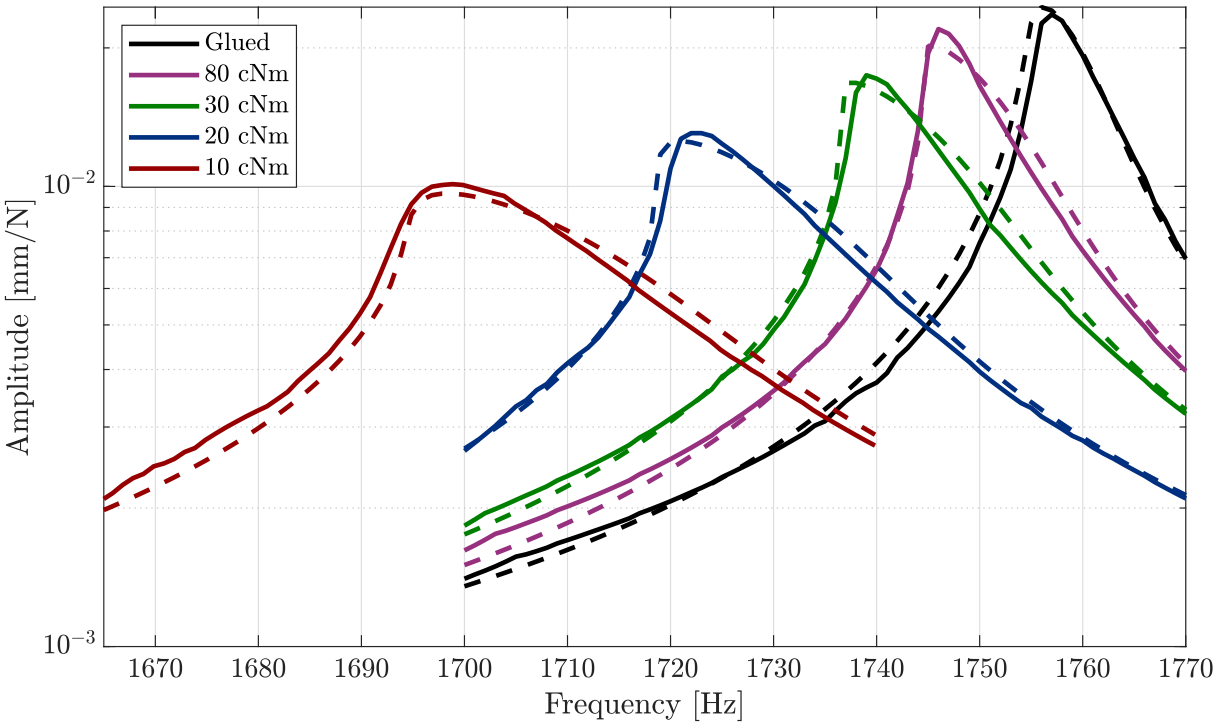

Source: Teloli *et al.* (2022).

Several works propose to approximate isolated nonlinear modes of bolted structures based on SDoF models, such as those presented by Eriten *et al.* (2013) and Segalman *et al.* (2015). A convenient discussion raised in both papers is that a single parametric model resulting from a specific data condition will not be globally descriptive. In parallel to this work, the same occurs with the Duffing-Van der Pol model proposed since, for each torque condition, a set of parameters had to be estimated. A limitation of the model that

Table 10 – Normalized mean square error between analytical responses and experimental data for several tightening torque conditions and multiple excitation level.

NMSE [%]	10 cNm	20 cNm	30 cNm	80 cNm	Glued
10 mN	6.79	6.34	6.01	5.38	5.09
50 mN	6.68	6.42	6.16	5.41	4.96
100 mN	6.66	6.37	6.05	5.26	4.63
150 mN	6.65	6.07	5.80	5.00	4.16
200 mN	6.53	5.73	5.44	4.67	3.80
250 mN	6.39	5.62	5.09	4.50	3.72

Source: Teloli *et al.* (2022).

needs further investigation is its ability to predict the response for force values beyond 250 mN for low torque values such as 10 cNm, 20 cNm, and 30 cNm, since other effects are linked to micro-scale dynamics of the contact patches may be underestimated. Due to the polynomial form of the nonlinearity present in the proposed oscillator, it is also concluded that it would not be a satisfactory approximation for situations in which the structure undergoes macro slip, an effect that non-smooth models can characterize (FANTETTI *et al.*, 2019).

5.6 CONCLUDING REMARKS

This work presented an overview of good practices for designing and experimenting with dynamically excited jointed structures, aiming to provide more vibration damping without compromising structural integrity. These aspects were addressed considering the Orion beam, a new lap-joint configuration with small contact patches at each bolt connection. The central bolt is responsible for maintaining the nominal frequency by setting the normal load with the fully tightening torque condition, whereas the external bolts experience several tightening torques to assess how the friction effects affect the system's damping.

The experimental setup considered the clamped-free boundary condition and a shaker attached close to the Orion beam's clamped end. Step-sine tests were adopted to study the dynamic behavior of the assembled system. The interface load showed higher nonlinear properties. A feedback controller was designed to perform an amplitude control, thus avoiding the force drop-off phenomenon in the resonance frequencies' vicinity. Regarding the Orion beam's design, results from subsection 5.4.1 related to the 3rd bending mode introduced the influence of contact patches on the dynamic behavior of the structure.

One could verify that the contribution of the central patch to the system's damping is of less importance when compared to the contribution of the external ones.

Although there exist pronounced variabilities in the system's response after complete assembly and disassembly procedures, the structure maintained impressive repeatability after several experimental measurements without complete disassembly (see subsection 5.4.2). In addition, contact patches, which are proper to retain the contact interface on a small area, minimized dynamic clearances and provided a contact pressure slightly sensitive to shape imperfections.

The effects of amplitude attenuation proved to be quite sensitive to changes in the tightening torque applied in the external bolts. The Orion beam presented a more significant attenuation of the vibration amplitude for lower tightening values, as showed Fig. 60, even operating in the linear regime of motion. The results show that it is possible to benefit amplitude attenuation without significant losses in the contact stiffness. Alternatively, this feature paves the way for proposing new control techniques of the vibration amplitude in jointed structures based on the applied bolt preload. However, caution with this approach is advised since it has only be demonstrated on the present system configuration.

In comparison to the results presented for the 3rd mode, it is noted for the 6th mode that besides substantial vibration amplitude attenuation, there is also a variation in frequency related to the softening effect for higher excitation amplitudes. Thus, from the frequency curves of both vibration modes, the results suggest that more pronounced displacements in the vicinity of the central patch may lead to micro slip, but of less importance than external patches when considering torque values of 10, 20 and 30 cNm.

Furthermore, although the nonlinear behavior of the curves presented in Fig. 62 was expected, i.e., the presence of softening effects as the excitation amplitude increases, the new lap-joint configuration separated well the correlations between the parameters analyzed for several torques and excitation amplitudes since there is no overlapping among different curves and conditions, as illustrated in Fig. 63. Therefore, this new lap-joint and the results obtained can refer to researchers who wish to develop methods for predicting damping in joints.

A Duffing-Van der Pol oscillator was proposed to approximate the experimental measurements analytically. Simultaneously, the model parameters could provide physical insight into how different tightening torque affects the Orion beam's behavior. The parameters were estimated into a harmonic balance identification framework, as described

in section 5.5. The performance of the model could be improved by considering more harmonic terms in the solution proposed. However, the analytical responses predicted the primary characteristics present in the frequency response curves for several tightening torques and multiple excitations amplitude. The equivalent stiffness was moderately altered for several preload, whereas the equivalent damping almost doubled its value from the glued condition to the low preload condition due to patches in the Orion beam design.

Finally, the whole experimental measurements presented in this work, including the geometry design data, are open access. We suggest using this design and experimental tools to characterize the friction dissipation through the damping patches, induced micro-sliding, roughness, and flatnesses on the joint interface, to facilitate new techniques to measure and predict the nonlinear behavior jointed structures.

Still in the context of models to represent isolated vibrating modes, the next chapter presents the use of the GP-NARX model applied to the BERT benchmark to emulate its nonlinear behavior.

6 NON-PARAMETRIC APPROACH FOR PREDICTING HYSTERETICAL BEHAVIOR OF JOINTS

Although the advance in FE methods has been significant, some applications involving bolted joints, such as detection of bolt loosening for structural health monitoring (SHM) purposes (LI; JING, 2020; LI; JING, 2017), require predictive models that demand relatively less-expensive computational cost while only relying on input and output data. Towards this objective, data-based models that do not depend directly on physical parameters to be identified, so-called black-box models, emerge as an alternative to model structures assembled by bolted joints, despite being only slightly explored within this context identify hysteretic systems. Worden *et al.* (2007) surveyed identification techniques structured in grey and black-box approaches to predict friction effects present in a tribometer device by using, for instance, Nonlinear Autoregressive with eXogenous inputs (NARX) and neural networks models. Later, Worden and Barthorpe (2012) proposed using a NARX structure with model parameters expanded into a non-polynomial basis function to identify the input-output process of a Bouc-Wen oscillator. Leva and Piroddi (2002) presented a NARX-based modeling strategy to describe hysterical dynamic behavior for control purposes of magnetorheological dampers. Although the authors consider an approach that the NARX model is not polynomial but preserves linearity in its parameters, only one-step-ahead predictions were performed. Those future output predictions depend on the previously actual output measurements of the system under analysis. Then, to generalize polynomial NARX models for describing systems with hysteresis, Martins and Aguirre (2016) introduced a new way to construct NARX models by using the concept of bounding functions that seek to encode the hysteresis loop into the structure of such models for estimating the data produced by a magnetorheological damper. Noël *et al.* (2017) proposed a framework to identify the dynamic behavior of a Bouc-Wen model benchmark based on the nonlinear state-space approach expanded into a nonlinear polynomial basis. However, a potential limitation of black-box models lies in the

fact that the model structure should be carefully selected to reproduce the memory effect of hysteresis (input-output dependency (VISINTIN, 2013)) while avoiding these models from being restricted to reproduce only output signals with the same characteristics used during their identification process.

In order to address the above-mentioned technical issues that black-box models may have in capturing hysteresis, this work aims to examine the GP-NARX model's benefits to predict the dynamic output signals from structures assembled by bolted joints. This model combines the machine learning Gaussian Process (GP) regression model with the NARX framework, providing a representation of the system of interest with natural probabilistic confidence intervals based on the model uncertainties. The inclusion of the confidence intervals makes the GP-NARX framework very suitable for decision processes, like those required in SHM applications. One of the main advantages of considering the GP-NARX model over other non-parametric models is that it considers the Bayesian inference to learn from the available data, which decreases the possibility of overparameterizing the nonlinear function responsible for mapping the output given a known input. Furthermore, the inference is performed directly over the nonlinear function that describes the input-output relation, not over model parameters. Therefore, the Bayesian inference is commonly used to estimate nonlinear models based on models' parameters estimation. It is also important to highlight that, still, in comparison with other non-parametric models, the model used in this work does not require prior knowledge of its structure (model order), as the classic approach made by NARX models (BILLINGS, 2013). Moreover, GP-NARX is a nonlinear model class widely known in the machine learning community, with recent applications for identification purposes in engineering (KOCIJAN *et al.*, 2005), including the wave force prediction on offshore structures (WORDEN *et al.*, 2018) and the identification of the vertical flow of water in the cascaded tanks benchmark (SCHOUKENS *et al.*, 2016; WORDEN *et al.*, 2018). This model should help monitor the hysteresis' fluctuations qualitatively caused by loss of torque applied in the bolts using indirect measurement data.

This Chapter begins with a brief description of the method, presenting the main aspects of identifying the GP-NARX model throughout section 6.1. For further details, the readers are invited to find more information in the literature made accessible. Then, section 6.2 outlines the step-by-step procedure to construct the GP-NARX model used in this work to reproduce the behavior of dynamic systems with a hysteresis. Next, to evaluate the applicability of the model to describe hysteretic systems, section 6.3 provides a numerical application of the GP-NARX model to approximate the outputs

and hysteresis loops of the Bouc-Wen benchmark proposed by Noël and Schoukens (2016b). Then, after establishing a methodology of model identification for the numerical benchmark with hysteresis, section 6.4 presents a practical application of the proposed model to reproduce the nonlinear dynamic behavior present in the first vibrating mode of a structure with a lap-type bolted joint connection, named as BoltEd stRucTure (BERT). Finally, section 6.5 reports the final remarks, main conclusions, and the path forward for future inquiry.

6.1 GP-NARX model

A GP regression model is based on the idea of Bayesian inference; however, unlike the inference of the model's parameters used in classic Bayesian regression, the GP model considers the inference directly over functional space (WILLIAMS; RASMUSSEN, 2006). Thus, this model can be described as a generalization of a Bayesian regression method, in which any two or more observations that one wants to describe follow a multivariate Gaussian distribution (SCHULZ; SPEEKENBRINK; KRAUSE, 2018). In this sense, consider a general regression problem to represent the process observations $y_i \in \mathbb{R}$ as

$$y_i = f(\mathbf{x}_i) + \varepsilon_i^{(y)}, \quad i = 1, 2, \ldots, N \text{ samples} \tag{118}$$

where $f(\cdot)$ is a nonlinear function mapping the output to an input $\mathbf{x}_i \in \mathbb{R}^D$, and $\varepsilon_i^{(y)}$ is a stochastic variable representing inherent randomness in the observations. This randomness is assumed to be Gaussian distributed with zero mean

$$\varepsilon_i^{(y)} \sim \mathcal{N}\left(\varepsilon_i^{(y)} | 0, \sigma_y^2\right), \tag{119}$$

where σ_y^2 is the variance of the Gaussian noise observations.

In this work, in order to map the nonlinear effects related to the hysteresis, the NARX structure is considered as a nonlinear function that predicts the output y_i. Thus, the model's input $\mathbf{x}_i$ is formed by regression upon the excitation and output signals

$$\mathbf{x}_i = \left[y_{i-1}, ..., y_{i-n_y}, u_i, u_{i-1}, ..., u_{i-n_u+1}\right]^{\mathrm{T}}, \tag{120}$$

where u_i represents the oscillatory input signal at the i^{th} sample, and n_u and n_y are the number of regressors in the input and output signals, respectively.

Keeping in mind that the regression in equation (118) is represented by a Gaussian

Process, the NARX structure $f(\mathbf{x}_i)$ is then formed by the assumption of a multivariate Gaussian prior distribution of zero mean

$$\mathbf{f} = f(\mathbf{x}_i) \sim \mathcal{N}(\mathbf{f}|0, \mathbf{K}), \tag{121}$$

resulting in the so-called GP-NARX model structure, where $\mathbf{K} \in \mathbb{R}^{N \times N}$ is the covariance matrix whose elements are described as $\mathbf{K}_{i,j} = k(\mathbf{x}_i, \mathbf{x}_j)$. The variable $k(\cdot, \cdot)$ is a covariance function, also named a kernel function, that models the dependence between the function values at different input samples. Due to the versatility in the GP-NARX model, the zero mean is assumed for simplicity.

The construction of the model function used for the regression process depends directly on the knowledge acquired about the system of interest. Thus, assuming a set of training data available and making use of a simplified notation, one obtains

$$\mathscr{D} = (\mathbf{x}_i, y_i)_{i=1}^{N} \equiv (\mathcal{X}, \mathcal{Y}), \tag{122}$$

where $\mathcal{X} \in \mathbb{R}^{N \times D}$ is the regression matrix, and $\mathcal{Y} \in \mathbb{R}^{N}$ is the output vector. Since data observations for training contribute Gaussian white noise, the joint distribution of the training data and test samples, according to the prior distribution, is given by (WILLIAMS; RASMUSSEN, 2006)

$$\begin{pmatrix} \mathcal{Y} \\ \mathbf{f}_* \end{pmatrix} \sim \mathcal{N}\left(\begin{pmatrix} \mathcal{Y} \\ \mathbf{f}_* \end{pmatrix} \middle| 0, \begin{bmatrix} \mathbf{K}(\mathcal{X}, \mathcal{X}) + \sigma_y^2 \mathbf{I} & \mathbf{K}(\mathcal{X}, \mathbf{x}_*) \\ \mathbf{K}(\mathbf{x}_*, \mathcal{X}) & \mathbf{K}(\mathbf{x}_*, \mathbf{x}_*) \end{bmatrix} \right), \tag{123}$$

where $\mathbf{f}_*$ denotes the predicted function at new input samples $\mathbf{x}_*$. $\mathbf{K}(\mathcal{X}, \mathcal{X})$ is the covariance matrix computed between the training input samples each other with elements $k(\mathbf{x}_i, \mathbf{x}_j)$, $\mathbf{K}(\mathcal{X}, \mathbf{x}_*)$ is the covariance matrix computed between the training and new input samples with elements $k(\mathbf{x}_i, \mathbf{x}_*)$ and $\mathbf{K}(\mathbf{x}_*, \mathcal{X}) = \mathbf{K}(\mathcal{X}, \mathbf{x}_*)^T$. Finally, $\mathbf{K}(\mathbf{x}_*, \mathbf{x}_*)$ is the covariance matrix between the new input samples and $\mathbf{I} \in \mathbb{R}^{N \times N}$ is an identity matrix.

Then, the Bayesian inference strategy is used to condition a posterior predictive distribution $\pi(\mathbf{f}_*|\mathbf{x}_*, \mathcal{X}, \mathcal{Y})$ over $\mathbf{f}_*$ based on the new available input, which gives the main relationship for the GP regression (WILLIAMS; RASMUSSEN, 2006)

$$\pi(\mathbf{f}_*|\mathbf{x}_*, \mathcal{X}, \mathcal{Y}) \sim \mathcal{N}(\mathbf{f}_*|\mu_*, \sigma_*^2), \tag{124}$$

where the posterior predictive mean is given by

$$\mu_* = k(\mathbf{x}_*, \mathcal{X}) \left[\mathbf{K}(\mathcal{X}, \mathcal{X}) + \sigma_y^2 \mathbf{I}\right]^{-1} \mathcal{Y}, \tag{125}$$

and the posterior predictive variance is given by

$$\sigma_*^2 = k(\mathbf{x}_*, \mathbf{x}_*) - \mathbf{K}(\mathbf{x}_*, \mathcal{X}) \left[\mathbf{K}(\mathcal{X}, \mathcal{X}) + \sigma_y^2 \mathbf{I}\right]^{-1} \mathbf{K}(\mathcal{X}, \mathbf{x}_*). \tag{126}$$

Using equations (125)-(126), one can predict the new values of the function $\mathbf{f}_*$ as well as the values of $\mathbf{y}_*$ taking into account the model uncertainties, once both predictive distributions are similar. The variance σ_y^2 and the covariance function $k(\cdot, \cdot)$ need to be estimated based on the available data from the system under analysis. Many covariance functions were proposed over the years, with special attention to RBF, Exponential, Matérn 3/2, Matérn 5/2, Polynomial, Rational Quadratic, among others. The choice of the best kernel structure depends on the relations between the input/output data and the previous knowledge available on the system behavior. It is noteworthy that new kernel functions can also be proposed, just by considering a new formulation or even making use of a combination of existing functions (SEEGER, 2004). In the context of this work, which explores the application of the GP-NARX model to represent hysteretic systems, the best results were achieved, considering the available data, by selecting a combination of two covariance kernels:

- Matérn 3/2:

$$k_1(\mathbf{x}, \mathbf{x}') = \sigma_m^2 \left(1 + \frac{\sqrt{3}\,|\mathbf{x} - \mathbf{x}'|}{l}\right) \exp\left(-\frac{\sqrt{3}\,|\mathbf{x} - \mathbf{x}'|}{l}\right), \tag{127}$$

  where σ_m is the Matérn kernel variance and l the lengthscale.

- Cubic polynomial:

$$k_2(\mathbf{x}, \mathbf{x}') = \sigma_p^2 \left[s(\mathbf{x}\mathbf{x}') + b\right]^3, \tag{128}$$

  where σ_p is the Polynomial kernel variance, s the scale and b the bias parameter.

Thus, the new additive kernel is given by

$$k(\mathbf{x}, \mathbf{x}') = k_1(\mathbf{x}, \mathbf{x}') + k_2(\mathbf{x}, \mathbf{x}'). \tag{129}$$

Based on the unknown variables in the kernel, a vector of hyperparameters may be defined as $\boldsymbol{\Theta} = \left[\sigma_m^2, l, \sigma_p^2, s, b, \sigma_y^2\right]$ and then estimated by conducting a maximization of the marginal log-likelihood of the observed data (MATTOS *et al.*, 2016)

$$\log \pi(\mathcal{Y}|\mathcal{X}, \boldsymbol{\Theta}) = -\frac{1}{2} \log |\mathbf{K} + \sigma_y^2 \mathbf{I}| - \frac{1}{2} \mathcal{Y}^{\mathrm{T}} (\mathbf{K} + \sigma_y^2 \mathbf{I})^{-1} \mathbf{y} - \frac{N}{2} \log(2\pi). \tag{130}$$

Such a maximization procedure is performed using a gradient method, and the optimum model is used to predict new outputs as a consequence of new inputs. As a result, the GP-NARX model can describe a wide variety of structural dynamic behavior, taking advantage of its capability to consider modeling uncertainties and predicting the trend curves of outputs with probabilistic confidences.

The GP-NARX model will be used as a surrogate model to predict the hysterical behavior present in complex systems dynamics. As mentioned previously, the advantage of dealing with the GP-NARX model when compared to the classic NARX model (BILLINGS, 2013) lies in the possibility of estimating the nonlinear relation between the regressors and the output based directly on the inference over the training data, which is a feature of GP regression, only by knowing the maximum number of input/output lags (n_y and n_u) (WORDEN *et al.*, 2018).

6.2 IDENTIFICATION FRAMEWORK

The identification workflow proposed herein may be stated as follows:

- *Step 1: Data acquisition*

Systems with hysteresis present more pronounced nonlinear energy dissipation, which can be visualized through the opening of the hysteresis loops, increasing the response amplitude (FESTJENS; CHEVALLIER; DION, 2013). Depending on the excitation amplitude applied these systems also present changes in their resonant frequencies due to hardening or softening effects. In these circumstances, identifying the GP-NARX model is conducted considering training data generated by swept sine excitation tests in the resonant frequency vicinity. These tests were also used in the *Model verification* step, but considering different excitation amplitudes from those used during the *Model training* step. Stationary sinusoidal testing and white noise signals with several excitation amplitudes were considered to validate the proposed GP-NARX model. In numerical simulations it is interesting to add some synthetic white noise, avoiding overparameterization and making the inversion of the matrix $\left[\mathbf{K}(\mathcal{X},\mathcal{X}) + \sigma_y^2\mathbf{I}\right]$ easier when strongly correlated training data is considered.

- *Step 2: Model training*

This step comprises the optimization of hyperparameters $\boldsymbol{\Theta}$ by maximizing the

marginal log-likelihood from equation (130) and also the estimation of the maximum number of input/output lags. Based on the training data $(\mathcal{X}, \mathcal{Y})$, a surface involving the number of lags and the output fit measured at each combination of lags is constructed. The model-fit, which corresponds to the mean relative square error (MSRE) metric, is evaluated by the following formulation

$$fit\,[\%] = 100 \times \left(1 - \sqrt{\frac{\sum_{i=1}^{N} \left(y_{\text{exp,i}} - \mu(\hat{y}_i)\right)^2}{\sum_{i=1}^{N} y_{\text{exp,i}}^2}} \right), \tag{131}$$

where $y_{\text{exp,i}}$ is the experimental output signal and $\mu(\hat{y}_i)$ is the model mean output signal, both at the i^{th} instant of time. With the surface $(n_y \times n_u \times fit)$ estimated, the number of lags is chosen in the region that guarantees the best value of fit using a minimal number of lags. Of course, using a different output signal in the lag estimations from the one used in the model training step produces a better description of the system's dynamics.

- *Step 3: GP-NARX model verification and validation*

The model's predictive capability must be assessed once the model with the lags and hyperparameters has been defined. The reader will see that when we consider *infinite-step-ahead* prediction or *model predicted output* (BILLINGS, 2013), those future output predictions depend on the previously predicted one that is approximated as a Gaussian random variable, defined by its mean μ_y and variance σ_y^2. As a consequence, the GP-NARX formulation is affected by the backpropagation of the model uncertainties. Depending on the covariance function chosen, the backpropagation of the uncertainties may be computed analytically (CANDELA *et al.*, 2003). However, for a more general formulation based on the model-predicted output as used in this paper, Monte Carlo simulations are instead used to propagate all the model uncertainties, using the estimated Gaussian distribution (ROBERT; CASELLA, 2010).

6.3 NUMERICAL ASSESSMENT OF THE GP-NARX MODEL: THE BOUC-WEN BENCHMARK

This section introduces the use of the GP-NARX model first in a numerical application involving the Bouc-Wen benchmark already presented in Chapter 3, which is given by

(NOËL; SCHOUKENS, 2016b)

$$m\ddot{y}(t) + c\dot{y}(t) + ky(t) + \mathcal{Z}(y,\dot{y}) = u(t) \tag{132}$$

$$\dot{\mathcal{Z}}(y,\dot{y}) = \alpha\dot{y}(t) - \beta\left(\gamma|\dot{y}||\mathcal{Z}(y,\dot{y})|^{\nu-1}\mathcal{Z}(y,\dot{y}) + \delta\dot{y}(t)|\mathcal{Z}(y,\dot{y})|^{\nu}\right), \tag{133}$$

where m [kg], c [Ns/m] and k [N/m] are the mass, damping and stiffness coefficients, respectively, and α [N/m], β, γ [m^{-1}], δ [m^{-1}], and ν are the Bouc-Wen model parameters. Additionally, $\ddot{y}(t)$ [m/s^2], $\dot{y}(t)$ [m/s], and $y(t)$ [m] are the acceleration, velocity, and displacement, respectively, for an excitation input $u(t)$ [N]. $\mathcal{Z}(y,\dot{y})$ [N] represents the hysteretic restoring force which obeys the ordinary differential equation (133) of $\dot{\mathcal{Z}}(y,\dot{y})$ [N/s]. This model presents challenging issues for conventional system identification techniques such as the existence of a hysteretic force with multiple solutions (non-smooth nonlinearity), memory dependency, the presence of multiple harmonics in the oscillator output, among others. Further details involving the hysteretic benchmark are also addressed by Bajrić and Høgsberg (2018), Rebillat and Schoukens (2018), Teloli and Silva (2019) and Miguel, Teloli and Silva (2020).

Table 11 shows the model parameters selected according to (NOËL; SCHOUKENS, 2016b). All simulations with the benchmark presented in this work use a sampling frequency of 750 Hz. The oscillator's responses were obtained through a numerical integration scheme with the 4^{th} order Runge-Kutta method and variable time-step.

Table 11 – Bouc-Wen benchmark parameters (NOËL; SCHOUKENS, 2016b).

m [kg]	c [Ns/m]	k [N/m]	α [N/m]	β	γ [m^{-1}]	δ [m^{-1}]	ν
2	10	5×10^4	5×10^4	1×10^3	0.8	-1.1	1

Source: Teloli *et al.* (2021).

It should be pointed out that the objective herein is to predict the Bouc-Wen oscillator's response described in equations (132) and (133) bounded by probabilistic confidence intervals produced by the GP-NARX model. This work is different from that proposed by Bhattacharyya, Jacquelin and Brizard (2020), who consider a stochastic version of the Bouc-Wen oscillator described by random variables and then use the Kriging-NARX model to predict its response. Unlike the GP-NARX version, which takes into account the inference over functions, the Kriging-NARX model considers the stochastic expansion of the NARX model's coefficients and then becomes not helpful to describe dynamic systems subject to white noise excitation for predicting statistically characterized responses.

6.3.1 Model training

One of the main aspects to be considered in constructing a numerical model is related to the training data and how these are conditioned to the excitation signal applied in the dynamic system. Some key elements should be highlighted within this context, such as the system operating range, vibration modes of interest, whether the nonlinearity is amplitude-dependent or frequency-dependent, and so on. The GP-NARX model is constructed considering swept sine tests in the resonance frequency vicinity to encode and reproduce this nonlinearity from the hysteretic oscillator. Such tests provide an attractive, cost-effective ratio between the excitation level amplitude, frequency control, and testing time (particularly for practical applications).

Thus, the training data $(\mathcal{X}, \mathcal{Y})$ used for the GP-NARX model inference and estimation of hyperparameters Θ consist of a pair of responses of the Bouc-Wen oscillator for a swept sine test applied from 5 up to 150 Hz, with input amplitude levels of 10 and 80 N (low and high) and both with a frequency increase rate of ≈ 53 Hz/s. Additionally, to emulate experimental conditions during the training, verification, and validation steps of the GP-NARX model construction, white noise was added to the response data, considering 10% of the total energy of the response signal for input with the lowest level of excitation amplitude (10 N).

In the lag optimization procedure, the GP-NARX model is estimated several times, considering different combinations of n_u and n_y. In contrast, the model performance is measured using Eq. (131), taking into account the same swept sine test, with an input amplitude level of 50 N (medium). Using a different amplitude signal improves the procedure, ensuring that the number of lags will be satisfactory in different motion regimes. Figure 66 presents the lags optimization surface with emphasis on the optimal values found, which correspond to the regression order of $n_y = 20$ lags in the output and $n_u = 17$ lags in the input for a fit of 92.4%. Then, having defined the model structure, the next step lies in verifying its performance to reproduce the Bouc-Wen oscillator's responses by assuming sweep sine signals with the same characteristics and several excitation amplitudes.

Figure 66 – Lags optimization surface $n_y \times n_u \times fit$. The optimal value of the lags (•) corresponds to 20 lags in the output and 17 lags in the input for a fit of 92.4 %.

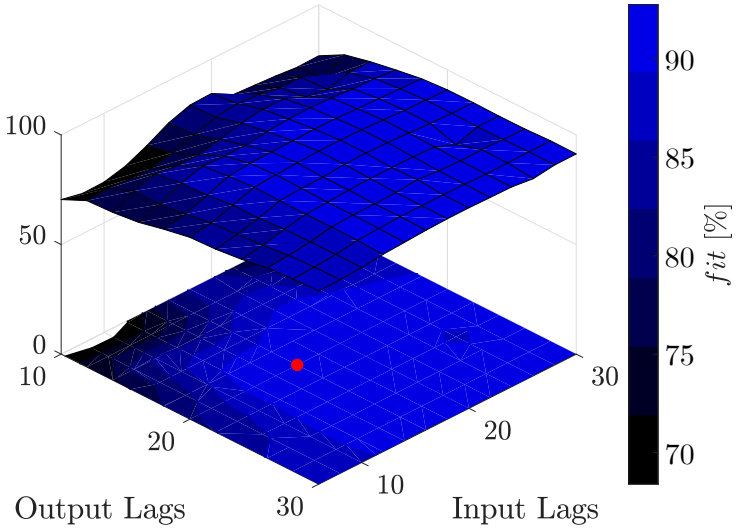

Source: Teloli *et al.* (2021).

6.3.2 GP-NARX model verification and validation

Throughout this subsection, all the model statistics were estimated considering the backpropagation of uncertainties through Monte Carlo simulations with 1024 samplings, ensuring that all the model uncertainty is considered in the predictions. Additionally, all figures consider 99% statistical confidence bounds.

Figure 67 presents the assessment of the GP-NARX model, considering a low level of excitation amplitude (10 N). Figs. 67(a) and (b) depict the model-predicted output in direct comparison with the displacement response of the Bouc-Wen model. The results show that the confidence bounds could accommodate the model's response, with a narrower band in the resonance region than near the end of the signal (≈ 1.5 and 2 seconds), primarily due to signal-to-noise. Figure 67(c) shows a close-up view of the power spectrum density (PSD) of responses over a frequency range of 5 – 150 Hz, evidencing that the model-predicted output carries the same frequency content as the Bouc-Wen oscillator response. All spectra presented throughout this subsection for sweeping sine tests have been calculated with Welch's periodogram, considering a rectangular window over the entire signal length. Figure 67(d) exhibits the numerically integrated hysteresis loop compared to the predicted one. Although the hysteresis loop is almost closed to a low level of excitation amplitude, the black-box model can accommodate the system's accuracy with hysteresis, having the model mean output enclosing substantially the same area Bouc-Wen oscillator in the restoring force *versus* displacement plane.

Figure 67 – Verification of the GP-NARX model for low excitation amplitude (10 N) considering a swept sine test. ▓ represents the 99% model-predicted output confidence bands, — is the model response mean and • represents the Bouc-Wen data obtained by numerical integration.

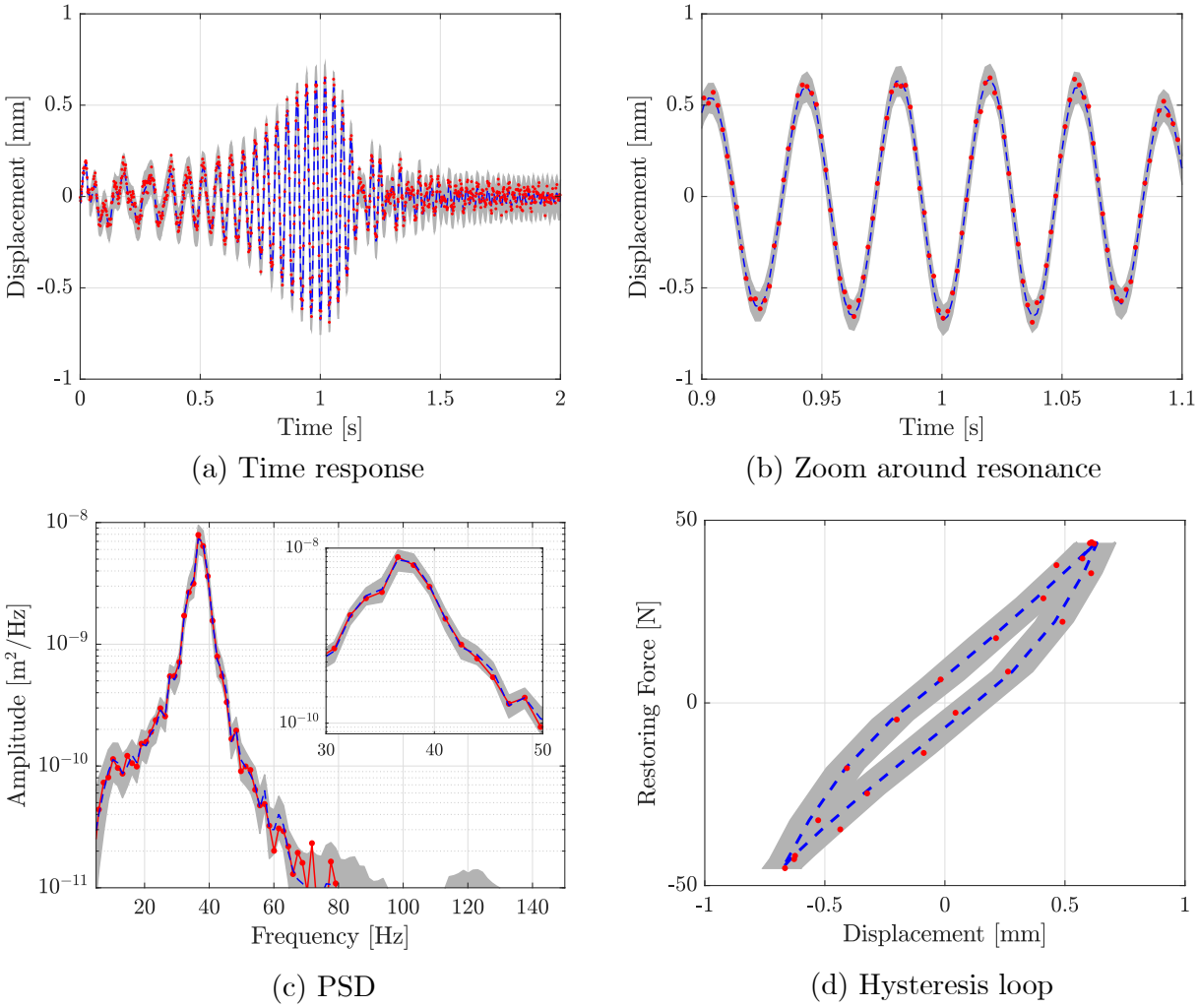

(a) Time response

(b) Zoom around resonance

(c) PSD

(d) Hysteresis loop

Source: Teloli *et al.* (2021).

Figures 68 and 69 exhibit the model-predicted output with 99% of statistical confidence in comparison with Bouc-Wen data for two levels of excitation amplitude, medium (50 N) and high (80 N), respectively. From these figures, note that the GP-NARX model can reproduce the dynamics of the Bouc-Wen's oscillator even at higher excitation amplitudes, where the effects of nonlinear energy dissipation are evidenced through the pronounced opening of hysteresis loops. A comparison between the spectra of Figs. 67(c), 68(c) and 69(c) shows that the model is able to follow the hardening effect present in the Bouc-Wen oscillator ($\gamma + \delta < 0$) (BABER; WEN, 1981), which is characterized by increasing the resonance frequency for higher response amplitudes.

It is also important to note that the confidence bounds for a higher excitation level

are narrower about the mean prediction. This is due to the lower signal-to-noise in higher amplitude signals and the fact that the model uncertainty is lower in regions close to the training data.

Figure 68 – Verification of the GP-NARX model for medium excitation amplitude (50 N) considering a swept sine test. ■ represents the 99% model-predicted output confidence bands, — is the model response mean and • represents the Bouc-Wen data obtained by numerical integration.

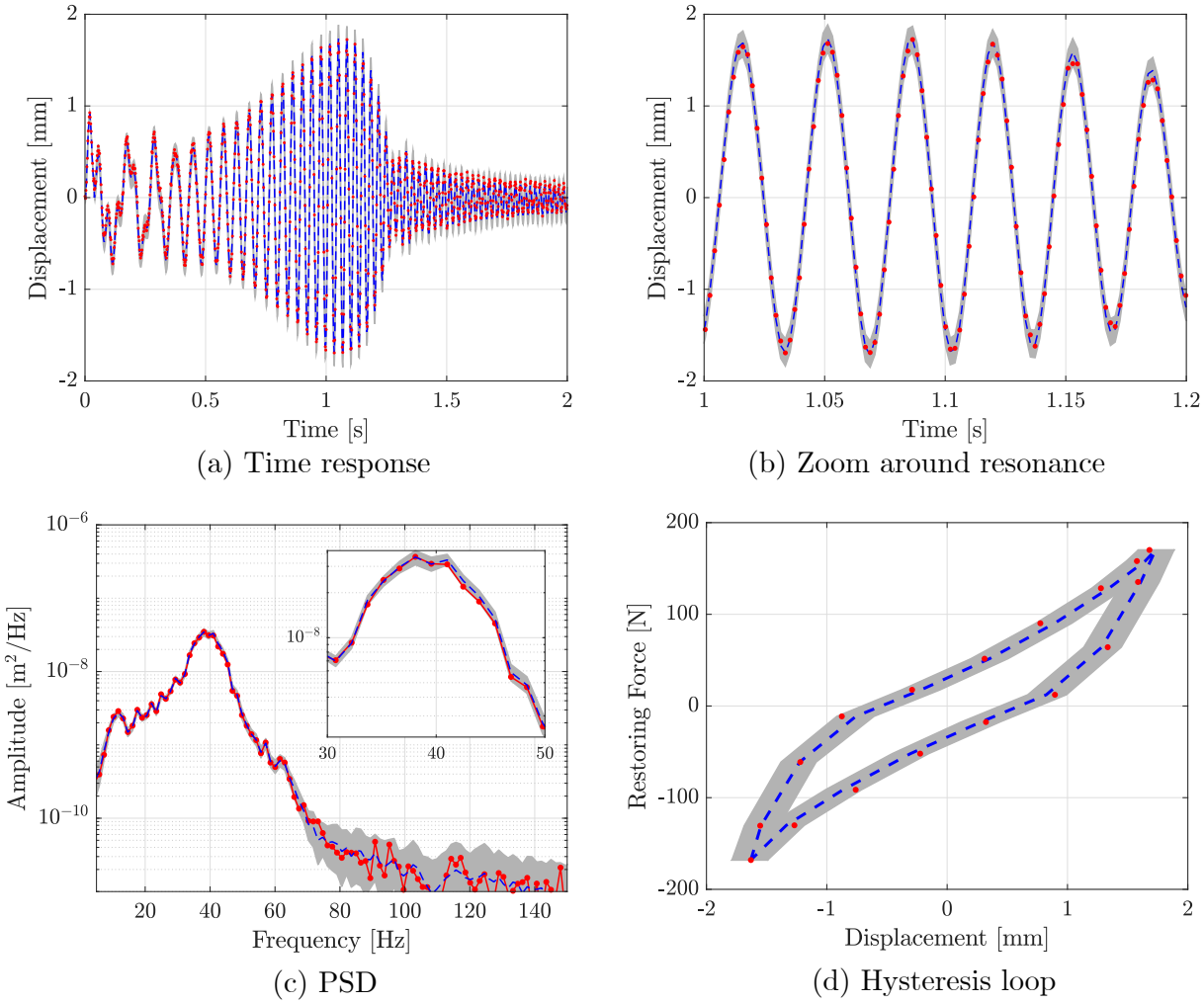

(a) Time response (b) Zoom around resonance

(c) PSD (d) Hysteresis loop

Source: Teloli *et al.* (2021).

In general, the construction of black-box models may involve some pitfalls. One of them is that these models can be over-conditioned by the training data used in their construction, such as the Kriging-NARX model proposed by Bhattacharyya, Jacquelin and Brizard (2020). In other words, this might mean that a model identified to describe a nonlinear system based on sinusoidal inputs as training data may only reproduce the responses of such a system that feature the same characteristics in the input. In this context, this subsection discusses the robustness and validity of the GP-NARX model in

Figure 69 – Verification of the GP-NARX model for high excitation amplitude (80 N) considering a swept sine test. ▓ represents the 99% model-predicted output confidence bands, — is the model response mean and • represents the Bouc-Wen data obtained by numerical integration.

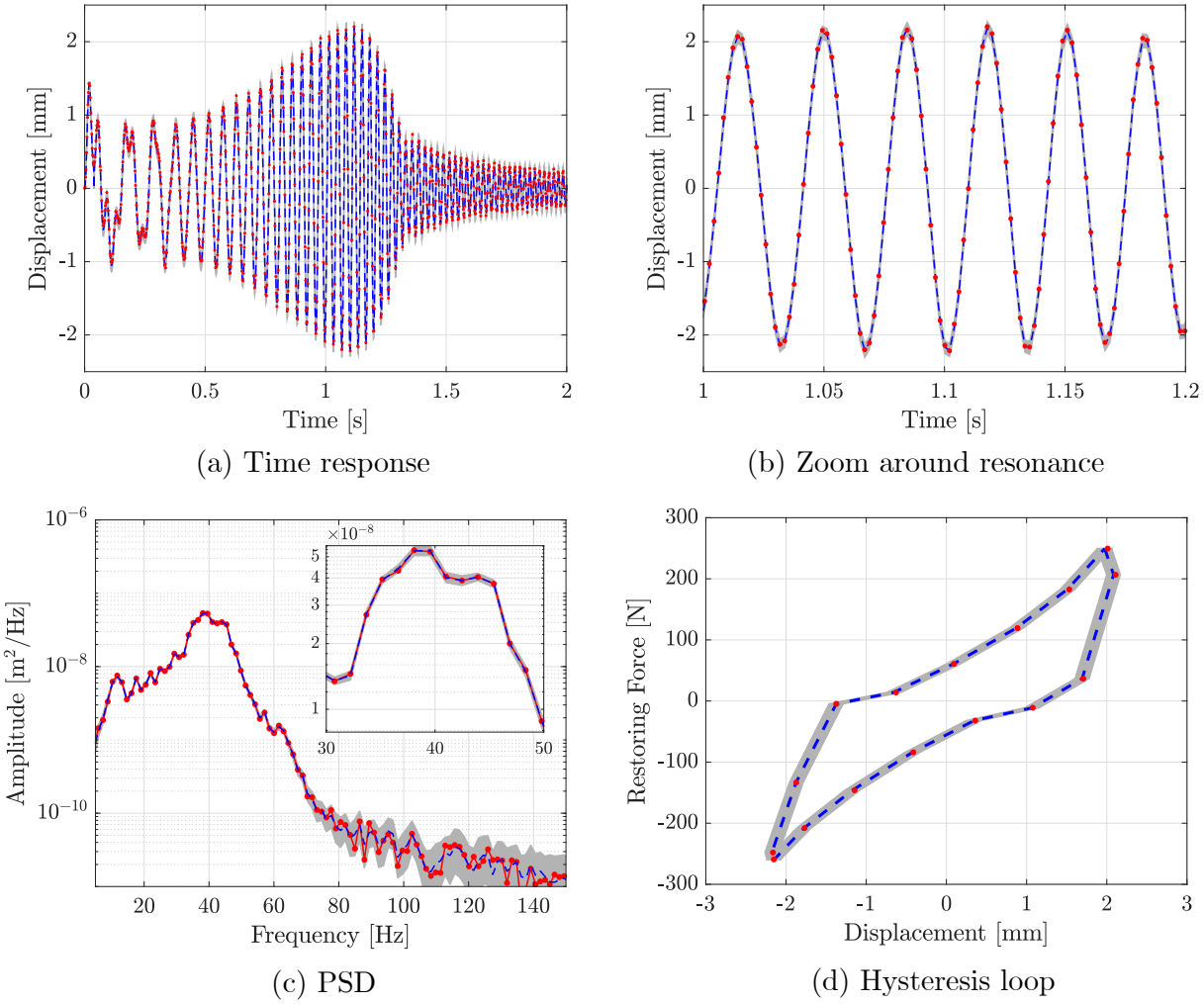

(a) Time response

(b) Zoom around resonance

(c) PSD

(d) Hysteresis loop

Source: Teloli *et al.* (2021).

reproducing the hysterical behavior of the Bouc-Wen benchmark assuming inputs different from those used in its construction, such as a stationary sinusoidal and a random phase multi-sine excitation (NOËL; SCHOUKENS, 2016b) for low (10 N), medium (50 N) and high (80 N) amplitude levels.

Figures 70, 71 and 72 provide an overview of the model-predicted outputs in comparison with Bouc-Wen data for three levels of excitation amplitude, low (10 N), medium (50 N) and high (80 N), respectively, for a sinusoidal input $u(t) = A\sin(2\pi\omega_n t)$ with excitation frequency at the linear resonance $\omega_n = 35.59$ Hz. On the one hand, for a low excitation amplitude, Fig. 70 depicts that the Bouc-Wen system operates with reduced severity of nonlinear effects, showing through the Fig. 70(c) that the spectrum

of responses has no contributions of odd higher-order harmonics, e.g., third, fifth and seventh-order harmonics. Welch's periodogram with a Hanning window every $N = 2^9$ sample was used to reveal this. On the other hand, for medium and high excitation amplitudes, Figs. 71(c) and 72(c) emphasizes the GP-NARX model's ability to reproduce nonlinear distortions present in the Bouc-Wen's system response while accommodating the odd harmonics of the output within the confidence bands.

The Bouc-Wen model carries the rate-independent hysteresis property, which means that for the same excursion interval of the output bounded between amplitudes $y_{\min} \leqslant y(t) \leqslant y_{\max}$, the restoring force $\mathcal{Z}(y, \dot{y})$ of the system will present the same hysteresis loop when it is excited by a $T-$periodic input signal with a loading-unloading regime defined in a period $T \in \mathbb{R}^+$ (IKHOUANE; RODELLAR, 2007; TELOLI; SILVA, 2019). Therefore, note that the excursion intervals on displacement present in the hysteresis loops of Figs. 70(d), 71(d) and 72(d) are approximately the same presented in Figs. 67(d), 68(d) and 69(d), respectively; this shows that the GP-NARX model is able to reproduce the rate-independent hysteresis property through the model-predicted outputs for input signals with a harmonic characteristic, also representing both system responses with a similar confidence bands, e. g., Figs. 70(d) and 67(d).

The model-predicted outputs for a random phase multi-sine excitation (NOËL; SCHOUKENS, 2016b; NOËL *et al.*, 2017) over a frequency range of 5 – 150 Hz are shown in Figs. 73, 74 and 75, considering low (10 N), medium (50 N) and high (80 N) excitation amplitudes, respectively. As the model is used to predict the system behavior for random characteristics that are substantially different from the data observed in training, it should be stressed that the further away from the training data region one wants to make predictions using the model estimated (e.g., using a random excitation), more uncertainty will be present in the model's output. This means that the model will not necessarily make wrong predictions far from the training data, but the forecasts will be more uncertain, and in some situations, the mean prediction value may become unrepresentative. For all the levels of excitation considered, the confidence bands of the model-predicted outputs accommodate the responses from the Bouc-Wen oscillator.

Figure 70 – Validation of the GP-NARX model for low excitation amplitude (10 N) considering a sinusoidal input with excitation frequency at the linear resonance ω_n = 35.59 Hz. ▓ represents the 99% model-predicted output confidence bands, — is the model response mean and • represents the Bouc-Wen data obtained by numerical integration.

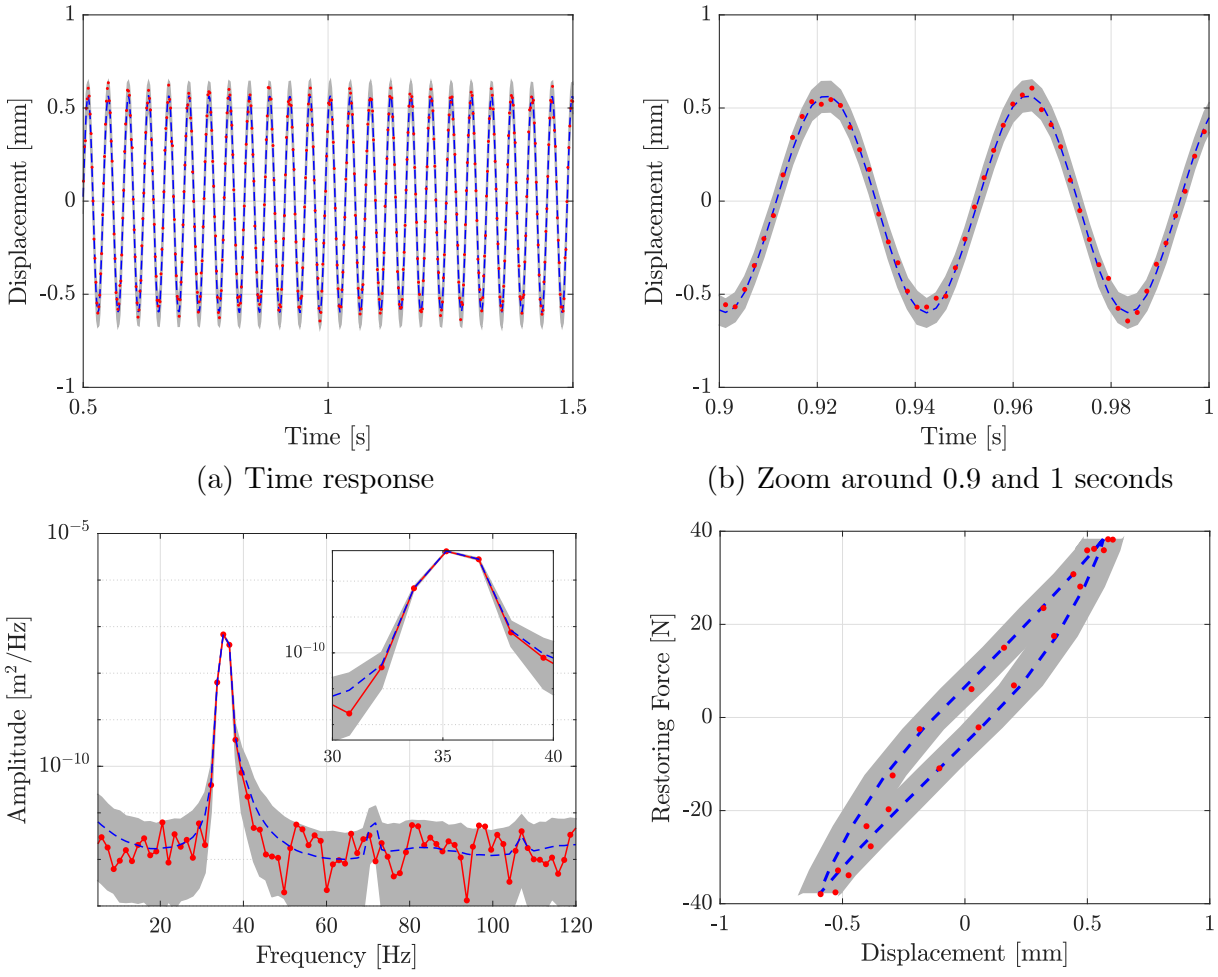

(a) Time response

(b) Zoom around 0.9 and 1 seconds

(c) PSD

(d) Hysteresis loop

Source: Teloli *et al.* (2021).

Figure 71 – Validation of the GP-NARX model for medium excitation amplitude (50 N) considering a sinusoidal input with excitation frequency at the linear resonance ω_n = 35.59 Hz. ▓ represents the 99% model-predicted output confidence bands, — is the model response mean and • represents the Bouc-Wen data obtained by numerical integration.

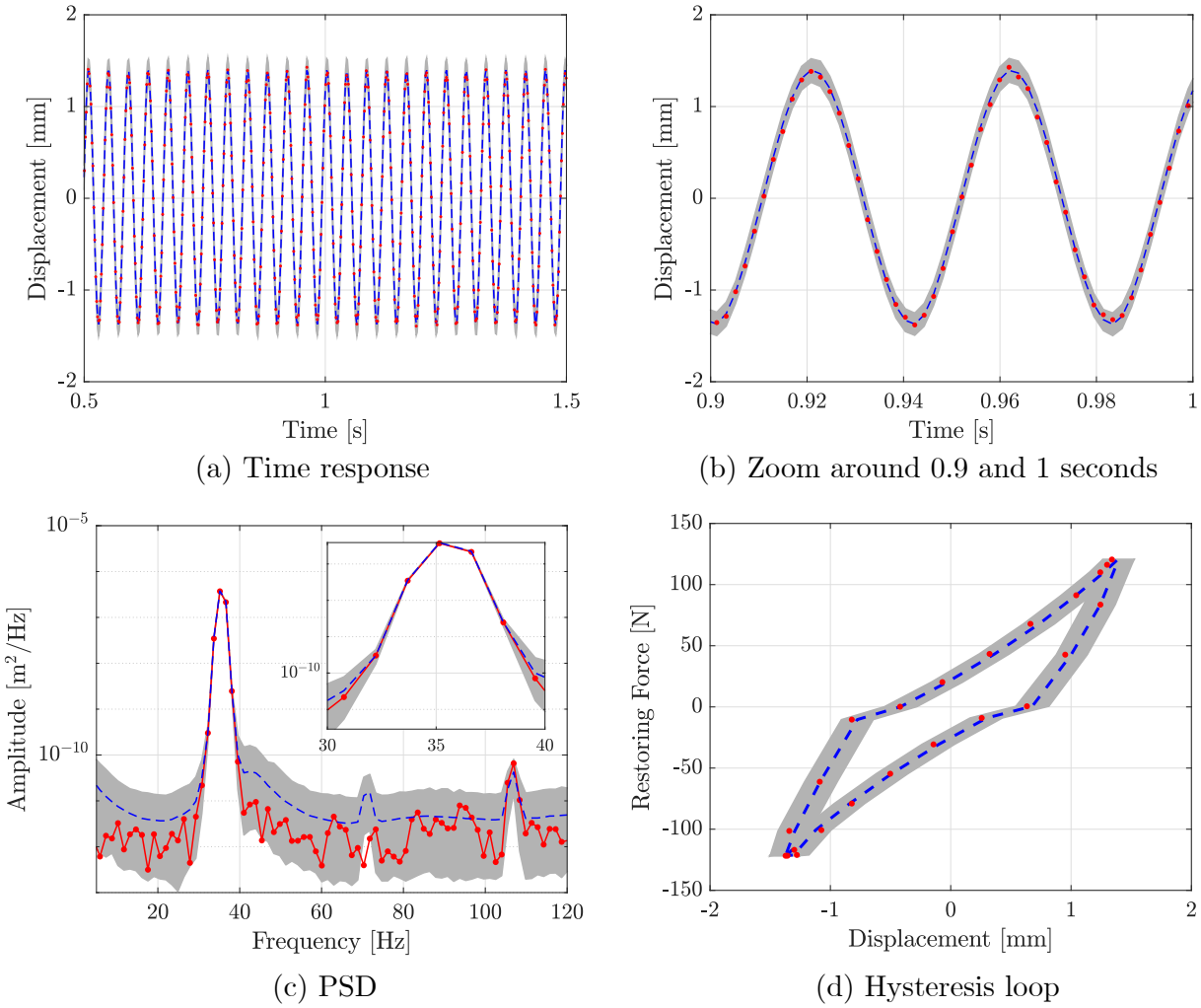

(a) Time response

(b) Zoom around 0.9 and 1 seconds

(c) PSD

(d) Hysteresis loop

Source: Teloli *et al.* (2021).

Figure 72 – Validation of the GP-NARX model for high excitation amplitude (80 N) considering a sinusoidal input with excitation frequency at the linear resonance ω_n = 35.59 Hz. ▓ represents the 99% model-predicted output confidence bands, — is the model response mean and • represents the Bouc-Wen data obtained by numerical integration.

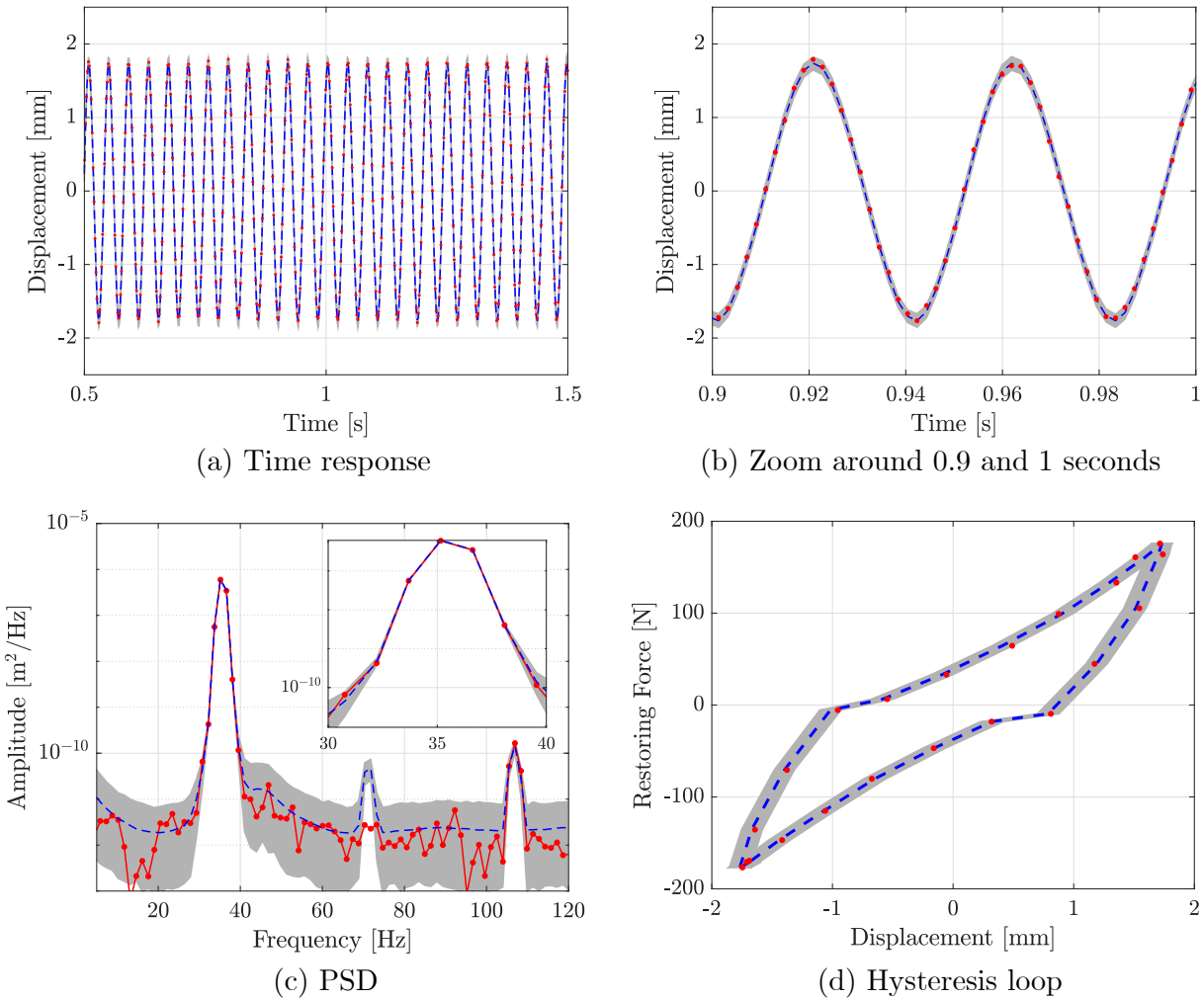

(a) Time response

(b) Zoom around 0.9 and 1 seconds

(c) PSD

(d) Hysteresis loop

Source: Teloli *et al.* (2021).

Figure 73 – Validation of the GP-NARX model for low excitation amplitude (10 N) considering a random phase multisine excitation. ▓ represents the 99% model-predicted output confidence bands, — is the model response mean and • represents the Bouc-Wen data obtained by numerical integration.

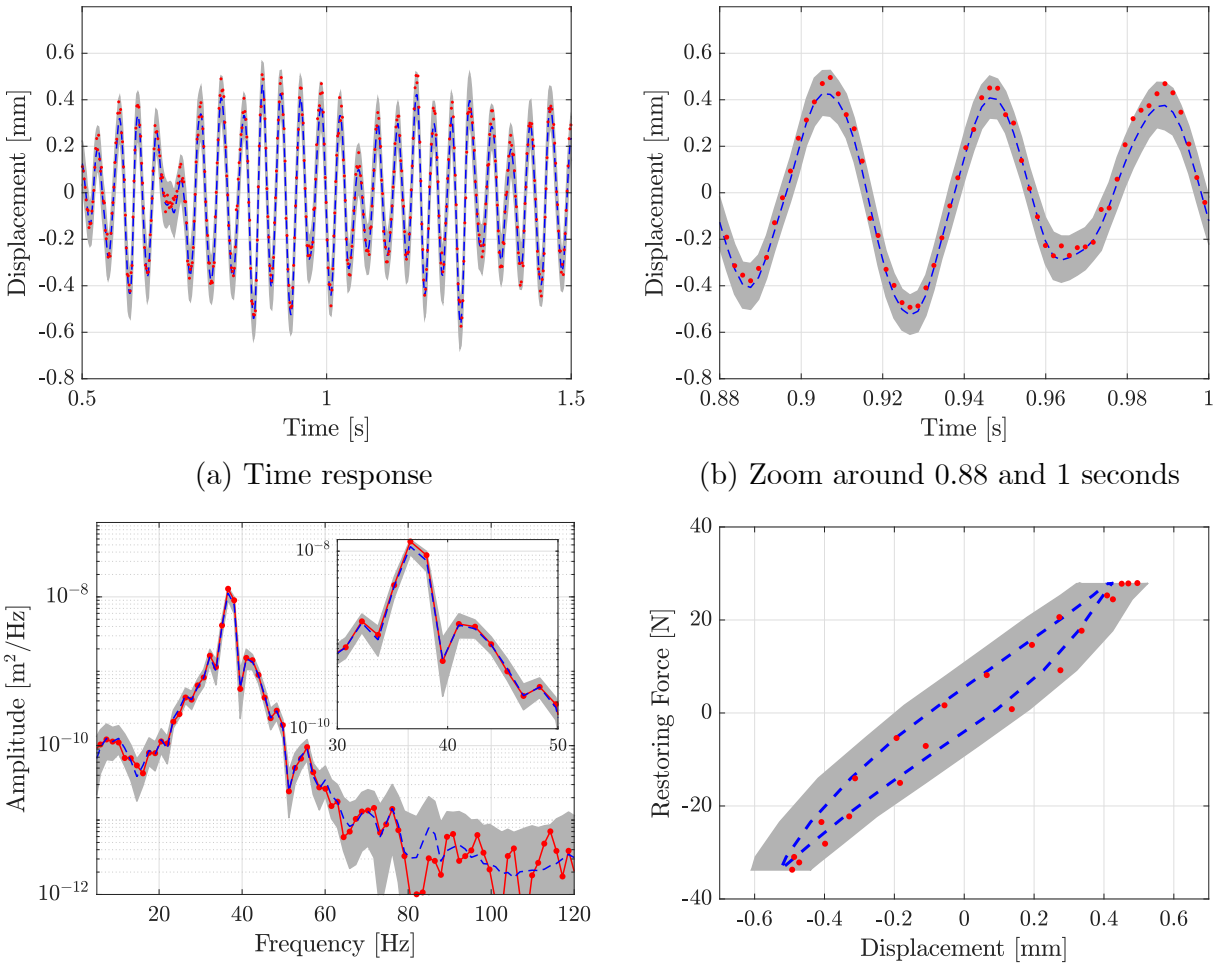

(a) Time response

(b) Zoom around 0.88 and 1 seconds

(c) PSD

(d) Hysteresis loop

Source: Teloli *et al.* (2021).

Figure 74 – Validation of the GP-NARX model for medium excitation amplitude (50 N) considering a random phase multisine excitation. ▓ represents the 99% model-predicted output confidence bands, — is the model response mean and • represents the Bouc-Wen data obtained by numerical integration.

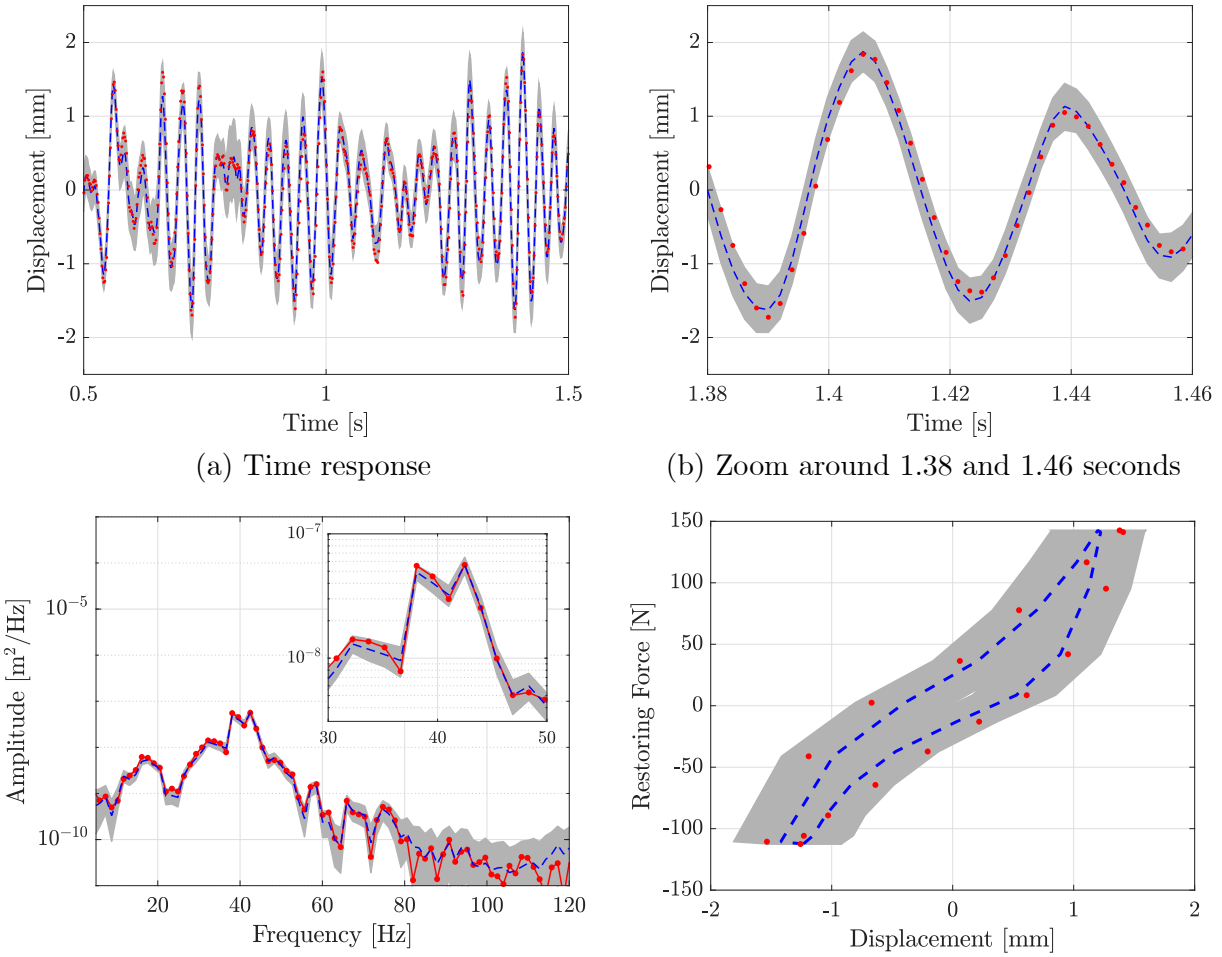

(a) Time response

(b) Zoom around 1.38 and 1.46 seconds

(c) PSD

(d) Hysteresis loop

Source: Teloli *et al.* (2021).

Figure 75 – Validation of the GP-NARX model for high excitation amplitude (80 N) considering a random phase multisine excitation. ▓ represents the 99% model-predicted output confidence bands, — is the model response mean and • represents the Bouc-Wen data obtained by numerical integration.

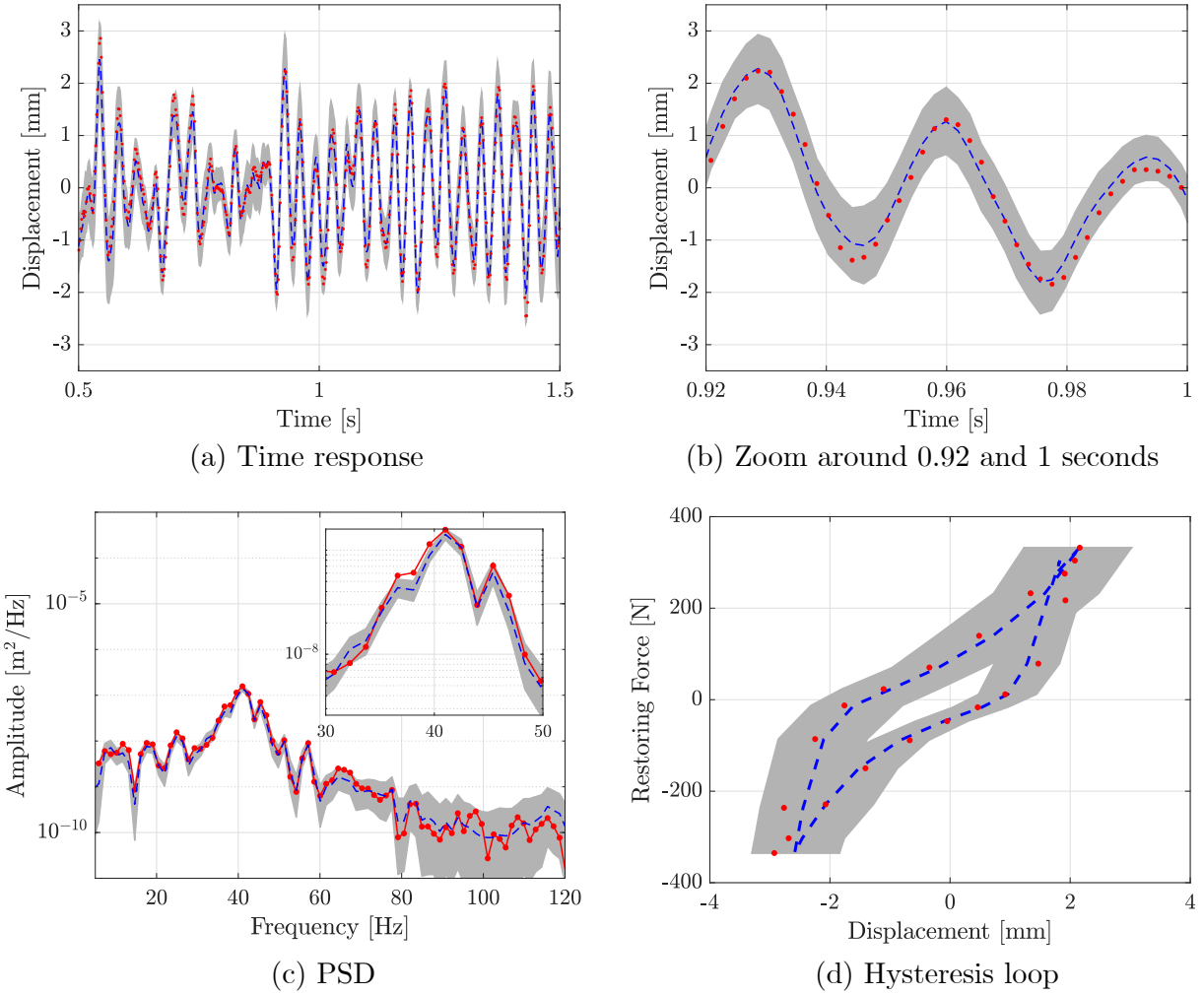

(a) Time response

(b) Zoom around 0.92 and 1 seconds

(c) PSD

(d) Hysteresis loop

Source: Teloli *et al.* (2021).

6.4 EXPERIMENTAL ASSESSMENT OF THE GP-NARX MODEL: THE BERT BENCHMARK

The section begins by recalling the description of the BERT benchmark in subsection 6.4.1. Afterward, subsection 6.4.2 introduces the strategy adopted for training the GP-NARX model, and subsection 6.4.3, in turn, illustrates the model verification and model validation procedures.

6.4.1 Description of the experimental setup

This subsection recalls the BoltEd stRucTure (BERT) benchmark[1] shown in Fig. 76, which is considered as a bolted jointed structure to test the robustness of the GP-NARX model when dealing with experimental hysteretic systems. The experimental setup consists of two aluminum beams assembled in a clamped-free boundary condition, each with dimensions of $270 \times 25.4 \times 6.35$ mm and connected by two M5 bolts, spaced along a length of 40 mm, with a tightening torque of 5 Nm. An electromagnetic Modal Shop 2400E shaker is placed at 85 mm from the clamped end to minimize shaker-structure interaction (PEETERS; KERSCHEN; GOLINVAL, 2011b). For observability purposes, since this work considers the first mode of vibration of the structure in interest, all measurements considered herein were made at the free end of the assembled beam by a laser vibrometer Polytec OFV-525/5000S. The data acquisition was performed by an LMS SCADAS system using a sampling frequency of 1024 Hz. The input signals applied to excite the structure were conducted, assuming different voltage amplitude levels applied to the shaker amplifier, from low to high values (0.05, 0.10, 0.15, and 0.20 [V]). Further details regarding the excitation are addressed in the following subsections. Figure 76 shows the schematic top view of the test-rig.

Figure 77 illustrates a preliminary analysis of the nonlinear behavior of the BERT benchmark through the frequency response curves around its first resonant frequency ($\approx$ 18.8 Hz). Figure 77(a) corresponds to the magnitude plot of the receptance, which was estimated from the structures' response to the swept sine test from 0 up to 40 Hz (sweep rate of 5 Hz/s) collected with 16384 samples and a burst of 50 %, regarding low (0.05 V), medium (0.10 V) and high (0.20 V) levels of amplitude. Thus, one can verify that the FRFs do not overlay for different input levels, exhibiting distortions, changes in resonance frequency, and a more significant attenuation of vibration amplitude for higher excitation

[1] Data available on https://github.com/shm-unesp/DATASET$_$BOLTEDBEAM.

Figure 76 – BERT setup and the schematic representation illustrating the clamped-free beam conveying a bolted joint connection.

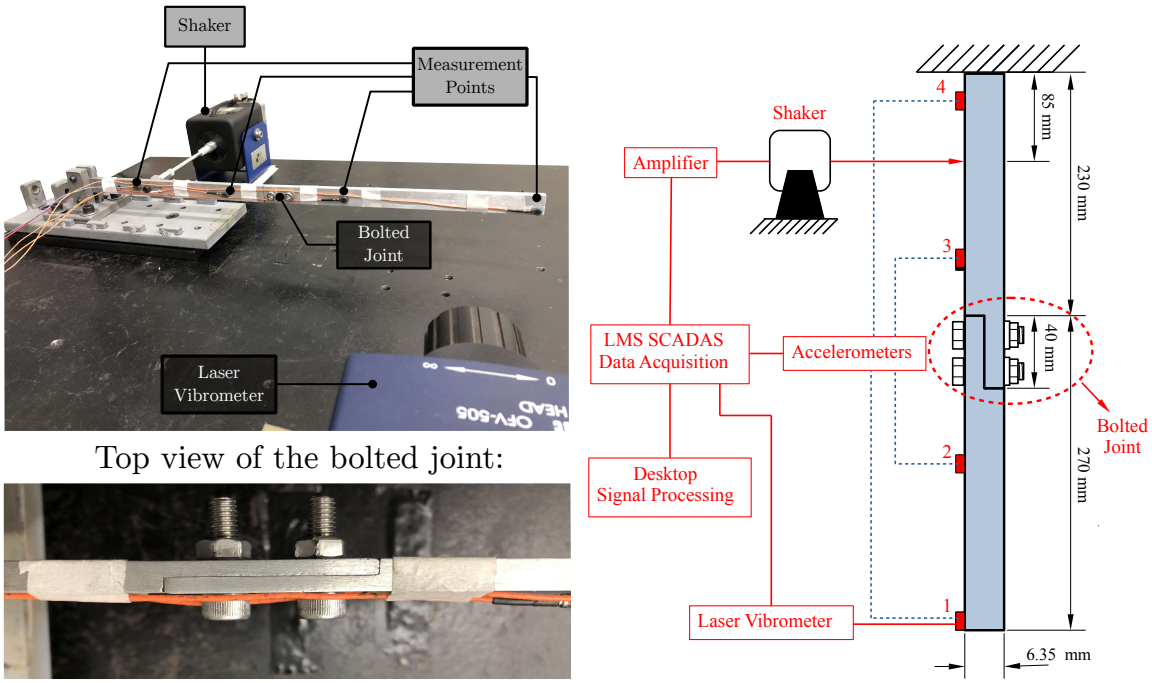

(a) Experimental setup (b) Schematic top view of the experimental setup.

Source: Teloli *et al.* (2021).

levels.

In a complementary way, Fig. 77(b) exemplifies the frequency response curve of the assembled structure obtained from stepped sine tests sweeping up from 3 to 23 Hz, with incremental steps of 0.1 Hz and 32 seconds of oscillations to ensure steady-state condition at each excitation frequency. It is noteworthy that, as well as several bolted jointed structures, the BERT benchmark presents amplitude-dependent nonlinearity, with a decrease in the value of its resonant frequency when increasing the input amplitude. This illustrates the fact that the lap-joint inevitably softens the total rigidity of the system. Recently, Teloli *et al.* (2021) demonstrated that the behavior of the benchmark around its first mode of vibration could be well approximated by a stochastic version of the Bouc-Wen oscillator.

Figure 78 exemplifies the data fluctuation on frequency response curves considering several experimental measurements and is shown with 99% statistical confidence bounds. The experimental measurements were conducted over different days, and only the tightening torque in the joint connection was controlled after each experimental realization.

Figure 77 – Frequency response curves for different excitation amplitudes: — is low (0.05 V), △ medium (0.10 V), and ∘ high (0.20 V) amplitude levels.

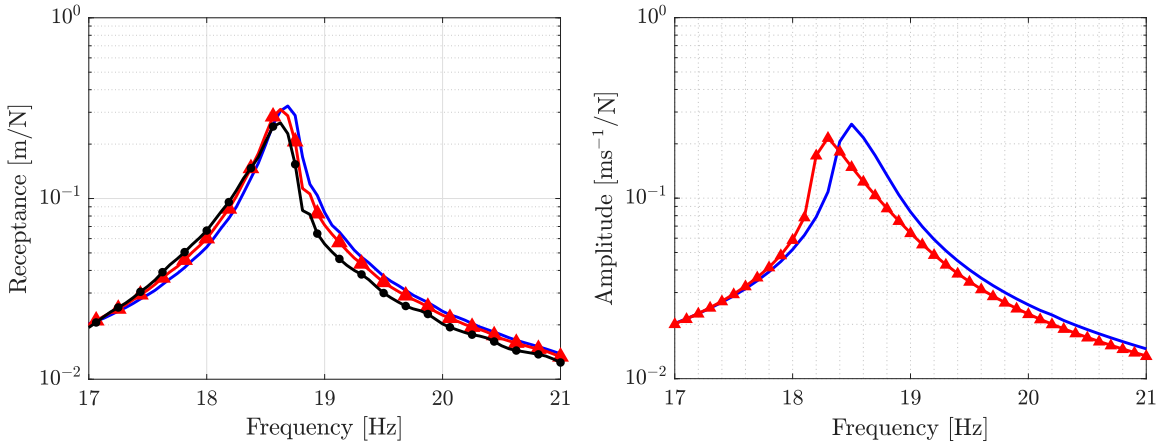

(a) Magnitude plot of the receptance.

(b) Experimental frequency response curve for a stepped sine test.

Source: Teloli *et al.* (2021).

Figure 78 – Variation of the Frequency Response Function calculated for different excitation amplitudes with 99% of confidence bands. ▩ represents the confidence bands, whereas — is the mean values.

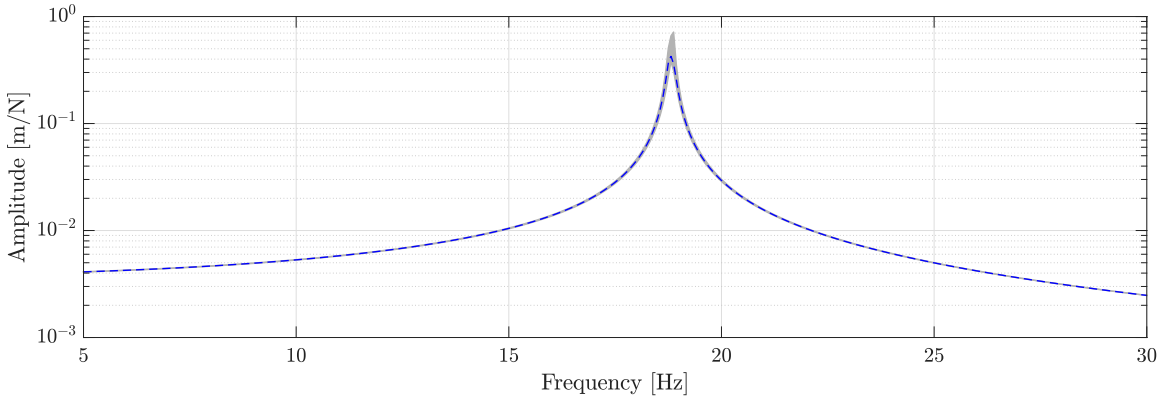

(a) Low level of excitation amplitude (0.05 V).

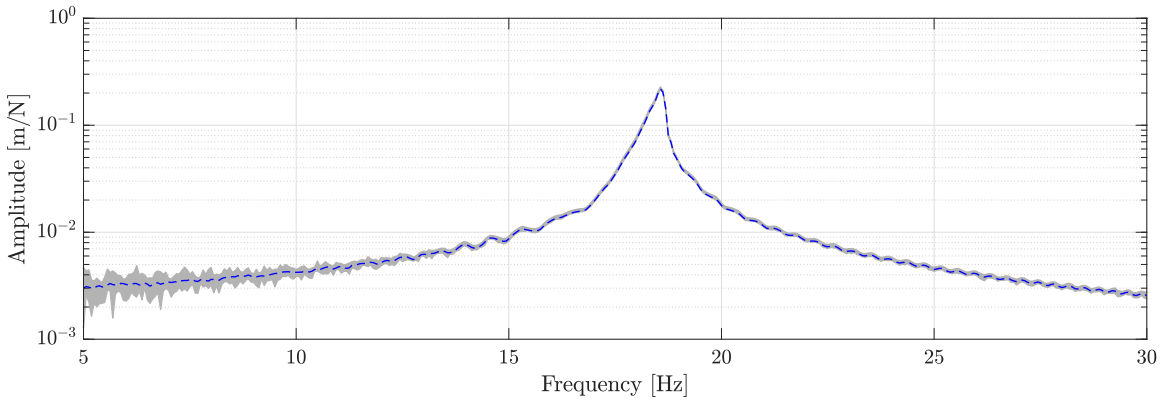

(b) High level of excitation amplitude (0.20 V).

Source: Teloli *et al.* (2021).

6.4.2 Model training

Following the same identification framework discussed in section 6.2 and exemplified on the numerical benchmark of section 6.3, the training data set $(\mathcal{X}, \mathcal{Y})$ used for the GP-NARX model inference and estimation of hyperparameters Θ consists of a pair of experimental responses collected from the BERT system for the swept sine test described previously and considering amplitude levels of 0.05 and 0.20 V (low and high), respectively. In this work, the shaker amplifier's voltage signal is used as input data for training, verification, and validation of the GP-NARX model. This approach is considered as excitation once this signal is constant over a frequency range (VILLANI *et al.*, 2019).

Also, to take into account the data fluctuation observed in Fig. 78 during the construction of the GP-NARX model, the training data consider data points randomly chosen from 50 available experimental realizations, using only samples of the time data acquired around the region of maximum response amplitudes due to the presence of resonance. This procedure is performed to reduce the computational cost necessary in the *Model training* step, considering only the part of the data that has the most predominating dynamics. Additionally, the model can predict the experimental uncertainty related to the variability from one realization to another using this strategy.

Figure 79 presents the surface $n_y \times n_u \times fit$ [%] resulting from the GP-NARX model lags optimization procedure considering signals from the swept sine test for an input amplitude of 0.10 V, which was used to improve the model performance, as mentioned above. It was found that optimal values of 16 lags in the output and 10 lags in the input produced a fit of 96.1%.

Figure 79 – Lags optimization surface $n_y \times n_u \times fit$. The optimal value of the lags (•) corresponds to 16 lags in the output and 10 lags in the input for a fit of 96.1 %.

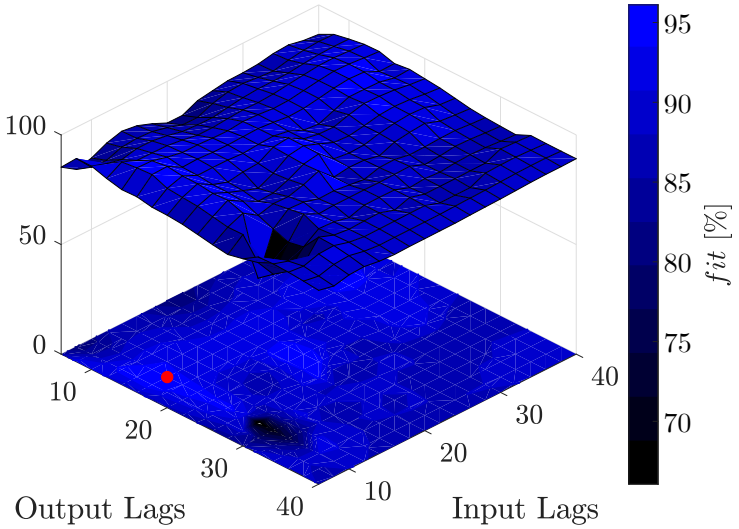

Source: Teloli *et al.* (2021).

6.4.3 GP-NARX model verification and validation

To ensure convergence in estimating the model's statistical properties, all practical application results assume the backpropagation of the uncertainties considering 4096 Monte Carlo simulations.

The model verification is presented through Figs. 80, 81 and 82 whereby the GP-NARX model-predicted outputs are compared to the BERT benchmark's experimental results for low (0.05 V), medium (0.10 V) and high (0.20 V) levels of excitation amplitude, respectively. The black-box model presents good agreement with the experimental measurements since the model training step was conducted regarding these curves. The confidence bands accommodate several experimental realizations, which indicates that the model can make accurate predictions of the structure's behavior and response, even in the presence of nonlinear effects and data variability. Figures 80(c), 81(c) and 82(c) show that even with the increase in the excitation amplitude, an accurate fit of the frequency components of the experimental responses is achieved by the model.

Nevertheless, special attention is given to Figs. 80(d), 81(d) and 82(d), which present a comparison between the hysteresis loops obtained from the model response and those obtained from the experimental data. It can be seen that the mean response of the model can capture the evolution of the experimental data in the restoring force × displacement plane. It should be stressed that the restoring force considered in this comparison represents the projection of all nonlinear forces actuating on the first vibrating mode

of the assembled structure around the resonance region (maximum amplitude).

Figure 80 – Verification of the GP-NARX model for low excitation amplitude (0.05 V) considering a swept sine test. ▩ represents the 99% model-predicted output confidence bands, — is the model response mean and • represents ten experimental realizations.

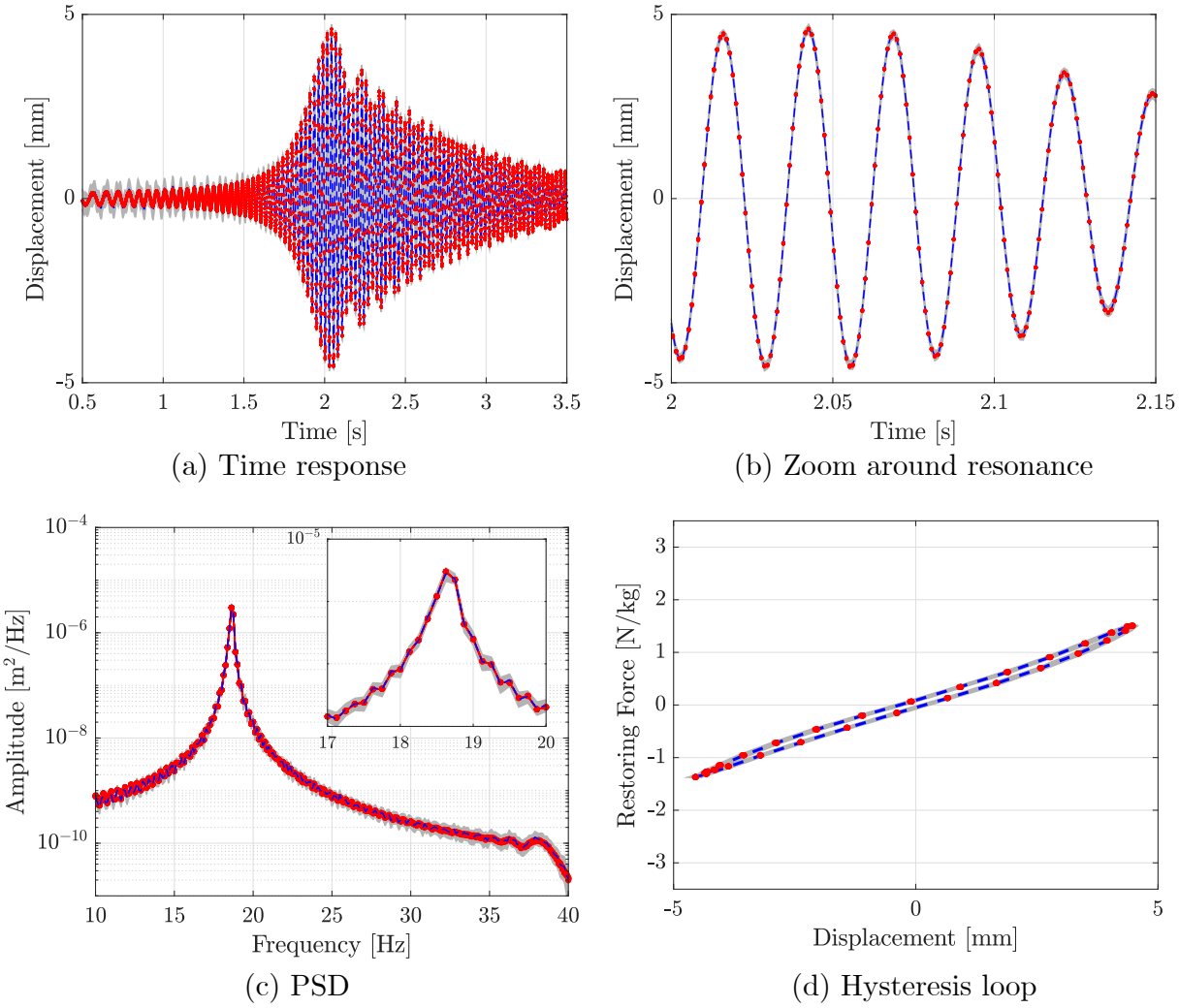

(a) Time response (b) Zoom around resonance

(c) PSD (d) Hysteresis loop

Source: Teloli *et al.* (2021).

Different input conditions are then tested from data that were not used to infer the model's parameters to validate the proposed model. Figure 83 depicts the model-predicted output considering the swept sine test with excitation amplitude at 0.15 V. For this excitation with intermediate amplitude between medium and high levels, and the model showed it was able to reproduce the experimental measurements well. Although some points regarding the experimental realizations have exceeded the limits of the confidence bounds, which is apparent in the 83(d) concerning the hysteresis loops, there are no regions where the dynamics visualized in the experiment are different from those predicted by the model.

Figure 81 – Verification of the GP-NARX model for medium excitation amplitude (0.10 V) considering a swept sine test. ▓ represents the 99% model-predicted output confidence bands, — is the model response mean and • represents ten experimental realizations.

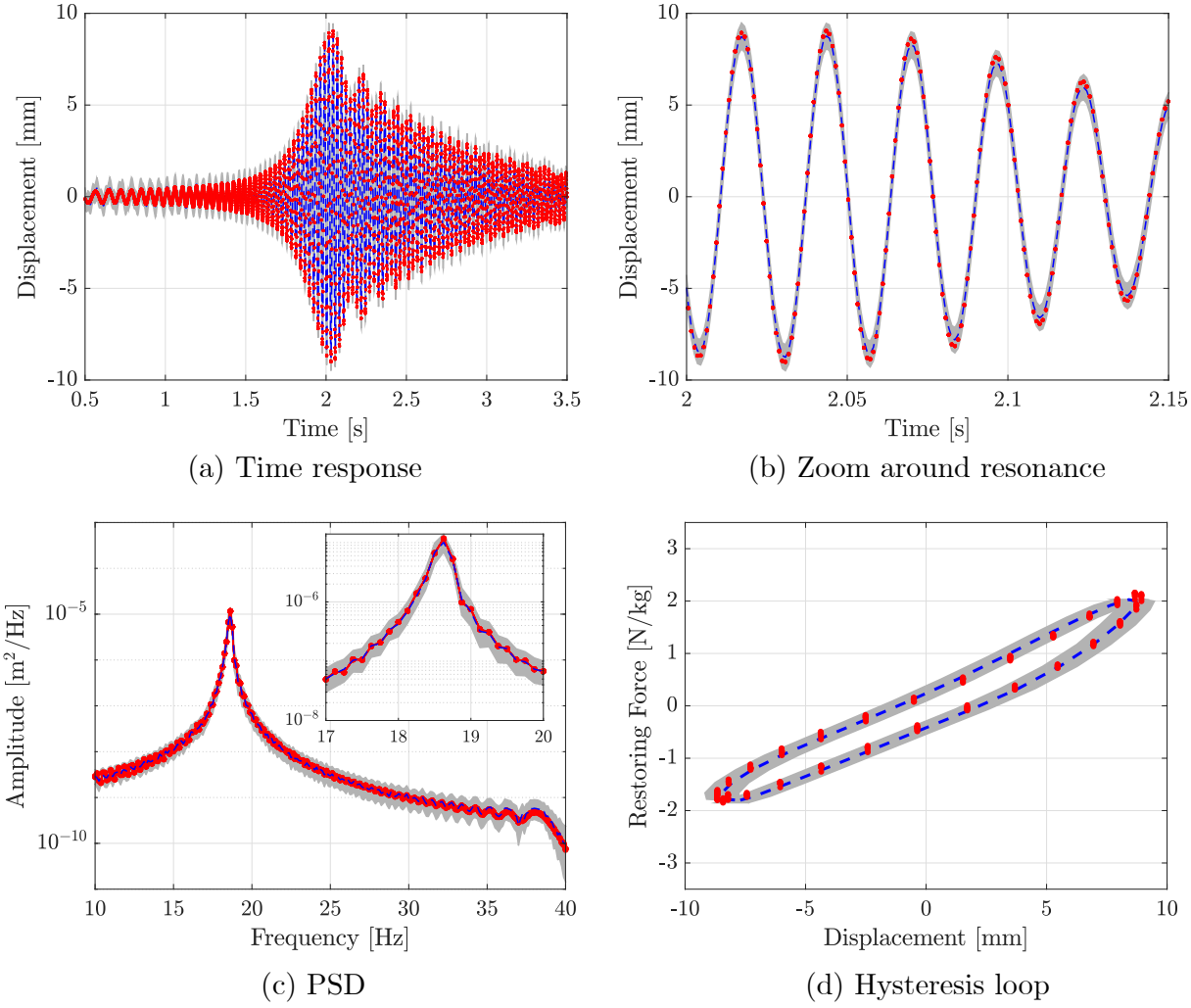

(a) Time response (b) Zoom around resonance

(c) PSD (d) Hysteresis loop

Source: Teloli *et al.* (2021).

Furthermore, in the context of model validation, the GP-NARX model-predicted output for a sinusoidal excitation with an amplitude level of 0.15 V and conducted close to the first resonance frequency (18 Hz) of the test-rig is shown in Fig. 84. From the PSD of the experimental response of the bolted structure present in Fig. 84(c), note that the numerical model can reproduce in its response the presence of multiple harmonics (2 and 3 times the fundamental frequency) that are also found in the experimental response. Thus, although it overestimates the third-order harmonic component, the model is suitable to represent the nonlinearities of even and odd harmonic order associated with the assembled structure's behavior. Then, the GP-NARX model brings forward the hysteresis curves predicted in Fig. 84, which illustrates that almost the same energy dissipation is predicted compared to the experimental measurements. Besides, the hysteresis loop's asymmetry

Figure 82 – Verification of the GP-NARX model for high excitation amplitude (0.20 V) considering a swept sine test. ▓ represents the 99% model-predicted output confidence bands, — is the model response mean and • represents ten experimental realizations.

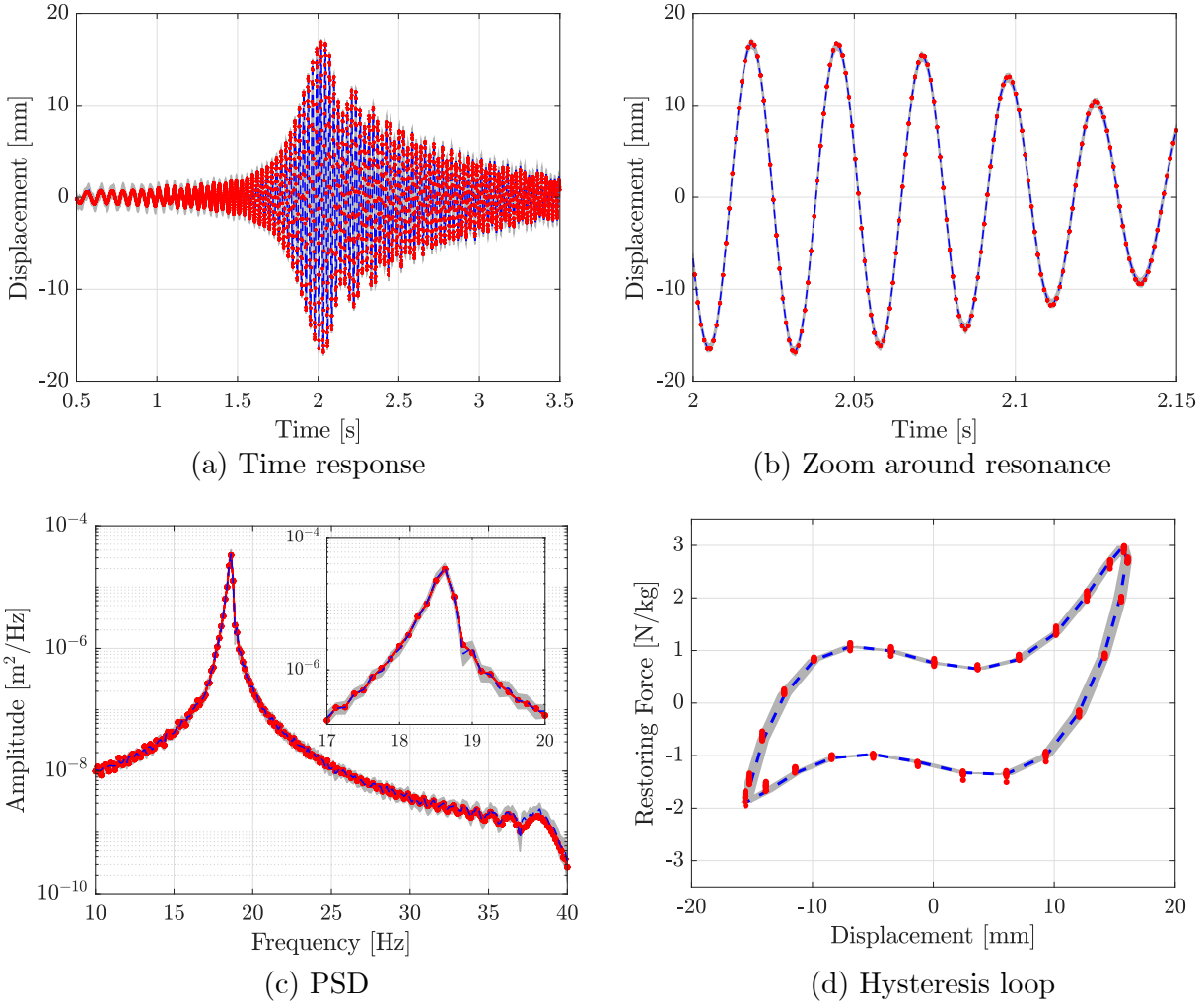

(a) Time response (b) Zoom around resonance

(c) PSD (d) Hysteresis loop

Source: Teloli *et al.* (2021).

concerning the zero axes of the displacement has been well-captured by the model.

Figure 85 depicts the model's performance in reproducing the behavior of the experimental structure for a white noise input conducted over the frequency range of 0 – 110 Hz with an amplitude level of 0.30 V. As expected since data with random characteristics are distant from those used for model training, the more uncertain is the model's predictions. This is reflected through the larger confidence bands. Another factor contributing to the more significant uncertainty of the model is related to the influence of noise on the experimental response since the maximum response amplitude for the random input is illustrated in Fig. 85(b) is less than 2 mm. In this condition, the system still operates close to the linear regime of motion, and the mean response of the model fits well with the experimental realization. Figure 85(c) presents the frequency components of both signals

Figure 83 – Validation of the GP-NARX model for medium excitation amplitude (0.15 V) considering a swept sine test. ▓ represents the 99% model-predicted output confidence bands, — is the model response mean and • represents ten experimental realizations.

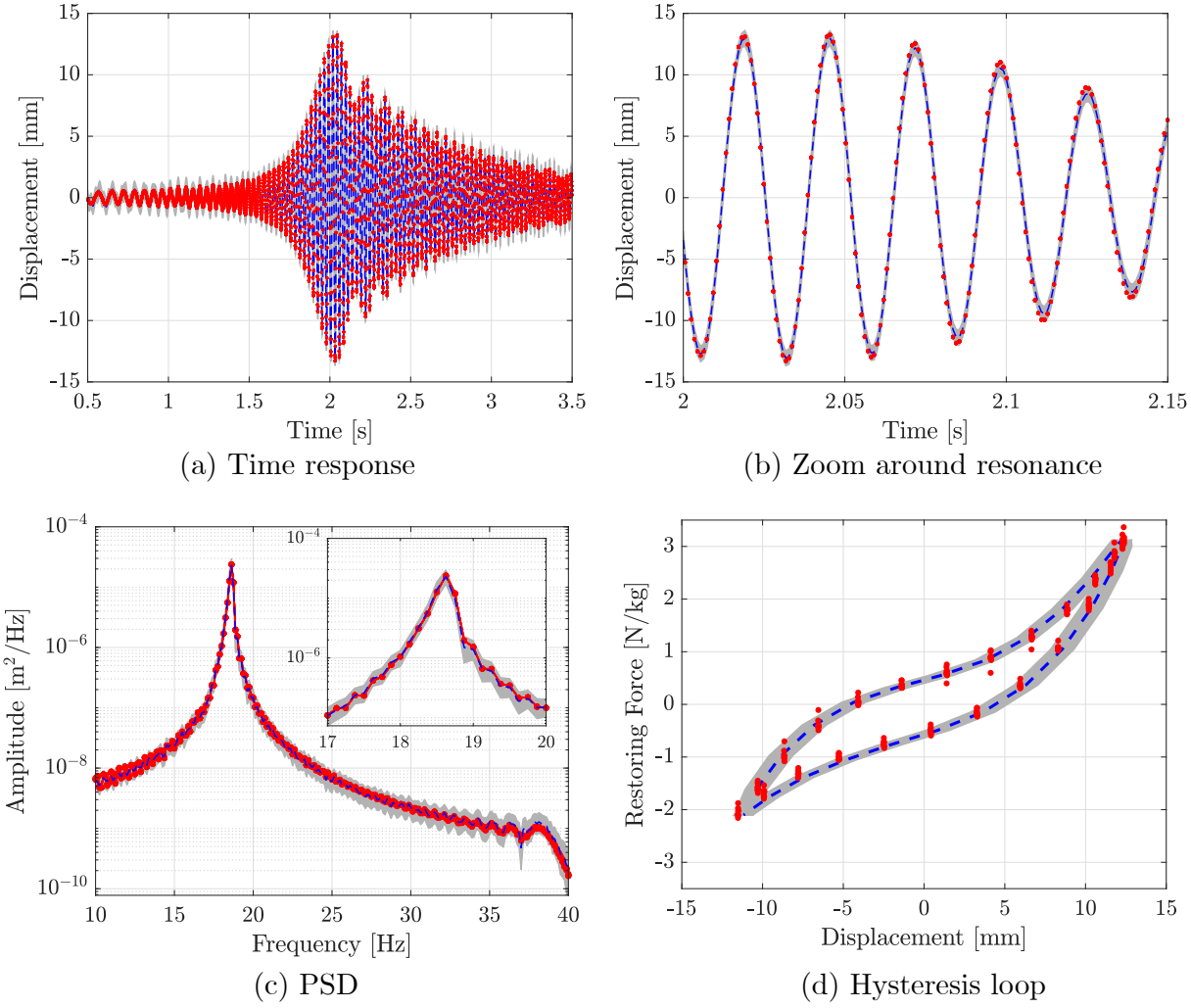

(a) Time response (b) Zoom around resonance

(c) PSD (d) Hysteresis loop

Source: Teloli *et al.* (2021).

through their estimated PSDs, showing that the identified model can adequately predict the experimental results.

Figure 84 – Validation of the GP-NARX model for a high excitation amplitude (0.15 V) considering a sinusoidal amplitude with excitation frequency at 18 Hz. ▓ represents the 99% model-predicted output confidence bands, — is the model response mean and • represents ten experimental realizations.

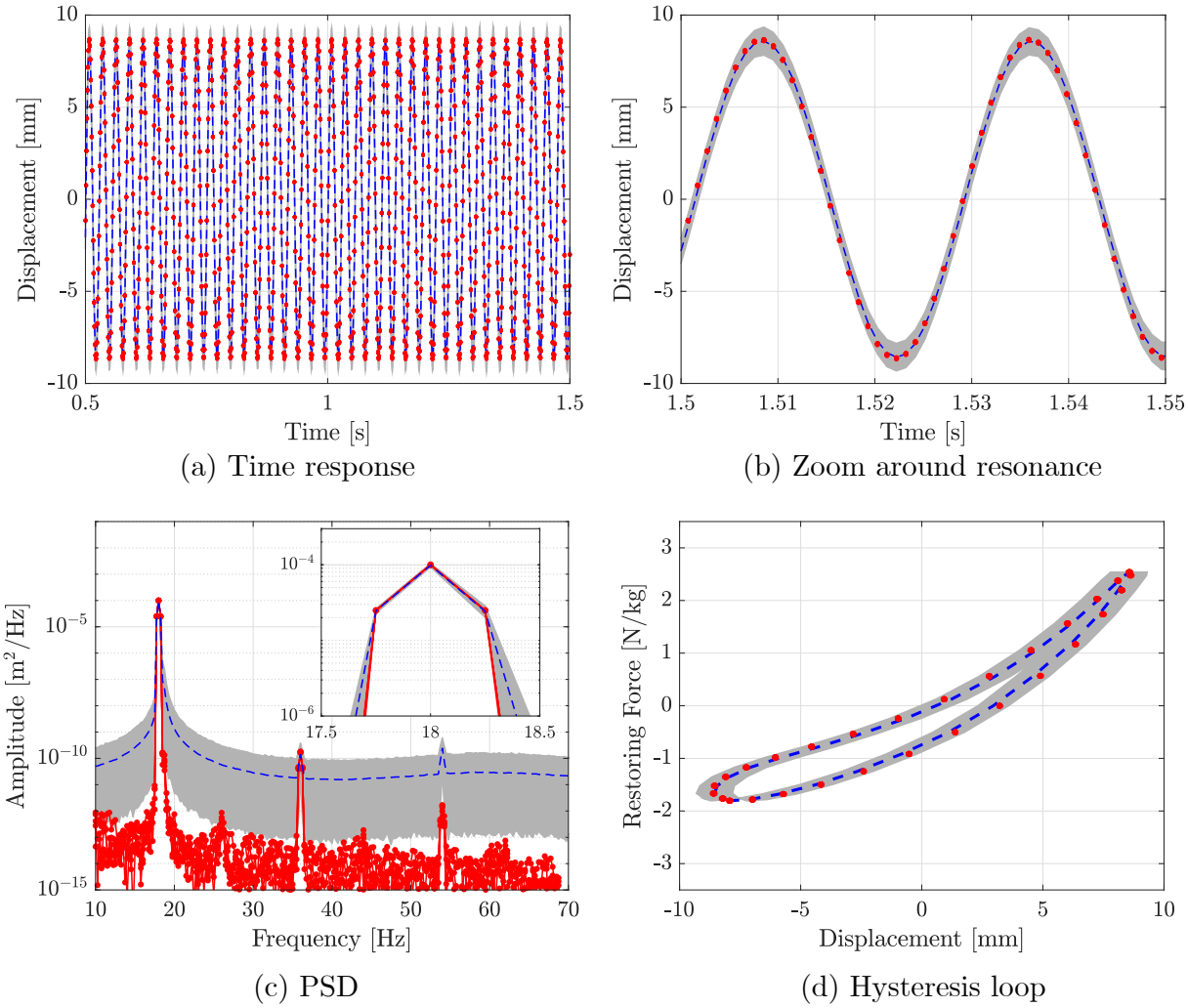

(a) Time response

(b) Zoom around resonance

(c) PSD

(d) Hysteresis loop

Source: Teloli *et al.* (2021).

Figure 85 – Validation of the GP-NARX model for an excitation amplitude of 0.30 V considering a white noise input. ▓ represents the 99% model-predicted output confidence bands, — is the model response mean and • represents the experimental data.

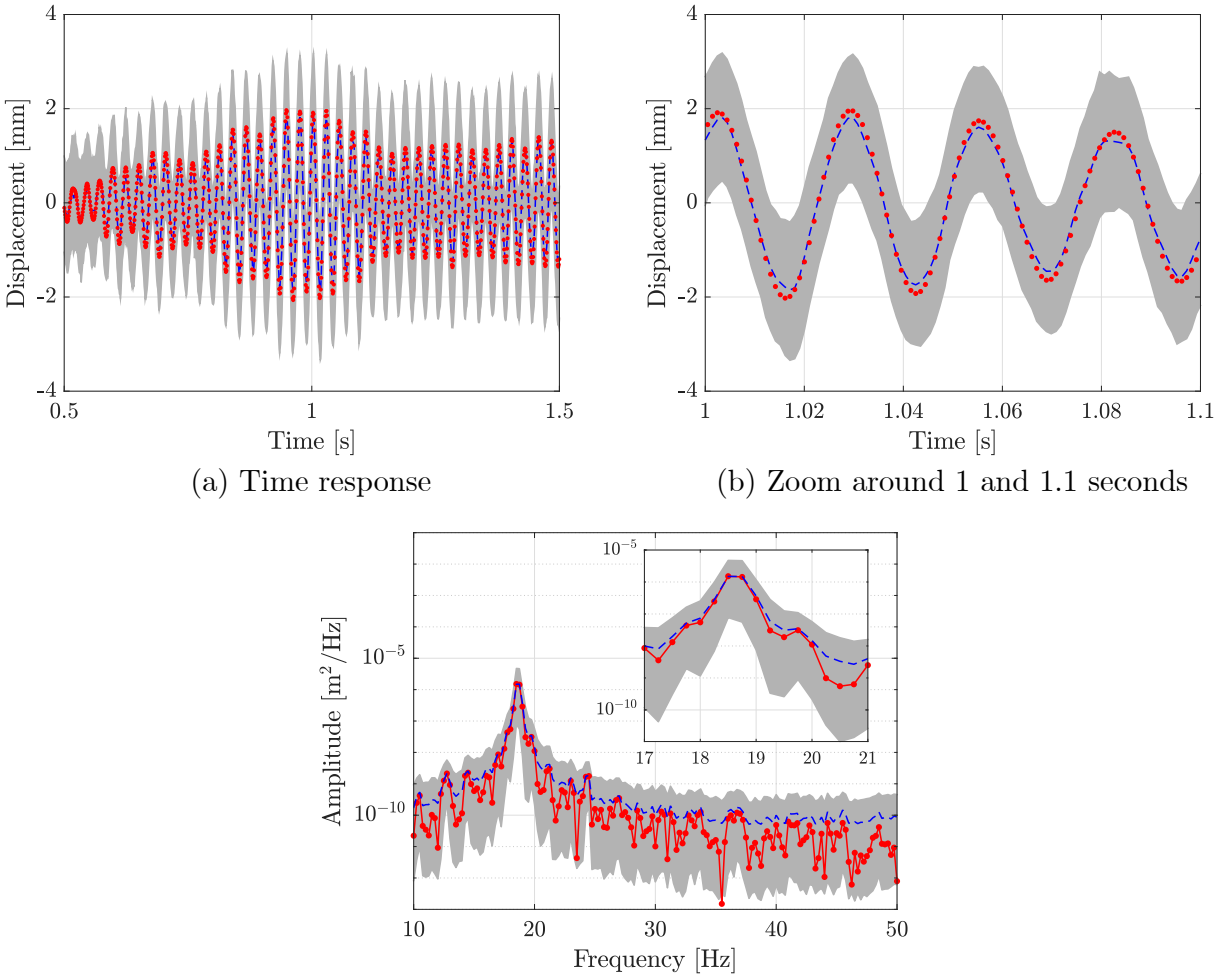

(a) Time response

(b) Zoom around 1 and 1.1 seconds

(c) PSD

Source: Teloli *et al.* (2021).

6.5 CONCLUDING REMARKS

In this work, a GP-NARX model was used to approximate the response of nonlinear systems characterized by hysteresis effects. This work's motivation arises from the need to represent the dynamics of complex dynamic systems in several operating regimes, such as structures joined by bolted joints that experience transient and operational steady-state regimes of motion, using only input and output data to construct the model. The identification framework of the GP-NARX model was based on the steps of *data acquisition, training, verification, and validation.*

At first, attention was placed on Bouc-Wen's benchmark. The model's training to reproduce the oscillator behavior was done using swept sine tests with different excitation amplitude levels. It is argued that from these data obtained in a transient regime around the resonant region of the system, the black-box model is trained to take into consideration the main aspects present in the dynamics of Bouc-Wen's oscillator, for example, the increase of the resonant frequency and pronounced opening of the hysteresis loops as one increases the excitation amplitudes. While the model verification was carried out assuming data of the same character as those used for training, the validation of the GP-NARX considered data originated in a different way, such as sinusoidal excitation in a steady-state regime applied at the linear resonant frequency of the system and the random phase multi-sine excitation. In contrast, in both cases, several levels of excitation amplitude were tested. Although the GP-NARX model's predictions have become more uncertain for conditions distant from the training data, the results indicate that the model has an adequate capacity to make the Bouc-Wen oscillator response predictions.

Next, the work addressed the model's performance in reproducing the BERT benchmark's behavior, taking into account uncertainties that result from the data acquisition procedure based on several experimental realizations. The experimental results were successfully correlated with predictions obtained from the GP-NARX model, assuming the experimental variability. Further to the observations that have already been made for the numerical application case, it is encouraging to note that in addition to inferring the model prediction uncertainties, the confidence bounds can also accommodate uncertainties related to the experimental measurement process, highlighting the advantage of using the GP-NARX model.

This work paves the way to explore the GP-NARX model's use in reproducing the behavior of more complex real engineering structures involving the presence of fastened

joints. Furthermore, the results presented exemplify the model's application for an available tightening torque applied to the experimental structure. Future work lies in exploring the use of the model to reproduce the behavior of the structures with uncertainties in the measurement process for several levels of tightening torque and, from that, explore features present in the response of the GP-NARX model for structural health monitoring (SHM) purposes that aim to detect the loss of tightening torque. At this point, it is important to point out that the structure of the NARX function does not take into account the amplitude dependence presented in structures joined by bolted joints. This is an issue that also lacks detail and needs to be investigated in future research, especially when involving experimental applications.

7 FINAL REMARKS

The work contained in this dissertation explored new contributions in the analysis and identification of mechanical systems with hysteresis, in particular, structures assembled by bolted joints. It is certain to state that there is no *free lunch* to handle these systems; one can opt for a realistic model with a high level of detail, but the computational cost required depending on the desired application may not be optimal and, in these circumstances, a simpler representation fits better. Furthermore, the complexity involved in their nonlinear behavior, with special emphasis on the damping and stiffness characteristics, is the result of the interaction between aspects present at different levels of observation ranging from surface roughness and pressure distribution in the contact area after assembly procedures to the experimental practices adopted to acquire vibration responses in a nonlinear regime of motion. For this reason, there is no unique algorithm that can solve and address all the challenges involved, although this is a current pursuit in the literature. Nevertheless, the investigations conducted by this dissertation are embedded in the global analysis of the nonlinear vibration of these structures, and from the methods proposed and evaluations conducted, give some indications of situations in which some methodologies may (or may not) perform well. Thus, section 7.1 presents a summary of the conclusions presented throughout this study. Additionally, section 7.2 proposes paths for future inquiry, and section 7.3 is dedicated to present the research papers published during the development of the Thesis.

7.1 SUMMARY

- Results presented in Chapter 3 indicate that it is possible to obtain closed-form solutions for models with hysteresis from conventional approximations formulated in the frequency domain through different strategies of smoothing the hysteresis restoring force. This conclusion is summarized on two fronts:
  - regarding the Volterra series, the strategy adopted consists of proposing an

equivalent oscillator capable of emulating the hysteresis effects using a smooth nonlinear operator. The construction of this operator is done using bounding functions in the polynomial form to encode the loading and unloading regimes in a hysteresis cycle. Thus, it turns possible to derive analytical expressions for the higher-order FRFs with the harmonic probing algorithm. The main advantages in this formulation lie in the possibility of splitting the linear and nonlinear contribution components present in the total response, which is an interesting insight into the dynamics of a nonlinear system and may become a useful framework for conducting parameter estimation procedures in a nonlinear system identification context. However, the Volterra series presents convergence problems, especially in the vicinity of the resonance region, where no convergence is possible unless the nonlinearity is weak;

- regarding the harmonic balance method, the strategy adopted consists of directly analyzing the possible existing analytical expressions to describe hysteresis loops in models, as is the case in Bouc-Wen, LuGre, and Dahl oscillators. However, these expressions may still not be given as a function of quantities that allow expansion into the Fourier series, such as displacement or velocity. In this sense, this work adopted the Taylor smoothing procedure, which allows approximating these expressions in a polynomial form, paving the way for representation by the HBM. It is important to point out that although the Taylor series was chosen, other methodologies could be adopted, such as the polynomial interpolation in the Lagrange form. Thus, unlike the Volterra series, the HBM proved to be less susceptible to convergence problems, giving satisfactory results for predicting the behavior of a Bouc-Wen oscillator for frequency intervals close to resonance.

- Even in laboratory conditions, the uncertainties related to measurement noise, the position of the sensors and actuators, and environmental changes render the system response susceptible to variations that must be considered in the parameter estimation process. In this context, Chapter 4 takes an excursion into using the stochastic version of the Bouc-Wen model for predicting the experimental responses of a structure assembled by bolted joints. Although it presents the possibility of emulating a wide variety of hysteresis loops, the Bouc-Wen oscillator has been rarely used for this purpose, as indicated by the literature review. One of the main reasons for this lack of contributions lies in difficulty in estimating its parameters. The employment of higher-order FRFs provided a possibility to circumvent possible

limitations in the identification of their parameters by being able to split the linear and nonlinear contributions in the system response. In order to take experimental variations into account during the parameter estimation procedure, Bayes inference strategy was used to calculate the probability density functions of the Bouc-Wen parameters, proving to be a powerful tool for NSI purposes. Regarding the BERT benchmark, further inquires must be performed to evaluate the influence of clamped conditions in the system behavior, since they might be a source of nonlinearities and uncertainties on the global response of the structure.

- In bolted joints, ‘‘is it possible to increase energy dissipation due to frictional contact without compromising the structural integrity of the system?’’ Discussions on this topic are raised in Chapter 5, in which the Orion beam is introduced. Although the study conducted in this Chapter is entirely experimental, focused on evaluating the variations that change in the tightening torque cause on the nonlinear modes, and still lacks *in situ* investigations that further analyze physical aspects of the dynamic interactions at the contact interface, it was found that it is possible to improve energy dissipation in bolted systems. However, detailed studies on the surface of the contact patches after experimental realizations still need to be conducted. The improved damping comes from an increase in interfacial friction, which directly leads to an increase in wear and fretting fatigue. This, in turn, will lead to a premature failure of the system if used in a dynamic environment for an extended amount of time. Another interesting point in the Chapter that also deserves to be highlighted is the repeatability between experimental measurements in these systems. Even with an assembly protocol established for the Orion beam, it was found that the variations, especially on the resonance frequencies, are more pronounced than those caused only by the nonlinear behavior. In this sense, it is noted that even when dealing geometrically with the same beam in the experimental repetitions, the changes in the aspects present in the contact scale lead the structure to behave as a different system.

- Chapter 6 presented the GP-NARX model for predicting the behavior of systems with a hysteresis. The methodology was applied in numerical simulations to describe the Bouc-Wen model and experimental investigations to emulate the behavior of the BERT benchmark. In both applications, the GP-NARX model proved to be an effective tool to represent hysteretic systems, even in the presence of uncertainties from the measurement procedure. This is an advantage concerning other black-box models tested in the literature for non-smooth systems because,

as already mentioned, there are limitations in describing the response of systems with a hysteresis for input conditions other than those used during the training phase. Another issue covered was selecting the lags needed to build the model, which contrasts with the selection of basis function terms from the perspective of polynomial NARX models. Even so, GP-NARX is a black-box model, and as much as it offers the possibility of emulating dependent amplitude nonlinearities, it cannot still incorporate physical knowledge, which may become possible employing a grey-box philosophy. Finally, note that the systems discussed in this Chapter are for proof-of-concept only, and it is necessary to evaluate the representativeness of the GP-NARX in real applications with more complex nonlinear characteristics than the BERT benchmark, involving, for example, multiple vibrating modes.

7.2 PERSPECTIVES OF FUTURE WORK

Some of the proposals for future work have already been introduced throughout the concluding remarks of each Chapter (please, see 3.6, 4.4, 5.6 and 6.5). Some other specific suggestions for future research that have emerged in the progress of this work are outlined next:

7.2.1 Vibration reduction of assembled structures by the control of the tightening torque

As discussed in Chapter 1, there is a noticeable increase of interest in dry friction damping over the past decades, and indirectly, this interest also extends to applications where assembled structures are present. Especially in applications that experience environments with wide temperature ranges and the damping due to viscoelastic materials might be compromised, friction-induced damping is well suited.

The idea about the Orion beam design proceeded along the path of initially deciding on geometries of the structure (including dimensions of the contact patches). Only while conducting experiments the influence of different tightening torques on its behavior was assessed. In other words, the nonlinear damping of the structure was not previously predicted in a model design. Thus, one prospect of future work lies in controlling the vibration amplitude through the tightening torque applied to the external patches, requiring that a model of the Orion beam be determined first so that control techniques can then be investigated. For example, Bouaziz *et al.* (2016) investigated two control laws

that are based on, first, determining an optimal tightening torque for each excitation amplitude level, and second, adapting the tightening torque for each frequency range. Having a model of the Orion beam that incorporates dependence on torque paves the way for these control strategies to be investigated and reproduced in experimental tests.

7.2.2 Structural health monitoring of bolted joint structures

During operating conditions, vibration in bolted structures can lead to tightening torque loss in bolts. Under these circumstances, alarming consequences are bound to occur, such as structural collapse. Moreover, the torque loss usually occurs gradually, and it is important to establish some detection algorithm capable of investigating structural changes at an early stage, making it possible to repair.

One way to detect variations is by having torque measurements embedded at each bolt, or at least for regions near the joints. However, depending on the number of bolts present in a structure, performing such monitoring requires numerous measuring points and might become unfeasible. Thus, to circumvent possible limitations on the availability of instruments is to use indirect vibration measurements that allow for a global assessment of the structure, with a simple and clear indicator to quantify these torque values.

In this context, the implementation of non-parametric stochastic models that consider measurement uncertainties and model uncertainties as to the GP-NARX model and the Polynomial Chaos Expansion - kriging (PCE-kriging) are a very interesting tool to compare the performance of bolted joints under different state conditions. Due to the results presented for several torque values, the Orion beam is a good candidate benchmark for training detection algorithms. Studies on this subject are currently being conducted by the Ph.D. student Luccas Miguel.

7.2.3 Hysteresis model for predicting internal rolling displacement of tires

Aiming to reduce environmental impacts, the automobile industry has sought to develop technologies that aim to improve vehicle performance, minimize fuel consumption, and reduce pollutant emissions. This posture encourages the tire industry to adopt the same practices and investigate different energy dissipation mechanisms in tires, such as the rolling resistance. Thus, it is important to modify properties in tires that affect such resistance in motion to reduce the rolling resistance, making the modeling and tire design steps of utmost importance.

In the industry, the FE analysis is primarily used, but at the same time, it is computationally expensive. One way to speed up numerical simulations is through ROMs, which approximate the hysteresis loops by constitutive models. Due to the possibility of approximating different loop shapes, the Bouc-Wen model stands as a possible approach to predict the internal rolling displacement of tires, which currently has viscoelastic models as the largest exponents. Studies on this subject are currently being conducted by the Ph.D. student Rafael Raqueti.

7.3 CONTRIBUTIONS TO THE LITERATURE

The Thesis contributes to the literature by proposing a new way for harmonic probing of hysteretic systems through the concept of nonlinear smooth operators, which later turned into an identification framework for structures assembled by bolted joints. Another contribution addressed was the discussion of good practices for designing and experimental testing of dynamically excited jointed structures through the proposition of the Orion beam, a new benchmark for the literature. Identification of systems with hysteresis from the standpoint of non-parametric approximations was also a contribution pursued by the Thesis through using the GP-NARX model. Some of the results were published in the following journal articles:

- **Rafael de O. Teloli** and Samuel da Silva, ‘‘A new way for harmonic probing of hysteretic systems through nonlinear smooth operators’’, Mechanical Systems and Signal Processing, 2019;
- Luccas P. Miguel, **Rafael de O. Teloli** and Samuel da Silva, ‘‘Some practical regards on the application of the harmonic balance method for hysteresis models’’, Mechanical Systems and Signal Processing, 2020;
- **Rafael de O. Teloli**, Thiago G. Ritto, Samuel da Silva and Gaël Chevallier, ‘‘Bayesian model identification of higher-order frequency response functions for structures assembled by bolted joints’’, Mechanical Systems and Signal Processing, 2021;
- **Rafael de O. Teloli**, Luís G. G. Villani, Samuel da Silva, and Michael D. Todd, ‘‘On the use of the GP-NARX model for predicting hysteresis effects of bolted joint structures’’, Mechanical Systems and Signal Processing, 2021.

There are also manuscripts under review related to this work:

- **Rafael de O. Teloli**, Pauline Butaud, Gaël Chevallier and Samuel da Silva, ‘‘Good practices for designing and experimental testing of dynamically excited jointed structures: the Orion beam’’, Mechanical Systems and Signal Processing.
- **Rafael de O. Teloli**, Pauline Butaud, Gaël Chevallier and Samuel da Silva, ‘‘Dataset of experimental measurements for the Orion beam structure’’, Data in Brief.
- Luccas P. Miguel, **Rafael de O. Teloli** and Samuel da Silva, ‘‘Bayesian model identification through the harmonic balance method for hysteresis prediction in bolted joints’’, Nonlinear Dynamics.
- Samuel da Silva, Luccas P. Miguel, **Rafael de O. Teloli** and Gaël Chevallier, ‘‘Probabilistic machine learning for detection of tightening torque in bolted joints’’, Structural Health and Monitoring.

The following Conferences were attended in the period:

- **Rafael de O. Teloli**, Luís G. G. Villani, Samuel da Silva and Americo Cunha Jr., ‘‘Uso do método de superfície de resposta para estimar um modelo estocástico de uma viga não linear com rigidez cúbica’’, IX CONEM, 2016 (TELOLI *et al.*, 2016).
- **Rafael de O. Teloli** and Samuel da Silva, ‘‘Parametric frequency response method of hysteretic system with a dynamical nonlinearity subjected to harmonic excitation’’, 2018 (TELOLI; da SILVA, 2018b).
- **Rafael de O. Teloli** and Samuel da Silva, ‘‘Higher-order frequency response functions of Bouc-Wen model subjected to harmonic excitation’’, International Conference on Structural Dynamics and Diagnosis (CSNDD), 2018 (TELOLI; da SILVA, 2018a).
- **Rafael de O. Teloli**, ‘‘Identification through frequency-domain methods of hysteretic models for bolted joints of assembled structures’’, Surveillance Vibrations Shocks and Noise (SURVISHNO), 2019 (TELOLI, 2019).
- **Rafael de O. Teloli**, Samuel da Silva and Gaël Chevalier, ‘‘Parameters estimation by harmonic probing of hysteresis models of bolted jointed structures’’, Dynamical Systems Theory and Applications (DSTA), 2019 (TELOLI; SILVA; CHEVALLIER, 2019).

A book chapter has also been published with contributions related to the Thesis:

- Luccas P. Miguel, **Rafael de O. Teloli** and Samuel da Silva, ‘‘Harmonic balance of Bouc-Wen model to identify hysteresis effects in bolted joints’’, Vibration Engineering and Technology of Machinery book, 2021 (MIGUEL; TELOLI; SILVA, 2021).

REFERENCES

AHMADIAN, H.; JALALI, H. Generic element formulation for modelling bolted lap joints. **Mechanical Systems and Signal Processing**, London, v. 21, n. 5, p. 2318--2334, 2007. Available from: https://www.sciencedirect.com/science/article/pii/S0888327006002263. Access on: 20 July, 2021.

AHMADIAN, H.; JALALI, H. Identification of bolted lap joints parameters in assembled structures. **Mechanical Systems and Signal Processing**, London, v. 21, n. 2, p. 1041 -- 1050, 2007. Available from: http://www.sciencedirect.com/science/article/pii/S0888327005001263. Access on: 20 July, 2021.

AL-HABABI, T.; CAO, M.; SALEH, B.; ALKAYEM, N. F.; XU, H. A critical review of nonlinear damping identification in structural dynamics: Methods, applications, and challenges. **Sensors**, Multidisciplinary Digital Publishing Institute, Basel, v. 20, n. 24, p. 7303, 2020. Access on: 20 July, 2021.

ANDRÉ, H.; LECLÈRE, Q.; ANASTASIO, D.; BENAÏCHA, Y.; BILLON, K.; BIREM, M.; BONNARDOT, F.; CHIN, Z.; COMBET, F.; DAEMS, P.; DAGA, A.; De Geest, R.; ELYOUSFI, B.; GRIFFATON, J.; GRYLLIAS, K.; HAWWARI, Y.; HELSEN, J.; LACAZE, F.; LAROCHE, L.; LI, X.; LIU, C.; MAURICIO, A.; MELOT, A.; OMPUSUNGGU, A.; PAILLOT, G.; PASSOS, S.; PEETERS, C.; PEREZ, M.; QI, J.; SIERRA-ALONSO, E.; SMITH, W.; THOMAS, X. Using a smartphone camera to analyse rotating and vibrating systems: Feedback on the SURVISHNO 2019 contest. **Mechanical Systems and Signal Processing**, London, v. 154, p. 107553, 2021. Available from: https://www.sciencedirect.com/science/article/pii/S0888327020309390. Access on: 20 July, 2021.

ARMAND, J.; SALLES, L.; SCHWINGSHACKL, C.; SÜSS, D.; WILLNER, K. On the effects of roughness on the nonlinear dynamics of a bolted joint: A multiscale analysis. **European Journal of Mechanics - A/Solids**, Issy les Moulineaux Cedex, v. 70, p. 44--57, 2018. Available from: https://www.sciencedirect.com/science/article/pii/S0997753817305612. Access on: 20 July, 2021.

AVITABILE, P. Modal space-in our own little world. **Experimental Techniques**, Springer, New York, v. 39, n. 1, p. 3--10, 2015. Access on: 20 July, 2021.

AVITABILE, P. **Modal testing: a practitioner's guide**. New York: John Wiley & Sons, 2017.

BABER, T. T.; WEN, Y.-K. Random vibration hysteretic, degrading systems. **Journal of the Engineering Mechanics Division**, ASCE, Reston, v. 107, n. 6, p. 1069--1087, 1981.

BAJRIĆ, A.; HØGSBERG, J. Estimation of hysteretic damping of structures by stochastic subspace identification. **Mechanical Systems and Signal Processing**, London, v. 105, p. 36 -- 50, 2018. Available from: http://www.sciencedirect.com/science/article/pii/S0888327017306246. Access on: 20 July, 2021.

BALAJI, N. N.; BRAKE, M. R. The surrogate system hypothesis for joint mechanics. **Mechanical Systems and Signal Processing**, London, v. 126, p. 42--64, 2019. Available from: https://www.sciencedirect.com/science/article/pii/S0888327019300962. Access on: 20 July, 2021.

BALAJI, N. N.; CHEN, W.; BRAKE, M. R. Traction-based multi-scale nonlinear dynamic modeling of bolted joints: Formulation, application, and trends in micro-scale interface evolution. **Mechanical Systems and Signal Processing**, London, v. 139, p. 106615, 2020. Available from: https://www.sciencedirect.com/science/article/pii/S0888327020300017. Access on: 20 July, 2021.

BARAFF, D. Non-penetrating rigid body simulation. **State of the art reports**, 1993. Available from: https://www.cs.cmu.edu/~baraff/papers/eg93.pdf. Access on: 20 July, 2021.

BEARDS, C. **Structural vibration: analysis and damping**. New York: Elsevier, 1996.

BEAUDOIN, M.-A.; BEHDINAN, K. Analytical lump model for the nonlinear dynamic response of bolted flanges in aero-engines casings. **Mechanical Systems and Signal Processing**, Elsevier, London, v. 115, p. 14 -- 28, 2019. Available from: https://www.sciencedirect.com/science/article/pii/S0888327018303157. Access on: 20 July, 2021.

BEDROSIAN, E.; RICE, S. O. The output properties of Volterra systems (nonlinear systems with memory) driven by harmonic and Gaussian inputs. **Proceedings of the IEEE**, Piscataway, v. 59, n. 12, p. 1688--1707, Dec 1971.

BEER, M.; FERSON, S.; KREINOVICH, V. Imprecise probabilities in engineering analyses. **Mechanical Systems and Signal Processing**, London, v. 37, n. 1, p. 4--29, 2013. Available from: https://www.sciencedirect.com/science/article/pii/S0888327013000812. Access on: 20 July, 2021.

BHATTACHARYYA, B.; JACQUELIN, E.; BRIZARD, D. A Kriging-NARX model for uncertainty quantification of nonlinear stochastic dynamical systems in time domain. **Journal of Engineering Mechanics**, Reston, v. 146, n. 7, p. 04020070, 2020. Available from: https://ascelibrary.org/doi/abs/10.1061/%28ASCE%29EM.1943-7889.0001792. Access on: 20 July, 2021.

BILLINGS, S. A. **Nonlinear system identification: NARMAX methods in the time, frequency, and spatio-temporal domains**. New York: John Wiley & Sons, 2013.

BISWAS, S.; CHATTERJEE, A. A two-state hysteresis model for bolted joints, with minor loops from partial unloading. **International Journal of Mechanical Sciences**, Oxford, v. 140, p. 506--520, 2018. Available from: https://www.sciencedirect.com/science/article/pii/S0020740317320775. Access on: 20 July, 2021.

BOGRAD, S.; REUSS, P.; SCHMIDT, A.; GAUL, L.; MAYER, M. Modeling the dynamics of mechanical joints. **Mechanical Systems and Signal Processing**, London, v. 25, n. 8, p. 2801--2826, 2011. Available from: https://www.sciencedirect.com/science/article/pii/S0888327011000203. Access on: 20 July, 2021.

BOGRAD, S.; SCHMIDT, A.; GAUL, L. Joint damping prediction by thin-layer elements. 2008. Available from: https://www.imperial.ac.uk/media/imperial-college/research-centres-and-groups/dynamics/bograd_schmidt_gaul.pdf. Access on: 20 July, 2021.

BOUAZIZ, H.; PEYRET, N.; ABBES, M. S.; CHEVALLIER, G.; HADDAR, M. Vibration reduction of an assembly by control of the tightening load. **International Journal of Applied Mechanics**, Tehran, v. 08, n. 06, p. 1650081, 2016. Access on: 20 July, 2021.

BOUC, R. Forced vibration of mechanical systems with hysteresis. In: **PROCEEDINGS OF THE FOURTH CONFERENCE ON NON-LINEAR OSCILLATION,4,1967,Prague**. [S.l.]: Proceedings of the [...]. Prague: [s.n.], 1967.

BOUC, R. A mathematical model for hysteresis. **Acta Acustica united with Acustica**, Stuttgart, v. 24, n. 1, p. 16--25, 1971. Available from: https://www.ingentaconnect.com/content/dav/aaua/1971/00000024/00000001/art00004. Access on: 20 July, 2021.

BOUCHAALA, N.; DION, J.-L.; PEYRET, N. Microslip induced damping in the contact of nominally flat surfaces with geometric defects. In: BRAKE, M. R. W. (Ed.). **The Mechanics of Jointed Structures: Recent Research and Open Challenges for Developing Predictive Models for Structural Dynamics**. Cham: Springer International Publishing, 2018. p. 331--353. Available from: https://doi.org/10.1007/978-3-319-56818-8_19. Access on: 20 July, 2021.

BOWDEN, F. P.; BOWDEN, F. P.; TABOR, D. **The friction and lubrication of solids**. Oxford: Oxford university press, 2001.

BRAKE, M. R. W. The role of epistemic uncertainty of contact models in the design and optimization of mechanical systems with aleatoric uncertainty. **Nonlinear Dynamics**, Dordrecht, v. 77, n. 3, p. 899--922, 2014. Available from: https://doi.org/10.1007/s11071-014-1350-0. Access on: 20 July, 2021.

BRAKE, M. R. W. Constitutive modeling of contact for elastic-plastic materials engaged in micro/macroslip. In: BRAKE, M. R. W. (Ed.). **The Mechanics of Jointed Structures: Recent Research and Open Challenges for Developing Predictive Models for Structural Dynamics**. Cham: Springer International Publishing, 2018. p. 279--329. Available from: https://doi.org/10.1007/978-3-319-56818-8_18. Access on: 20 July, 2021.

BRAKE, M. R. W. **The Mechanics of Jointed Structures: Recent Research and Open Challenges for Developing Predictive Models for Structural Dynamics**. Cham: Springer, 2018.

BRAKE, M. R. W. The next generation of joints research. In: BRAKE, M. R. W. (Ed.). **The Mechanics of Jointed Structures: Recent Research and Open Challenges for Developing Predictive Models for Structural Dynamics**. Cham: Springer International Publishing, 2018. p. 675--689. Access on: 20 July, 2021.

BRAKE, M. R. W. Round robin systems. In: BRAKE, M. R. W. (Ed.). **The Mechanics of Jointed Structures: Recent Research and Open Challenges for Developing Predictive Models for Structural Dynamics**. Cham: Springer International Publishing, 2018. p. 45--58. Available from: https://doi.org/10.1007/978-3-319-56818-8_5. Access on: 20 July, 2021.

BRAKE, M. R. W.; EWINS, D. J.; WYNN, C. B. Are joints necessary? In: BRAKE, M. R. W. (Ed.). **The Mechanics of Jointed Structures: Recent Research and Open Challenges for Developing Predictive Models for Structural Dynamics**. Cham: Springer International Publishing, 2018. p. 25--36. Available from: https://doi.org/10.1007/978-3-319-56818-8_3. Access on: 20 July, 2021.

BRAKE, M. R. W.; KRACK, M.; SCHWINGSHACKL, C. W. Special Issue: Tribomechadynamics. **Journal of Vibration and Acoustics**, New York, v. 142, n. 5, 08 2020. 050301. Available from: https://doi.org/10.1115/1.4048185. Access on: 20 July, 2021.

BRAKE, M. R. W.; REUSS, P.; SEGALMAN, D. J.; GAUL, L. Variability and repeatability of jointed structures with frictional interfaces. In: ALLEN, M.; MAYES, R. L.; RIXEN, D. J. (Ed.). **Dynamics of Coupled Structures, Volume 1**. Cham: Springer, 2014. p. 245--252.

BRAKE, M. R. W.; SCHWINGSHACKL, C.; REUSS, P. Observations of variability and repeatability in jointed structures. **Mechanical Systems and Signal Processing**, London, v. 129, p. 282 -- 307, 2019. Available from: http://www.sciencedirect.com/science/article/pii/S0888327019302511. Access on: 20 July, 2021.

BRØNS, M.; KASPER, T. A.; CHAUDA, G.; KLAASSEN, S. W. B.; SCHWINGSHACKL, C. W.; BRAKE, M. R. W. Experimental Investigation of Local Dynamics in a Bolted Lap Joint Using Digital Image Correlation. **Journal of Vibration and Acoustics**, New York, v. 142, n. 5, 07 2020. Available from: https://doi.org/10.1115/1.4047699. Access on: 20 July, 2021.

BUSSETTA, P.; SHIKI, S. B.; SILVA, S. da. Nonlinear updating method: a review. **Journal of the Brazilian Society of Mechanical Sciences and Engineering**, Springer, Heidlberg, v. 39, n. 11, p. 4757--4767, 2017. Available from: https://doi.org/10.1007%2Fs40430-017-0905-7. Access on: 20 July, 2021.

CABBOI, A.; KAMPHUIS, T.; van VELDHUIZEN, E.; SEGEREN, M.; HENDRIKSE, H. Vibration-assisted decommissioning of a slip joint: Application to an offshore wind turbine. **Marine Structures**, London, v. 76, p. 102931, 2021. Available from: https://www.sciencedirect.com/science/article/pii/S0951833920302215. Access on: 20 July, 2021.

CAFFERTY, S.; TOMLINSON, G. Characterization of automotive dampers using higher order frequency response functions. **Proceedings of the Institution of Mechanical Engineers, Part D: Journal of Automobile Engineering**, Sage Publications, London, v. 211, n. 3, p. 181--203, 1997. Available from: https://doi.org/10.1243/0954407971526353. Access on: 20 July, 2021.

CAIGNOT, A.; LADEVÉZE, P.; NÉRON, D.; LOCH, S. L.; GALLO, V. L.; MA, K. M.; ROMEUF, T. Prediction of damping in space lauch vehicles using a virtual testing strategy. In: **PROCEEDINGS OF INTERNATIONAL SYMPOSIUM ON LAUNCHER TECHNOLOGIES, 6, 2005, Munich**. [S.l.]: Proceedings of the [...]. Munich: [s.n.], 2005.

CAIGNOT, A.; LADEVÉZE, P.; NÉRON, D.; DURAND, J. Virtual testing for the prediction of damping in joints. **Engineering Computations**, Bingley, v. 27, p. 621--644, 2010.

CAMERON, T. M.; GRIFFIN, J. H. An Alternating Frequency/Time Domain Method for Calculating the Steady-State Response of Nonlinear Dynamic Systems. **Journal of Applied Mechanics**, Tehran, v. 56, n. 1, p. 149--154, 03 1989.

CANDELA, J. Q.; GIRARD, A.; LARSEN, J.; RASMUSSEN, C. E. Propagation of uncertainty in Bayesian kernel models - application to multiple-step ahead forecasting. In: **2003 IEEE International Conference on Acoustics, Speech, and Signal Processing, 2003. Proceedings. (ICASSP '03).** Proceedings of the [...]. Hong Kong: IEEE, 2003. v. 2, p. 2--701. Available from: http://ieeexplore.ieee.org/document/1202463. Access on: 17 Oct., 2019.

CASTELLO, D.; RITTO, T. **Quantificação de incertezas e estimação de parâmetros em dinâmica estrutural: uma introdução a partir de exemplos computacionais**. São Carlos: Sociedade Brasileira de Matemática Aplicada e Computacional, 2016.

CATALFAMO, S.; SMITH, S. A.; MORLOCK, F.; BRAKE, M. R. W.; REUSS, P.; SCHWINGSHACKL, C. W.; ZHU, W. D. Effects of experimental methods on the measurements of a nonlinear structure. In: ALLEN, M.; MAYES, R. L.; RIXEN, D. (Ed.). **Dynamics of Coupled Structures, Volume 4**. Cham: Springer International Publishing, 2016. p. 491--500.

CAUGHEY, T. Response of a nonlinear string to random loading. **Journal of Applied Mechanics**, Tehran, v. 26, n. 3, p. 341--344, 1959.

CHABRIER, R.; SADOULET-REBOUL, E.; CHEVALLIER, G.; FOLTÊTE, E.; JEANNIN, T. Full-field measurements with Digital Image Correlation for vibro-impact characterisation. **Mechanical Systems and Signal Processing**, London, v. 156, p. 107658, 2021. Available from: https://www.sciencedirect.com/science/article/pii/S0888327021000534. Access on: 20 July, 2021.

CHATTERJEE, A. Identification and parameter estimation of a bilinear oscillator using Volterra series with harmonic probing. **International Journal of Non-Linear Mechanics**, Oxford, v. 45, n. 1, p. 12 -- 20, 2010. Available from:

http://www.sciencedirect.com/science/article/pii/S0020746209001632. Access on: 20 July, 2021.

CHATTERJEE, A. Structural damage assessment in a cantilever beam with a breathing crack using higher order frequency response functions. **Journal of Sound and Vibration**, London, v. 329, n. 16, p. 3325 -- 3334, 2010. Available from: http://www.sciencedirect.com/science/article/pii/S0022460X10001495. Access on: 20 July, 2021.

CHATTERJEE, A.; VYAS, N. S. Non-linear parameter estimation with Volterra series using the method of recursive iteration through harmonic probing. **Journal of Sound and Vibration**, London, v. 268, n. 4, p. 657 -- 678, 2003. Available from: http://www.sciencedirect.com/science/article/pii/S0022460X02015377. Access on: 20 July, 2021.

CHATTERJEE, A.; VYAS, N. S. Non-linear parameter estimation in multi-degree-of-freedom systems using multi-input Volterra series. **Mechanical Systems and Signal Processing**, London, v. 18, n. 3, p. 457 -- 489, 2004. Available from: http://www.sciencedirect.com/science/article/pii/S0888327003000165. Access on: 20 July, 2021.

CHEN, W.; DENG, X. Structural damping caused by micro-slip along frictional interfaces. **International Journal of Mechanical Sciences**, Oxford, v. 47, n. 8, p. 1191--1211, 2005. Available from: https://www.sciencedirect.com/science/article/pii/S0020740305001165. Access on: 20 July, 2021.

CHEN, Y.; Escalera Mendoza, A. S.; GRIFFITH, D. T. Experimental and numerical study of high-order complex curvature mode shape and mode coupling on a three-bladed wind turbine assembly. **Mechanical Systems and Signal Processing**, London, v. 160, p. 107873, 2021. Available from: https://www.sciencedirect.com/science/article/pii/S0888327021002685. Access on: 20 July, 2021.

CHENG, C.; PENG, Z.; ZHANG, W.; MENG, G. Volterra-series-based nonlinear system modeling and its engineering applications: A state-of-the-art review. **Mechanical Systems and Signal Processing**, London, v. 87, p. 340 -- 364, 2017. Available from: http://www.sciencedirect.com/science/article/pii/S0888327016304393. Access on: 20 July, 2021.

CHOU, D. **Dahl friction modeling**. Thesis (Ph. D.) --- Massachusetts Institute of Technology, Massachusetts, 2004. Available from: https://dspace.mit.edu/handle/1721.1/32826. Access on: 20 July, 2021.

CHRONOPOULOS, D.; ICHCHOU, M.; TROCLET, B.; BAREILLE, O. Predicting the broadband response of a layered cone-cylinder-cone shell. **Composite Structures**, London, v. 107, p. 149--159, 2014. Available from: https://www.sciencedirect.com/science/article/pii/S0263822313003930. Access on: 20 July, 2021.

CLAEYS, M.; SINOU, J.-J.; LAMBELIN, J.-P.; TODESCHINI, R. Experiments and numerical simulations of nonlinear vibration responses of an assembly with friction joints - Application on a test structure named ‘‘Harmony’’. **Mechanical Systems and Signal Processing**, London, v. 70-71, p. 1097--1116, 2016. Available from:

https://www.sciencedirect.com/science/article/pii/S0888327015003866. Access on: 20 July, 2021.

CLAEYS, M.; SINOU, J.-J.; LAMBELIN, J.-P.; TODESCHINI, R. Modal interactions due to friction in the nonlinear vibration response of the ‘‘Harmony’’ test structure: Experiments and simulations. **Journal of Sound and Vibration**, London, v. 376, p. 131--148, 2016. Available from: https://www.sciencedirect.com/science/article/pii/S0022460X16300426. Access on: 20 July, 2021.

COLLET, M.; OUISSE, M.; ICHCHOU, M. N. Structural energy flow optimization through adaptive shunted piezoelectric metacomposites. **Journal of Intelligent Material Systems and Structures**, London, v. 23, n. 15, p. 1661--1677, 2012. Available from: https://doi.org/10.1177/1045389X12449915. Access on: 20 July, 2021.

DAHL, P. R. **A solid friction model**. [S.l.], 1968. Available from: https://apps.dtic.mil/sti/citations/ADA041920. Access on: 20 July, 2021.

DEANER, B. J.; ALLEN, M. S.; STARR, M. J.; SEGALMAN, D. J.; SUMALI, H. Application of Viscous and Iwan Modal Damping Models to Experimental Measurements From Bolted Structures. **Journal of Vibration and Acoustics**, London, v. 137, n. 2, 2015. Available from: https://doi.org/10.1115/1.4029074. Access on: 20 July, 2021.

DENIMAL, E.; WONG, C.; SALLES, L.; PESARESI, L. On the Efficiency of a Conical Underplatform Damper for Turbines. **Journal of Engineering for Gas Turbines and Power**, New York, v. 143, n. 2, 02 2021. 021020. Available from: https://doi.org/10.1115/1.4049665. Access on: 20 July, 2021.

DION, J.; CHEVALLIER, G.; PENAS, O.; RENAUD, F. A new multicontact tribometer for deterministic dynamic friction identification. **Wear**, Amsterdam, v. 300, n. 1, p. 126--135, 2013. Available from: https://www.sciencedirect.com/science/article/pii/S0043164813001221. Access on: 20 July, 2021.

DION, J.-L.; CHEVALLIER, G.; PEYRET, N. Improvement of measurement techniques for damping induced by micro-sliding. **Mechanical Systems and Signal Processing**, London, v. 34, n. 1, p. 106--115, 2013. Available from: https://www.sciencedirect.com/science/article/pii/S0888327012003093. Access on: 20 July, 2021.

DONESCU, P.; VIRGIN, L. N.; WU, J. J. Periodic solutions of an unsymmetric oscillator including a comprehensive study of their stability characteristics. **Journal of Sound and Vibration**, London, v. 192, n. 5, p. 959--976, 1996. Available from: https://doi.org/10.1006%2Fjsvi.1996.0228. Access on: 20 July, 2021.

DOSSOGNE, T.; JEROME, T. W.; LANCEREAU, D. P. T.; SMITH, S. A.; BRAKE, M. R. W.; PACINI, B. R.; REUSS, P.; SCHWINGSHACKL, C. W. Experimental assessment of the influence of interface geometries on structural dynamic response. In: ALLEN, M.; L., M. R.; RIXEN, D. (Ed.). **Dynamics of Coupled Structures**. Cham: Springer International Publishing, 2017. p. 255--261.

DOYLE, F. J.; PEARSON, R. K.; OGUNNAIKE, B. A. **Identification and control using Volterra models**. London: Springer, 2002.

DREHER, T.; BRAKE, M. R. W.; SEEGER, B.; KRACK, M. In situ, real-time measurements of contact pressure internal to jointed interfaces during dynamic excitation of an assembled structure. **Mechanical Systems and Signal Processing**, London, v. 160, p. 107859, 2021. Available from: https://www.sciencedirect.com/science/article/pii/S0888327021002545. Access on: 20 July, 2021.

ERITEN, M.; KURT, M.; LUO, G.; Michael McFarland, D.; BERGMAN, L. A.; VAKAKIS, A. F. Nonlinear system identification of frictional effects in a beam with a bolted joint connection. **Mechanical Systems and Signal Processing**, London, v. 39, n. 1, p. 245--264, 2013. Available from: https://www.sciencedirect.com/science/article/pii/S0888327013001039. Access on: 20 July, 2021.

ERITEN, M.; POLYCARPOU, A. A.; BERGMAN, L. A. Surface Roughness Effects on Energy Dissipation in Fretting Contact of Nominally Flat Surfaces. **Journal of Applied Mechanics**, Tehran, v. 78, n. 2, 11 2010. Available from: https://doi.org/10.1115/1.4002433. Access on: 20 July, 2021.

ESFAHANI, A. F.; DREESEN, P.; TIELS, K.; NOËL, J.-P.; SCHOUKENS, J. Parameter reduction in nonlinear state-space identification of hysteresis. **Mechanical Systems and Signal Processing**, London, v. 104, p. 884 -- 895, 2018. Available from: http://www.sciencedirect.com/science/article/pii/S0888327017305502. Access on: 20 July, 2021.

EWINS, D. J. **Modal testing: theory, practice and application**. New York: John Wiley & Sons, 2009.

EWINS, D. J. Exciting vibrations: the role of testing in an era of supercomputers and uncertainties. **Meccanica**, Dordrecht, v. 51, p. 3241--3258, 2016.

EWINS, D. J.; WEEKES, B.; Delli CARRI, A. Modal testing for model validation of structures with discrete nonlinearities. **Philosophical Transactions of the Royal Society A: Mathematical, Physical and Engineering Sciences**, London, v. 373, n. 2051, p. 20140410, 2015.

FANTETTI, A.; TAMATAM, L. R.; VOLVERT, M.; LAWAL, I.; LIU, L.; SALLES, L.; BRAKE, M. R. W.; SCHWINGSHACKL, C. W.; NOWELL, D. The impact of fretting wear on structural dynamics: Experiment and simulation. **Tribology International**, Oxford, v. 138, p. 111--124, 2019. Available from: https://www.sciencedirect.com/science/article/pii/S0301679X19302828. Access on: 20 July, 2021.

FEENY, B.; GURAN, A.; HINRICHS, N.; POPP, K. A Historical Review on Dry Friction and Stick-Slip Phenomena. **Applied Mechanics Reviews**, New York, v. 51, n. 5, p. 321--341, 05 1998. Available from: https://doi.org/10.1115/1.3099008. Access on: 20 July, 2021.

FESTJENS, H.; CHEVALLIER, G.; DION, J. Nonlinear model order reduction of jointed structures for dynamic analysis. **Journal of Sound and Vibration**, London,

v. 333, n. 7, p. 2100 -- 2113, 2014. Available from: http://www.sciencedirect.com/science/article/pii/S0022460X13009930. Access on: 20 July, 2021.

FESTJENS, H.; CHEVALLIER, G.; DION, J.-l. A numerical tool for the design of assembled structures under dynamic loads. **International Journal of Mechanical Sciences**, Oxford, v. 75, p. 170--177, 2013. Available from: https://www.sciencedirect.com/science/article/pii/S0020740313001860. Access on: 20 July, 2021.

GAMERMAN, D.; LOPES, H. F. **Markov Chain Monte Carlo: stochastic simulation for Bayesian inference**. London: Chapman and Hall/CRC, 2006.

GAUL, L.; LENZ, J. Nonlinear dynamics of structures assembled by bolted joints. **Acta Mechanica**, Wien, v. 125, n. 1, p. 169--181, 1997.

GAUL, L.; NITSCHE, R. The Role of Friction in Mechanical Joints. **Applied Mechanics Reviews**, New York, v. 54, n. 2, p. 93--106, 03 2001. Available from: https://doi.org/10.1115/1.3097294. Access on: 20 July, 2021.

GILL, P. E.; WONG, E. **Sequential Quadratic Programming Methods**. [S.l.]. Available from: https://www.math.uh.edu/~rohop/fall_06/Chapter4.pdf. Access on: 20 July, 2021.

GIRI, F.; RADOUANE, A.; BROURI, A.; CHAOUI, F.-Z. Combined frequency-prediction error identification approach for Wiener systems with backlash and backlash-inverse operators. **Automatica**, Oxford, v. 50, n. 3, p. 768 -- 783, 2014. Available from: http://www.sciencedirect.com/science/article/pii/S000510981300589X. Access on: 20 July, 2021.

GIRI, F.; ROCHDI, Y.; RADOUANE, A.; BROURI, A.; CHAOUI, F. Frequency identification of nonparametric Wiener systems containing backlash nonlinearities. **Automatica**, Oxford, v. 49, n. 1, p. 124 -- 137, 2013. Available from: http://www.sciencedirect.com/science/article/pii/S0005109812004864. Access on: 20 July, 2021.

GLOTH, G.; SINAPIUS, M. Analysis of swept-sine runs during modal identification. **Mechanical Systems and Signal Processing**, London, v. 18, n. 6, p. 1421 -- 1441, 2004. Available from: http://www.sciencedirect.com/science/article/pii/S0888327003000876. Access on: 20 July, 2021.

GOYDER, H.; IND, P.; BROWN, D. Measurement of Damping due to Bolted Joints. In: **INTERNATIONAL DESIGN ENGINEERING TECHNICAL CONFERENCES AND COMPUTERS AND INFORMATION IN ENGINEERING CONFERENCE, 25**. Portland: Proceedings of the [...]. Portland: ASME, 2013.

GREEN, P. L.; WORDEN, K. Bayesian and Markov chain Monte Carlo methods for identifying nonlinear systems in the presence of uncertainty. **Philosophical Transactions of the Royal Society A: Mathematical, Physical and Engineering Sciences**, London, v. 373, n. 2051, p. 20140405, 2015. Available from: https://royalsocietypublishing.org/doi/abs/10.1098/rsta.2014.0405. Access on: 20 July, 2021.

GREENWOOD, J. A.; WILLIAMSON, J. P. Contact of nominally flat surfaces. **Proceedings of the royal society of London. Series A. Mathematical and physical sciences**, London, v. 295, n. 1442, p. 300--319, 1966.

GRIFFIN, J. H. A review of friction damping of turbine blade vibration. **International Journal of Turbo and Jet Engines**, Berlin, v. 7, n. 3-4, p. 297--308, 1990.

GUO, K.; ZHANG, X.; LI, H.; HUA, H.; MENG, G. A new dynamical friction model. **International Journal of Modern Physics B**, Singapore, v. 22, n. 08, p. 967--980, 2008. Available from: https://doi.org/10.1142/S0217979208039010. Access on: 20 July, 2021.

GUO, S.; YANG, S.; PAN, C. Dynamic modeling of Magnetorheological Damper behaviors. **Journal of Intelligent Material Systems and Structures**, London, v. 17, n. 1, p. 3--14, 2006. Available from: https://doi.org/10.1177/1045389X06055860. Access on: 20 July, 2021.

GWINNER, J.; BROSOWSKI, B. A penalty approximation for a unilateral contact problem in non-linear elasticity. **Mathematical Methods in the Applied Sciences**, Oxford, v. 11, n. 4, p. 447--458, 1989. Available from: https://onlinelibrary.wiley.com/doi/abs/10.1002/mma.1670110403. Access on: 20 July, 2021.

HASSANI, V.; TJAHJOWIDODO, T.; DO, T. N. A survey on hysteresis modeling, identification and control. **Mechanical Systems and Signal Processing**, London, v. 49, n. 1, p. 209 -- 233, 2014. Available from: http://www.sciencedirect.com/science/article/pii/S0888327014001186. Access on: 20 July, 2021.

HELLER, L. **Amortissement dans les structures assemblées**. Thesis (Ph. D.) --- Université Bourgorne Franche-Comté, Besançon, 2005. Available from: http://www.theses.fr/2005BESA2050. Access on: 20 July, 2021.

HELLER, L.; FOLTETE, E.; PIRANDA, J. Experimental identification of nonlinear dynamic properties of built-up structures. **Journal of Sound and Vibration**, London, v. 327, n. 1, p. 183--196, 2009. Available from: https://www.sciencedirect.com/science/article/pii/S0022460X09004945. Access on: 20 July, 2021.

HERSHEY, J. R.; OLSEN, P. A. Approximating the Kullback Leibler Divergence between Gaussian Mixture Models. In: **IEEE INTERNATIONAL CONFERENCE ON ACOUSTICS, SPEECH AND SIGNAL PROCESSING - ICASSP'07, 2007**. Honolulu: Proceedings of the [...]. Honolulu: IEEE, 2007. v. 4, p. 317--320.

HERTZ, H. Über die berührung fester elastischer körper (on the contact of elastic solids). **Journal Fur Die Reine und Angewandte Mathematik**, Berlin, v. 92, p. 156--171, 1882. Available from: https://home.uni-leipzig.de/pwm/web/download/Hertz1881.pdf. Access on: 20 July, 2021.

HUANG, X.-R.; JÉZÉQUEL, L.; BESSET, S.; LI, L.; SAUVAGE, O. Nonlinear modal synthesis for analyzing structures with a frictional interface using a generalized Masing model. **Journal of Sound and Vibration**, London, v. 434, p. 166 -- 191, 2018.

Available from: http://www.sciencedirect.com/science/article/pii/S0022460X18304711. Access on: 20 July, 2021.

HUYNH, T.-C.; DANG, N.-L.; KIM, J.-T. Preload monitoring in bolted connection using piezoelectric-based smart interface. **Sensors**, Basel, v. 18, n. 9, 2018. Available from: https://www.mdpi.com/1424-8220/18/9/2766. Access on: 20 July, 2021.

IKHOUANE, F.; HURTADO, J. E.; RODELLAR, J. Variation of the hysteresis loop with the Bouc-Wen model parameters. **Nonlinear Dynamics**, Dordrecht, v. 48, n. 4, p. 361--380, 2007. Available from: https://doi.org/10.1007/s11071-006-9091-3. Access on: 20 July, 2021.

IKHOUANE, F.; RODELLAR, J. On the hysteretic Bouc-Wen model. **Nonlinear Dynamics**, Dordrecht, v. 42, n. 1, p. 79--95, 2005. Available from: https://doi.org/10.1007/s11071-005-0070-x. Access on: 20 July, 2021.

IKHOUANE, F.; RODELLAR, J. **Systems with hysteresis: analysis, identification and control using the Bouc-Wen model**. London: John Wiley & Sons, 2007.

IRANZAD, M.; AHMADIAN, H. Identification of nonlinear bolted lap joint models. **Computers & Structures**, Oxford, v. 96-97, p. 1--8, 2012. Available from: https://www.sciencedirect.com/science/article/pii/S0045794912000260. Access on: 20 July, 2021.

ISMAIL, M.; IKHOUANE, F.; RODELLAR, J. The hysteresis Bouc-Wen model, a survey. **Archives of Computational Methods in Engineering**, Dordrecht, v. 16, n. 2, p. 161--188, 2009. Available from: https://doi.org/10.1007/s11831-009-9031-8. Access on: 20 July, 2021.

IWAN, W. D. A Distributed-Element Model for Hysteresis and Its Steady-State Dynamic Response. **Journal of Applied Mechanics**, Tehran, v. 33, n. 4, p. 893--900, 12 1966. Available from: https://doi.org/10.1115/1.3625199. Access on: 20 July, 2021.

IWAN, W. D. On a Class of Models for the Yielding Behavior of Continuous and Composite Systems. **Journal of Applied Mechanics**, Tehran, v. 34, n. 3, p. 612--617, 09 1967. Available from: https://doi.org/10.1115/1.3607751. Access on: 20 July, 2021.

JALALI, H. An alternative linearization approach applicable to hysteretic systems. **Communications in Nonlinear Science and Numerical Simulation**, Amsterdam, v. 19, n. 1, p. 245 -- 257, 2014. Available from: http://www.sciencedirect.com/science/article/pii/S1007570413002220. Access on: 20 July, 2021.

JALALI, H.; AHMADIAN, H.; MOTTERSHEAD, J. E. Identification of nonlinear bolted lap-joint parameters by force-state mapping. **International Journal of Solids and Structures**, Oxford, v. 44, n. 25, p. 8087 -- 8105, 2007. Available from: http://www.sciencedirect.com/science/article/pii/S0020768307002417. Access on: 20 July, 2021.

JALALI, H.; KHODAPARAST, H. H.; MADINEI, H.; FRISWELL, M. Stochastic modelling and updating of a joint contact interface. **Mechanical Systems and Signal Processing**, London, v. 129, p. 645 -- 658, 2019. Available from:

http://www.sciencedirect.com/science/article/pii/S0888327019302353. Access on: 20 July, 2021.

JAUMOUILLÉ, V.; SINOU, J.-J.; PETITJEAN, B. An adaptive harmonic balance method for predicting the nonlinear dynamic responses of mechanical systems - application to bolted structures. **Journal of Sound and Vibration**, London, v. 329, n. 19, p. 4048 -- 4067, 2010. Available from: http://www.sciencedirect.com/science/article/pii/S0022460X10002464. Access on: 20 July, 2021.

JAYAKUMAR, P. **Modeling and identification in structural dynamics**. Thesis (Ph. D.) --- California Institute of Technology, California, 1987. Available from: https://thesis.library.caltech.edu/11411/. Access on: 20 July, 2021.

JEFFREYS, H.; JEFFREYS, B. **Methods of mathematical physics**. Cambridge: Cambridge university press, 1999.

JEWELL, E.; ALLEN, M. S.; ZARE, I.; WALL, M. Application of quasi-static modal analysis to a finite element model and experimental correlation. **Journal of Sound and Vibration**, London, v. 479, p. 115376, 2020. Available from: https://www.sciencedirect.com/science/article/pii/S0022460X20302078. Access on: 20 July, 2021.

JING, X. J.; LANG, Z. Q.; BILLINGS, S. A. Magnitude bounds of generalized frequency response functions for nonlinear Volterra systems described by NARX model. **Automatica**, Oxford, v. 44, n. 3, p. 838 -- 845, 2008. Available from: http://www.sciencedirect.com/science/article/pii/S0005109807003469. Access on: 20 July, 2021.

JOHNSON, K. L.; JOHNSON, K. L. **Contact mechanics**. Cambridge: Cambridge university press, 1987.

KARAAĞAÇLI, T.; ÖZGÜVEN, H. N. Experimental modal analysis of nonlinear systems by using response-controlled stepped-sine testing. **Mechanical Systems and Signal Processing**, London, v. 146, p. 107023, 2021. Available from: https://www.sciencedirect.com/science/article/pii/S088832702030409X. Access on: 20 July, 2021.

KERSCHEN, G.; PEETERS, M.; GOLINVAL, J.; VAKAKIS, A. Nonlinear normal modes, part I: A useful framework for the structural dynamicist. **Mechanical Systems and Signal Processing**, London, v. 23, n. 1, p. 170--194, 2009. Special Issue: Non-linear Structural Dynamics. Available from: https://www.sciencedirect.com/science/article/pii/S0888327008001015. Access on: 20 July, 2021.

KERSCHEN, G.; WORDEN, K.; VAKAKIS, A. F.; GOLINVAL, J.-C. Past, present and future of nonlinear system identification in structural dynamics. **Mechanical Systems and Signal Processing**, London, v. 20, n. 3, p. 505--592, 2006. Available from: https://www.sciencedirect.com/science/article/pii/S0888327005000828. Access on: 20 July, 2021.

KIM, W.-J.; PERKINS, N. Harmonic balance/Galerkin method for non-smooth dynamic systems. **Journal of Sound and Vibration**, London, v. 261, n. 2, p. 213 -- 224, 2003.

Available from: http://www.sciencedirect.com/science/article/pii/S0022460X02009495. Access on: 20 July, 2021.

KING, M. E.; VAKAKIS, A. F. An Energy-Based Formulation for Computing Nonlinear Normal Modes in Undamped Continuous Systems. **Journal of Vibration and Acoustics**, London, v. 116, n. 3, p. 332--340, 1994. Available from: https://doi.org/10.1115/1.2930433. Access on: 20 July, 2021.

KOCIJAN, J.; GIRARD, A.; BANKO, B.; MURRAY-SMITH, R. Dynamic systems identification with Gaussian processes. **Mathematical and Computer Modelling of Dynamical Systems**, Abingdon, v. 11, n. 4, p. 411--424, 2005. Available from: https://doi.org/10.1080/13873950500068567. Access on: 20 July, 2021.

KOH, K.-H.; GRIFFIN, J. H.; FILIPPI, S.; AKAY, A. Characterization of Turbine Blade Friction Dampers. **Journal of Engineering for Gas Turbines and Power**, New York, v. 127, n. 4, p. 856--862, 2004. Available from: https://doi.org/10.1115/1.1926312. Access on: 20 July, 2021.

KOVACIC, I.; BRENNAN, M. J. **The Duffing equation: nonlinear oscillators and their behaviour**. London: John Wiley & Sons, 2011.

KRACK, M. Nonlinear modal analysis of nonconservative systems: Extension of the periodic motion concept. **Computers & Structures**, Oxford, v. 154, p. 59--71, 2015. Available from: https://www.sciencedirect.com/science/article/pii/S0045794915000978. Access on: 20 July, 2021.

KRACK, M.; BERGMAN, L. A.; VAKAKIS, A. F. On the efficacy of friction damping in the presence of nonlinear modal interactions. **Journal of Sound and Vibration**, London, v. 370, p. 209--220, 2016. Available from: https://www.sciencedirect.com/science/article/pii/S0022460X16000882. Access on: 20 July, 2021.

KRACK, M.; GROSS, J. **Harmonic balance for nonlinear vibration problems**. New York: Springer, 2019.

KRACK, M.; SALLES, L.; THOUVEREZ, F. Vibration prediction of bladed disks coupled by friction joints. **Archives of Computational Methods in Engineering**, Dordrecht, v. 24, n. 3, p. 589--636, 2017. Available from: https://doi.org/10.1007/s11831-016-9183-2. Access on: 20 July, 2021.

LACAYO, R.; PESARESI, L.; GROSS, J.; FOCHLER, D.; ARMAND, J.; SALLES, L.; SCHWINGSHACKL, C.; ALLEN, M.; BRAKE, M. Nonlinear modeling of structures with bolted joints: A comparison of two approaches based on a time-domain and frequency-domain solver. **Mechanical Systems and Signal Processing**, London, v. 114, p. 413 -- 438, 2019. Available from: http://www.sciencedirect.com/science/article/pii/S0888327018302875. Access on: 20 July, 2021.

LACAYO, R. M.; ALLEN, M. S. Updating structural models containing nonlinear iwan joints using quasi-static modal analysis. **Mechanical Systems and Signal Processing**, London, v. 118, p. 133--157, 2019. Available from: https://www.sciencedirect.com/science/article/pii/S0888327018305739. Access on: 20 July, 2021.

LACAYO, R. M.; DEANER, B. J.; ALLEN, M. S. A numerical study on the limitations of modal Iwan models for impulsive excitations. **Journal of Sound and Vibration**, London, v. 390, p. 118--140, 2017. Available from: https://www.sciencedirect.com/science/article/pii/S0022460X1630712X. Access on: 20 July, 2021.

LAXALDE, D.; THOUVEREZ, F.; SINOU, J.-J. Dynamics of a linear oscillator connected to a small strongly non-linear hysteretic absorber. **International Journal of Non-Linear Mechanics**, Oxford, v. 41, n. 8, p. 969 -- 978, 2006. Available from: http://www.sciencedirect.com/science/article/pii/S0020746206000795. Access on: 20 July, 2021.

LEVA, A.; PIRODDI, L. NARX-based technique for the modelling of magneto-rheological damping devices. **Smart Materials and Structures**, Bristol, v. 11, n. 1, p. 79--88, 2002. Available from: https://doi.org/10.1088/0964-1726/11/1/309. Access on: 20 July, 2021.

LI, D.; BOTTO, D.; XU, C.; GOLA, M. Fretting wear of bolted joint interfaces. **Wear**, Amsterdam, v. 458-459, p. 203411, 2020. Available from: https://www.sciencedirect.com/science/article/pii/S004316482030870X. Access on: 20 July, 2021.

LI, D.; XU, C.; KANG, J.; ZHANG, Z. Modeling tangential friction based on contact pressure distribution for predicting dynamic responses of bolted joint structures. **Nonlinear Dynamics**, Dordrecht, v. 101, n. 1, p. 255--69, 2020. Available from: https://doi.org/10.1007/s11071-020-05765-6. Access on: 20 July, 2021.

LI, D.; XU, C.; LIU, T.; GOLA, M. M.; WEN, L. A modified Iwan model for micro-slip in the context of dampers for turbine blade dynamics. **Mechanical Systems and Signal Processing**, London, v. 121, p. 14--30, 2019. Available from: https://www.sciencedirect.com/science/article/pii/S0888327018307222. Access on: 20 July, 2021.

LI, Q.; JING, X. A second-order output spectrum approach for fault detection of bolt loosening in a satellite-like structure with a sensor chain. **Nonlinear Dynamics**, Dordrecht, v. 89, n. 1, p. 587--606, 2017. Available from: https://doi.org/10.1007/s11071-017-3473-6. Access on: 20 July, 2021.

LI, Q.; JING, X. Fault diagnosis of bolt loosening in structures with a novel second-order output spectrum-based method. **Structural Health Monitoring**, London, v. 19, n. 1, p. 123--141, 2020. Available from: https://doi.org/10.1177/1475921719836379. Access on: 20 July, 2021.

LI, Y.; HAO, Z. Experimental and constitutive investigation on tangential sliding behavior of bolted joints with high preload. **Journal of Manufacturing Processes**, London, v. 64, p. 889--897, 2021. Available from: https://www.sciencedirect.com/science/article/pii/S1526612521001134. Access on: 20 July, 2021.

LIN, R.; NG, T. Higher-order FRFs and their applications to the identifications of continuous structural systems with discrete localized nonlinearities. **Mechanical Systems and Signal Processing**, London, v. 108, p. 326 -- 346, 2018. Available from:

http://www.sciencedirect.com/science/article/pii/S0888327018300980. Access on: 20 July, 2021.

LOTSBERG, I. Structural mechanics for design of grouted connections in monopile wind turbine structures. **Marine Structures**, London, v. 32, p. 113--135, 2013. Available from: https://www.sciencedirect.com/science/article/pii/S0951833913000191. Access on: 20 July, 2021.

MAIA, N. M. M.; SILVA, J. M. M. e. **Theoretical and experimental modal analysis**. Taunton: Research Studies Press, 1997.

MALDONADO, G. O. **Stochastic Response of Single Degree of Freedom Hysteretic Oscillators**. Dissertação (Mestrado) --- Faculty of Virginia Polytechnic Institute and State University, Virginia, 1987.

MANSON, G.; WORDEN, K. Higher-order frequency response functions for hysteretic systems. In: **NONLINEAR DYNAMICS, PROCEEDINGS OF THE IMAC, A CONFERENCE AND EXPOSITION ON STRUCTURAL DYNAMICS, 34, 2016**. Cham: Proceedings of [...]. Cham: Springer International Publishing, 2016. p. 191--201. Available from: http://dx.doi.org/10.1007/978-3-319-29739-218. Access on: 20 July, 2021.

MARTINS, S. A. M.; AGUIRRE, L. A. Sufficient conditions for rate-independent hysteresis in autoregressive identified models. **Mechanical Systems and Signal Processing**, London, v. 75, p. 607 -- 617, 2016. Available from: http://www.sciencedirect.com/science/article/pii/S0888327015005968. Access on: 20 July, 2021.

MASING, G. Eigenspannumyen und verfeshungung beim messing. In: **SECOND INTERNATIONAL CONGRESS FOR APPLIED MECHANICS, 1926, Zurich**. Zurich: Proceedings of the [...]. Zurich: [s.n.], 1926. p. 332--335.

MASRI, S.; CAFFREY, J.; CAUGHEY, T.; SMYTH, A.; CHASSIAKOS, A. Identification of the state equation in complex non-linear systems. **International Journal of Non-Linear Mechanics**, Oxford, v. 39, n. 7, p. 1111 -- 1127, 2004. Available from: http://www.sciencedirect.com/science/article/pii/S0020746203001094. Access on: 20 July, 2021.

MASUKO, M.; ITO, Y.; YOSHIDA, K. Theoretical analysis for a damping ratio of a jointed cantibeam. **Bulletin of JSME**, Tokyo, v. 16, n. 99, p. 1421--1432, 1973.

MATHIS, A. T.; BALAJI, N. N.; KUETHER, R. J.; BRINK, A. R.; BRAKE, M. R. W.; QUINN, D. D. A Review of Damping Models for Structures With Mechanical Joints. **Applied Mechanics Reviews**, New York, v. 72, n. 4, 07 2020. Available from: https://doi.org/10.1115/1.4047707. Access on: 20 July, 2021.

MATTOS, C. L. C.; DAMIANOU, A.; BARRETO, G. A.; LAWRENCE, N. D. Latent Autoregressive Gaussian Processes Models for Robust System Identification. **IFAC-PapersOnLine**, London, v. 49, n. 7, p. 1121 -- 1126, 2016. Available from: http://www.sciencedirect.com/science/article/pii/S2405896316305602. Access on: 20 July, 2021.

MAYER, M.; GAUL, L. Segment-to-segment contact elements for modelling joint interfaces in finite element analysis. **Mechanical Systems and Signal Processing**, London, v. 21, n. 2, p. 724--734, 2007. Available from: https://www.sciencedirect.com/science/article/pii/S0888327005001676. Access on: 20 July, 2021.

MAYES, R. L. An introduction to the SEM substructures focus group test bed - the Ampair 600 wind turbine. In: MAYES, R. L. (Ed.). **Topics in Experimental Dynamics Substructuring and Wind Turbine Dynamics**. New York: Springer, 2012. p. 61--70.

MCCONNELL, K. G.; VAROTO, P. S. **Vibration testing: theory and practice**. New York: John Wiley & Sons, 1995.

MEURDEFROID, A. **Dynamique des structures assemblées-Amortissement non linéaire**. Thesis (Ph. D.) --- Université Paris-Saclay, Paris, 2020. Available from: https://tel.archives-ouvertes.fr/tel-03028262/. Access on: 20 July, 2021.

MIGUEL, L. P.; TELOLI, R. d. O.; SILVA, S. da. Some practical regards on the application of the harmonic balance method for hysteresis models. **Mechanical Systems and Signal Processing**, London, v. 143, p. 106842, 2020. Available from: https://www.sciencedirect.com/science/article/pii/S0888327020302284. Access on: 20 July, 2021.

MIGUEL, L. P.; TELOLI, R. O.; SILVA, S. da. Harmonic balance of Bouc-Wen model to identify hysteresis effects in bolted joints. In: _____. **Vibration Engineering and Technology of Machinery**. Cham: Springer International Publishing, 2021. p. 65--79.

MILANESE, A.; MARZOCCA, P. **Volterra Kernels Identification Using Continuous Time Impulses Applied to Nonlinear Aeroelastic Problems**. [S.l.], 2009. Available from: https://arc.aiaa.org/doi/abs/10.2514/6.2009-2321. Access on: 20 July, 2021.

MINDLIN, R. D. Compliance of Elastic Bodies in Contact. **Journal of Applied Mechanics**, Tehran, v. 16, n. 3, p. 259--268, 04 1949. Available from: https://doi.org/10.1115/1.4009973. Access on: 20 July, 2021.

MUTO, M.; BECK, J. L. Bayesian updating and model class selection for hysteretic structural models using stochastic simulation. **Journal of Vibration and Control**, London, v. 14, n. 1-2, p. 7--34, 2008. Available from: https://doi.org/10.1177/1077546307079400. Access on: 20 July, 2021.

NAJERA-FLORES, D. A.; KUETHER, R. J. A Study of Whole Joint Model Calibration Using Quasi-Static Modal Analysis. **Journal of Vibration and Acoustics**, London, v. 142, n. 5, 06 2020. Available from: https://doi.org/10.1115/1.4047247. Access on: 20 July, 2021.

NANDA, B. K. Study of the effect of bolt diameter and washer on damping in layered and jointed structures. **Journal of Sound and Vibration**, London, v. 290, n. 3, p. 1290--1314, 2006. Available from: https://www.sciencedirect.com/science/article/pii/S0022460X05003731. Access on: 20 July, 2021.

NASER, M. F. M.; IKHOUANE, F. Hysteresis loop of the LuGre model. **Automatica**, Oxford, v. 59, p. 48 -- 53, 2015. Available from: http://www.sciencedirect.com/science/article/pii/S0005109815002344. Access on: 20 July, 2021.

NAYFEH, A. **Perturbation Methods**. New York: Wiley, 2008. (Physics textbook).

NEUBAUER, M.; OLESKIEWICZ, R.; POPP, K.; KRZYZYNSKI, T. Optimization of damping and absorbing performance of shunted piezo elements utilizing negative capacitance. **Journal of Sound and Vibration**, London, v. 298, n. 1, p. 84--107, 2006. Available from: https://www.sciencedirect.com/science/article/pii/S0022460X06004159. Access on: 20 July, 2021.

NI, Y.; KO, J.; WONG, C. Identification of non-linear hysteretic isolators from periodic vibration tests. **Journal of Sound and Vibration**, London, v. 217, n. 4, p. 737 -- 756, 1998. Available from: http://www.sciencedirect.com/science/article/pii/S0022460X98918041. Access on: 20 July, 2021.

NOËL, J.; ESFAHANI, A.; KERSCHEN, G.; SCHOUKENS, J. A nonlinear state-space approach to hysteresis identification. **Mechanical Systems and Signal Processing**, London, v. 84, n. Part B, p. 171 -- 184, 2017. Recent advances in nonlinear system identification. Available from: http://www.sciencedirect.com/science/article/pii/S0888327016303089. Access on: 20 July, 2021.

NOËL, J.; SCHOUKENS, M. F-16 aircraft benchmark based on ground vibration test data. In: **WORKSHOP ON NONLINEAR SYSTEM IDENTIFICATION BENCHMARKS, 2017**. Brussels: Workshop [...], 2016. p. 19 -- 23.

NOËL, J.; SCHOUKENS, M. Hysteretic benchmark with a dynamic nonlinearity. In: **WORKSHOP ON NONLINEAR SYSTEM IDENTIFICATION BENCHMARKS, 2016**. Brussels: Workshop [...]., 2016. p. 7 -- 14.

OKUIZUMI, N.; KIMURA, K. Multiple time scale analysis of hysteretic systems subjected to harmonic excitation. **Journal of Sound and Vibration**, London, v. 272, n. 3, p. 675 -- 701, 2004. Available from: http://www.sciencedirect.com/science/article/pii/S0022460X03004048. Access on: 20 July, 2021.

OLDFIELD, M.; OUYANG, H.; MOTTERSHEAD, J. E. Simplified models of bolted joints under harmonic loading. **Computers & Structures**, Oxford, v. 84, n. 1, p. 25 -- 33, 2005. Available from: http://www.sciencedirect.com/science/article/pii/S0045794905003184. Access on: 20 July, 2021.

OLOFSSON, U.; HAGMAN, L. A model for micro-slip between flat surfaces based on deformation of ellipsoidal elastic bodies. **Tribology International**, Oxford, v. 30, n. 8, p. 599--603, 1997. Available from: https://www.sciencedirect.com/science/article/pii/S0301679X97000285. Access on: 20 July, 2021.

OLSSON, H.; ÅSTRÖM, K. J.; WIT, C. C. D.; GÄFVERT, M.; LISCHINSKY, P. Friction models and friction compensation. **European Journal of Control**, Amsterdam, v. 4, n. 3, p. 176--195, 1998. Available from: https://www.sciencedirect.com/science/article/pii/S094735809870113X. Access on: 20 July, 2021.

PEETERS, M.; KERSCHEN, G.; GOLINVAL, J. Dynamic testing of nonlinear vibrating structures using nonlinear normal modes. **Journal of Sound and Vibration**, London, v. 330, n. 3, p. 486--509, 2011. Available from: https://www.sciencedirect.com/science/article/pii/S0022460X10005559. Access on: 20 July, 2021.

PEETERS, M.; KERSCHEN, G.; GOLINVAL, J. Modal testing of nonlinear vibrating structures based on nonlinear normal modes: Experimental demonstration. **Mechanical Systems and Signal Processing**, London, v. 25, n. 4, p. 1227 -- 1247, 2011. Available from: http://www.sciencedirect.com/science/article/pii/S0888327010003821. Access on: 20 July, 2021.

PEETERS, M.; KERSCHEN, G.; GOLINVAL, J.-C. Modal testing of nonlinear vibrating structures based on nonlinear normal modes: Experimental demonstration. **Mechanical Systems and Signal Processing**, London, v. 25, n. 4, p. 1227--1247, 2011. Available from: https://www.sciencedirect.com/science/article/pii/S0888327010003821. Access on: 20 July, 2021.

PEETERS, M.; VIGUIÉ, R.; SÉRANDOUR, G.; KERSCHEN, G.; GOLINVAL, J.-C. Nonlinear normal modes, part II: Toward a practical computation using numerical continuation techniques. **Mechanical Systems and Signal Processing**, London, v. 23, n. 1, p. 195--216, 2009. Special Issue: Non-linear Structural Dynamics. Available from: https://www.sciencedirect.com/science/article/pii/S0888327008001027. Access on: 20 July, 2021.

PENG, Z. K.; LANG, Z. Q. On the convergence of the Volterra-series representation of the Duffing's oscillators subjected to harmonic excitations. **Journal of Sound and Vibration**, London, v. 305, n. 1, p. 322--332, 2007. Available from: https://www.sciencedirect.com/science/article/pii/S0022460X07002416. Access on: 20 July, 2021.

PENNESTRÌ, E.; ROSSI, V.; SALVINI, P.; VALENTINI, P. P. Review and comparison of dry friction force models. **Nonlinear Dynamics**, Dordrecht, v. 83, n. 4, p. 1785--1801, 2016. Available from: https://doi.org/10.1007/s11071-015-2485-3. Access on: 20 July, 2021.

PERES, M. A.; BONO, R. W.; BROWN, D. L. **Practical aspects of shaker measurements for modal testing**. Cincinnati: University of Cincinnati, 2010. 2539-2550 p. Available from: https://www.modalshop.com/filelibrary/Practical-Aspects-of-Shaker_Measurements-for-Modal-Testing-Paper-(MD-0268).pdf. Access on: 20 July, 2021.

PESARESI, L.; ARMAND, J.; SCHWINGSHACKL, C. W.; SALLES, L.; WONG, C. An advanced underplatform damper modelling approach based on a microslip contact model. **Journal of Sound and Vibration**, London, v. 436, p. 327 -- 340, 2018. Available from: http://www.sciencedirect.com/science/article/pii/S0022460X18305200. Access on: 20 July, 2021.

PESARESI, L.; SALLES, L.; JONES, A.; GREEN, J.; SCHWINGSHACKL, C. Modelling the nonlinear behaviour of an underplatform damper test rig for turbine applications.

Mechanical Systems and Signal Processing, London, v. 85, p. 662--679, 2017. Available from: https://www.sciencedirect.com/science/article/pii/S0888327016303466. Access on: 20 July, 2021.

PETROV, E. P.; EWINS, D. J. Analytical Formulation of Friction Interface Elements for Analysis of Nonlinear Multi-Harmonic Vibrations of Bladed Disks . **Journal of Turbomachinery**, New York, v. 125, n. 2, p. 364--371, 04 2003. Available from: https://doi.org/10.1115/1.1539868. Access on: 20 July, 2021.

PEYRET, N.; DION, J.-L.; CHEVALLIER, G. A framework for backbone experimental tracking : Piezoelectric actuators, stop-sine signal and Kalman filtering. **Mechanical Systems and Signal Processing**, London, v. 78, p. 28 -- 42, 2016. Special Issue on Piezoelectric Technologies. Available from: http://www.sciencedirect.com/science/article/pii/S088832701500415X. Access on: 20 July, 2021.

PEYRET, N.; DION, J.-L.; CHEVALLIER, G.; ARGOUL, P. Micro-slip induced damping in planar contact under constant and uniform normal stress. **International Journal of Applied Mechanics**, Tehran, v. 02, n. 2, p. 281--304, 2010. Available from: https://doi.org/10.1142/S1758825110000597. Access on: 20 July, 2021.

PEYRET, N.; ROSATELLO, M.; CHEVALLIER, G.; DION, J.-L. A Mindlin derived Dahl friction model. **Mechanism and Machine Theory**, Oxford, v. 117, p. 48--55, 2017. Available from: https://www.sciencedirect.com/science/article/pii/S0094114X17306742. Access on: 20 July, 2021.

PREUMONT, A. **Vibration control of active structures: an introduction**. London: Springer, 2018.

RADOUANE, A.; GIRI, F.; IKHOUANE, F.; AHMED-ALI, T.; CHAOUI, F.-Z.; BROURI, A. System identification of a class of Wiener systems with hysteretic nonlinearities. **International Journal of Adaptive Control and Signal Processing**, Oxford, v. 31, n. 3, p. 332--359, 2017. Available from: http://dx.doi.org/10.1002/acs.2700. Access on: 20 July, 2021.

RAN, Q.; XIAO, M. L.; HU, Y. X. Nonlinear vibration with Volterra series method used in civil engineering: The Bouc-Wen hysteresis model of generalized frequency response. **Applied Mechanics and Materials**, Baech, v. 530, p. 561--566, 2014.

REAL, F. F.; BATOU, A.; RITTO, T. G.; DESCELIERS, C. Stochastic modeling for hysteretic bit-rock interaction of a drill string under torsional vibrations. **Journal of Vibration and Control**, London, v. 25, n. 10, p. 1663--1672, 2019. Available from: https://doi.org/10.1177/1077546319828245. Access on: 20 July, 2021.

REBILLAT, M.; SCHOUKENS, M. Comparison of least squares and exponential sine sweep methods for parallel Hammerstein models estimation. **Mechanical Systems and Signal Processing**, London, v. 104, p. 851 -- 865, 2018. Available from: http://www.sciencedirect.com/science/article/pii/S0888327017305976. Access on: 20 July, 2021.

RENSON, L.; KERSCHEN, G.; COCHELIN, B. Numerical computation of nonlinear normal modes in mechanical engineering. **Journal of Sound and Vibration**, London, v. 364, p. 177--206, 2016. Available from: https://www.sciencedirect.com/science/article/pii/S0022460X15007543. Access on: 20 July, 2021.

REZA, M. S.; BURSI, O. S.; PAOLACCI, F.; KUMAR, A. Enhanced seismic performance of non-standard bolted flange joints for petrochemical piping systems. **Journal of Loss Prevention in the Process Industries**, London, v. 30, p. 124--136, 2014. Available from: https://www.sciencedirect.com/science/article/pii/S0950423014000850. Access on: 20 July, 2021.

RITTO, T. G.; SAMPAIO, R.; AGUIAR, R. R. Uncertain boundary condition Bayesian identification from experimental data: A case study on a cantilever beam. **Mechanical Systems and Signal Processing**, London, v. 68, p. 176--188, 2016. Available from: https://www.sciencedirect.com/science/article/pii/S0888327015003714. Access on: 20 July, 2021.

ROBERT, C. P.; CASELLA, G. **Monte Carlo Statistical Methods**. New York: Springer, 2010.

ROETTGEN, D. R.; ALLEN, M. S. Nonlinear characterization of a bolted, industrial structure using a modal framework. **Mechanical Systems and Signal Processing**, London, v. 84, p. 152--170, 2017. Recent advances in nonlinear system identification. Available from: https://www.sciencedirect.com/science/article/pii/S0888327015005269. Access on: 20 July, 2021.

ROETTGEN, D. R.; ALLEN, M. S. The Ampair 600 wind turbine: An in-context benchmark system. In: BRAKE, M. R. W. (Ed.). **The Mechanics of Jointed Structures: Recent Research and Open Challenges for Developing Predictive Models for Structural Dynamics**. Cham: Springer International Publishing, 2018. p. 91--97. Available from: https://doi.org/10.1007/978-3-319-56818-8_8. Access on: 20 July, 2021.

ROJAS, E.; PUNLA-GREEN, S.; BROADMAN, C.; BRAKE, M. R. W.; PACINI, B. R.; FLICEK, R. C.; QUINN, D. D.; SCHWINGSHACKL, C. W.; DODGEN, E. A priori methods to assess the strength of nonlinearities for design applications. In: KERSCHEN, G.; BRAKE, M. R. W.; RENSON, L. (Ed.). **Nonlinear Structures and Systems**. Cham: Springer International Publishing, 2020. p. 243--246.

ROSENBERG, R. M. Normal Modes of Nonlinear Dual-Mode Systems. **Journal of Applied Mechanics**, Tehran, v. 27, n. 2, p. 263--268, 06 1960. Available from: https://doi.org/10.1115/1.3643948. Access on: 20 July, 2021.

RUGH, W. J. **Nonlinear System Theory - The Volterra/Wiener Approach**. [S.l.]: The Johns Hopkins University Press, 1991.

SABA, N.; JAWAID, M.; ALOTHMAN, O. Y.; PARIDAH, M. A review on dynamic mechanical properties of natural fibre reinforced polymer composites. **Construction and Building Materials**, Amsterdam, v. 106, p. 149--159, 2016. Available from: https://www.sciencedirect.com/science/article/pii/S0950061815307479. Access on: 20 July, 2021.

SAH, S. M.; THOMSEN, J. J.; BRØNS, M.; FIDLIN, A.; TCHERNIAK, D. Estimating bolt tightness using transverse natural frequencies. **Journal of Sound and Vibration**, London, v. 431, p. 137--149, 2018. Available from: https://www.sciencedirect.com/science/article/pii/S0022460X18303304. Access on: 20 July, 2021.

SALLES, L.; BLANC, L.; THOUVEREZ, F.; GOUSKOV, A. M.; JEAN, P. Dual Time Stepping Algorithms With the High Order Harmonic Balance Method for Contact Interfaces With Fretting-Wear. **Journal of Engineering for Gas Turbines and Power**, New York, v. 134, n. 3, 12 2011. 032503. Available from: https://doi.org/10.1115/1.4004236. Access on: 20 July, 2021.

SCHEEL, M.; KLEYMAN, G.; TATAR, A.; BRAKE, M. R.; PETER, S.; NOËL, J.-P.; ALLEN, M. S.; KRACK, M. Experimental assessment of polynomial nonlinear state-space and nonlinear-mode models for near-resonant vibrations. **Mechanical Systems and Signal Processing**, London, v. 143, p. 106796, 2020. Available from: https://www.sciencedirect.com/science/article/pii/S0888327020301825. Access on: 20 July, 2021.

SCHEEL, M.; PETER, S.; LEINE, R. I.; KRACK, M. A phase resonance approach for modal testing of structures with nonlinear dissipation. **Journal of Sound and Vibration**, London, v. 435, p. 56 -- 73, 2018. Available from: http://www.sciencedirect.com/science/article/pii/S0022460X18304486. Access on: 20 July, 2021.

SCHEEL, M.; SCHULZ, T.; KRACK, M. Potential and limitation of a nonlinear modal testing method for friction-damped systems. In: KERSCHEN, G.; BRAKE, M. R. W.; RENSON, L. (Ed.). **Nonlinear Structures and Systems**. Cham: Springer International Publishing, 2020. p. 95--97.

SCHEEL, M.; WEIGELE, T.; KRACK, M. Challenging an experimental nonlinear modal analysis method with a new strongly friction-damped structure. **Journal of Sound and Vibration**, London, v. 485, p. 115580, 2020. Available from: http://www.sciencedirect.com/science/article/pii/S0022460X20304120. Access on: 20 July, 2021.

SCHETZEN, M. **The Volterra and Wiener Theories of Nonlinear Systems**. New York: John Wiley and Sons, 1980.

SCHOUKENS, J.; LJUNG, L. Nonlinear System Identification: A User-Oriented Road Map. **IEEE Control Systems Magazine**, v. 39, n. 6, p. 28--99, 2019.

SCHOUKENS, M.; MATTSSON, P.; WIGREN, T.; NOËL, J. Cascaded tanks benchmark combining soft and hard nonlinearities. In: **Workshop on Nonlinear System Identification Benchmarks**. Brussels: Workshop [...]. Brussels, 2016. p. 20 -- 23.

SCHULZ, E.; SPEEKENBRINK, M.; KRAUSE, A. A tutorial on Gaussian process regression: Modelling, exploring, and exploiting functions. **Journal of Mathematical Psychology**, Maryland Heights, v. 85, p. 1 -- 16, 2018. Available from:

http://www.sciencedirect.com/science/article/pii/S0022249617302158. Access on: 20 July, 2021.

SCHWINGSHACKL, C.; PETROV, E.; EWINS, D. Measured and estimated friction interface parameters in a nonlinear dynamic analysis. **Mechanical Systems and Signal Processing**, London, v. 28, p. 574--584, 2012. Interdisciplinary and Integration Aspects in Structural Health Monitoring. Available from: https://www.sciencedirect.com/science/article/pii/S088832701100402X. Access on: 20 July, 2021.

SCUSSEL, O. **On the use of the Volterra series in structural dynamics: contributions from the input-output to output-only analysis and identification**. Thesis (Ph. D.) --- Faculdade de Engenharia - Universidade Estadual Paulista, Ilha Solteira, 2017. Available from: https://repositorio.unesp.br/handle/11449/150506. Access on: 20 July, 2021.

SCUSSEL, O.; SILVA, S. da. The harmonic probing method for output-only nonlinear mechanical systems. **Journal of the Brazilian Society of Mechanical Sciences and Engineering**, Heidelberg, v. 39, n. 9, p. 3329--3341, Sep 2017. Available from: https://doi.org/10.1007/s40430-017-0723-y. Access on: 20 July, 2021.

SEEGER, M. Gaussian Process for Machine Learning. **International Journal of Neural Systems**, Singapore, v. 14, n. 02, p. 69--106, 2004. Available from: https://doi.org/10.1142/S0129065704001899. Access on: 20 July, 2021.

SEGALMAN, D. J. A Four-Parameter Iwan Model for Lap-Type Joints. **Journal of Applied Mechanics**, London, v. 72, n. 5, p. 752--760, 02 2005. Available from: https://doi.org/10.1115/1.1989354. Access on: 20 July, 2021.

SEGALMAN, D. J. Modelling joint friction in structural dynamics. **Structural Control and Health Monitoring**, Oxford, v. 13, n. 1, p. 430--453, 2006.

SEGALMAN, D. J. **A modal approach to modeling spatially distributed vibration energy dissipation**. Albuquerque: SNL, 2010.

SEGALMAN, D. J.; ALLEN, M. S.; ERITEN, M.; HOPPMAN, K. Experimental Assessment of Joint-Like Modal Models for Structures. In: **INTERNATIONAL DESIGN ENGINEERING TECHNICAL CONFERENCES AND COMPUTERS AND INFORMATION IN ENGINEERING CONFERENCE, CONFERENCE ON MECHANICAL ENGINEERING VIBRATION AND NOISE, 27, 2015**. Massachussets: Proceedings of the [...]. Massachussets: ASME, 2015.

SEGALMAN, D. J.; GREGORY, D. L.; STARR, M. J.; RESOR, B. R.; JEW, M. D.; LAUFFER, J. P.; AMES, N. M. Handbook on dynamics of jointed structures. In: **INTERNATIONAL DESIGN ENGINEERING TECHNICAL CONFERENCES AND COMPUTERS AND INFORMATION IN ENGINEERING CONFERENCE, 24, CONFERENCE ON MECHANICAL VIBRATION AND NOISE, Parts A and B 2009**. Albuquerque: Proceedings of the [...]. Albuquerque: Sandia National Laboratories, 2009. p. 441--449. Available from: https://doi.org/10.1115/DETC2012-71534. Access on: 20 July, 2021.

SEGALMAN, D. J.; STARR, M. J. Iwan Models and Their Provenance. In: **INTERNATIONAL DESIGN ENGINEERING TECHNICAL CONFERENCES AND COMPUTERS AND INFORMATION IN ENGINEERING CONFERENCE, CONFERENCE ON MECHANICAL VIBRATION AND NOISE, Parts A and B, 2009**. Albuquerque: Proceedings of the [...]. Albuquerque: Sandia National Laboratories, 2012. p. 441--449. Available from: https://doi.org/10.1115/DETC2012-71534. Access on: 20 July, 2021.

SHARMA, K. G.; DESAI, C. S. Analysis and implementation of thin-layer element for interfaces and joints. **Journal of Engineering Mechanics**, Reston, v. 118, n. 12, p. 2442--2462, 1992. Available from: https://ascelibrary.org/doi/abs/10.1061/%28ASCE%290733-9399%281992%29118%3A12%282442%29. Access on: 20 July, 2021.

SHAW, S.; PIERRE, C. Normal Modes for non-linear vibratory systems. **Journal of Sound and Vibration**, London, v. 164, n. 1, p. 85--124, 1993. Available from: https://www.sciencedirect.com/science/article/pii/S0022460X83711983. Access on: 20 July, 2021.

SHEN, Y.; GOLNARAGHI, M. F.; HEPPLER, G. R. Analytical and experimental study of the response of a suspension system with a Magnetorheological Damper. **Journal of Intelligent Material Systems and Structures**, London, v. 16, n. 2, p. 135--147, 2005. Available from: https://doi.org/10.1177/1045389X05048330. Access on: 20 July, 2021.

SHIKI, S. B. **Application of Volterra series in nonlinear mechanical system identification and in structural health monitoring problems**. Thesis (Ph. D.) --- Faculdade de Engenharia, Universidade Estadual Paulista, Ilha Solteira, 2016. Available from: https://repositorio.unesp.br/handle/11449/137761. Access on: 20 July, 2021.

SHIKI, S. B.; SILVA, S. da; TODD, M. D. On the application of discrete-time Volterra series for the damage detection problem in initially nonlinear systems. **Structural Health Monitoring**, London, v. 16, n. 1, p. 62--78, 2017. Available from: https://doi.org/10.1177/1475921716662142. Access on: 20 July, 2021.

SIEWERT, C.; PANNING, L.; WALLASCHEK, J.; RICHTER, C. Multiharmonic Forced Response Analysis of a Turbine Blading Coupled by Nonlinear Contact Forces. **Journal of Engineering for Gas Turbines and Power**, New York, v. 132, n. 8, 05 2010. 082501. Available from: https://doi.org/10.1115/1.4000266. Access on: 20 July, 2021.

SILVA, S. d.; COGAN, S.; FOLTÊTE, E.; BUFFE, F. Metrics for nonlinear model updating in structural dynamics. **Journal of the Brazilian Society of Mechanical Sciences and Engineering**, Springer, Heidelberg, v. 31, n. 1, p. 27--34, 2009. Available from: https://doi.org/10.1016/j.ijnonlinmec.2010.09.014. Access on: 20 July, 2021.

SILVA, S. da. Data-driven model identification of guided wave propagation in composite structures. **Journal of the Brazilian Society of Mechanical Sciences and Engineering**, Heidelberg, v. 40, p. 543, 2018.

SILVA, S. da; COGAN, S.; FOLTÊTE, E. Nonlinear identification in structural dynamics based on Wiener series and Kautz filters. **Mechanical Systems and Signal Processing**, London, v. 24, n. 1, p. 52 -- 58, 2010. Available from:

http://www.sciencedirect.com/science/article/pii/S0888327009001897. Access on: 20 July, 2021.

SIMO, J.; LAURSEN, T. An augmented Lagrangian treatment of contact problems involving friction. **Computers & Structures**, Oxford, v. 42, n. 1, p. 97--116, 1992. Available from: https://www.sciencedirect.com/science/article/pii/004579499290540G. Access on: 20 July, 2021.

SINGH, A.; SCAPOLAN, M.; SAITO, Y.; ALLEN, M. S.; ROETTGEN, D.; PACINI, B.; KUETHER, R. J. Experimental characterization of a new benchmark structure for prediction of damping nonlinearity. In: KERSCHEN, G. *et al.* (Ed.). **Nonlinear Dynamics**. Cham: Springer International Publishing, 2019. p. 57--78.

SMITH, S.; BILBAO-LUDENA, J. C.; CATALFAMO, S.; BRAKE, M. R. W.; REUSS, P.; SCHWINGSHACKL, C. W. The effects of boundary conditions, measurement techniques, and excitation type on measurements of the properties of mechanical joints. In: KERSCHEN, G. *et al.* (Ed.). **Nonlinear Dynamics**. Cham: Springer International Publishing, 2015. p. 415.

SONG, Y. Simulation of dynamics of beam structures with bolted joints using adjusted Iwan beam elements. **Journal of Sound and Vibration**, London, v. 273, n. 1-2, p. 249--276, 2004. Available from: https://www.sciencedirect.com/science/article/pii/S0022460X03004991. Access on: 20 July, 2021.

STACHOWIAK, G.; BATCHELOR, A. W. **Engineering tribology**. London: Butterworth-Heinemann, 2013.

STRIBECK, R. Die wesentlichen eigenschaften der gleit-und rollenlager. **Zeitschrift des Vereines Deutscher Ingenieure**, Duesseldorf, v. 46, p. 1341--1348, 1902.

SÜSS, D.; JANEBA, A.; WILLNER, K. The Gaul resonator: Experiments for the isolated investigation of a bolted lap joint. In: BRAKE, M. R. W. (Ed.). **The Mechanics of Jointed Structures: Recent Research and Open Challenges for Developing Predictive Models for Structural Dynamics**. Cham: Springer International Publishing, 2018. p. 59--72. ISBN 978-3-319-56818-8. Available from: https://doi.org/10.1007/978-3-319-56818-8_6. Access on: 20 July, 2021.

SÜSS, D.; WILLNER, K. Investigation of a jointed friction oscillator using the Multiharmonic Balance Method. **Mechanical Systems and Signal Processing**, London, v. 52-53, p. 73 -- 87, 2015. Available from: http://www.sciencedirect.com/science/article/pii/S0888327014003197. Access on: 20 July, 2021.

SWAIN, A. K.; BILLINGS, S. A. Generalized frequency response function matrix for MIMO non-linear systems. **International Journal of Control**, Taylor & Francis, Abingdon, v. 74, n. 8, p. 829--844, 2001. Available from: https://doi.org/10.1080/00207170010030144. Access on: 20 July, 2021.

TANG, B.; BRENNAN, M.; GATTI, G. Use of the dynamic stiffness method to interpret experimental data from a nonlinear system. **Journal of Sound and Vibration**, London, v. 421, p. 91--110, 2018. Available from: https://www.sciencedirect.com/science/article/pii/S0022460X18300063. Access on: 20 July, 2021.

TANG, B.; BRENNAN, M.; LOPES, J. V.; SILVA, S. da; RAMLAN, R. Using nonlinear jumps to estimate cubic stiffness nonlinearity: An experimental study. **Proceedings of the Institution of Mechanical Engineers, Part C: Journal of Mechanical Engineering Science**, London, v. 230, n. 19, p. 3575--3581, 2016.

TAWFIQ, I.; VINH, T. Contribution to the extension of modal analysis to non-linear structure using Volterra functional series. **Mechanical systems and signal processing**, Elsevier, London, v. 17, n. 2, p. 379--407, 2003. Available from: http://www.sciencedirect.com/science/article/pii/S0888327002914998. Access on: 20 July, 2021.

TELOLI, R. de O.; BUTAUD, P.; CHEVALLIER, G.; da SILVA, S. Good practices for designing and experimental testing of dynamically excited jointed structures: The Orion beam. **Mechanical Systems and Signal Processing**, London, v. 163, p. 108172, 2022. Available from: https://www.sciencedirect.com/science/article/pii/S0888327021005495. Access on: 20 July, 2021.

TELOLI, R. O. Identification through frequency-domain methods of hysteretic models for bolted joints of assembled structures. In: . Lyon: [s.n.], 2019. Available from: https://www.researchgate.net/publication/334290942_Identification_through_Frequency-Domain_Method_of_Hysteretic_Model_for_Bolted_Joints_of_Assembled_Structures. Access on: 20 July, 2021.

TELOLI, R. O.; BUTAUD, P.; CHEVALLIER, G.; da SILVA, S. Dataset of experimental measurements for the Orion beam structure. **Manuscript submitted for publication in the data in brief journal**, 2021. No prelo.

TELOLI, R. O.; da SILVA, S. Higher-order frequency response functions of Bouc-Wen model subjected to harmonic excitation. In: **INTERNATIONAL CONFERENCE ON STRUCTURAL NONLINEAR DYNAMICS AND DIAGNOSIS - CSNDD, 2018**. Tanger: Proceedings of the [...]. Tanger: [s.n.], 2018.

TELOLI, R. O.; da SILVA, S. Parametric frequency response method of hysteretic system with a dynamical nonlinearity subjected to harmonic excitation. In: **SYMPOSIUM OF INTELLIGENT MATERIALS AND CONTROL**. Barcelona, Spain: [s.n.], 2018.

TELOLI, R. O.; da Silva, S.; RITTO, T. G.; CHEVALLIER, G. Bayesian model identification of higher-order frequency response functions for structures assembled by bolted joints. **Mechanical Systems and Signal Processing**, London, v. 151, p. 107333, 2021. Available from: https://www.sciencedirect.com/science/article/pii/S0888327020307196. Access on: 20 July, 2021.

TELOLI, R. O.; SILVA, S. da. A new way for harmonic probing of hysteretic systems through nonlinear smooth operators. **Mechanical Systems and Signal Processing**, London, v. 121, p. 856--875, 2019. Available from: http://www.sciencedirect.com/science/article/pii/S0888327018307659. Access on: 20 July, 2021.

TELOLI, R. O.; SILVA, S. da; CHEVALLIER, G. Parameters estimation by harmonic probing of hysteresis models of bolted jointed structures. In: **DYNAMICAL**

SYSTEMS - THEORY AND APPLICATIONS - DSTA, 15, 2019. Lodz: Proceedings of the [...]. Lodz: [s.n.], 2019.

TELOLI, R. O.; VILLANI, L. G.; SILVA, S. da; TODD, M. D. On the use of the GP-NARX model for predicting hysteresis effects of bolted joint structures. **Mechanical Systems and Signal Processing**, London, v. 159, p. 107751, 2021. Available from: https://www.sciencedirect.com/science/article/pii/S0888327021001461. Access on: 20 July, 2021.

TELOLI, R. O.; VILLANI, L. G. G.; SILVA, S. da; CUNHA Jr, A. Uso do método de superfície de resposta para estimar um modelo estocástico de uma viga não linear com rigidez cúbica. In: **CONGRESSO NACIONAL DE ENGENHARIA MECÂNICA, CONEM, 9**. Fortaleza: Anais [...]. ABCM, 2016. Available from: https://www.researchgate.net/publication/306227353_Uso_do_Metodo_de_Superficie_de_Resposta_para_Estimar_um_Modelo_Estocastico_de_uma_Viga_Nao_Linear_com_Rigidez_Cubica. Access on: 20 July, 2021.

TOMLINSON, G.; MANSON, G.; LEE, G. A simple criterion for establishing an upper limit to the harmonic excitation level of the Duffing oscillator using the Volterra series. **Journal of Sound and Vibration**, London, v. 190, n. 5, p. 751 -- 762, 1996. Available from: http://www.sciencedirect.com/science/article/pii/S0022460X96900917. Access on: 20 July, 2021.

TORSTENFELT, B.; KLARBRING, A. Conceptual optimal design of modular car product families using simultaneous size, shape and topology optimization. **Finite Elements in Analysis and Design**, Amsterdam, v. 43, n. 14, p. 1050--1061, 2007. Available from: https://www.sciencedirect.com/science/article/pii/S0168874X0700073X. Access on: 20 July, 2021.

VILLANI, L. G.; SILVA, S. da; CUNHA, A.; TODD, M. D. Damage detection in an uncertain nonlinear beam based on stochastic Volterra series: An experimental application. **Mechanical Systems and Signal Processing**, London, v. 128, p. 463 -- 478, 2019. Available from: http://www.sciencedirect.com/science/article/pii/S0888327019302250. Access on: 20 July, 2021.

VILLANI, L. G. G. **Robust damage detection in uncertain nonlinear systems**. Thesis (Ph. D.) --- Faculdade de Engenharia, Universidade Estadual Paulista, Ilha Solteira, 2019. Available from: https://repositorio.unesp.br/handle/11449/191200. Access on: 20 July, 2021.

VILLANI, L. G. G.; SILVA, S. da; JR, A. C.; TODD, M. D. On the detection of a nonlinear damage in an uncertain nonlinear beam using stochastic volterra series. **Structural Health Monitoring**, London, v. 19, n. 4, p. 1137--1150, 2020. Available from: https://doi.org/10.1177/1475921719876086. Access on: 20 July, 2021.

VIRGIN, L. On the harmonic response of an oscillator with unsymmetric restoring force. **Journal of Sound and Vibration**, Elsevier, London, v. 126, n. 1, p. 157--165, 1988. Available from: https://doi.org/10.1016%2F0022-460x%2888%2990405-1. Access on: 20 July, 2021.

VISINTIN, A. **Differential models of hysteresis**. New York: Springer Science & Business Media, 2013.

VOLTERRA, V. Theory of functionals and of integral and integro-differential equations. Dover: [s.n.], 1959.

WANG, D.; XU, C. Combination reduction dynamic analysis for complex jointed structures with local hysteresis nonlinearity. **Nonlinear Dynamics**, Dordrecht, v. 101, p. 171--190, 2020. Available from: https://doi.org/10.1007/s11071-020-05751-y. Access on: 20 July, 2021.

WEN, Y.-K. Method for random vibration of hysteretic systems. **Journal of the Engineering Mechanics Division**, Reston, v. 102, n. 2, p. 249--263, 1976. Available from: https://ascelibrary.org/doi/abs/10.1061/JMCEA3.0002106. Access on: 20 July, 2021.

WIENER, N. **Response of a non-linear device to noise**. [S.l.], 1942. Available from: https://archive.org/details/ResponseNonLinearDeviceNoise_Wiener/page/n3/mode/2up. Access on: 20 July, 2021.

WILLIAMS, C. K. I.; RASMUSSEN, C. E. **Gaussian processes for machine learning**. Cambridge: MIT Press Cambridge, MA, 2006.

WILLNER, K.; GAUL, L. A penalty approach for contact description by FEM based on interface physics. **Transactions on Engineering Sciences**, Southampton, v. 7, 1970. Available from: https://www.witpress.com/Secure/elibrary/papers/CON95/CON95030FU.pdf. Access on: 20 July, 2021.

WIT, C. Canudas de; OLSSON, H.; ASTROM, K.; LISCHINSKY, P. A new model for control of systems with friction. **IEEE Transactions on Automatic Control**, Piscataway, v. 40, n. 3, p. 419--425, 1995.

WONG, C.; NI, Y. Q.; KO, J. M. Steady-state oscillation of hysteretic differential model. II: Performance analysis. **Journal of Engineering Mechanics**, Reston, v. 120, n. 11, p. 2299 -- 2325, 1994. Access on: 20 July, 2021.

WORDEN, K.; BARTHORPE, R.; CROSS, E.; DERVILIS, N.; HOLMES, G.; MANSON, G.; ROGERS, T. On evolutionary system identification with applications to nonlinear benchmarks. **Mechanical Systems and Signal Processing**, London, v. 112, p. 194 -- 232, 2018. Available from: http://www.sciencedirect.com/science/article/pii/S0888327018301912. Access on: 20 July, 2021.

WORDEN, K.; BARTHORPE, R. J. Identification of hysteretic systems using NARX models, part I: Evolutionary identification. In: SIMMERMACHER, T.; COGAN, S.; HORTA, L. G.; BARTHORPE, R. (Ed.). **Topics in Model Validation and Uncertainty Quantification**. New York: Springer, 2012. p. 49--56.

WORDEN, K.; BECKER, W. E.; ROGERS, T. J.; CROSS, E. J. On the confidence bounds of Gaussian process NARX models and their higher-order frequency response functions. **Mechanical Systems and Signal Processing**, London, v. 104, p. 188 -- 223, 2018. Available from: http://www.sciencedirect.com/science/article/pii/S0888327017305149. Access on: 20 July, 2021.

WORDEN, K.; HENSMAN, J. Parameter estimation and model selection for a class of hysteretic systems using Bayesian inference. **Mechanical Systems and Signal Processing**, London, v. 32, p. 153 -- 169, 2012. Uncertainties in Structural Dynamics. Available from: http://www.sciencedirect.com/science/article/pii/S0888327012001240. Access on: 20 July, 2021.

WORDEN, K.; MANSON, G.; TOMLINSON, G. A harmonic probing algorithm for the multi-input Volterra series. **Journal of Sound and Vibration**, London, v. 201, n. 1, p. 67 -- 84, 1997. Available from: http://www.sciencedirect.com/science/article/pii/S0022460X96907464. Access on: 20 July, 2021.

WORDEN, K.; TOMLIMSON, G. R. **Nonlinearity in structural dynamics: detection, identification and modelling**. [S.l.]: Institute of Physicis Publishing, Bristol and Philadelphia, 2001.

WORDEN, K.; WONG, C.; PARLITZ, U.; HORNSTEIN, A.; ENGSTER, D.; TJAHJOWIDODO, T.; AL-BENDER, F.; RIZOS, D.; FASSOIS, S. Identification of pre-sliding and sliding friction dynamics: Grey-box and black-box models. **Mechanical Systems and Signal Processing**, London, v. 21, n. 1, p. 514 -- 534, 2007. Available from: http://www.sciencedirect.com/science/article/pii/S0888327005001408. Access on: 20 July, 2021.

YUAN, J.; SCHWINGSHACKL, C.; WONG, C.; SALLES, L. On an improved adaptive reduced-order model for the computation of steady-state vibrations in large-scale non-conservative systems with friction joints. **Nonlinear Dynamics**, Dordrecht, v. 103, n. 4, p. 3283--3300, 2021. Available from: https://doi.org/10.1007/s11071-020-05890-2. Access on: 20 July, 2021.

YUAN, P.-P.; REN, W.-X.; ZHANG, J. Dynamic tests and model updating of nonlinear beam structures with bolted joints. **Mechanical Systems and Signal Processing**, London, v. 126, p. 193--210, 2019. Available from: https://www.sciencedirect.com/science/article/pii/S0888327019301141. Access on: 20 July, 2021.

ZARE, I.; ALLEN, M. S. Adapting a contact-mechanics algorithm to predict damping in bolted joints using quasi-static modal analysis. **International Journal of Mechanical Sciences**, Oxford, v. 189, p. 105982, 2021. Available from: https://www.sciencedirect.com/science/article/pii/S0020740320303647. Access on: 20 July, 2021.

ZHANG, M.; LU, L.; WANG, W.; ZENG, D. The roles of thread wear on self-loosening behavior of bolted joints under transverse cyclic loading. **Wear**, Amsterdam, v. 394-395, p. 30--39, 2018. Available from: https://www.sciencedirect.com/science/article/pii/S0043164817310670. Access on: 20 July, 2021.

ZHAO, Y.; WU, H.; YANG, C.; LIU, Z.; CHENG, Q. Tangential damping model of bolted joint with the physics-based friction coefficient. **International Journal of Precision Engineering and Manufacturing**, Seoul, v. 22, n. 5, p. 865--875, 2021. Available from: https://doi.org/10.1007/s12541-021-00485-2. Access on: 20 July, 2021.

ZHAO, Y.; YANG, C.; CAI, L.; SHI, W.; LIU, Z. Surface contact stress-based nonlinear virtual material method for dynamic analysis of bolted joint of machine tool. **Precision Engineering**, Philadelphia, v. 43, p. 230--240, 2016. Available from: https://www.sciencedirect.com/science/article/pii/S0141635915001464. Access on: 20 July, 2021.

APPENDIX A – CONSTITUTIVE MODELS FOR REPRESENTING HYSTERESIS

The Appendix A is intended to illustrate models available in the literature commonly used not only to describe hysteresis effects, but also the dynamic behavior of jointed structures. The most representative features of the Coulomb, Stribeck, Dahl, LuGre, Bouc-Wen, Masing and Iwan models will be presented. The interested reader is invited to read the reviews done by Olsson *et al.* (1998), Gaul and Nitsche (2001), Bograd *et al.* (2011), Hassani, Tjahjowidodo and Do (2014), Pennestrì *et al.* (2016) and Mathis *et al.* (2020), which provide insights into the applicability of some of these models.

Figure A.1 depicts the notation considered throughout this Chapter. Two bodies in contact condition are subjected to a sliding motion due to an external force F_e, which generates the relative velocity v_{ij} of solid $i = 1$ with respect to solid $j = 2$, the friction force $F_T^{i \mapsto j}$ and the normal force F_N on the bodies.

Figure A.1 – Schematic illustration of two bodies subjected to sliding motion, with emphasis on the variables of interest considered throughout the Chapter.

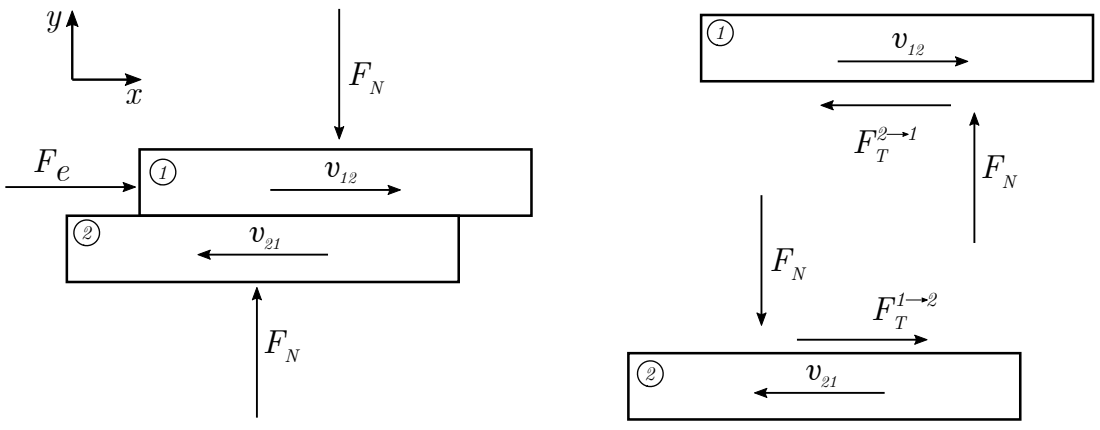

Source: Adapted from Heller (2005).

In general, there are two categories of models that are distinguished by the way in which the friction force is defined. In the first category there lie constitutive models that explicitly represent the friction force by the relative velocity term are known as static models. In the second category, in turn, the restoring force is governed by internal variables that do not explicitly express dependence on displacement or velocity. Consequently, the friction force does not only depend on relative velocity, but also on its state variables. Models that fall into this category are called dynamic models. Because of these distinctions, there are effects that can be properly captured by static models and not by dynamic models, and vice versa, which will be addressed hereinafter .

A.1 STATIC MODELS

A.1.1 Coulomb friction model

Known as the first mathematical model to represent friction from the extension of concepts initially investigated by Leonardo da Vinci and Guillaume Amontons, the Coulomb friction model[1] states that the magnitude of the friction force is proportional to the normal force applied to the surface and to its coefficient of friction μ, resulting in the following relation:

$$F_T^{j\mapsto i} = \mu\,|F_N|\,\mathrm{sign}\left(v_{ji}\right), \quad i = j = 1,2 \quad \text{such that } i \neq j, \tag{A.1}$$

where the force presents a dependence on the velocity by the *signum* function. For conditions where the relative motion between surfaces is null (adhesion conditions at zero velocity), there is a discontinuity in the force, as illustrated in Fig. A.2(a). Thus, note that the model is not capable of capturing the partial sliding and sticking effect that exists at the interface before the full sliding regime is initiated (GAUL; NITSCHE, 2001), requiring an individual basis for dealing with each of theses effects.

A.1.2 Stribeck friction model

There are extended versions of the classic Coulomb model as, for example, the viscous friction model, and the version of Coulomb model that introduces the stiction to describe relative motion in conditions at rest. Toward this background, Stribeck (1902) proposed a

[1] Charles-Augustin de Coulomb ($\star$1736 – †1806) original work is entitled as ''Théorie des machines simples, en ayant égard au frottment de leurs parties, et à la roideur des cordages'', initially published in the author's native language.

more complex formulation between velocity and friction force in which, for low velocities, there is the adhesion force representing the sliding limit, such that the adhesion force can be greater than the frictional force once sliding has started. The model is written as follows:

$$F_T^{j\mapsto i} = \begin{cases} \mathcal{F}(v_{ji}) & \text{if } v_{ji} \neq 0 \\ F_e & \text{if } v_{ji} = 0 \text{ and } |F_e| < F_s \\ F_s \text{sign}(F_e) & \text{otherwise,} \end{cases} \tag{A.2}$$

where F_e is an external force, F_s is the adhesion force and $\mathcal{F}(v_{ji})$ represents an arbitrary function of the friction force, which may assume the following form (OLSSON *et al.*, 1998):

$$\mathcal{F}(v_{ji}) = \left(\mu|F_N| + (F_s - \mu|F_N|) \exp\left[-\left(\frac{v_{ji}}{v_s} \right)^{\delta_s} \right] \right) \text{sign}(v_{ji}) + F_v v_{ji}, \tag{A.3}$$

in which v_s is called as Stribeck velocity, F_v is a viscous friction force and δ_s depends on the application's geometry. The schematic representation of the Stribeck model for the frictional force is illustrated in Fig. A.2(b).

Figure A.2 – Schematic illustration of the friction force produced by (a) the Coulomb friction model and by (b) the Stribeck friction model.

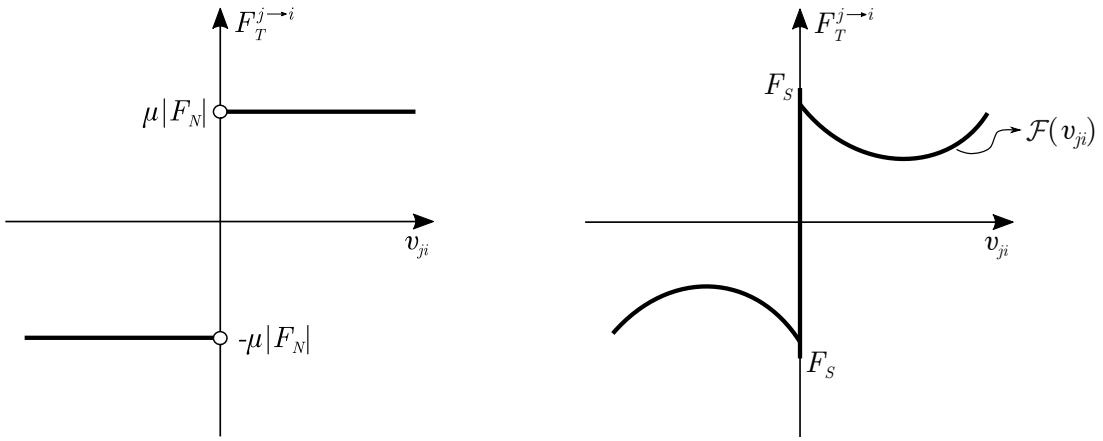

(a) Coulomb friction model.

(b) Stribeck friction model.

Source: Prepared by the author.

A.2 DYNAMIC MODELS

A.2.1 Dahl model

The Dahl model was initially developed by Dahl (1968) to characterize the sliding and rolling friction involving applications with ball bearings. From experimental investigations, the author observed that for conditions close to rest (low amplitudes), ball bearings exhibit an elastic resistance to input forces before a permanent displacement (sliding) between the surfaces starts, which corresponds to the stress-strain curve in classical solid mechanics. This elasticity produces hysteretic behavior, which is described by Dahl model as follows:

$$\frac{dF_T^{j\mapsto i}}{dx} = \sigma\left(1 - \frac{F_T^{j\mapsto i}}{\mu|F_N|}\text{sign}\left(v_{ji}\right)\right)^{\alpha}, \tag{A.4}$$

where σ is the stiffness coefficient responsible for the initial slope of the friction force and α is a parameter that determines the shape of the stress-strain curve. As pointed by Chou (2004), for $0 \leq \alpha \leq 1$, the force-deflection behavior is similar to the one presented by bristle materials; for $\alpha \geq 1$, the stress-strain curve is similar to ductile materials. The advantages of this model are in the presence of the rate-independent hysteresis property and dependence on few parameters, which simplifies the application of model calibration procedures.

Moreover, Peyret *et al.* (2017) demonstrated that the Dahl model can emulate the Mindlin model, a constitutive model recurrently used to represent contact problems in joints, and also follows the Masing hypothesis. However, the model is not capable of reproducing the Stribeck effect. Figure A.3 illustrates a schematic representation of the Dahl model's hysteretic force.

Figure A.3 – Schematic illustration of the friction force produced by the Dahl model.

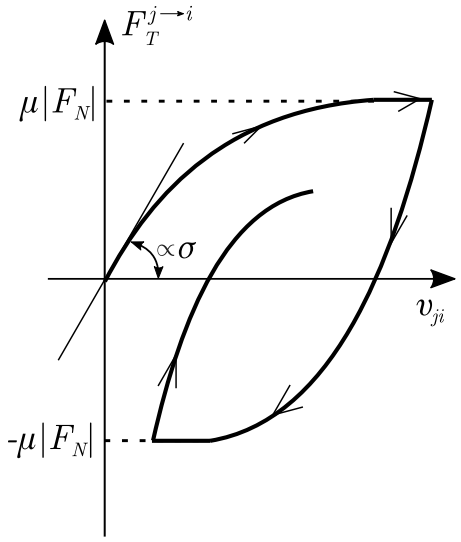

Source: Prepared by the author.

A.2.2 LuGre model

Proposed by Wit *et al.* (1995) in the context of friction compensation for controlling purposes, the LuGre[1] model is an enhancement of the Dahl model, with the advantage of representing the Stribeck effect appropriately. The model is formulated based on the supposition of contact between two rigid bodies by elastic bristles at the microscopic level, such that when a tangential force is applied, the bristles deflect and produce the frictional force. The model equation is given by:

$$
\begin{aligned}
F_T^{j\mapsto i} &= \sigma_0 z + \sigma_1 \dot{z} + b v_{ji}, \\
\dot{z} &= v_{ji} - \frac{\sigma_0 |v_{ji}|}{\mathcal{G}(v_{ji})} z, \\
\mathcal{G}(v_{ji}) &= \mu|F_N| + (F_s - \mu|F_N|) \exp\left[-\left(\frac{v_{ji}}{v_0}\right)\right],
\end{aligned}
\tag{A.5}
$$

where z is the bristle deformation, σ_0 and σ_1 denote the microstiffness and microdamping coefficients, respectively, and v_0 is the Stribeck velocity. Note the similarities between the functional term $\mathcal{G}(v_{ij})$ and the arbitrary function $\mathcal{F}(v_{ji})$ to represent the friction force in the Stribeck model. Thus, the LuGre model allows the friction force to be dependent on the sliding velocity (rate dependent hysteresis property) and also approximates the adhesion condition present in the Stribeck model.

[1]The name is an acronym of the research groups that developed the model, Lund and Grenoble.

Dion *et al.* (2013) demonstrated the use of LuGre model to characterize everything from sticking to complete sliding of a contact pair in a tribometer. Moreover, for reducing the complexity in dealing with the constitutive equation of the LuGre model, Naser and Ikhouane (2015) developed an alternative way to reproduce the loading and unloading regimes based on the concept of consistency and strong consistency.

A.2.3 Bouc-Wen model

Discussed throughout this Thesis, the model introduced by Bouc (1971) and expanded by Wen (1976) describes a generic hysteresis force, and not necessarily the friction force, in which different sets of parameters lead to the same output behavior. Such a generalized version can be seen in equation (5). Thus, to eliminate this redundancy, Ikhouane and Rodellar (2005) introduced the normalized form of the Bouc-Wen model, which is given by:

$$\Phi_{BW} = k_w w, \tag{A.6}$$

$$\dot{w} = \rho\left(\dot{x} - \sigma|\dot{x}||w|^{n-1}w + (\sigma - 1)\dot{x}|w|^n\right), \tag{A.7}$$

where the normalized terms are defined as:

$$w = \frac{\mathcal{Z}}{\mathcal{Z}_0}, \quad \mathcal{Z}_0 = \left(\frac{\alpha}{\beta(\gamma+\delta)}\right)^{1/n}, \quad \rho = \frac{\alpha}{\mathcal{Z}_0} > 0, \quad \sigma = \beta\left(\frac{\gamma}{\gamma+\delta}\right) \geq 0, \quad k_w = k\mathcal{Z}_0.$$

Thus, based on this normalized version, Guo *et al.* (2008) introduced a Bouc-Wen model to represent the friction force $F_T^{j\mapsto i} = \Phi_{BW}$, in which $\mathcal{Z}_0 = \mu|F_N|$ is the friction limit, $v_{ji} = \dot{x}$ is the sliding velocity, $\rho = \frac{\alpha}{\mu|F_T|}$ is the contact stiffness, n and σ control the smoothness of the transition from microslip to macroslip and the shape of the hysteresis loop, respectively. This new representation allows a physical interpretation on the Bouc-Wen parameters. Recently, Fantetti *et al.* (2019) adapted equations (A.6)-(A.7) to emulate the wear evolution present in a friction test-rig during experimental measurements. Although the Bouc-Wen model does not follow the Masing hypotheses, it is argued that this model can emulate any Iwan model, just by selecting its parameters properly.

A.2.4 Masing model

There is a parallel between the behavior present in joints and metal plasticity, in fact several models currently used in joints are derived from the metal plasticity standpoint (plasticity models). As mentioned throughout the Chapter 2, there are realistic representations of joints to describe hysteretic effects; but there are also simplified constitutive models also capable of emulating elasto-plasticity and hysteretic force-deformation curves of joints. In this context, Masing (1926) proposed a one-dimensional hysteretic system that is composed of an arrangement of ideal elasto-plastic elements, a linear spring in series with a slider (each of these cells is called as Jenkins element), carrying a distribution of different yield strengths (MUTO; BECK, 2008). Figure A.4(a) depicts a schematic generalization of the Masing model with N Jenkins elements. The total force necessary to impose a displacement x is given by the sum of the friction forces applied to the different elements:

$$F_T = \sum_{n=1}^{N} F_T^{(n)}, \quad \text{such that:} \begin{cases} F_T^{(n)} = k_n x, & \text{if} \quad \dfrac{\mu F_N^{(1)}}{k_1} \geq x \\ \\ F_T^{(n)} = \mu F_N^{(n)}, & \text{if} \quad \dfrac{\mu F_N^{(1)}}{k_1} < x \leq X, \quad n = 1, 2, \ldots, N. \end{cases} \tag{A.8}$$

Moreover, Masing (1926) formulated a description that simplifies obtaining a complete hysteresis cycle in the steady-state motion, recurrently referred to as Masing hypothesis. Simply put, it states that the force × displacement hysteresis curve can be extrapolated from the initial loading curve (JAYAKUMAR, 1987), so-called ''backbone curve''. Thus, if a $T-$periodic input is applied, only 1/4 of the total response cycle needs to be calculated, such that from the backbone curve, the remaining response interval can be deduced. In some applications involving bolted joints, it is assumed that each vibrating mode fulfills the Masing hypothesis (LACAYO; ALLEN, 2019). Figure A.4(b) illustrates a force × displacement curve that follows the Masing hypothesis.

Assuming that a joint is subjected to an initial cyclic deformation $0 \leq x \leq X_0$ and the initial loading force F follows the function $F = \mathcal{F}(x)$ up to the point $A(X_0, F_0)$, the unload regime is then written by the continuous function:

$$\mathcal{F}^{\downarrow}(x) = \mathcal{F}(X_0) - 2\mathcal{F}\left(\frac{X_0 - x}{2}\right). \tag{A.9}$$

Similarly, the loading path BC from $B(X_d, F_d)$ to $C(X_r, F_r)$ is given by:

$$\mathcal{F}^{\uparrow}(x) = \mathcal{F}^{\downarrow}(X_d) + 2\mathcal{F}\left(\frac{x - X_d}{2}\right). \tag{A.10}$$

To deduce a new path, simply consider equations (A.9)-(A.10) and replace the displacement X_0 with the current displacement X_r. Masing's hypothesis considers that the loading and unloading history depends only on its extremes, namely the reversal points (HELLER, 2005), and can be expanded to accommodate general hysteresis paths (SEGALMAN; STARR, 2012). Moreover, note that the hysteresis curve obtained during the loading path is assumed to have the same shape as the backbone curve, except for an expansion factor of order 2, whereas the unloading path also holds the same shape, but it is reflected across the origin. In general, Masing hypothesis simplifies the estimation of the energy dissipated per cycle for steady-state structural conditions, and is a key assumption for applying QSMA (FESTJENS; CHEVALLIER; DION, 2013).

Figure A.4 – (a) represents a schematic illustration of Masing model, whereas (b) is the force × displacement plane, ▬ is the backbone curve and ◯ are the reversal points.

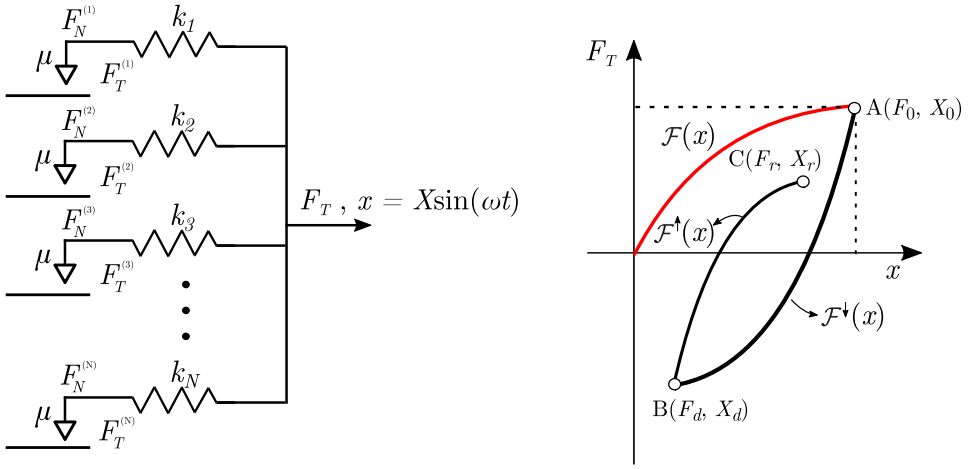

(a) Schematic representation of elasto-plastic elements.

(b) Force × displacement curve based on the Masing hypothesis.

Source: Prepared by the author.

A.2.5 Iwan model

The concept behind the Masing model was then expanded by Iwan (IWAN, 1966; IWAN, 1967) to reproduce the elasto-plasticity of metals using different arrangements of Jenkins elements, as illustrated in Fig. A.5. Such elements can be connected in series, in

parallel, or even a combination of both in order to represent different relationships between tangential force and displacement. As pointed out by Segalman and Starr (2012), all Iwan models are Masing models and all Masing models can be represented by Iwan models.

Figure A.5 – Different arrangements of the Iwan model: (a) is the parallel-series arrangement, whereas (b) is the series-parallel.

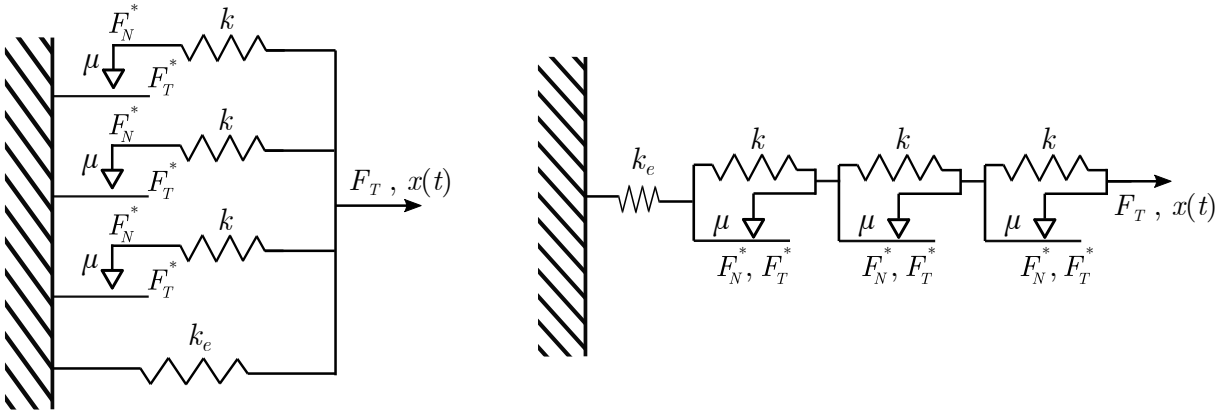

(a) Parallel-series Iwan model.

(b) Series-parallel Iwan model.

Source: Prepared by the author.

In the context of jointed structures, it is convenient to represent Iwan's model from a continuous domain point of view (LI *et al.*, 2020b), where the tangential force that leads to sliding is based on a Jenkins element distribution. Mathematically, the tangential force based on the Iwan constitutive model can be conveniently expressed as:

$$F_T = \int_0^\infty \mu F_N^* \pi(F_N^*) dF_N^*, \tag{A.11}$$

where the pressure at the interface is defined by the density function of Jenkins elements:

$$\int_0^\infty \pi(F_N^*) dF_N^* = 1. \tag{A.12}$$

The force associated to the initial displacement is given by:

$$F(x) = \int_0^{kx/\mu} \mu F_N^* \pi(F_N^*) dF_N^* + kx \int_{kx/\mu}^\infty \pi(F_N^*) dF_N^* + k_e x. \tag{A.13}$$

By substituting the friction force into the above equation, eq. (A.13) yields:

$$F(x) = \underbrace{\int_0^{kx} \mu F_T^* \pi(F_T^*) dF_T^*}_{\text{sliding regime}} + \underbrace{kx \int_{kx}^\infty \pi(F_T^*) dF_T^*}_{\text{adhesion regime}} + k_e x, \tag{A.14}$$

where $\pi(F_T^*) = \pi\left(\frac{F_T^*}{\mu}\right)$ represents the density distribution of the friction force. Moreover, the first term in equation (A.14) denotes the contribution of elements in sliding, whereas the second one is the elements in adhesion. Iwan (1967) demonstrated that the density distribution function can be deduced from the initial backbone curve by applying:

$$\pi(F_T^*) = \frac{1}{k^2}\frac{\partial^2 F}{\partial x^2}. \tag{A.15}$$

Figure A.6 illustrates a schematic representation of the force × displacement plane produced by a Iwan model. One of the main features present in the model is the possibility to describe the hysteresis loop from Masing hypothesis, thereby extending the applicability of the model to describe nonlinear dissipation effects in bolted joints.

Figure A.6 – Schematic illustration of a hysteresis loop generated by the Iwan model following the Masing hypothesis, where — is the backbone curve.

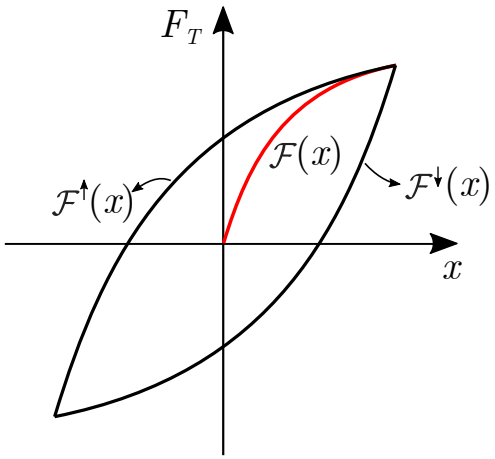

Source: Prepared by the author.

There are also extensions of the Iwan model, with emphasis on the Four-Parameter Iwan model proposed by Segalman (2005) due to its physical interpretation in applications involving bolted joints (MATHIS *et al.*, 2020).